

JSCSEN 88(9)811–935(2023)

ISSN 1820-7421(Online)

Journal of the Serbian Chemical Society

Electronic
version

VOLUME 88

No 9

BELGRADE 2023

Available on line at



www.shd.org.rs/JSCS/

The full search of JSCS
is available through

DOAJ DIRECTORY OF
OPEN ACCESS
JOURNALS
www.doaj.org

The **Journal of the Serbian Chemical Society** (formerly Glasnik Hemijskog društva Beograd), one volume (12 issues) per year, publishes articles from the fields of chemistry. The **Journal** is financially supported by the **Ministry of Education, Science and Technological Development of the Republic of Serbia**.

Articles published in the **Journal** are indexed in **Clarivate Analytics products: Science Citation Index-ExpandedTM** – accessed via **Web of Science[®]** and **Journal Citation Reports[®]**.

Impact Factor announced on 28 June, 2023: **1.000**; **5-year Impact Factor**: **1.100**.

Articles appearing in the **Journal** are also abstracted by: **Scopus**, **Chemical Abstracts Plus (CAplusSM)**, **Directory of Open Access Journals**, **Referativnii Zhurnal (VINITI)**, **RSC Analytical Abstracts**, **EuroPub**, **Pro Quest** and **Asian Digital Library**.

Publisher:

Serbian Chemical Society, Karnegijeva 4/III, P. O. Box 36, 1120 Belgrade 35, Serbia
tel./fax: +381–11–3370–467, E-mails: **Society** – shd@shd.org.rs; **Journal** – jscs@shd.org.rs
Home Pages: **Society** – <http://www.shd.org.rs/>; **Journal** – <http://www.shd.org.rs/JSCS/>
Contents, Abstracts and full papers (from Vol 64, No. 1, 1999) are available in the electronic form at the Web Site of the **Journal** (<http://www.shd.org.rs/JSCS/>).

Internet Service:

Former Editors:

Nikola A. Pušin (1930–1947), **Aleksandar M. Leko** (1948–1954),
Panta S. Tutundžić (1955–1961), **Miloš K. Mladenović** (1962–1964),
Đorđe M. Dimitrijević (1965–1969), **Aleksandar R. Despić** (1969–1975),
Slobodan V. Ribnikar (1975–1985), **Dragutin M. Dražić** (1986–2006).

Editor-in-Chief:

BRANISLAV Ž. NIKOLIĆ, Serbian Chemical Society (E-mail: jscs-ed@shd.org.rs)

Deputy Editor:

DUŠAN SLADIĆ, Faculty of Chemistry, University of Belgrade

Sub editors:

Organic Chemistry

DEJAN OPSENICA, Institute of Chemistry, Technology and Metallurgy, University of Belgrade

Biochemistry and

Biotechnology

JÁNOS CSANÁDI, Faculty of Science, University of Novi Sad

Inorganic Chemistry

OLGICA NEDIĆ, INEP – Institute for the Application of Nuclear Energy, University of Belgrade

Theoretical Chemistry

MILOŠ ĐURAN, Serbian Chemical Society

Physical Chemistry

IVAN JURANIĆ, Serbian Chemical Society

Electrochemistry

LJILJANA DAMJANOVIĆ-VASILJIĆ, Faculty of Physical Chemistry, University of Belgrade

Analytical Chemistry

SNEŽANA GOJKOVIĆ, Faculty of Technology and Metallurgy, University of Belgrade

Polymers

RADA BAOŠIĆ, Faculty of Chemistry, University of Belgrade

Thermodynamics

BRANKO DUNJIĆ, Faculty of Technology and Metallurgy, University of Belgrade

Chemical Engineering

MIRJANA KIJEVCANIN, Faculty of Technology and Metallurgy, University of Belgrade

Materials

TATJANA KALUĐEROVIĆ RADOIČIĆ, Faculty of Technology and Metallurgy, University of Belgrade

Metallic Materials and

Metallurgy

RADA PETROVIĆ, Faculty of Technology and Metallurgy, University of Belgrade

Environmental and

Geochemistry

ANA KOSTOV, Mining and Metallurgy Institute Bor, University of Belgrade

History of and

Education in Chemistry

VESNA ANTIĆ, Faculty of Agriculture, University of Belgrade

English Language

DRAGICA TRIVIĆ, Faculty of Chemistry, University of Belgrade

Editors:

LYNNE KATSIKAS, Serbian Chemical Society

VLATKA VAJS, Serbian Chemical Society

JASMINA NIKOLIĆ, Faculty of Technology and Metallurgy, University of Belgrade

Technical Editors:

VLADIMIR PANIĆ, Institute of Chemistry, Technology and Metallurgy, University of Belgrade

MARIO ZLATOVIĆ, Faculty of Chemistry, University of Belgrade

Journal Manager &

Web Master:

MARIO ZLATOVIĆ, Faculty of Chemistry, University of Belgrade

Office:

VERA ČUŠIĆ, Serbian Chemical Society

Editorial Board

From abroad: **R. Adžić**, Brookhaven National Laboratory (USA); **A. Casini**, University of Groningen (The Netherlands); **G. Cobb**, Baylor University (USA); **D. Douglas**, University of British Columbia (Canada); **G. Inzelt**, Etvos Lorand University (Hungary); **J. Kenny**, University of Perugia (Italy); **Ya. I. Korenman**, Voronezh Academy of Technology (Russian Federation); **M. D. Lechner**, University of Osnabrueck (Germany); **S. Macura**, Mayo Clinic (USA); **M. Spiteller**, INFU, Technical University Dortmund (Germany); **M. Stratakis**, University of Crete (Greece); **M. Swart**, University de Girona (Cataluna, Spain); **G. Vunjak-Novaković**, Columbia University (USA); **P. Worsfold**, University of Plymouth (UK); **J. Zagal**, Universidad de Santiago de Chile (Chile).

From Serbia: **B. Abramović**, **V. Antić**, **R. Baošić**, **V. Beškoski**, **J. Csanadi**, **Lj. Damjanović-Vasiljić**, **A. Dekanski**, **V. Dondur**, **B. Dunjić**, **M. Đuran**, **S. Gojković**, **I. Gutman**, **B. Jovančević**, **I. Juranić**, **T. Kaluđerović Radiočić**, **L. Katsikas**, **M. Kijevčanin**, **A. Kostov**, **V. Leovac**, **S. Milonjić**, **V.B. Mišković-Stanković**, **O. Nedić**, **B. Nikolić**, **J. Nikolić**, **D. Opsenica**, **V. Panić**, **M. Petkovska**, **R. Petrović**, **I. Popović**, **B. Radak**, **S. Ražić**, **D. Sladić**, **S. Sovilj**, **S. Šerbanović**, **B. Šolaja**, **Ž. Tešić**, **D. Trivić**, **V. Vajs**, **M. Zlatović**.

Subscription: The annual subscription rate is **150.00 €** including postage (surface mail) and handling. For Society members from abroad rate is **50.00 €**. For the proforma invoice with the instruction for bank payment contact the Society Office (E-mail: shd@shd.org.rs) or see JSCS Web Site: <http://www.shd.org.rs/JSCS/>, option Subscription.

Godišnja pretplata: Za članove SHD: **2.500,00 RSD**, za penzionere i studente: **1000,00 RSD**, a za ostale: **3.500,00 RSD**; za organizacije i ustanove: **16.000,00 RSD**. Uplate se vrše na tekući račun Društva: **205-13815-62**, poziv na broj **320**, sa naznakom "pretplata za JSCS".

Nota: Radovi čiji su svi autori članovi SHD prioritarno se publikuju.

Odlukom Odbora za hemiju Republičkog fonda za nauku Srbije, br. 66788/1 od 22.11.1990. godine, koja je kasnije potvrđena odlukom Saveta Fonda, časopis je uvršten u kategoriju međunarodnih časopisa (**M-23**). Takođe, aktom Ministarstva za nauku i tehnologiju Republike Srbije, 413-00-247/2000-01 od 15.06.2000. godine, ovaj časopis je proglašen za publikaciju od posebnog interesa za nauku. **Impact Factor** časopisa objavljen 28. juna 2023. godine je **1,000**, a petogodišnji **Impact Factor** **1,100**.



CONTENTS*

Organic Chemistry

- A. M. Lazić, A. D. Mašulović, J. M. Lađarević and N. V. Valentić: Assessing the pharmacological potential of selected xanthene derivatives 811
- O. Babatunde, S. Hameed, K. A. Mbachu, F. Saleem, S. Chigurupati, A. Wadood, A. Ur Rehman, V. Venugopal, K. M. Khan, M. Taha, O. Ekundayo and M. A. Khan: Evaluation of derivatives of 2,3-dihydroquinazolin-4(1H)-one as inhibitors of cholinesterases and their antioxidant activity: *In vitro*, *in silico* and kinetics studies 825

Biochemistry and Biotechnology

- S. Ceauranu, V. Ostafe and A. Isvoran: Impaired local hydrophobicity, structural stability and conformational flexibility due to point mutations in SULT1 family of enzymes 841

Theoretical Chemistry

- P. J. P. Tjitda, F. O. Nitbani, D. Mbunga and T. D. Wahyuningsih: Natural flavonoids in *Delonix regia* leaf as an antimycobacterial agent: An *in silico* study 859

Inorganic Chemistry

- T. Vitomirov, B. Čobeljić, A. Pevec, D. Radanović, I. Novaković, M. Savić, K. Anđelković and M. Šumar-Ristović: Binuclear azide-bridged hydrazone Cu(II) complex: Synthesis, characterization and evaluation of biological activity 877

Electrochemistry

- P. L. Marucci, M. G. Sica, L. I. Brugnoli and M. B. González: Bactericidal effects of copper–polypyrrole composites modified with silver nanoparticles against Gram-positive and Gram-negative bacteria 889

Chemical Engineering

- D. Jaćimovski, K. Šučurović, M. Đuriš, Z. Arsenijević, S. Krstić and N. Bošković-Vragolović: Mass transfer in inverse fluidized beds 905

Environmental

- M. Marković, M. Gorgievski, N. Štrbac, K. Božinović, V. Grekulović, A. Mitovski and M. Zdravković: Copper ions biosorption onto bean shells: Kinetics, equilibrium and process optimization studies 921

Published by the Serbian Chemical Society
Karnegijeva 4/III, P.O. Box 36, 11120 Belgrade, Serbia
Printed by the Faculty of Technology and Metallurgy
Karnegijeva 4, P.O. Box 35-03, 11120 Belgrade, Serbia

* For colored figures in this issue please see electronic version at the Journal Home Page:
<http://www.shd.org.rs/JSCS/>



J. Serb. Chem. Soc. 88 (9) 811–824 (2023)
JSCS–5664

Assessing the pharmacological potential of selected xanthene derivatives

ANITA M. LAZIĆ^{1*}, ALEKSANDRA D. MAŠULOVIĆ¹, JELENA M. LAĐAREVIĆ²
and NATAŠA V. VALENTIĆ²

¹Innovation Center, Faculty of Technology and Metallurgy, Belgrade, Serbia, and ²University of Belgrade, Faculty of Technology and Metallurgy, Belgrade, Serbia

(Received 31 January, revised 21 February, accepted 8 July 2023)

Abstract: A convenient and efficient approach toward the synthesis of seven aromatically substituted xanthendiones **1–7** and one structurally-related xanthenone **8** through condensation of dimedone and the appropriate aromatic aldehyde is reported. Further, their chemical structure was confirmed by melting points, elemental analysis, FT-IR, ¹H-, ¹³C-NMR and UV-Vis spectroscopic methods. The relationship between the chemical structure and pharmacological activity was determined empirically using appropriate software packages and *in vitro* using the 2,2'-azinobis-(3-ethylbenzothiazoline-6-sulfonic acid (ABTS) method. The results of *in silico* prediction suggested that all investigated compounds possess good oral bioavailability. The results of the ABTS assay indicate that five compounds possess the ability to scavenge the ABTS^{•+} radical cation. Based on the comparison of the IC₅₀ values, the activity of the compounds was found to be as follows: **6** > **1** > **7** > **2** > **8**. The effects of solvent dipolarity/polarizability and solute solvent-hydrogen-bonding interactions on the shifts of the absorption maxima were rationalized by means of the linear solvation energy relationship concepts proposed by Kamlet-Taft and Catalán.

Keywords: heterocycles; chemoinformatics prediction models; antioxidant activity; LSER analysis; solvatochromism.

INTRODUCTION

The expansion of degenerative diseases induced by oxidative stress and incorporation of free radicals, including atherosclerosis, ischemic heart disease, diabetes mellitus and cancer, presents one of the main problems of today's society.^{1,2} Scientists are in a constant search for a novel scaffold with structural diversity and complexity to play a fundamental role in the drug discovery pipeline. Herein, fused benzene or hetero benzene rings in linear, angular or clustered arrangements present interesting compounds due to their chemical structures and

* Corresponding author. E-mail: alazic@tmf.bg.ac.rs
<https://doi.org/10.2298/JSC230131035L>



biological activities.³ Moreover, numerous compounds containing fused rings with oxygenated phenyl moieties, are used as anticancer and anti-inflammatory agents⁴⁻⁶ and have shown to inhibit the growth of cancer cells.⁷ On this behalf, an oxygen-incorporating tricyclic compound, xanthene, arises as an interesting structural scaffold with various beneficial heterogeneous pharmacological activities.⁸ The literature review showed that xanthene nucleus has been reported to be a versatile and suitable towards obtaining compounds for different biological targets.⁹ For example, xanthendiones (1,8-dioxooctahydroxanthenes) are a special class of oxygen-incorporating tricyclic compounds⁹ bearing as a basic feature a pyran nucleus fused on either side with cyclohex-2-enone rings.¹⁰ They are often found as a structural motif in natural products with a wide range of biological activities, such as: antioxidant¹¹⁻¹⁴ antimicrobial,^{11,12,15} trypanocidal,¹⁶ antiinflammatory,¹⁶ antiproliferative^{11,12} and anticancer.^{17,18} Besides, xanthendiones are effective inhibitors of trypanothione reductase, bone morphogenetic protein (BMP-2)-targeted osteogenic agents, selective positive allosteric modulators of the δ -opioid receptors and estrogen receptors.¹⁹

As expected, the substitution pattern of the xanthene core will define the respective pharmacological response of the synthesized molecule.⁹ Bhat *et al.* demonstrated that xanthendiones with electron-withdrawing halogen substituents show a broad spectrum of antibacterial activity against both Gram-positive and Gram-negative bacteria. Also, xanthendiones bearing the nitro group in *meta* position of the phenyl ring are two times more potent against *Candida albicans* and four times more potent against *Aspergillus clavatus* when compared to referent drug griseofulvin.¹⁵ Moreover, Zukić *et al.*⁹ showed that slight variations in structure lead to different activities of xanthendiones. Compounds bearing two hydroxy groups in *meta* and *para* position of the phenyl ring possess high antioxidant activity, while compounds bearing bromine atom in their structure exhibit high antimicrobial activity against *Escherichia coli* and *Salmonella aureus*.¹² Results of the antitubercular screening indicated that xanthene derivatives with the electron-withdrawing substituents possess prominent antimycobacterial activity against the MTB H37Ra and *Mycobacterium bovis* BCG.¹⁹ Recent studies have shown that incorporating heterocyclic rings in molecular structure ameliorates antibacterial ability of newly synthesized compounds.²⁰ Small heterocycle-structured molecules targeting RNA in living cells and providing successful therapeutic agents have been reported in the literature.²¹ For example, docking studies showed that these xanthendiones exhibit high binding affinity towards the amino acid residues of ATP binding pocket of human PIM1 kinase receptor through van der Waals interactions, steric favorable interactions and hydrogen bonding, thus being promising anticancer drugs.¹⁵ Ilangovan *et al.*⁸ demonstrated that 14-aryl-14*H*-dibenzo[*a,j*]xanthene derivatives act as good radical scavengers against DPPH and ABTS^{•+} due to the presence of butterfly-like planar naphthal-

ene rings on both sides of pyran ring and the presence of strong electron-donating substituents on the phenyl ring. Besides their pharmacological activity, xanthendiones can also be used in the preparation of stable laser dyes, fluorescent sensors and protein labeling fluorophores used in laser technology, functional materials for visualization of biomolecular assemblies, photodynamic therapy and as antagonists.¹⁸

Drug discovery is an inventive process of finding new potentially pharmacologically active compounds based on a combination of computational, experimental and clinical models and the knowledge of biological targets.²² Drug-likeness of the compounds should present appropriate absorption, distribution, metabolism, excretion–toxicity (ADMET) properties leading progression from pre-clinical assessment to clinical evaluation. The rules of good bioavailability are often applied, among which the most popular is Lipinski's rule. According to the "rule of five", good oral absorption can be expected for compounds whose set of physicochemical parameters is in the following ranges: partition coefficient ($\log P$) < 5 , number of hydrogen bond donors < 5 , number of hydrogen bond acceptors < 10 , relative molecular mass < 500 .²³ Potentially pharmacologically active compounds often bear numerous functional groups capable of forming hydrogen bonds, making them soluble and giving them the ability to form specific interactions with their biomolecular targets.²⁴ Hydrogen bonding influences the interactions of potentially pharmacologically active organic compounds at different levels of complexity, going from those with other small molecules, up to the highest supramolecular assemblies, *e.g.*, proteins and membranes. These interactions considerably affect the pharmacological activity, pharmacokinetics and physicochemical properties of drugs, hence making hydrogen bonding an important subject of study in drug discovery and development.²⁵ Therefore, solvatochromic study gives an insight into possible different solute–solvent interactions mimicking the interactions of potentially pharmacologically active organic compounds with their environment.

Keeping in mind the above stated application and activities of xanthene derivatives, seven xanthendiones (**1–7**) and one structurally-related xanthenone (**8**) are synthesized and thoroughly characterized. Sulfur and oxygen-containing heterocycles are widely used because of their key function in fulfilling needs in medicinal chemistry,^{26–28} and therefore are incorporated into xanthendione scaffolds in compounds **3** and **4**. In aspiration to achieve new and high potent anti-oxidant agents, herein, we examined radical scavenging properties of the synthesized compounds using the 2,2'-azinobis-(3-ethylbenzothiazoline-6-sulfonic acid (ABTS) method. *In silico* prediction was performed in order to evaluate pharmacokinetic profiles of the synthesized compounds related to absorption properties and biophysical-kinetic profiles of the synthesized compounds related to metabolism properties. The effects of specific solvent-solute interactions (hydro-

gen bonding) which are related to the molecular structure of a compound and nonspecific solvent–solute interactions (dipolarity/polarizability of solvents) on the absorption maxima shifts were interpreted by using the linear solvation energy relationship (LSER) concept proposed by Kamlet, Taft and Catalán.^{29,30}

EXPERIMENTAL

The general information

All chemicals, reagents and solvents were supplied by Sigma–Aldrich and were used without further purification.

Spectroscopic measurements

¹H-NMR spectra were recorded on a Bruker Ascend 400 spectrophotometer at 400 MHz, while ¹³C-NMR spectra were recorded at 100 MHz at to the same device. ¹H- and ¹³C-NMR spectra of compounds **1** and **7** were recorded at room temperature in deuterated dimethyl sulfoxide (DMSO-*d*₆), while the ¹H- and ¹³C-NMR spectra of compounds **2–6** and **8** were recorded in deuterated chloroform (CDCl₃). The chemical shifts are expressed in ppm in relation to the reference TMS ($\delta_{\text{H}} = 0$ ppm). FT-IR spectra of all synthesized compounds were recorded in the range from 400 to 4000 cm⁻¹ using a Thermo Scientific Nicolet iS10 spectrometer, within the spectral resolution range of 400–4000 cm⁻¹. Elemental analysis of all studied compounds was performed using a microanalyzer brand Elemental Vario EL III.

General procedure for synthesis of compounds 1–8

The synthesis of compounds **1–7** is illustrated in Scheme 1, while the synthesis of compound **8** is presented in Scheme 2.³¹ 3,5-Dibromo-4-hydroxybenzaldehyde and 3-chloro-4-hydroxybenzaldehyde, used for further synthesis of compounds **2** and **7**, respectively, were synthesized according to the procedures illustrated on Schemes S-1 and S-2 (Supplementary material to this paper). 5,5-Dimethylcyclohexane-1,3-dione (2 mmol) was dissolved in water prior to the addition of 1 mmol of corresponding aldehyde. The reaction mixture was stirred at room temperature for 60 min while the course of the reaction was monitored by TLC. The reaction was completed for 60 min. Solid product was isolated by simple filtration and dried.³² Obtained solid product (1 mmol) was dissolved in absolute ethanol (10 mL) in an Erlenmeyer flask (50 mL) with gentle heating. Furthermore, water (2.5 mL) and HCl (6 M, six drops) were added to the solution, and the mixture was boiled for 5 min. After cooling, water was added dropwise until the mixture became cloudy. The suspension was cooled at 0 °C, for 10 min. Crystals were collected by vacuum filtration and washed with several portions (10 mL total volume) of ice cold ethanol:water (1:1 volume ratio) to yield compounds **1–8**. The solid products **1–8** were fully characterized by FT-IR, ¹H- and ¹³C-NMR spectra (Supplementary material, Figs. S-1–S-8) and elemental analysis.

In-silico prediction

Determination of the relevant molecular descriptors for all synthesized compounds was assessed employing the following software packages: SwissADME (Swiss Institute of Bioinformatics, Switzerland³³) and PreADMET (East China University of Science and Technology, China³⁴).

Antioxidant activity

The antioxidant activity of investigated compounds **1–8** was determined using ABTS radical-scavenging assay.³⁵ A stock solution of ABTS^{•+} was prepared in the reaction of ABTS (4.912 mL, 7 mM in phosphate-buffered saline (PBS)) and potassium persulfate (0.088 mL,

140 mM in distilled water). After 16 h of incubation in the dark, the stock solution was diluted with methanol until the recorded absorbance at 734 nm was 0.700 ± 0.02 . Subsequently, 20 μL of the methanolic solutions of the investigated compounds (5 mM) were mixed with 2 mL of the ABTS radical solution, shaken and stored in the dark for 10 min. Afterward the absorbance was measured at 734 nm. Each test was done in triplicate. The inhibition percentage of $\text{ABTS}^{\bullet+}$ was calculated using the formula:

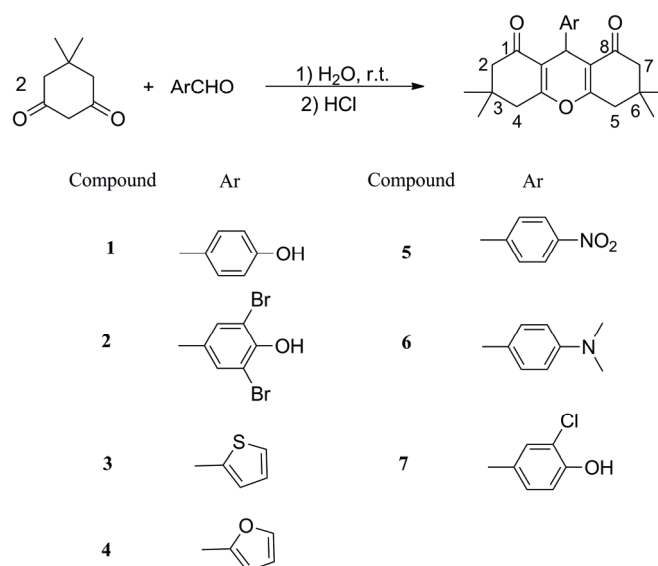
$$\text{Inhibition} = 100(A_c - A_s)/A_c \quad (1)$$

where A_c is the absorbance of the control solution (20 μL of methanol in 2 mL of ABTS solution) and A_s is the absorbance of the sample solution. Ascorbic acid was used as a standard antioxidant. The antioxidant ability of the most promising derivatives **1**, **2** and **6–8** was further evaluated by determination of the IC_{50} values. The methanolic solutions of the synthesized compounds and ascorbic acid were prepared at concentrations ranging from 5 to 0.5 mM, and obtained IC_{50} were compared. The tests were performed in triplicate. The resulting IC_{50} values are presented as means with standard deviation ($\pm SD$) from three experiments ($n = 3$).

RESULTS AND DISCUSSION

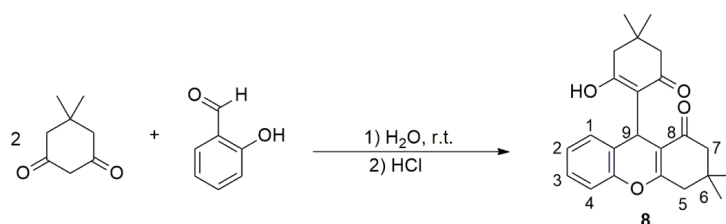
Synthesis and characterization

The synthesis of compounds **1–7** is illustrated in Scheme 1, while the synthesis of compound **8** is presented in Scheme 2. 3,5-Dibromo-4-hydroxybenzaldehyde and 3-chloro-4-hydroxybenzaldehyde, used for further synthesis of compounds **2** and **7**, respectively, were synthesized according to procedures illustrated on Schemes S-1 and S-2. The synthesis of compounds **1–7** involves the formation of a Knoevenagel product **A**, which, through the addition of **B**, was further converted in the Michael adduct intermediate **C** (Scheme S-3 of the Sup-



Scheme 1. Synthesis of compounds **1–7**.

plementary material). Nucleophilic attack of the –OH group on the C=C moiety gave compounds **1–7**.^{36,37} On the other hand, when using salicylaldehyde in the reaction with dimedone, the reaction course occurs according to Scheme S-4 (Supplementary material) and results in a formation of 9-(2-hydroxy-4,4-dimethyl-6-oxocyclohex-1-enyl)-3,3-dimethyl-2,3,4,9-tetrahydro-1*H*-xanthen-1-one (**8**).^{38,39}



Scheme 2. Synthesis of compound **8**.

Multiparameter optimization of molecular descriptors of 1–8

First essential aspect of the potentially pharmacologically active compounds, to be considered, is their drug-likeness. Therefore, the pharmacokinetic profile of compounds **1–8** was evaluated by predicting the appropriate ADMET characteristics, using various empirical rules and appropriate software packages.

Molecules considered to have properties similar to standard drugs must not show more than one deviation from Lipinski's rule. According to Veber's criterion, adequate oral bioavailability is achieved with molecules that have less than 10 rotatable bonds and a topological polar surface of less than 140 Å².⁴⁰ According to the modified versions of these two concepts, for compounds whose physicochemical properties satisfy the following ranges: 160 ≤ relative molecular mass ≤ 500; –0.4 ≤ WLOGP < 5.6; 40 ≤ molar refractivity ≤ 130; 20 ≤ number of atoms ≤ 70 (Goose's criterion) and WLOGP ≤ 5.88, *TPSA* (topological polar surface area) < 131.6 Å² (Egan's criterion), there is a high probability of manifesting therapeutic effects.⁴¹ Based on the values of the molecular descriptors described in these rules (Tables S-I and S-II, Supplementary material), it can be concluded that the examined compounds (except compound **2** with the molecular weight > 500 g/mol and log *P* > 5) meet all the stated empirical criteria. Tables S-I and S-II show that they fulfill the theoretical condition for adequate biological availability in the body and therefore possess a pharmacological potential. Based on the calculated values of the topological polar surface area of the molecule, it is expected that in *in vivo* conditions, the investigated compounds will show good intestinal absorption. Furthermore, a small number of rotatable bonds suggests that significant conformational changes upon solvation and binding to appropriate receptors are not expected.²³

Hence, the complete series of compounds was further examined with SwissADME and PreADMET *in silico* tools regarding their BBB permeation,

P-gp inhibition, inhibition of cytochrome P450 (CYP) (1A2, 2C19, 2C9, 2D6, 3A4) and considerations were performed in accordance with the information gathered. Comprehensive results are presented in Supplementary material (Tables S-II and S-III).⁹ The data presented in Table S-II show that different partition coefficient values were obtained for the same compound, which is a consequence of different mathematical algorithms for calculating this parameter within the used software packages.^{19,20} The highest values of the partition coefficient were obtained for compound **2**, which enables this molecule to more successfully pass through the blood–brain barrier by passive diffusion, as well as to more successfully bind to the active sites on the corresponding receptors.

Obtained data indicated that compounds **1**, **4**, **6** and **7** were found to be BBB permeant and only compound **5** was found not to be P-gp inhibitor.⁹ According to obtained results, it can be concluded that all investigated compounds possess high gastrointestinal absorption, inhibit isoenzymes CYP2C19 and CYP2C9 and don't inhibit isoenzymes CYP1A2 and CYP2D6. Based on the optimal values of the molecular descriptors obtained by applying appropriate software packages, it can be concluded that the compounds synthesized in this work meet all the necessary empirical criteria, which further qualify them as interesting drug candidates.

Antioxidant activity of the investigated compounds 1–8

Evaluation of the antioxidant properties of the synthesized compounds was assessed using the ABTS assay and the scavenging activity was further compared to the activity of ascorbic acid (Fig. 1a). As antioxidants provide either hydrogen atoms or electrons to neutralize the single electron originating from free radicals, exploring effective antioxidants is of importance in medicinal chemistry.⁴² The obtained data indicate variable activity of the compounds, designating that substituents in position 9 of xanthendiones affect the antioxidant ability of the molecules. Considering most of the compounds bear *p*-substituted phenyl scaffold (**1**, **2** and **5–7**) as a substituent in position 9 of xanthendione moiety, the choice of thiophene and furan rings should be further explained, in this section, from the aspect of antioxidant activity. Compounds **1** (with the 4-hydroxy phenyl ring), **2** (3,5-dibromo-4-hydroxy substituted phenyl ring), **6** (with the 4-dimethylamino substituted phenyl ring), **7** (with the 3-chloro-4-hydroxy substituted phenyl ring) and **8** exhibited excellent ability to scavenge the ABTS^{•+}, comparing to the inhibition of ascorbic acid. Other compounds (**3–5**) showed weak or no antioxidant properties. Despite the expected data, wherein incorporating thiophene and furan nuclei with other heterocyclic compounds improves antioxidant activity,^{26–28,43,44} compounds **3** and **4** do not exhibit significant amelioration in activity when compared to analogues. Incorporating these scaffolds, as pharmacophores of choice for designing antioxidant drugs, known for the excellent results through various

mechanisms of action,^{26–28,43,44} has shown to have little to no effect on the antioxidant potential as substituents on xanthendione moiety in this case.

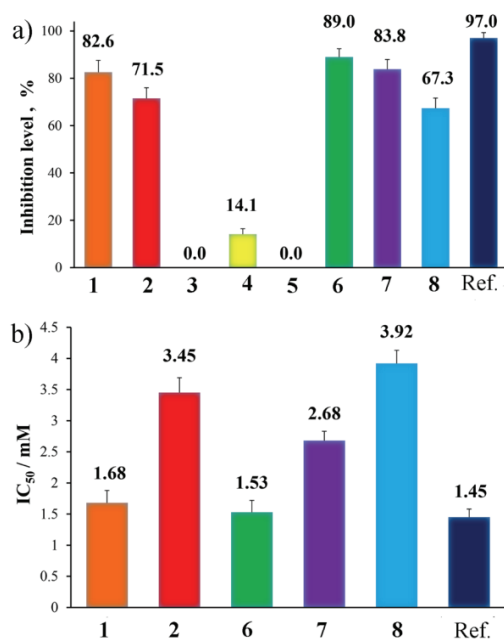


Fig. 1. The antioxidant properties of investigated compounds compared to the ascorbic acid. a) The scavenging activity at the sample concentration of 5mM; b) the IC_{50} values of compounds 1, 2 and 6–8 and ascorbic acid used as reference.

The antioxidant activity of candidates 1, 2 and 6–8 was further evaluated by the determination of IC_{50} values (Fig. 1b). The high IC_{50} values generally suggest low antioxidant activity. The IC_{50} values of the samples, ranging from 1.53 to 3.92 mM, indicate that these compounds demonstrate good antioxidant capacity in comparison to IC_{50} value of ascorbic acid (1.45 mM). Based on the comparison of the IC_{50} values, the activity of these compounds was found to be as follows: 6 > 1 > 7 > 2 > 8. Based on the obtained results and literature survey, it could be concluded that the antioxidant activity is mainly associated with the presence of –OH group in the *para*-position of the phenyl ring which is in line with the well-established fact that phenolic functionality has considerable scavenging potential.^{43,45} Notably, the most potent compound 6 bears *p*-dimethyl-amino group in the phenyl ring indicating that this group imparts significant antioxidant activity and is in accordance with the literature data.^{46,47}

Solvatochromic analysis of the investigated compounds 1–8

It is known that the physicochemical and photochemical properties of different π -conjugated structures are influenced by the extent of their π -electron con-

jugation and the nature of functional groups attached to the conjugated chain as well as the nature of the surrounding medium.⁴⁸ Bearing this in mind, we directed our solvatochromic research towards an extensive analysis of the influence of specific and non-specific solvent interactions on the absorption maxima shift of these compounds containing different chromophores and auxochromes.

The solvatochromic properties of compounds **1–8** were investigated by determining the corresponding UV–Vis absorption spectra in a selected solvent set of different polarity (seven protic, ten aprotic and two nonpolar solvents) in the wavelength range 200–500 nm. The UV–Vis absorption spectra of the investigated compounds **1–8** showed no dependence of compound concentration suggesting that no dimmers or higher aggregates are formed. Representative UV–Vis spectra are presented in Figs. S-9–S-11 (Supplementary material), while the values of the absorption maxima are given in Table S-IV (Supplementary material). The observed trends in the absorption maxima shifts are in accordance with previously published results.^{49–51} Namely, the absorption spectra of all investigated compounds are characterized by the presence of one dominant band corresponding to the $\pi \rightarrow \pi^*$ transition, which appears in the wavelength range of 220–270 nm in the polar protic solvents and the range of 280–300 nm in polar aprotic solvents and non-polar solvents. In addition, based on the data presented in Table S-IV, when polar protic solvents are used, all investigated compounds show additional absorption maxima in the wavelength range of 290–300 nm. This splitting of the absorption band could be attributed to a protonation reaction which is likely to occur at the carbonyl moieties and hydroxyl groups.³⁰ In the case of compound **6**, a shoulder at *ca.* 250 nm appears in diethyl ether and acetonitrile. Based on the data given in Table S-IV and the absorption spectra presented in Figs. S-9–S-11, it can be concluded that increasing solvent polarity causes bathochromic shifts of absorption maxima.

The influence of the solvent parameters (the effects of solvent polarity and hydrogen bonding) on the position of the absorption maxima is of very complex nature and was therefore analyzed mathematically in more detail⁵² using general solvatochromic equations established by Kamlet–Taft (Eq. (2)) and Catalán (Eq. (3)):

$$\nu_{\max} = \nu_{\max 0} + a\alpha + b\beta + s\pi^* \quad (2)$$

$$\nu_{\max} = \nu_{\max 0} + aSA + bSB + cSP + dSdP \quad (3)$$

where ν_{\max} is a solvent-dependent physicochemical property in a given solvent, $\nu_{\max 0}$ is a statistical quantity that corresponds to the absorption frequency in cyclohexane as a reference solvent, α is a measure of the acidity of the solvent, describing its ability to donate a proton when establishing a hydrogen bond, β is a measure of the basicity of the solvent, *i.e.*, its ability to receive a proton when establishing a hydrogen bond, π^* is a measure of dipolarity/polarizability of the solvent, (Table S-V, Supplementary material).⁵³

SA is a measure of the acidity of the solvent, *i.e.*, it describes its ability to donate a proton when establishing a hydrogen bond, *SB* is a measure of the basicity of the solvent, *i.e.*, its ability to receive a proton when establishing a hydrogen bond and *SPP* is a measure of dipolarity/polarizability of the solvent. Parameters *SA*, *SB* and *SPP* (Table S-V) are equivalent to the Kamlet–Taft α , β and π^* solvatochromic parameters.

In 2004, Catalán and Hopf²⁷ developed another important solvatochromic parameter, known as solvent polarizability, *SP*. *a*, *b*, *c* and *d* are regression coefficients describing the sensitivity of properties α , β and π^* , that is *SA*, *SB*, *SPP* and *SP* to the different solute–solvent interactions.

The values of the regression coefficients with a probability of 95 %, together with the percentage contribution of solvatochromic parameters are shown in Tables S-VI and S-VII (Supplementary material). The respective correlation coefficients obtained for both solvent parameter sets are in a good agreement with each other, therefore both models are equally suitable for describing specific/nonspecific solute–solvent interactions. Based on the high values of the obtained regression coefficients and the Fisher parameter, the results of the correlation of absorption frequencies with solvatochromic parameters can be considered satisfactory.

The data presented in Table S-VI indicate a bathochromic shift of the absorption maxima with the increasing solvent polarity expressed by the negative coefficient *s*. This indicates that a better stabilization of the excited state of the molecule compared to its ground state was confirmed. The negative values of coefficient *b* (compounds **1–3** and **7**, Table S-VI) indicate that the solvent basicity affects the molecule more in the excited than in the ground state. In the same manner, the negative values of the coefficient *a* (compounds **1**, **3**, **4**, **6** and **7**, Table S-VI) indicate that the solvent acidity affects the molecule more in the excited than in the ground state. The negative values of *a* term could be explained by the strong intermolecular hydrogen bonding of hydrogen bond donor (HBD) solvents with the carbonyl moieties of investigated compounds, which further reduces their electron density and thus increases the push–pull character of the chromophore. Based on the values of the percentages of solvatochromic parameters (Table S-VI), it can be concluded that for compounds **2** and **5–7**, the dipolarity/polarizability of the solvent is more dominant in relation to its acid–base properties, while with compounds **3**, **4** and **8**, the acidity of the solvent is more dominant and with compound **1** the basicity of the solvent. The strongest influence of the acidity of the solvent in compounds **3** and **4** can be ascribed to furanyl- and thiophenyl-groups used as substituents in position 9 of the xanthenone moiety.⁵²

Analogously to the previously applied model, it was observed that the negative values of the coefficients *a*, *b*, *c* and *d* in the Catalán model (Table S-VII)

indicate that the solvent effects are more pronounced in the excited than in the ground state of the studied molecules. It is also confirmed that the dipolar investigated compounds (with the exception of compounds **3** and **5**) show positive solvatochromism with regard to dipolarity/polarizability as indicated by negative *c* and *d* terms (Table S-VII). Considering the solvent acidity, the exception from the series are compounds **5** and **6**, where positive values of the coefficient *a* indicate that the hydrogen bonding better stabilizes the ground than the excited state of the molecule. The disagreement between the results obtained by these two models is influenced by different solvatochromic probes used for the determination of the parameters, thus reflecting different solvent–solute interactions. The Kamlet–Taft empirical parameters are obtained as average experimental values of numerous solvatochromic probes, while Catalán’s empirical solvent scales are based on well-defined reference probe systems.⁵⁴

CONCLUSION

In this study, we synthesized seven aromatically substituted xanthendiones **1–7** and one structurally-related xanthenone **8** and screened their potential pharmacokinetic properties using convenient chemoinformatics prediction models (SwissADME and PreADMET). The results of chemoinformatics prediction models showed that almost all investigated compounds (with the exception of compound **2**) meet Lipinski’s rule of five and its extensions, such as Veber’s, Egan’s and Goose’s criterion, indicating their good oral bioavailability. The antioxidant screening carried out according to the ABTS assay revealed the anti-radical properties of the investigated compounds. This study also revealed that the antioxidant activities were in the following order: **6** > **1** > **7** > **2** > **8**, based on the comparison of their *IC*₅₀ values. Compound **6** is the most active with *IC*₅₀ value comparable with *IC*₅₀ value of ascorbic acid. The results obtained by general solvatochromic equations established by Kamlet–Taft and Catalán indicate that the position of the UV–Vis absorption maxima depends on the nature (polarity, acidity and basicity) of the solvent. With their high antioxidant activities and good oral bioavailability, the investigated compounds have set the path for the preparation of new pharmacologically active compounds and a better understanding of the structure–activity relationship.

SUPPLEMENTARY MATERIAL

Additional data and information are available electronically at the pages of journal website: <https://www.shd-pub.org.rs/index.php/JSCS/article/view/12258>, or from the corresponding author on request.

Acknowledgement. This work was supported by the Ministry of Science, Technological Development and Innovation of the Republic of Serbia (Contracts No. 451-03-47/2023-01/200135 and 451-03-47/2023-01/200287).

ИЗВОД

ОДРЕЂИВАЊЕ ФАРМАКОЛОШКЕ АКТИВНОСТИ ДЕРИВАТА КСАНТЕНА

АНИТА М. ЛАЗИЋ¹, АЛЕКСАНДРА Д. МАШУЛОВИЋ¹, ЈЕЛЕНА М. ЛАЂАРЕВИЋ² и НАТАША В. ВАЛЕНТИЋ²¹Иновациони центар Технолошко–металуришкој факултетиа, Београд и ²Универзитет у Београду, Технолошко–металуришки факултетиа, Београд

У овом раду, представљена је једноставна метода у два корака за синтезу седам деривата ксантендиона и једног деривата ксантенона који садрже различите ароматичне супституенте, полазећи од димедона и одговарајућих ароматичних алдехида. Карактеризација синтетисаних једињења извршена је одређивањем температуре топљења, као и применом елементарне анализе, FT-IR, ¹H-NMR и ¹³C-NMR спектроскопских метода. Веза између хемијске структуре ових једињења и њихове фармаколошке активности успостављена је емпиријски коришћењем одговарајућих софтверских пакета (за предикцију фармаколошке активности) и *in vitro* одређивањем њихове антиоксидативне активности применом АВТС методе. Резултати АВТС методе показују да од целокупне серије тестираних једињења, пет једињења показује значајну антиоксидативну активност. На основу међусобног поређења *IC*₅₀ вредности испитиваних једињења показано је да њихова антиоксидативна активност опада у следећем низу: **6** > **1** > **7** > **2** > **8**. Једињење **6** је најактивније у анализираној серији и има *IC*₅₀ вредност приближне вредности као аскорбинска киселина. Резултати солватохромних једначина које су развили Камлет (Kamlet), Тафт (Taft) и Каталан (Catalán), указују да положај апсорпционих максимума проучаваних једињења зависи од природе (поларности и кисело-базних својстава) употребљених растварача. Са високим вредностима антиоксидативне активности и добром оралном биорасположивошћу, деривати ксантендиона и ксантенона са ароматичним супституентима, представљају добру полазну основу за синтезу нових фармаколошки активних једињења и боље разумевање утицаја структуре на фармаколошку активност.

(Примљено 31. јануара, ревидирано 21. фебруара, прихваћено 8. јула 2023)

REFERENCES

1. N. Karmaker, D. N. Lira, B. K. Das, U. Kumar, A.S. S. Rouf, *Dhaka Univ. J. Pharm. Sci.* **16** (2017) 245 (<https://dx.doi.org/10.3329/dujps.v16i2.35263>)
2. T. K. Khatab, A. El-Mekabaty, Z. M. Gamala, E. M. Kandil, *Egypt. J. Chem.* **61** (2018) 661 (<https://dx.doi.org/10.21608/ejchem.2018.3381.1285>)
3. A. G. Ghahsare, Z. S. Nazifi, S. M. R. Nazifi, *Curr. Org. Synth.* **16** (2019) 1071 (<https://dx.doi.org/10.2174/1570179416666191017094908>)
4. W. A. A. Fadaly, Y. A. M. M. Elshaier, M. T. M. Nemr, K. R. A. Abdellatif, *Bioorg. Chem.* **134** (2023) 106428 (<https://dx.doi.org/10.1016/j.bioorg.2023.106428>)
5. M. T. M. Nemr, A.M. AboulMagd, *Bioorg. Chem.* **103** (2020) 104134 (<https://dx.doi.org/10.1016/j.bioorg.2020.104134>)
6. A. H. M. Hussein, A. A. Khames, A.-B. A El-Adasy, A. A. Atalla, M. Abdel-Rady, M. I. A. Hassan, M. T. M. Nemr, Y. A. A. M.Elshaier, *RSC Adv.* **10** (2020) 29723 (<https://dx.doi.org/10.1039/d0ra05561a>)
7. M. T. M. Nemr, A. Sonousi, A. A. Marzouk, *Bioorg. Chem.* **105** (2020) 104446 (<https://dx.doi.org/10.1016/j.bioorg.2020.104446>)
8. Shagufta, I. Ahmad, *Eur. J. Med. Chem.* **116** (2016) 267 (<https://dx.doi.org/10.1016/j.ejmech.2016.03.058>)
9. M. Maia, D. I. S. P. Resende, F. Durães, M. M. M. Pinto, E. Sousa, *Eur. J. Med. Chem.* **210** (2021) 113085 (<https://dx.doi.org/10.1016/j.ejmech.2020.113085>)

10. Í. E. Poly da Silva, M. Lopes da Silva, R. Sousa Dias, E. Gonçalves Santos, M. C. Brangioni de Paula, A. Silva de Oliveira, A. F. Costa da Silveira Oliveira, F. Marques de Oliveira, C. Canedo da Silva, R. R. Teixeira, S. Oliveira de Paula, *Microbes Infect.* **22** (2020) 489 (<https://dx.doi.org/10.1016/j.micinf.2020.04.007>)
11. E. Veljović, S. Špirtović-Halilović, S. Muratović, A. Osmanović, I. Novaković, S. Trifunović, D. Završnik, *Bull. Chem. Technol. Bosnia Herzegovina* **51** (2018) 13
12. S. Zukić, E. Veljović S. Špirtović-Halilović, S. Muratović, A. Osmanović, S. S. Trifunović, I. Novaković, D. Završnik, *Croat. Chem. Acta* **91** (2018) 1 (<https://dx.doi.org/10.5562/cca3225>).
13. R. Retnosari, K. K. Sari, S. Marfu'ah, Sutrisno, I. B. Rachman, *Commun. Sci. Technol.* **7** (2022) 181 (<https://dx.doi.org/10.21924/cst.7.2.2022.963>)
14. R. Retnosari, N. Ultiyati, A. Santoso, S. Marfu'ah, I. B. Rachman, *J. Kim. Kemasan* **43** (2021) 117 (<https://dx.doi.org/10.24817/jkk.v43i2.7027>)
15. A. H. Bhat, V. R. Shah, M. R. Rawal, *World J. Pharm. Res.* **118** (2019) 100 (<https://dx.doi.org/10.20959/wjpr20179-9254>)
16. A. P. de Jesus Menezes, M. Lopes da Silva, W. Luiz Pereira, G. de Paula Costa, A. Luciano Horta, A. Aparecida Santos Mendonça, A. C. Alvarenga Carneiro, D. M. Soares de Souza, R. Dias Novaes, R. R. Teixeira, A. Talvani, *J. Glob. Antimicrob. Resist.* **22** (2020) 466 (<https://dx.doi.org/10.1016/j.jgar.2020.04.005>)
17. M. Alagumuthu, A. Siva Kumar, P. S. Nigam, A. A. Napoleon, *Anti-Cancer Agents Med. Chem.* **20** (2020) 909 (<https://dx.doi.org/10.2174/1871520620666200318094138>)
18. S. Khandelwal, Y. K. Tailor, E. Rushell, M. Kumar, *Green Approaches in Medicinal Chemistry for Sustainable Drug Design*, Elsevier Inc., Amsterdam, 2020, pp. 245–352 (<https://dx.doi.org/10.1016/B978-0-12-817592-7.00009-5>)
19. M. A. Bhat, A. M. Naglah, S. Akber Ansari, H. M. Al-Tuwajiria, A. Al-Dhfyhan, *Molecules* **26** (2021) 3667 (<https://dx.doi.org/10.3390/molecules26123667>)
20. M. T. M. Nemr, M. A. M. AboulMagd, H. M. Hassan, A. A. Hamed, M. I. A. Hamed, M. T. Elsaadi, *RSC Adv.* **11** (2021) 26241 (<https://dx.doi.org/10.1039/D1RA05277B>)
21. M. T. M. Nemr, M. N. M. Yousif, J. Barciszewski, *Arch. Pharm. (Weinheim)* **352** (2019) 1 (<https://dx.doi.org/10.1002/ardp.201900062>)
22. S. F. Zhou, W. Z. Zhong, *Molecules* **22** (2017) 1 (<https://dx.doi.org/10.3390/molecules22020279>)
23. M. Remko, M. Swart, F. M. Bickelhaupt, *Bioorg. Med. Chem.* **14** (2006) 1715 (<https://dx.doi.org/10.1016/j.bmc.2005.10.020>)
24. B. Kuhn, P. Mohr, M. Stahl, *J. Med. Chem.* **53** (2010) 2601 (<https://dx.doi.org/10.1021/jm100087s>)
25. G. M. Ghiandoni, E. Caldeweyher, *Sci. Rep.* **13** (2023) 4143 (<https://dx.doi.org/10.1038/s41598-023-30089-x>)
26. E. Khan, S. A. Khan, A. S. hahzad, A. Noor, *J. Chem. Crystallogr.* **45** (2015) 238 (<https://dx.doi.org/10.1007/s10870-015-0588-9>)
27. H. M. Metwally, N. A. Khalaf, E. Abdel-Latif, M. A. Ismail, *BMC Chem.* **17** (2023) 1 (<https://dx.doi.org/10.1186/s13065-023-00917-2>)
28. R. Mishra, N. Kumar, N. Sachan, *Mini. Rev. Med. Chem.* **22** (2022) 1420 (<https://dx.doi.org/10.2174/1389557521666211022145458>)
29. N. Banjac, N. Trišović, Ž. Vitnik, V. Vitnik, N. Valentić, G. Ušćumlić, I. Juranić, *Monatsh. Chem.* **144** (2013) 1525 (<https://dx.doi.org/10.1007/s00706-013-1052-1>)
30. M. Bauer, A. Rollberg, A. Barth, S. Spange, *Eur. J. Org. Chem.* **26** (2008) 4475 (<https://dx.doi.org/10.1002/ejoc.200800355>)

31. A. M. Reeve, *J. Chem. Educ.* **92** (2015) 582 (<https://dx.doi.org/10.1021/ed400457c>)
32. M. Bayat, H. Imanieh, S. H. Hossieni, *Chin. Chem. Lett.* **20** (2009) 656 (<https://dx.doi.org/10.1016/j.ccl.2008.12.050>)
33. <http://www.swissadme.ch/>. Accessed 10.01.2023
34. <https://preadmet.bmdrc.kr/>. Accessed 10.01.2023
35. R. Re, N. Pellegrini, A. Proteggente, A. Pannala, M. Yang, C. Rice-Evans, *Free Radic. Biol. Med.* **26** (1999) 1231 ([https://dx.doi.org/10.1016/s0891-5849\(98\)00315-3](https://dx.doi.org/10.1016/s0891-5849(98)00315-3))
36. P. Paliwal, S. R. Jeti, A. Bhatewara, T. Kadre, S. Jain, *ISRN Org. Chem.* (2013) **1** (<https://dx.doi.org/10.1155/2013/526173>)
37. Y. A. A. M. Elshaiyer, M. T. M. Nemr, M. S. Refaey, W. A. A. Fadaly, A. Barakat, *New J. Chem.* **46** (2022) 13383 (<https://dx.doi.org/10.1039/D2NJ00460G>)
38. M. Udayakumar, J. Kothandapani, S. S. Ganesan, V. N. Sathiyamoorthy, S. M. Kumar, K. Byrappa, S. Thamocharan, *J. Mol. Struct.* **1133** (2017) 510 (<https://dx.doi.org/10.1016/j.molstruc.2016.11.082>)
39. M. M. Heravi, V. Zadsirjan, M. Mollaiye, M. Heydari, A. T. K. Koshvandi, *Russ. Chem. Rev.* **87** (2018) 553 (<https://dx.doi.org/10.1070/rcr4780>)
40. A. K. Ghoshe, V. N. Viswanadhan, J. J. Wendoloski, *J. Comb. Chem.* **1** (1999) 55 (<https://dx.doi.org/10.1081/rrs-100107923>)
41. A. Bogdanović, A. Lazić, S. Grujić, I. Dimkić, S. Stanković, S. Petrović, *Arh. Hig. Rada Toksikol.* **72** (2021) 70 (<https://dx.doi.org/10.2478/aiht-2021-72-3483>)
42. P. Z. Li, Z. Q. Liu, *Tetrahedron* **69** (2013) 9898 (<https://dx.doi.org/10.1016/j.tet.2013.08.053>)
43. M. Spiegel, Z. Sroka, *Theor. Chem. Acc.* **141** (2022) 1 (<https://dx.doi.org/10.1007/s00214-022-02922-5>)
44. M. A. Gouda, G. E. Abd El-Ggani, M. A. Berghot, A. E. M. Khalil, *J. Heterocycl. Chem.* **56** (2019) 2036 (<https://dx.doi.org/10.1002/jhet.3584>)
45. M. Olszowy, *Plant Physiol. Biochem.* **144** (2019) 135 (<https://dx.doi.org/10.1016/j.plaphy.2019.09.039>)
46. G. L. Xi, Z. Q. Liu, *J. Agric. Food Chem.* **63** (2015) 3516 (<https://dx.doi.org/10.1021/acs.jafc.5b00399>)
47. T. Narsinghani, M. C. Sharma, S. Bhargav, *Med. Chem. Res.* **22** (2013) 4059 (<https://dx.doi.org/10.1007/s00044-012-0413-3>)
48. B. W. Domagalska, K. A. Wilk, S. Wysocki, *Phys. Chem. Chem. Phys.* **5** (2003) 696 (<https://dx.doi.org/10.1039/b208125c>)
49. S. M. Martinez Gomez, D. M. Alzate Sanchez, W. Rodríguez-Córdoba, C. A. Sierra, C. Ochoa-Puentes, *Synth. Commun.* **44** (2014) 648 (<https://dx.doi.org/10.1080/00397911.2013.831903>)
50. G. K. Verma, K. Raghuvanshi, R. K. Verma, P. Dwivedi, M. S. Singh, *Tetrahedron* **67** (2011) 3698 (<https://dx.doi.org/10.1016/j.tet.2011.03.078>)
51. T. Yempala, B. Sridhar, S. Kantevari, *J. Chem. Sci.* **127** (2015) 803 (<https://dx.doi.org/10.1007/s12039-015-0835-9>)
52. N. Friebe, K. Schreiter, J. Kübel, B. Dietzek, N. Moszner, P. Burtscher, A. Oehlke, S. Spange, *New J. Chem.* **39** (2015) 5171 (<https://dx.doi.org/10.1039/c5nj00256g>)
53. S. Hmuda, N. Trišović, J. Rogan, D. Poleti, Ž. Vitnik, V. Vitnik, N. Valentić, B. Božić, G. Ušćumlić, *Monatsh. Chem.* **145** (2014) 821 (<https://dx.doi.org/10.1007/s00706-013-1149-6>)
54. K. Hofmann, S. Brumm, C. Mende, K. Nagel, A. Seifert, I. Roth, D. Schaarschmidt, N. Lang, S. Spange, *New J. Chem.* **36** (2012) 1655 (<https://dx.doi.org/10.1039/C2NJ40313G>).

SUPPLEMENTARY MATERIAL TO
**Assessing the pharmacological potential of selected xanthene
derivatives**

ANITA M. LAZIĆ^{1*}, ALEKSANDRA D. MAŠULOVIĆ¹, JELENA M. LAĐAREVIĆ²
and NATAŠA V. VALENTIĆ²

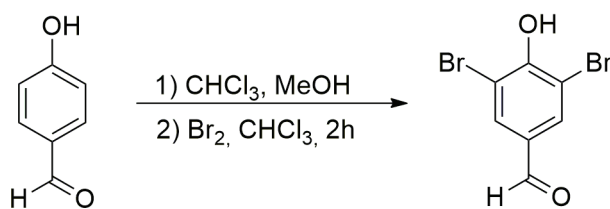
¹Innovation Center, Faculty of Technology and Metallurgy, Belgrade, Serbia, and ²University
of Belgrade, Faculty of Technology and Metallurgy, Belgrade, Serbia

J. Serb. Chem. Soc. 88 (9) (2023) 811–824

EXPERIMENTAL DETAILS

Synthesis of 3,5-dibromo-4-hydroxybenzaldehyde

The mixture of chloroform (20 mL) and methanol (2 mL) was used for dissolving 4-hydroxybenzaldehyde (2 g, 0.16 mmol) prior to addition of bromine solution (2.84 g, 0.18 mmol in 4 mL of chloroform). Moreover, the reaction mixture was additionally diluted by the dichloromethane and water. After stirring for 2 h, the obtained solution was washed with aqueous sodium thiosulfate and dried over MgSO₄. The solvent was removed by evaporation under reduced pressure and a solid 3,5-dibromo-4-hydroxybenzaldehyde was acquired. The crude product was purified by recrystallization from ethanol.¹ The obtained values of melting point and ¹H- and ¹³C-NMR spectra are in accordance with literature data.²

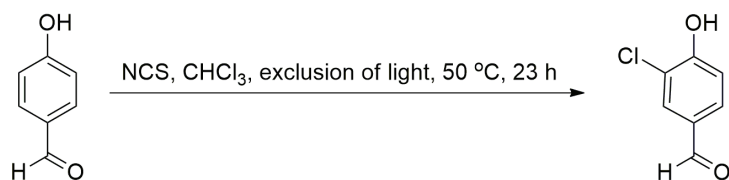


Scheme S-1. Synthesis of 3,5-dibromo-4-hydroxybenzaldehyde.

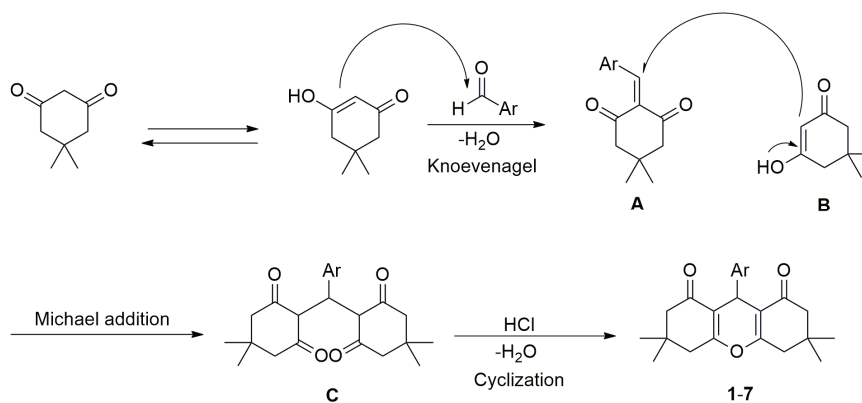
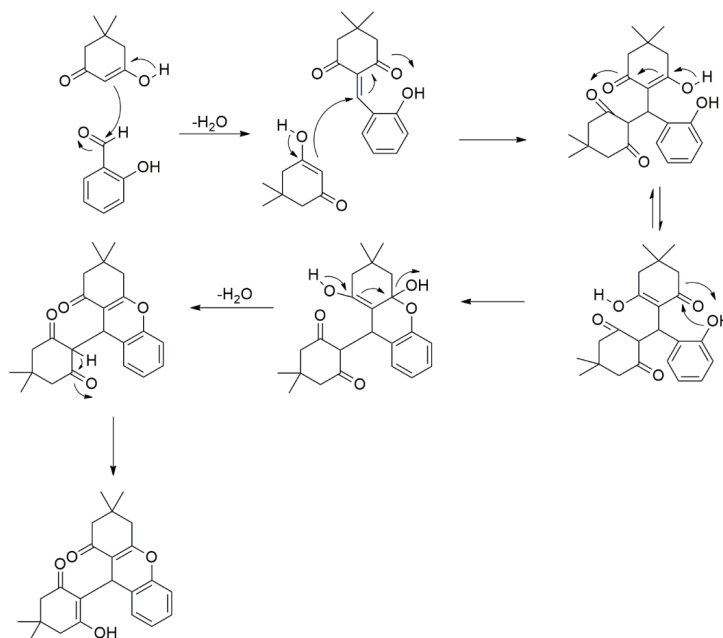
Synthesis of 3-chloro-4-hydroxybenzaldehyde

To a solution of 4-hydroxybenzaldehyde (2 g, 16.36 mmol) in dry chloroform (20 mL) one portion of *N*-chlorosuccinimide (2.2 g, 16.36 mmol) was added. The reaction mixture was stirred under exclusion of light at 50 °C for 23 h. After cooling to a room temperature, the reaction mixture was concentrated and the residue dissolved in CH₂Cl₂ (20 mL). The organic layer was washed with water (30 mL) and dried over Na₂SO₄. The crude product was purified by recrystallization from ethanol.³ The obtained values of melting point and ¹H- and ¹³C-NMR spectra are in accordance with literature data.⁴

* Corresponding author. E-mail: alazic@tmf.bg.ac.rs

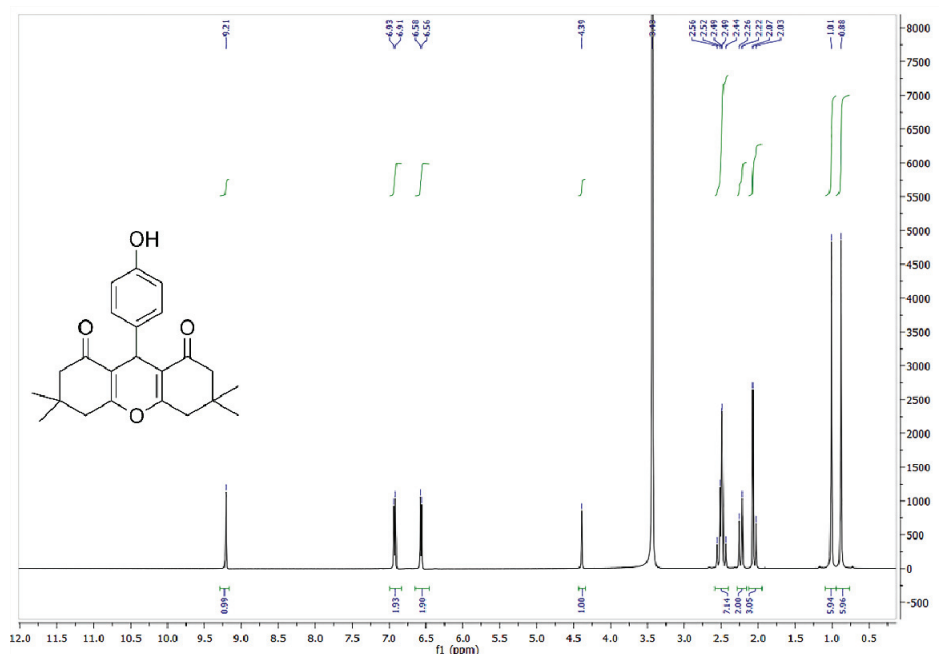


Scheme S-2. Synthesis of 3-chloro-4-hydroxybenzaldehyde.

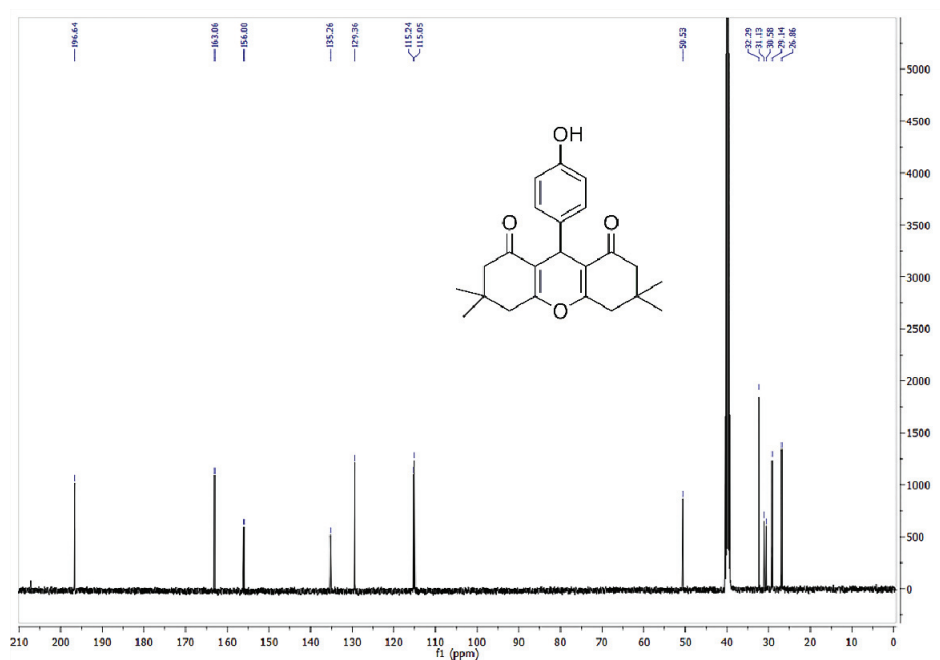
Scheme S3. Proposed mechanism of the synthesized compounds **1-7**.Scheme S-4. Proposed mechanism of the synthesized compound **8**.⁵

Characterization of compounds 1–8

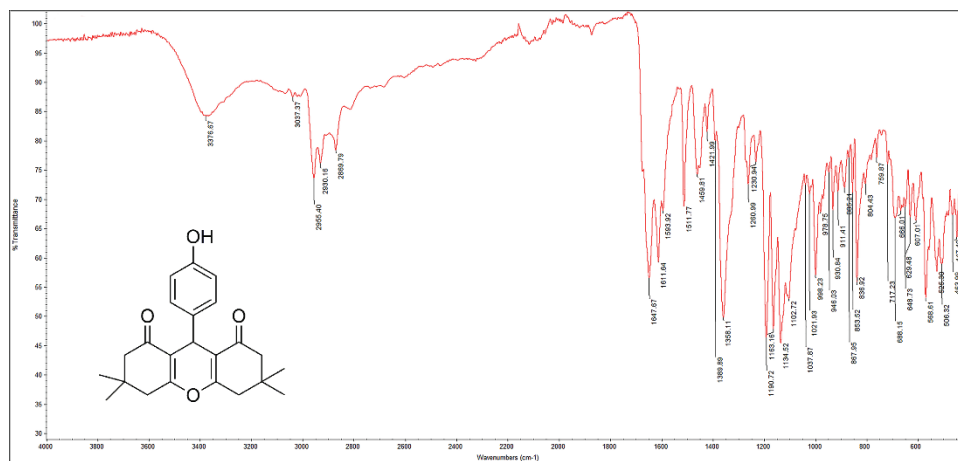
9-(4-Hydroxyphenyl)-3,3,6,6-tetramethyl-3,4,5,6,7,9-hexahydro-1H-xanthene-1,8(2H)-dione (1). Yield 300 mg (75 %). White solid melts at 240–243 °C. IR (ATR): 3377, 3038, 2955, 2930, 2870, 1648, 1612, 1594, 1512, 1460, 1422, 1390, 1358, 1261, 1231, 1191, 1163, 1134, 1103, 1038, 1022, 979, 946, 931, 911, 868, 853, 834, 804, 760, 717, 688, 666, 649, 630, 607, 569, 525, 506, 464, 447, 432, cm^{-1} . ^1H NMR (400 MHz, $\text{DMSO-}d_6$, δ): 9.21 (*s*, 1H, –OH), 6.92 (*d*, 2H, $J = 8.4$ Hz, $-\text{C}_6\text{H}_4$), 6.57 (*d*, 2H, $J = 8.4$ Hz, $-\text{C}_6\text{H}_4$), 4.39 (*s*, 1H, –CH), 2.56–2.03 (*m*, 8H, 4x- CH_2), 1.01 (*s*, 6H, 2x- CH_3), 0.88 (*s*, 6H, 2x- CH_3). ^{13}C NMR (100 MHz, $\text{DMSO-}d_6$, δ): 196.6, 163.1, 156.0, 135.3, 129.4, 115.2, 115.0, 50.5, 32.3, 31.1, 30.6, 29.1, 26.9. Elemental analysis for $\text{C}_{23}\text{H}_{26}\text{O}_4$: Calculated C 75.38, H 7.15, Found C 75.43, H 6.97.



(a)



(b)

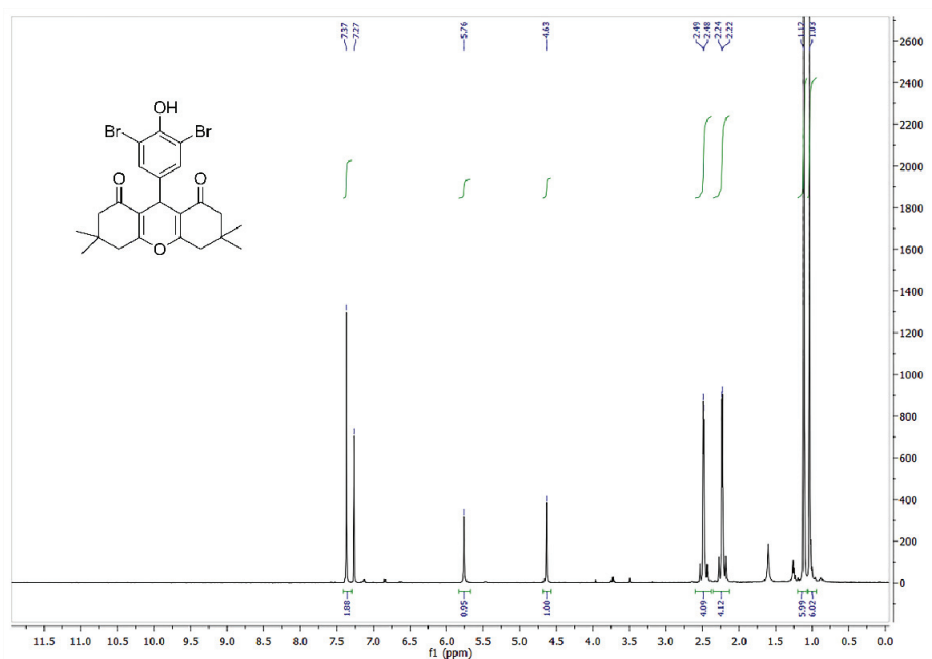


(c)

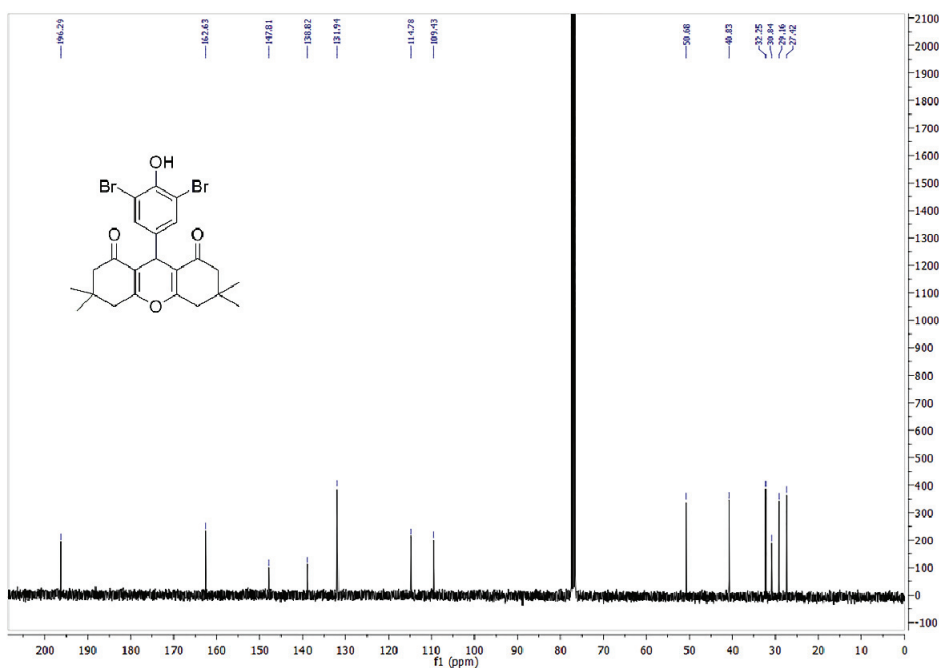
Fig. S-1. Spectra of 1: a) ¹H NMR; b) ¹³C NMR and c) FTIR.

9-(3,5-Dibromo-4-hydroxyphenyl)-3,3,6,6-tetramethyl-3,4,5,6,7,9-hexahydro-1H-xanthene-1,8(2H)-dione (2). Yield 580 mg (85 %). White solid melts at 263-266 °C. IR (ATR): 3355, 2956, 2926, 2869, 1673, 1651, 1616, 1562, 1512, 1463, 1424, 1390, 1356, 1307, 1263, 1240, 1219, 1193, 1164, 1134, 1105, 1038, 999, 945, 932, 911, 870, 853, 836,

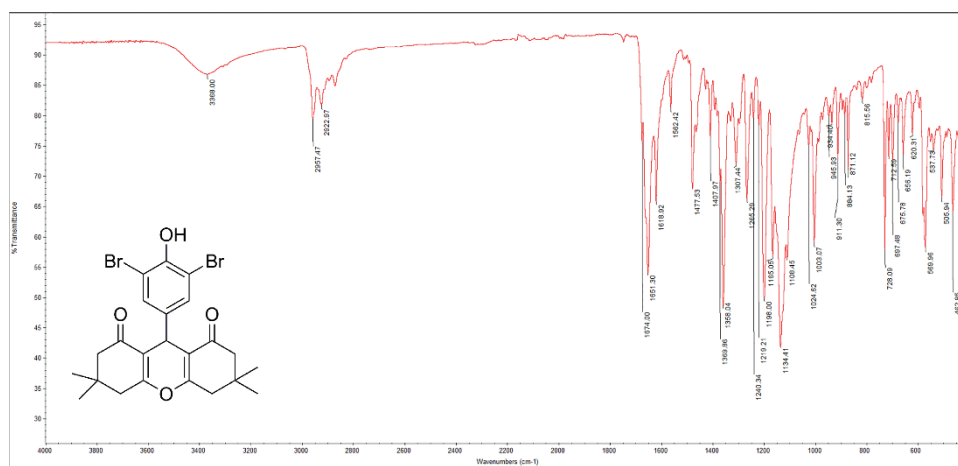
760, 727, 711, 695, 675, 656, 610, 568, 530, 505, 460, 448, 432, cm^{-1} . ^1H NMR (400 MHz, CDCl_3 , δ): 7.37 (s, 2H, $-\text{C}_6\text{H}_2$), 5.76 (s, 1H, $-\text{OH}$), 4.63 (s, 1H, $-\text{CH}$), 2.49 (d, 4H, $J = 3.6$ Hz, $2x -\text{CH}_2$), 2.23 (d, 4H, $J = 4.4$ Hz, $2x -\text{CH}_2$), 1.12 (s, 6H, $2x -\text{CH}_3$), 1.03 (s, 6H, $2x -\text{CH}_3$). ^{13}C NMR (100 MHz, CDCl_3 , δ): 196.3, 162.6, 147.8, 138.8, 131.9, 114.8, 109.4, 50.7, 40.8, 32.2, 30.8, 29.2, 27.4. Elemental analysis for $\text{C}_{23}\text{H}_{24}\text{Br}_2\text{O}_4$: Calculated C 52.69, H 4.61; Found C 52.59, H 4.71.



(a)



(b)

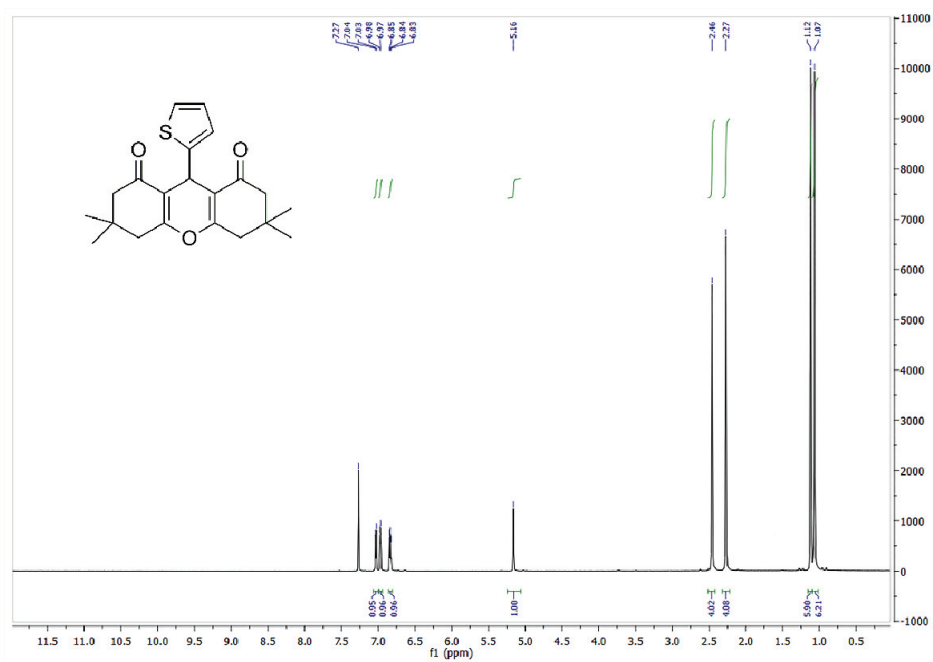


(c)

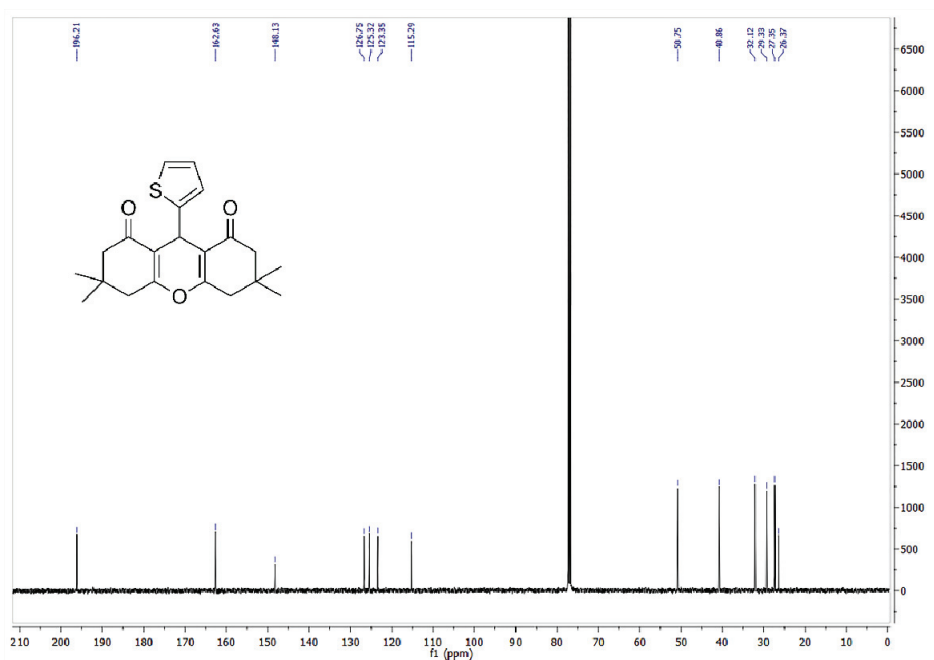
Fig. S-2. Spectra of **2**: a) ^1H NMR; b) ^{13}C NMR and c) FTIR.

3,3,6,6-Tetramethyl-9-(thiophen-2-yl)-3,4,5,6,7,9-hexahydro-1H-xanthene-1,8(2H)-dione (**3**). Yield 260 mg (65 %). White solid melts at 155-158 °C. IR (ATR): 3305, 2958, 2931, 2870, 1675, 1660, 1621, 1514, 1464, 1435, 1423, 1389, 1354, 1326, 1282, 1192, 1135, 1104, 1074, 1037, 1022, 1038, 997, 967, 931, 914, 888, 867, 853, 836, 803, 772, 760, 731, 716, 694,

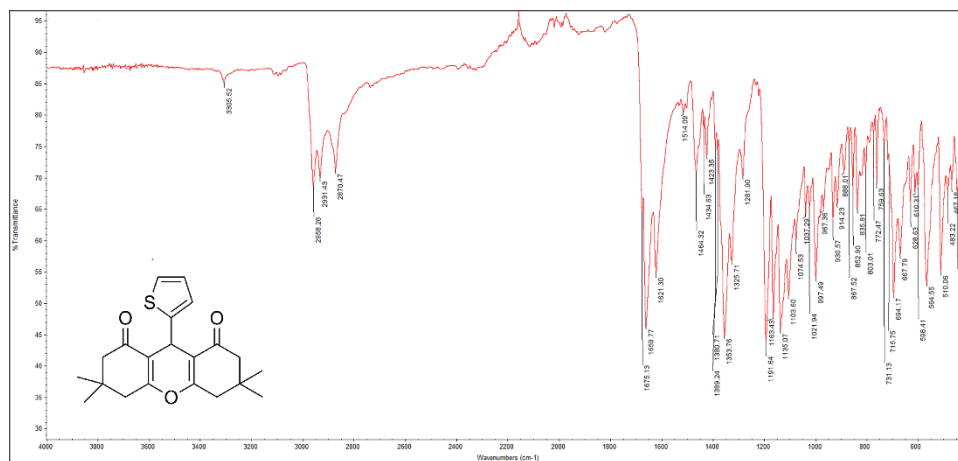
668, 629, 610, 598, 564, 510, 483, 445, 432, cm^{-1} . ^1H NMR (400 MHz, CDCl_3 , δ): 7.03 (*d*, 1H, $J = 5.2$ Hz, thiophen-2-yl), 6.97 (*d*, 1H, $J = 2.8$ Hz, thiophen-2-yl), 6.84 (*q*, 1H, $J = 3.2$ Hz, thiophen-2-yl), 5.16 (*s*, 1H, $-\text{CH}$), 2.46 (*s*, 4H, 2x $-\text{CH}_2$), 2.27 (*s*, 4H, 2x $-\text{CH}_2$), 1.12 (*s*, 6H, 2x $-\text{CH}_3$), 1.07 (*s*, 6H, 2x $-\text{CH}_3$). ^{13}C NMR (100 MHz, CDCl_3 , δ): 196.2, 162.6, 148.1, 126.7, 125.3, 123.3, 115.3, 50.7, 40.9, 32.1, 29.3, 27.3, 26.4. Elemental analysis for $\text{C}_{21}\text{H}_{24}\text{O}_3\text{S}$: Calculated C 70.75, H 6.79; Found C 70.73, H 6.81.



(a)



(b)

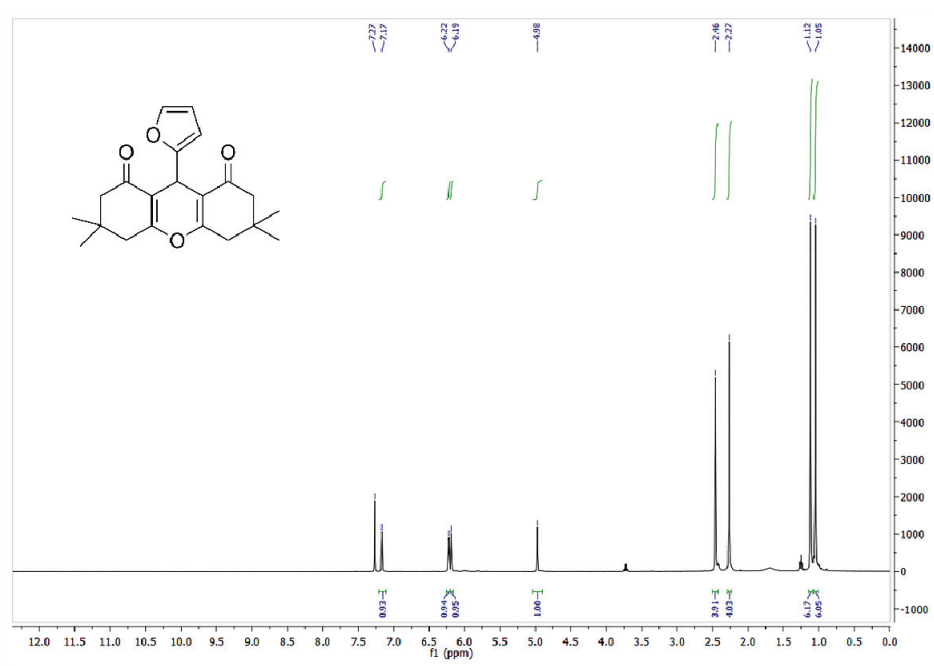


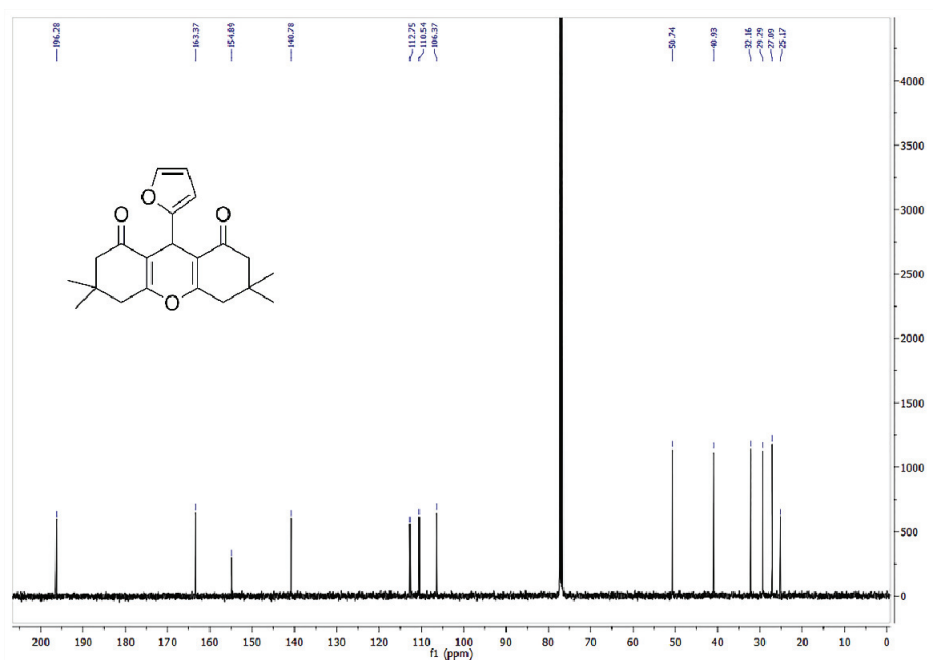
(c)

Fig. S-3. Spectra of **3**: a) ¹H NMR; b) ¹³C NMR and c) FTIR.

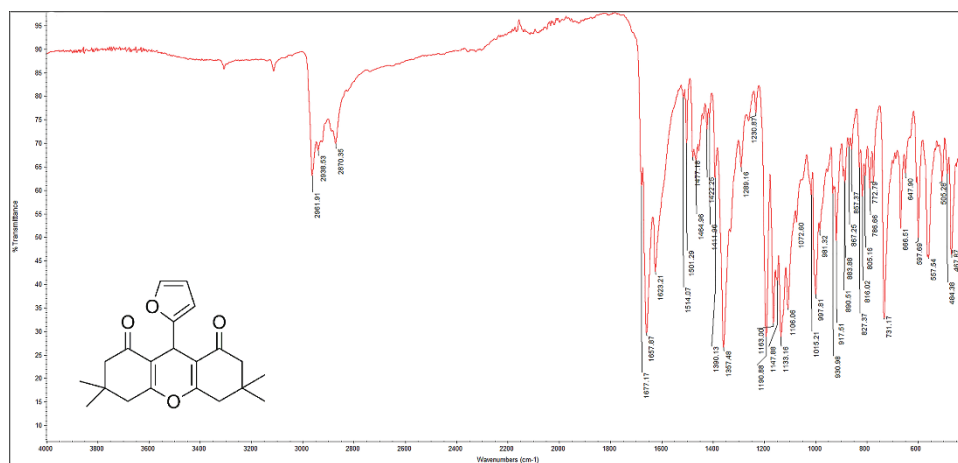
9-(Furan-2-yl)-3,3,6,6-tetramethyl-3,4,5,6,7,9-hexahydro-1H-xanthene-1,8(2H)-dione (**4**). Yield 230 mg (63 %). White solid melts at 140-143 °C. IR (ATR): 2962, 2938, 2870, 1677, 1656, 1623, 1514, 1501, 1465, 1423, 1390, 1357, 1289, 1231, 1191, 1163, 1148, 1106, 1073, 1015, 998, 981, 931, 917, 890, 884, 668, 657, 628, 598, 564, 510, 483, 445, 432, cm⁻¹.

^1H NMR (400 MHz, CDCl_3 , δ): 7.17 (s, 1H, furan-2-yl), 6.22 (s, 1H, furan-2-yl), 6.19 (s, 1H, furan-2-yl), 4.98 (s, 1H, $-\text{CH}$), 2.46 (s, 4H, $2\times -\text{CH}_2$), 2.27 (s, 4H, $2\times -\text{CH}_2$), 1.12 (s, 6H, $2\times -\text{CH}_3$), 1.05 (s, 6H, $2\times -\text{CH}_3$). ^{13}C NMR (100 MHz, CDCl_3 , δ): 196.3, 163.4, 154.9, 140.8, 112.7, 110.5, 106.4, 50.8, 40.9, 32.2, 29.3, 27.1, 25.2. Elemental analysis for $\text{C}_{21}\text{H}_{24}\text{O}_4$: Calculated C 74.09, H 7.11; Found C 74.07, H 7.13.





(b)

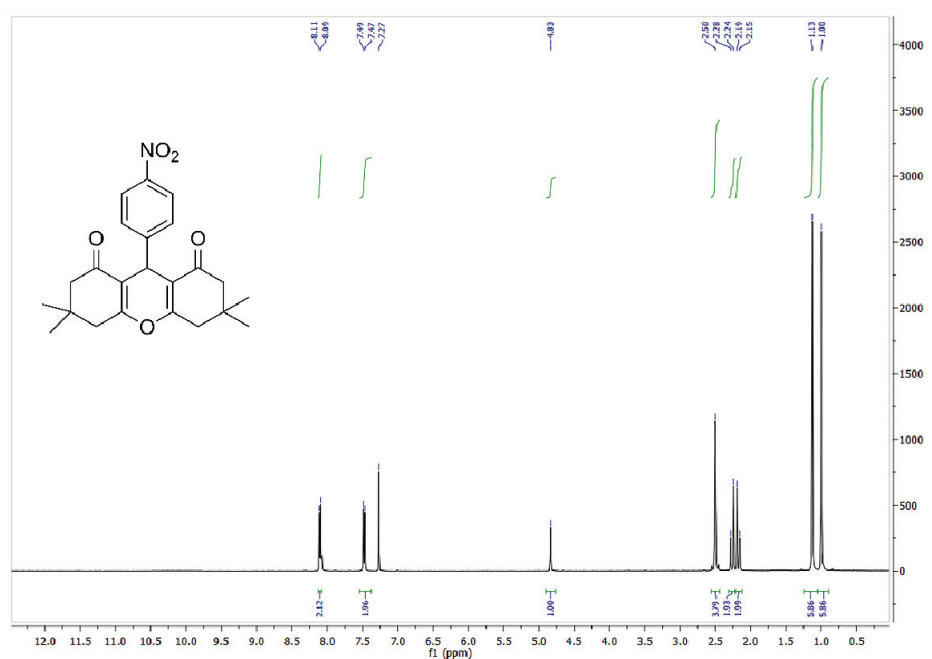


(c)

Fig. S-4. Spectra of 4: a) ¹H NMR; b) ¹³C NMR and c) FTIR.

3,3,6,6-Tetramethyl-9-(4-nitrophenyl)-3,4,5,6,7,9-hexahydro-1H-xanthene-1,8(2H)-dione (**5**). Yield 340 mg (80 %). Yellow solid melts at 190-193 °C. IR (ATR): 2958, 2867, 1660, 1651, 1614, 1601, 1587, 1512, 1470, 1423, 1412, 1390, 1359, 1341, 1314, 1193, 1165, 1137, 1107, 1013, 1000, 982, 934, 913, 891, 831, 815, 740, 706, 695, 667, 633, 610, 596, 563,

520, 501, 490, 437, cm^{-1} . ^1H NMR (400 MHz, CDCl_3 , δ): 8.10 (*d*, 2H, $J = 8.4$ Hz, $-\text{C}_6\text{H}_4$), 7.48 (*d*, 2H, $J = 8.8$ Hz, $-\text{C}_6\text{H}_4$), 4.83 (*s*, 1H, $-\text{CH}$), 2.50 (*s*, 4H, 2x $-\text{CH}_2$), 2.22 (*q*, 4H, $J = 16.4$ Hz, 2x $-\text{CH}_2$), 1.13 (*s*, 6H, 2x $-\text{CH}_3$), 1.00 (*s*, 6H, 2x $-\text{CH}_3$). ^{13}C NMR (100 MHz, CDCl_3 , δ): 196.2, 162.8, 151.5, 146.5, 129.3, 123.4, 114.6, 50.6, 40.8, 32.3, 32.2, 29.2, 27.3. Elemental analysis for $\text{C}_{23}\text{H}_{25}\text{NO}_5$: Calculated C 69.86, H 6.37, N 3.54; Found C 69.84, H 6.39, N 3.48.



(a)

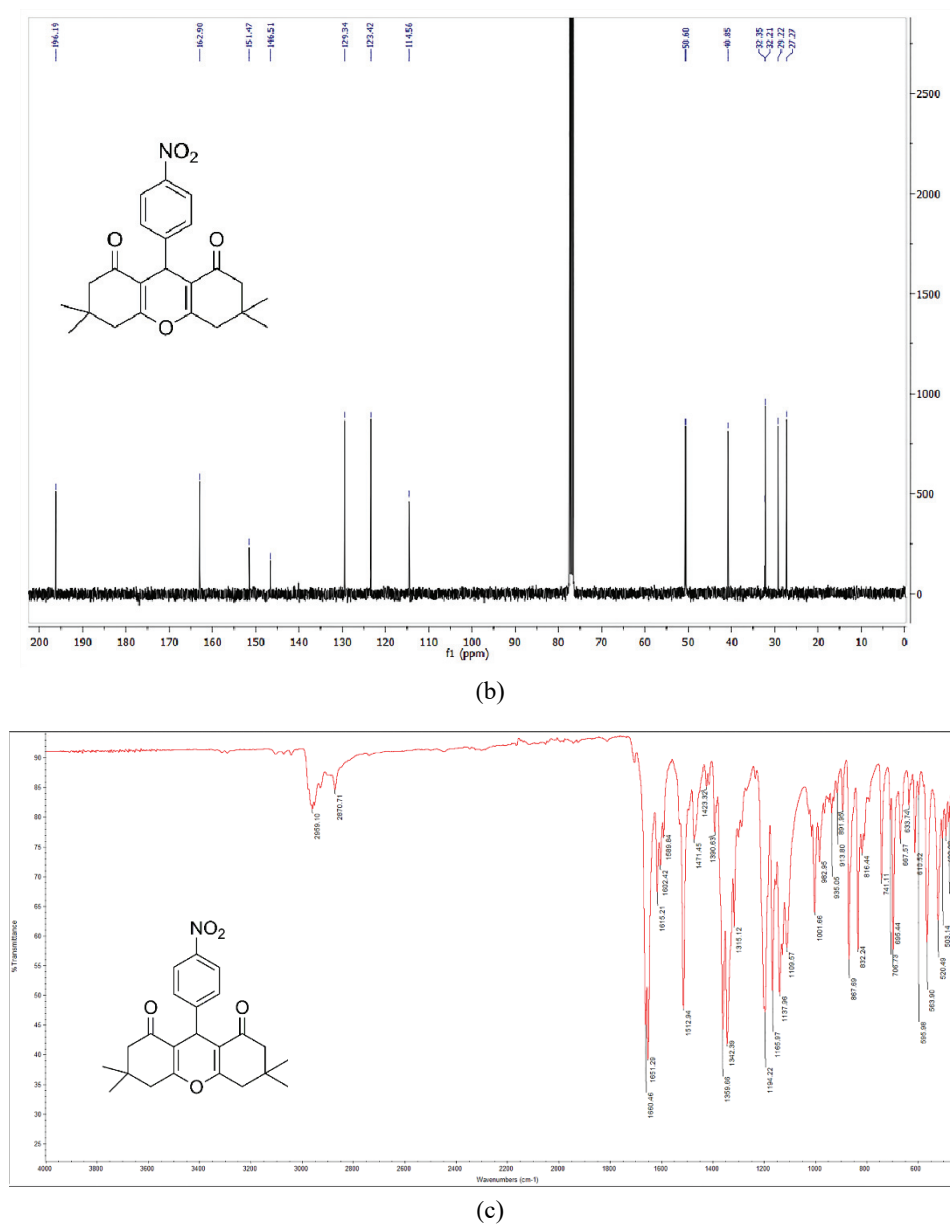
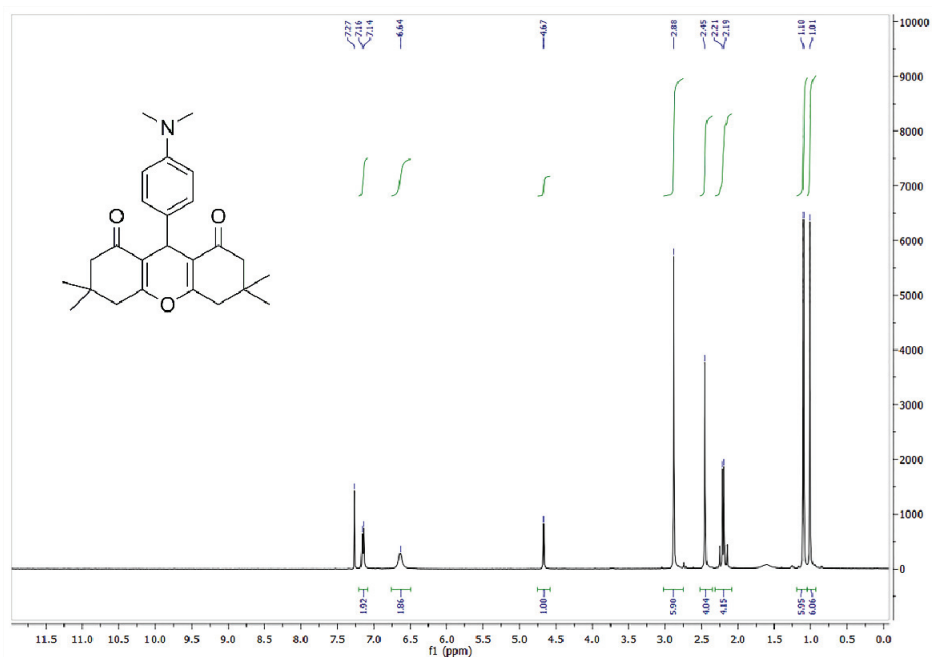


Fig. S-5. Spectra of **5**: a) ^1H NMR; b) ^{13}C NMR and c) FTIR.

9-(4-(Dimethylamino)phenyl)-3,3,6,6-tetramethyl-3,4,5,6,7,9-hexahydro-1H-xanthen-1,8(2H)-dione (**6**). Yield 320 mg (75 %). Yellow solid melts at 205-208 °C. IR (ATR): 2953, 2937, 2870, 2840, 2784, 1674, 1657, 1620, 1605, 1567, 1514, 1464, 1441, 1357, 1338, 1296, 1283, 1232, 1189, 1159, 1135, 1106, 1058, 1021, 998, 971, 946, 932, 914, 892, 846, 831, 816,

807, 784, 738, 722, 674, 640, 631, 603, 583, 557, 537, 497, 476, 432, cm^{-1} . ^1H NMR (400 MHz, CDCl_3 , δ): 7.15 (*d*, 2H, $J = 8.4$ Hz, $-\text{C}_6\text{H}_4$), 6.64 (*s*, 2H, $-\text{C}_6\text{H}_4$), 4.67 (*s*, 1H, $-\text{CH}$), 2.88 (*s*, 6H, $-\text{N}(\text{CH}_3)_2$), 2.45 (*s*, 4H, $2 \times -\text{CH}_2$), 2.20 (*d*, 4H, $J = 8.8$ Hz, $2 \times -\text{CH}_2$), 1.10 (*s*, 6H, $2 \times -\text{CH}_3$), 1.01 (*s*, 6H, $2 \times -\text{CH}_3$). ^{13}C NMR (100 MHz, CDCl_3 , δ): 196.5, 161.8, 150.2, 136.6, 129.0, 116.0, 114.6, 50.8, 40.9, 32.2, 30.7, 29.2, 27.5. Elemental analysis for $\text{C}_{25}\text{H}_{31}\text{NO}_3$: Calculated C 76.30, H 7.94, N 3.56; Found C 76.28, H 7.96, N 3.56.



(a)

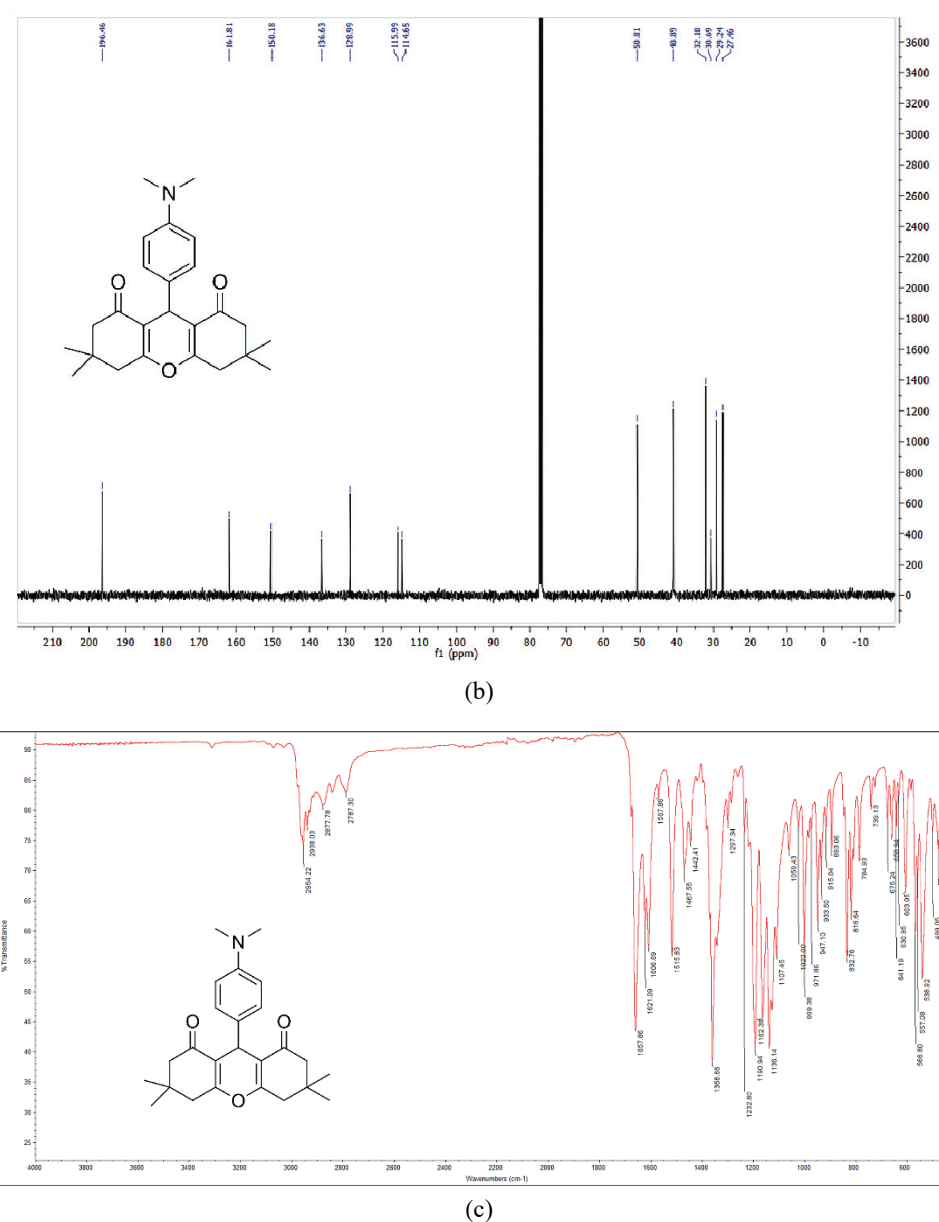
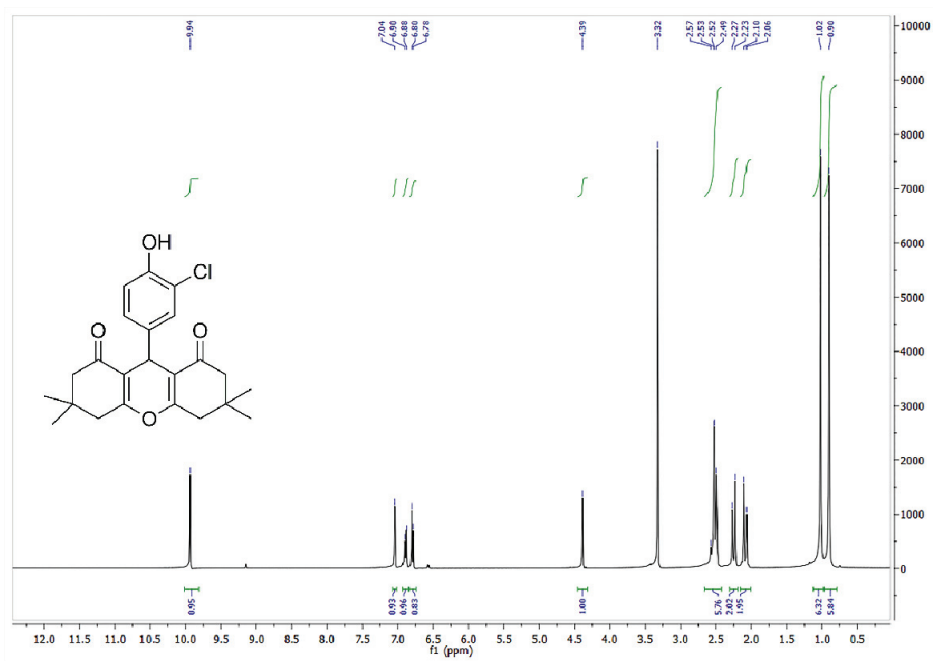
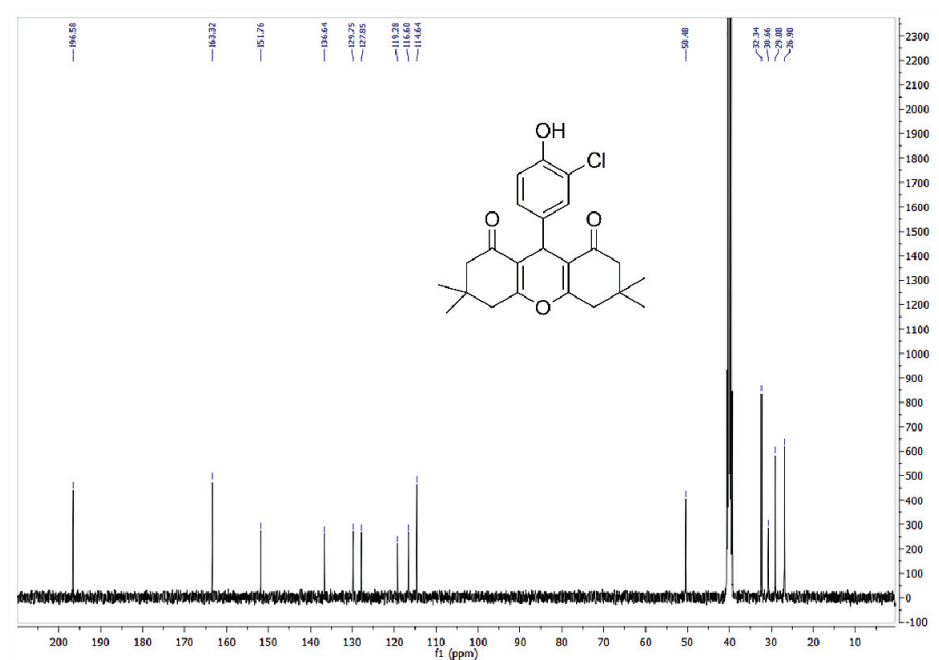


Fig. S-6. Spectra of **6**: a) ^1H NMR; b) ^{13}C NMR and c) FTIR.

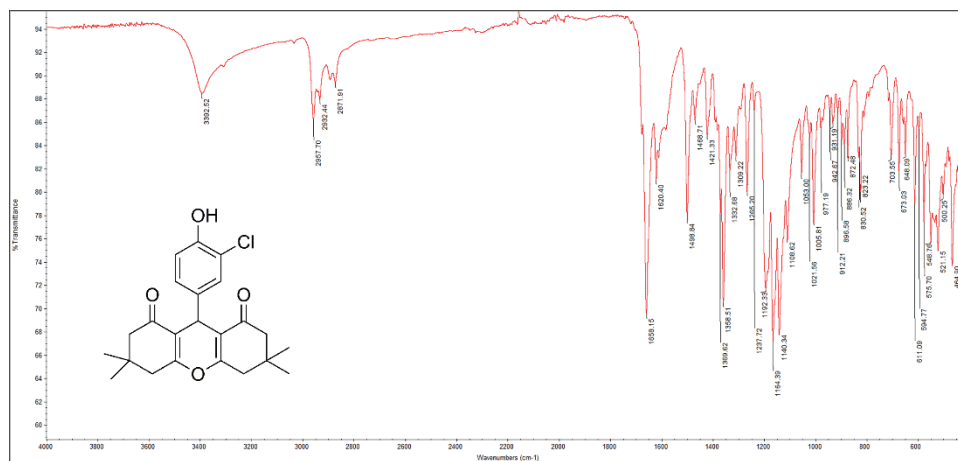
9-(3-Chloro-4-hydroxyphenyl)-3,3,6,6-tetramethyl-3,4,5,6,7,9-hexahydro-1H-xanthene-1,8(2H)-dione (7). Yield 370 mg (85 %). White solid melts at 264-266 °C. IR (ATR): 3614, 2984, 2974, 2848, 2789, 1678, 1652, 1624, 1615, 1569, 1511, 1462, 1440, 1356, 1334, 1292, 1281, 1235, 1187, 1154, 1134, 1102, 1053, 1020, 997, 975, 949, 934, 913, 898, 844, 830, 819,

806, 783, 734, 725, 679, 642, 630, 608, 585, 559, 538, 494, 473, 431, cm^{-1} . ^1H NMR (400 MHz, $\text{DMSO-}d_6$, δ): 9.94 (s, 1H, -OH), 7.04 (s, 1H, - C_6H_3), 6.89 (d, 1H, $J = 8.4$ Hz, - C_6H_3), 6.79 (d, 1H, $J = 8.4$ Hz, - C_6H_3), 4.39 (s, 1H, -CH), 2.57-2.49 (m, 4H, 2x - CH_2) 2.25 (d, 2H, $J = 16.4$ Hz, - CH_2), 2.08 (d, 2H, $J = 16.4$ Hz, - CH_2), 1.02 (s, 6H, 2x - CH_3), 0.90 (s, 6H, 2x - CH_3). ^{13}C NMR (100 MHz, $\text{DMSO-}d_6$, δ): 196.6, 163.3, 151.8, 136.6, 129.7, 127.8, 119.3, 116.6, 114.6, 50.5, 32.3, 30.7, 29.1, 26.9. Elemental analysis for $\text{C}_{23}\text{H}_{25}\text{ClO}_4$: Calculated C 68.91, H 6.29; Found C 68.88, H 6.32.





(b)

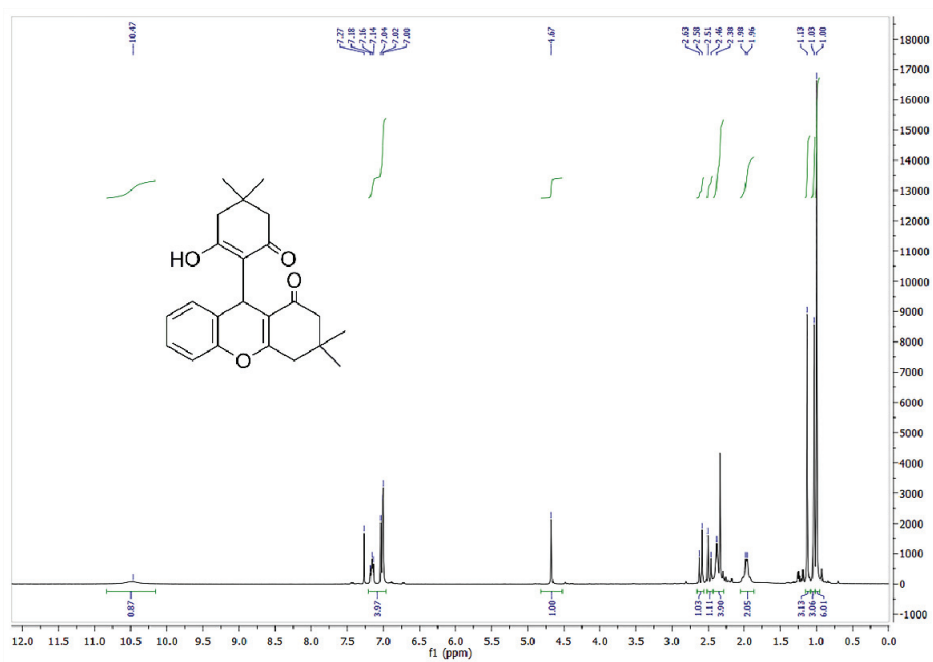


(c)

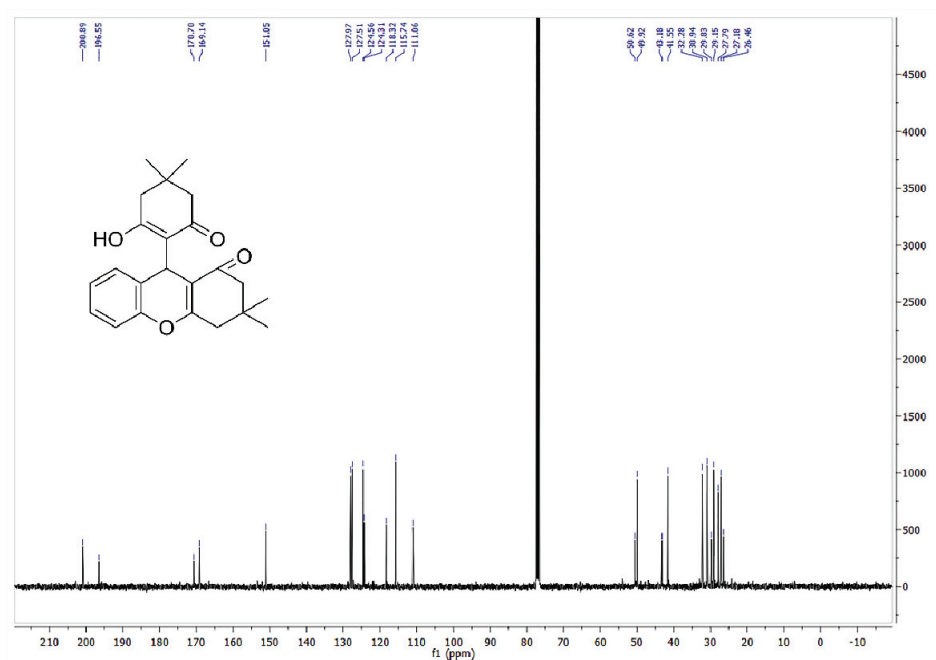
Fig. S-7. Spectra of 7: a) ¹H NMR; b) ¹³C NMR and c) FTIR.

9-(2-Hydroxy-4,4-dimethyl-6-oxocyclohex-1-enyl)-3,3-dimethyl-2,3,4,9-tetrahydro-1H-xanthen-1-one (**8**). Yield 340 mg (80 %). White solid melts at 190-193 °C. IR (ATR): 3182, 2958, 2928, 2867, 1651, 1587, 1423, 1412, 1376, 1235, 1193, 1165, 1137, 1107, 1013, 1000, 982, 934, 913, 891, 831, 815, 740, 706, 695, 667, 633, 610, 596, 563, 520, 501, 490, 437, cm⁻¹

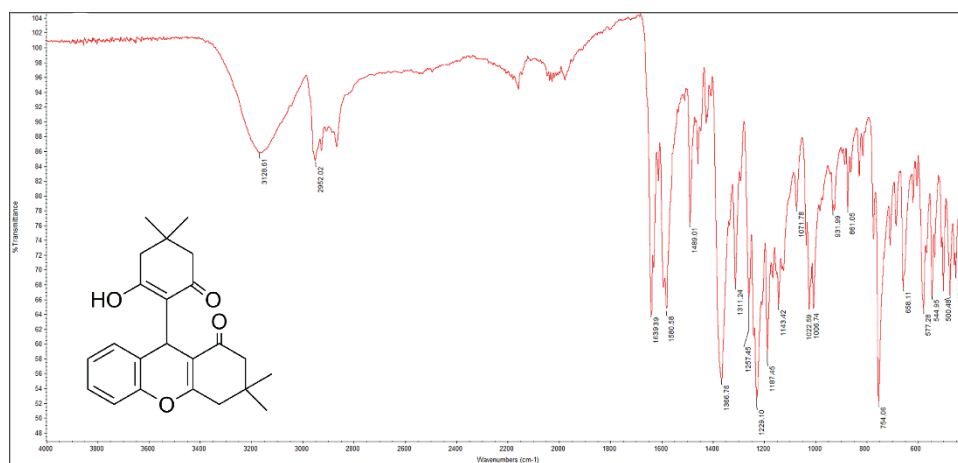
¹H NMR (400 MHz, CDCl₃, δ): 10.47 (*bs*, 1H, -OH), 7.18–7.00 (*m*, 4H), 4.67 (*s*, 1H, -CH), 2.63–2.38 (*m*, 6H, 3x -CH₂), 1.97 (*d*, 2H, *J* = 4.8 Hz, -CH₂), 1.13 (*s*, 3H, -CH₃), 1.03 (*s*, 3H, -CH₃), 1.00 (*s*, 6H, 2x -CH₃). ¹³C NMR (100 MHz, CDCl₃, δ): 200.9, 196.5, 170.7, 169.1, 151.0, 128.0, 127.5, 124.6, 124.3, 118.3, 115.7, 111.1, 50.6, 49.9, 43.2, 41.5, 32.3, 30.9, 29.8, 29.1, 27.8, 27.2, 26.5. Elemental analysis for C₂₃H₂₅NO₅: Calculated C 69.86, H 6.37; Found C 69.84, H 6.32. Obtained data are in accordance with literature.⁵



(a)



(b)



(c)

Fig. S-8. Spectra of **8**: a) ¹H NMR; b) ¹³C NMR and c) FTIR.

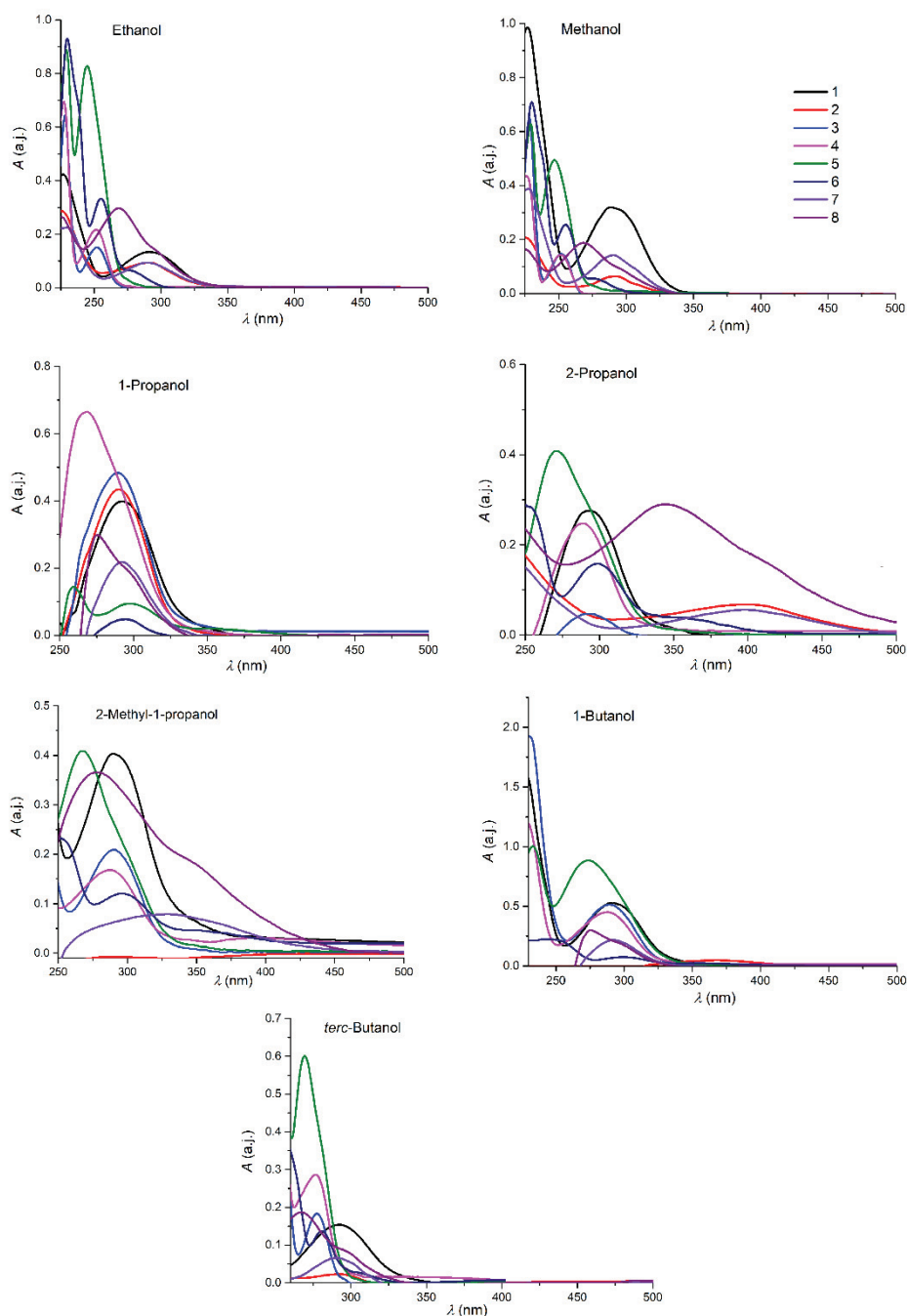


Fig. S-9. The UV-Vis spectra of investigated compounds **1–8** in alcohols.

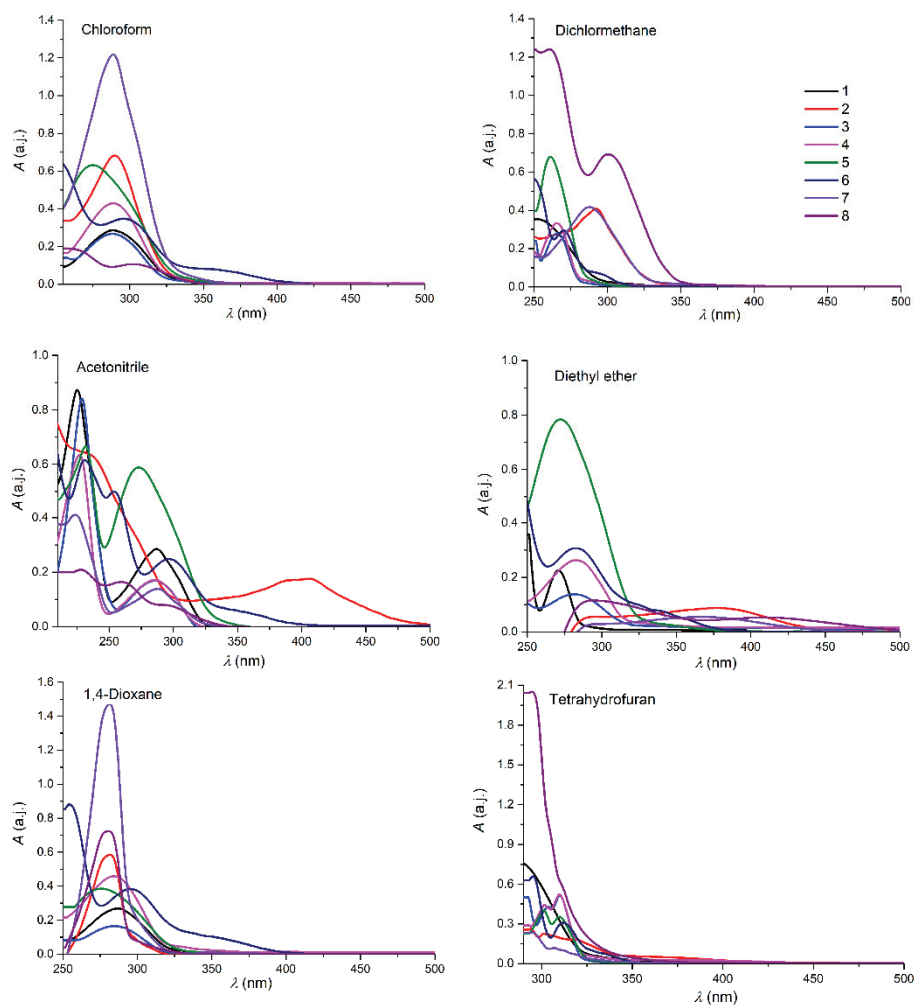


Fig. S-10. The UV-Vis spectra of investigated compounds 1–8 in selected solvents.

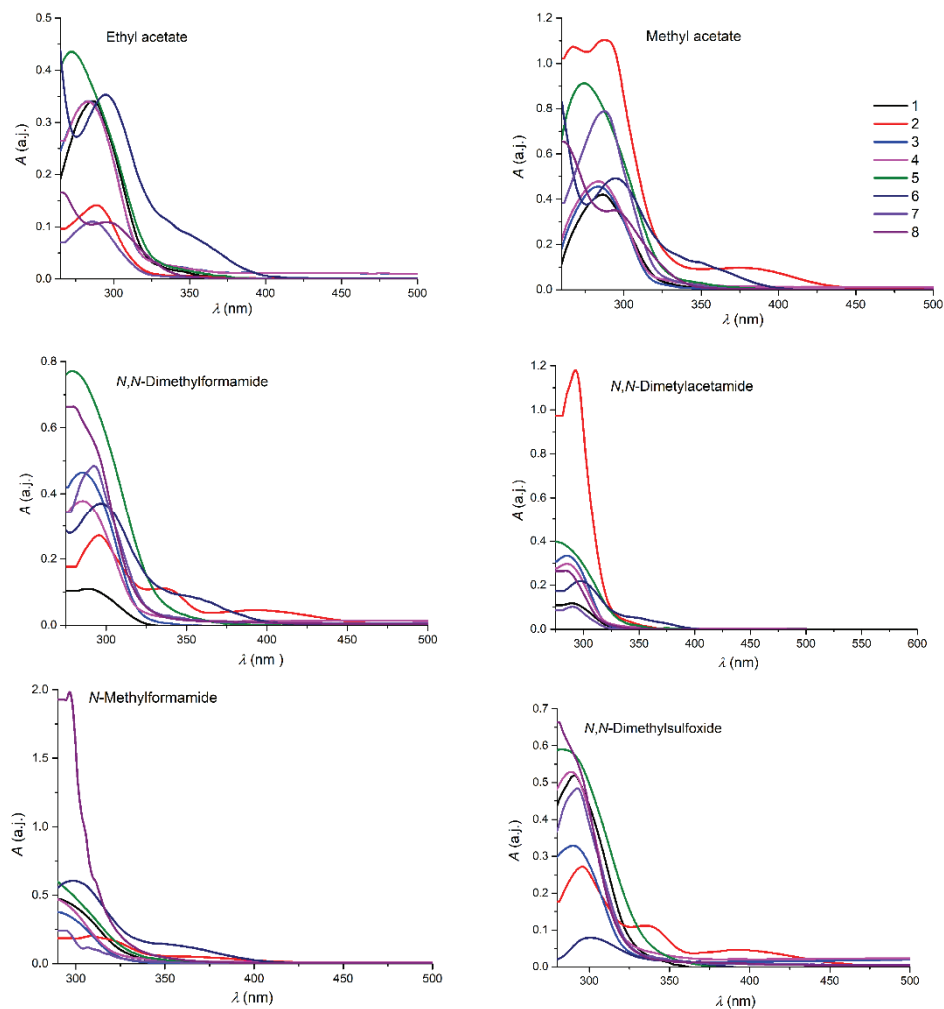


Fig. S-11. The UV-Vis spectra of investigated compounds 1–8 in selected solvents.

Table S-I. Physicochemical properties of the investigated compounds

No.	Molecular weight, g mol ⁻¹	Number of atoms	Number of rotatable bonds	Number of hydrogen bond donors	Number of hydrogen bond acceptors	Molar refractivity	Topological polar surface area, Å ²
1	366.45	27	1	1	4	104.02	63.60
2	524.24	29	1	1	4	119.42	63.60
3	356.48	25	1	0	3	99.87	71.61
4	340.41	25	1	0	4	94.26	56.51
5	395.45	29	2	0	5	110.82	89.19
6	393.52	29	2	0	3	116.20	46.61
7	400.90	28	1	1	4	109.03	63.60
8	366.45	27	1	1	4	104.02	63.60

Table S-II. Partition coefficients of the investigated compounds

No.	logP _{o/w} (XLOGP3)	logP _{o/w} (WLOGP)	logP _{o/w} (MLOGP)
1	3.61	4.79	2.58
2	5.00	6.32	3.74
3	3.69	5.15	2.77
4	3.07	4.68	1.92
5	3.80	5.52	2.07
6	4.09	5.15	3.00
7	4.24	5.45	3.06
8	3.61	4.79	2.58

Table S-III. QSAR pharmacokinetic profiles of the investigated compounds related to absorption properties

No	SwissADME Gastrointestinal absorption	PreADMET Gastrointestinal absorption, %	SwissADME The compound penetrates the blood-brain barrier	PreADMET The compound penetrating the blood-brain barrier (C _{brain} /C _{blood})	SwissADME The compound is a P-gp inhibitor	PreADMET The compound is a P-gp inhibitor
1	High	95.93	Yes	0.16	Yes	Yes
2	High	97.11	No	1.04	Yes	Yes
3	High	98.60	No	2.25	Yes	Yes
4	High	98.19	Yes	2.02	Yes	Yes
5	High	98.54	No	0.01	No	No
6	High	95.93	Yes	0.77	Yes	Yes
7	High	97.45	Yes	0.05	Yes	No
8	High	96.16	No	0.38	Yes	Yes

Table S-IV. Absorption maxima in nm of the investigated compounds **1–8** in selected solvent set

No.	Solvent	1	2	3	4	5	6	7	8
1.	Acetonitrile	225, 287	291	229, 287	228, 285	232; 273	231, 254, 297	224, 290	230, 262, 295
2.	1-Butanol	228, 293	289	231, 289	228, 288	234, 274	237, 300	294	275
3.	Chloroform	289	293	287	289	275	297	289	262, 303
4.	Dichlormethane	287	293	286	288	275	256, 299	290	260, 301
5.	Diethyl ether	224, 287	253	227, 283	225, 284	229; 272	228, 252 294	252	251
6.	N,N-Dimethylacetamide	289	293	286	285	277	297	291	294
7.	N,N-Dimethylformamide	289	337	285	286	278	297	292	295
8.	N,N-Dimethylsulfoxide	291	296, 337, 394	289	288	284	301	292	275
9.	1,4-Dioxane	287	281	285	284	276	254, 297	282	279
10.	Ethanol	226, 292	225, 290	230, 290	228, 289	233, 271	234	227, 292	224, 269
11.	Ethyl acetate	285	292	283	283	272	257, 295	288	258, 296
12.	Methanol	227, 288	225, 292	229, 288	229, 288	233, 278	235, 299	227, 290	225, 269
13.	Methyl acetate	287	266, 292	284	285	275	257, 296	287	261, 294
14.	2-Methyl-1-propanol	232, 290	270	234, 290	235, 288	239, 268	247, 298	290	269
15.	N-Methylformamide	289	307	288	287	278	298	303	303
16.	1-Propanol	236, 293	293	239, 290	235, 289	240, 275	261, 298	292	277
17.	2-Propanol	228, 293	225, 292	231, 293	229, 290	233, 272	233, 298	227, 293	224, 270
18.	tert-Butanol	232, 293	292, 353	232, 289	232, 289	234, 268	234, 297	292, 253	268, 358
19.	Tetrahydrofuran	289	296	289	273, 290	269, 291	253, 296	294	292

Table S-V. Solvent parameters

No.	Solvent	Kamlet-Taft			Catalán			
		π^*	β	α	SA	SB	SP	SdP
1.	Acetonitrile	0.75	0.31	0.19	0.044	0.286	0.645	0.974
2.	1-Butanol	0.47	0.88	0.79	0.341	0.809	0.674	0.655
3.	Chloroform	0.58	0.00	0.44	0.047	0.071	0.783	0.614
4.	Dichloromethane	0.82	0.00	0.30	0.040	0.178	0.761	0.769
5.	Diethyl ether	0.27	0.47	0.00	0.000	0.562	0.617	0.385
6.	N,N-Dimethylacetamide	0.88	0.76	0.00	0.028	0.650	0.763	0.987
7.	N,N-Dimethylformamide	0.88	0.69	0.00	0.031	0.613	0.759	0.977
8.	N,N-Dimethylsulfoxide	1.00	0.76	0.00	0.072	0.647	0.830	1.000
9.	1,4-Dioxane	0.55	0.37	0.00	0.000	0.444	0.737	0.312
10.	Ethanol	0.54	0.77	0.83	0.400	0.658	0.633	0.783
11.	Ethyl acetate	0.55	0.45	0.00	0.000	0.542	0.656	0.603
12.	Methanol	0.60	0.62	0.93	0.605	0.545	0.608	0.904
13.	Methyl acetate	0.60	0.37	0.00	/	/	/	/
14.	2-Metyl-1-propanol	0.41	0.93	0.41	0.000	0.590	0.710	0.630
15.	N-Methylformamide	0.90	0.80	0.62	/	/	/	/
16.	1-Propanol	0.52	0.90	0.78	0.367	0.782	0.658	0.748
17.	2-Propanol	0.48	0.95	0.76	0.283	0.830	0.633	0.808
18.	tert-Butanol	0.41	1.01	0.68	0.145	0.928	0.632	0.732
19.	Tetrahydrofuran	0.58	0.55	0.00	0.000	0.591	0.714	0.634

Table S-VI. Regression fits to solvatochromic parameters (Eq. (2)) and percentage contribution of solvatochromic parameters

No.	$\nu_0 /$ 10^3 cm^{-1}	$s /$ 10^3 cm^{-1}	$b /$ 10^3 cm^{-1}	$a /$ 10^3 cm^{-1}	R^a	s^b	F^c	$P_\pi / \%$	$P_\beta / \%$	$P_\alpha / \%$
1	35.14 (± 0.06)	-0.12 (± 0.04)	-0.59 (± 0.05)	-0.52 (± 0.04)	0.995	0.004	253	9.76	47.97	42.27
2	45.51 (± 0.66)	-13.52 (± 0.80)	-5.69 (± 0.54)	0.53 (± 0.18)	0.985	0.405	99	68.49	28.82	2.68
3	35.49 (± 0.10)	-0.41 (± 0.14)	-0.14 (± 0.04)	-0.82 (± 0.07)	0.975	0.081	52	29.93	10.22	59.85
4	35.31 (± 0.14)	-0.39 (± 0.18)	0.14 (± 0.04)	-0.89 (± 0.10)	0.951	0.110	25	27.46	9.86	62.68
5	37.77 (± 0.30)	-2.59 (± 0.39)	0.48 (± 0.04)	0.09 (± 0.04)	0.944	0.234	22	81.96	15.19	2.85
6	34.16 (± 0.06)	-0.62 (± 0.08)	0.05 (± 0.01)	-0.43 (± 0.04)	0.970	0.045	48	55.86	4.50	38.74
7	36.91 (± 0.28)	-2.48 (± 0.31)	-0.49 (± 0.16)	-1.74 (± 0.22)	0.963	0.175	34	52.65	10.40	36.94
8.	34.42 (± 0.90)	-2.27 (± 1.05)	2.12 (± 0.57)	2.54 (± 0.44)	0.971	0.456	45	32.76	30.59	36.65

^aCorrelation coefficient; ^bStandard error of the estimate; ^cFisher's test.

Table S-VII. Regression fits to solvatochromic parameters (Eq. (3)) and percentage contribution of solvatochromic parameters

No.	$\nu_0 / 10^3$ cm ⁻¹	$a / 10^3$ cm ⁻¹	$b / 10^3$ cm ⁻¹	$c / 10^3$ cm ⁻¹	$d / 10^3$ cm ⁻¹	R^a	s^b	F^c	$P_{SA} /$ %	$P_{SB} /$ %	$P_{SP} /$ %	$P_{SDP} /$ %
1	35.76 (±0.25)	-0.13 (±0.01)	-0.81 (±0.38)	-1.23 (±0.18)	-0.71 (±0.13)	0.984	0.07	55	4.51	28.12	42.71	24.65
2	57.65 (±2.76)	-0.90 (±0.15)	-2.70 (±1.01)	-22.61 (±3.98)	-8.33 (±1.34)	0.973	0.717	32	2.61	7.82	65.46	24.12
3	36.23 (±0.43)	-0.28 (±0.01)	-1.47 (±0.62)	-2.00 (±0.29)	0.25 (±0.03)	0.949	0.119	15	7.00	36.75	50.0	6.25
4	36.64 (±0.61)	-0.03 (±0.01)	-1.11 (±0.08)	-0.97 (±0.28)	-1.25 (±0.31)	0.936	0.128	12	0.89	33.04	28.87	37.20
5	42.13 (±0.78)	0.27 (±0.03)	-7.53 (±1.13)	0.19 (±0.06)	-1.14 (±0.30)	0.961	0.160	21	2.96	82.47	2.08	12.49
6	36.39 (±0.28)	0.30 (±0.11)	-3.55 (±0.40)	-1.31 (±0.13)	-0.52 (±0.13)	0.978	0.058	38	5.28	62.5	23.06	9.15
7	54.51 (±2.42)	-5.57 (±0.98)	-3.56 (±0.83)	-25.60 (±3.51)	-3.12 (±0.80)	0.983	0.421	50	14.71	9.40	67.64	8.24
8	61.63 (±2.68)	-1.24 (±0.32)	-4.11 (±0.72)	-26.78 (±3.46)	-8.70 (±1.09)	0.972	0.458	30	3.04	10.07	65.59	21.31

^aCorrelation coefficient; ^bStandard error of the estimate; ^cFisher's test.

REFERENCES

1. S. Rajiv, B. Rajesh, J. Pradip, G. Amitgiri, C. Rajendra, WO/2019/111218, 2019
2. J. A. Jiang, C. Chen, Y. Guo, D. H. Liao, X. D. Pan, Y. F. Ji, *Green Chem.* **16** (2014) 2807 (<https://dx.doi.org/10.1039/c4gc00003j>)
3. J. Geldsetzer, M. Kalesse, *Beilstein J. Org. Chem.* **16** (2020) 670 (<https://dx.doi.org/10.3762/bjoc.16.64>)
4. S. K. Sharma, *Res. J. Chem Sci.* **5** (2015) 54
5. M. R. Taghartapeh, N. Noropzi Pesyan, H. Rashidnejad, H. R. Khavasi, A. Soltani, *J. Mol. Struct.* **1149** (2017) 862 (<https://dx.doi.org/10.1016/j.molstruc.2017.08.054>).



J. Serb. Chem. Soc. 88 (9) 825–840 (2023)
JSCS–5665

Evaluation of derivatives of 2,3-dihydroquinazolin-4(1H)-one as inhibitors of cholinesterases and their antioxidant activity: *In vitro*, *in silico* and kinetics studies

OLUWATOYIN BABATUNDE¹, SHEHRYAR HAMEED¹, KINGSLEY ADIBE MBACHU^{1,2}, FAIZA SALEEM¹, SRIDEVI CHIGURUPATI³, ABDUL WADOOD⁴, ASHFAQ UR REHMAN⁴, VIJAYAN VENUGOPAL⁵, KHALID MOHAMMED KHAN^{1,7,*}, MUHAMMAD TAHA⁷, OLUSEGUN EKUNDAYO² and MARIA AQEEL KHAN⁶

¹H. E. J. Research Institute of Chemistry, International Center for Chemical and Biological Sciences, University of Karachi, Karachi-75270, Pakistan, ²Department of Chemistry, University of Ibadan, Nigeria, ³Department of Medicinal Chemistry and Pharmacognosy, College of Pharmacy, Qassim University, Buraydah-52571, Saudi Arabia, ⁴Department of Biochemistry, Computational Medicinal Chemistry Laboratory, UCSS, Abdul Wali Khan University, Mardan, Pakistan, ⁵Faculty of Pharmacy, AIMST University, Kedah-08100, Malaysia, ⁶Third World Center for Science and Technology, H. E. J. Research Institute of Chemistry, International Center for Chemical and Biological Sciences, University of Karachi, Karachi-75270, Pakistan and ⁷Department of Clinical Pharmacy, Institute for Research and Medical Consultations (IRMC), Imam Abdulrahman Bin Faisal University, P.O. Box 1982, Dammam, 31441, Saudi Arabia

(Received 6 November 2021, revised 17 May 2022, accepted 2 February 2023)

Abstract: In search of potent inhibitors of cholinesterase enzymes and antioxidant agents, synthetic derivatives of dihydroquinazolin-4(1H)-one (**1–38**) were evaluated as potential anti-Alzheimer agents through *in vitro* acetylcholinesterase (AChE) and butyrylcholinesterase (BChE) inhibitions and radical (DPPH and ABTS) scavenging activities. The structure–activity relationship (SAR) was mainly based on the different substituents at the aryl part which showed a significant effect on the inhibitory potential of enzymes and radical scavenging activities. The kinetic studies of most active compounds showed a noncompetitive mode of inhibition for AChE and a competitive mode of inhibition for the BChE enzyme. Additionally, molecular modelling studies were carried out to investigate the possible binding interactions of quinazolinone derivatives with the active site of both enzymes.

Keywords: quinazolinone; dual inhibitors; acetylcholinesterase; butyrylcholinesterase; antioxidant; *in vitro*; *in silico*; kinetic studies.

* Corresponding author. E-mail: khalid.khan@iccs.edu; drkhalidhej@gmail.com
<https://doi.org/10.2298/JSC211106005B>



INTRODUCTION

In the central nervous system (CNS), one of the preeminent neurotransmitters is acetylcholine (ACh) which is related to memory and cognition. Insufficient ACh levels in the CNS can lead to diseases such as Alzheimer's disease (AD).¹ AD is the most common cause of dementia in elderly people and is characterized by several impaired cortical functions, including judgment, memory loss, comprehension, orientation, language deficit, and learning capacity.² The predominant symptoms of all types of dementia are thought to be associated with the gradual decline of broad and compact cholinergic innervation of the human cerebral cortex. This decline contributes to the behavioural and cognitive deficits in AD and is also linked with the reduced levels of neurotransmitters, choline acetyltransferase, acetylcholinesterase (AChE) and Ach.³ AChE and butyrylcholinesterase (BChE) enzymes are hydrolytic enzymes that act on the neurotransmitter ACh by cleaving it into choline and acetate, thereby stopping their action in the synaptic cleft.⁴ Both enzymes are found in amyloid plaques and neurofibrillary tangles in the brain.⁵ AChE is the most important enzyme that regulates the level of acetylcholine in a healthy brain, while BChE plays an insignificant role. In AD patients, the AChE activity decreases, BChE activity increases and the ratio between AChE and BChE varies from normal to high levels (0.6–11) in the cortical regions of the brain that affect the disease.^{6,7} These observations lead to the concept of dual inhibition, and the most effective treatment approach has been suggested to increase ACh levels and limit cholinergic function by inhibiting AChE and BChE enzymes.

Quinazolinones are extensively explored and are considered important as bioactive synthetic molecules for the development of novel therapeutic agents.⁸ Quinazolinone belongs to the *N*-containing fused heterocyclic compounds is a quinazoline with a carbonyl group in the C₄N₂ ring. There are two isomers possible: 4-quinazolinone and 2-quinazolinone; however, the 4-quinazolinone isomer is more common.⁹ These compounds have raised universal concerns due to their broad and pronounced biopharmaceutical activities.¹⁰ Many substituted quinazolinones have a broad range of bioactivities such as antimicrobial, antimalarial, antifungal, antiprotozoal, anticancer, antiviral, anti-inflammatory, anti-tubercular, anticonvulsant, diuretic, acaricidal, muscle relaxant, antidepressant, weedicide and many other biological activities.¹¹ Quinazolinone compounds are also used in the syntheses of a variety of functional substances for synthetic chemistry and are also present in various drugs (Fig. 1).¹²

Antioxidant compounds exhibit an important part as health protection factors.¹³ Free radicals are ions, atoms or molecules possessing an unpaired electron such as hydroxyl, nitric oxide, and superoxide which are called reactive oxygen species (ROS).¹⁴ ROS are generated in the human body and can damage DNA, proteins, and lipids, which may lead to different complications such as inflame-

mation, toxicity and carcinogenesis. Plants-derived antioxidants include carotenes, phytoestrogens, vitamin C, vitamin E and phytates.¹⁵ Furthermore, chronic diseases which are life-limiting, such as diabetes, cancer, arteriosclerosis, AD, and aging, are developed by radical reactions.¹⁶ Natural or synthetic antioxidants compounds terminate the chain reactions by interacting with free radicals before essential molecules are damaged.¹⁷ Thus, the synthesis of new potent antioxidant compounds is of vital importance for rapidly quantifying the effectiveness of antioxidants in disease prevention.

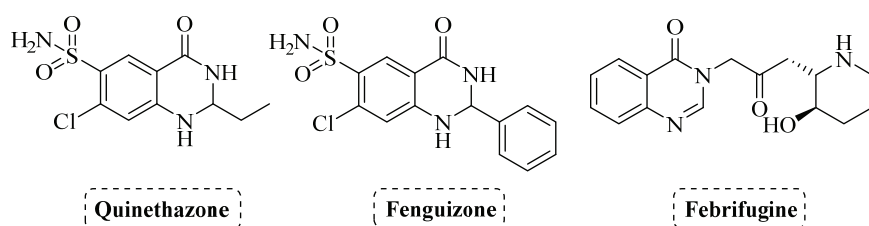


Fig. 1. Pharmacological importance of quinazolinone-based drugs.

Our research group is continuously doing efforts in search of lead compounds for two decades to discover new enzyme inhibitors.^{18–21} Previously, we have explored a large number of potent inhibitors based on quinazolinone derivatives, including α -amylase, α -glucosidase,^{22,23} β -glucuronidase²⁴ and antileishmanial activities.²⁵ These heterocycles are reported to possess various significant biological activities. Derivatives of dihydroquinazolin-4(1H)-one, in particular, has drawn more and more attention for synthesizing pharmaceuticals and in the field of agrochemicals. Herein we are going to report dihydroquinazolin-4(1H)-ones as a new class of inhibitors against acetylcholinesterase, butyrylcholinesterase enzymes and with its antioxidant potential (Fig. 2). In this study, dihydro-

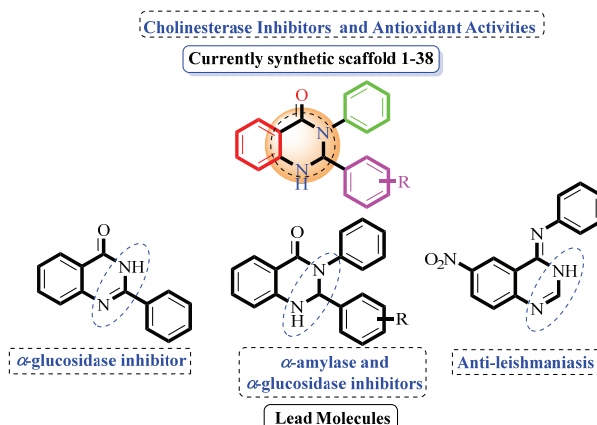


Fig. 2. Rationale of the current study.

quinazolin-4(1*H*)-ones (**1–38**, Table I) have been reported as antioxidant agents and potent cholinesterase inhibitors which may improve clinical outcomes for the development of anti-AD agents.

EXPERIMENTAL

Materials and methods

All enzymes were purchased from Sigma–Aldrich and used without further purification. The acetylcholinesterase enzyme from *Electrophorus electricus* (electric eel) supplied by Sigma–Aldrich (GmbH, USA) whereas butyrylcholinesterase from equine serum procured from Sigma–Aldrich, SRE020; 5,5-dithio-bis-nitrobenzoic acid (DTNB), acetylthiocholine iodide 99 % (ATChI), donepezil hydrochloride were obtained from Sigma–Aldrich. All reagents were purchased from Merck and Sigma–Aldrich. Thin-layer chromatography was carried out on precoated silica gel, GF-254 (Merck). Spots were visualized under ultraviolet light at 254 and 366 nm or iodine vapors. EI- and HREI-MS spectra were recorded on MAT 312 and MAT 113D mass spectrometers. The ¹H- and ¹³C-NMR were recorded on Bruker AM spectrometers, operating at 300 and 400 MHz. The chemical shift (δ) values are presented in ppm, relative to tetramethylsilane (TMS) as an internal standard, and the coupling constant (J) is in Hz.

Cholinesterase enzyme activity

The *in vitro* AChE and BChE inhibitory activity was measured using the methods described earlier.²⁶ Briefly, stock solutions (1 mg/mL) of test compounds were prepared using 0.01 % DMSO. Working solutions (0.01–100 μ g/mL) were prepared by serial dilutions. The various concentrations of test compounds (10 μ L) were pre-incubated with sodium phosphate buffer (0.1 M; pH 8.0; 150 μ L); AChE solution/ BChE (0.1 U/mL; 20 μ L) for 15 min at 25 °C and addition of DTNB (10 mM; 10 μ L). The reaction was initiated by the addition of ATChI (14 mM; 10 μ L). The reaction mixture was mixed using a cyclomixer and incubated for 10 min at room temperature. The absorbance was measured using a microplate reader at 410 nm wavelength against the blank reading containing 10 μ L DMSO instead of the test compound. The inhibition was calculated in %:

$$\text{Inhibition} = 100(1 - \text{absorbance sample/absorbance control}) \quad (1)$$

and the IC_{50} was calculated. Donepezil (0.01–100 μ g/mL) was used as the positive control.

Kinetic study assay

In derivatives of 2,3-dihydroquinazolin-4(1*H*)-one, seven compounds, **2**, **3**, **4**, **10**, **16**, **28** and **34** were selected for kinetic studies, based on their lower IC_{50} values (23.08 to 27.57 μ M). In kinetic studies, we used acetyl thiocholine iodide (ATCI)/butyrylthiocholine iodide (BTCl) as a substrate at various concentration (0.175, 0.35, 0.7 and 1.40 mM) and different concentration of AChE/BChE inhibitors (0, 0.625, 1.25 and 2.5 μ M) were applied. Enzyme inhibition kinetic mechanisms were determined by using Sigma Plot 14.0 software. The rate of substrate and inhibitor reactions was calculated. Based on the rate of reactions, the software showed the type of enzyme kinetics mechanism. Kinetic studies have shown all the compounds followed as non-competitive type inhibitors (Table I). The types of inhibition of AChE/BChE were determined by Lineweaver Burk plots. The reciprocal of the rate of the reaction was plotted against the reciprocal of substrate concentration to monitor the effect of the inhibitor on both K_m and highest inhibition rate, V_{max} , values. K_m is also known as the Michaelis constant representing the substrate concentration at which the reaction rate is 50 % of the V_{max} .

Radical scavenging assay

DPPH (2,2-diphenyl-1-picrylhydrazyl) radical activity. Preparation of DPPH solution was adopted from Molyneux²⁷ and Blois²⁸ with minor modification. All the test compounds were dissolved in 95 % ethanol. Briefly, 0.5 mL of test compounds were added (0 – blank control, 10, 25, 50, 100, 250, 500 and 1000 g/mL) to 0.5 mL of DPPH (2 μM in 95 % ethanol) and the mixture was incubated at room temperature for 30 min. The absorbance was measured at 517 nm,²⁹ and the percentage inhibition of test compounds was calculated using the following equation using Microsoft Excel software (version 2010):

$$\text{Scavenging} = 100(1 - (\text{absorbance sample} / \text{absorbance control})) \quad (2)$$

Ascorbic acid was used as the positive control.

The IC_{50} (half maximal inhibitory concentration) was calculated by constructing a non-linear regression graph between inhibition vs. concentration, using Graph Pad Prism software (version 5).

ABTS (2,2'-azino-bis(3-ethylbenzothiazoline-6-sulfonic acid)) free-radical cation activity. The ABTS free radical cation scavenging ability of the synthesized compounds was determined according to the procedure described earlier.³⁰ ABTS was dissolved in distilled water (7×10^{-3} M) and potassium persulphate (2.45×10^{-3} M) was added. This reaction mixture was left overnight (12–16 h) in the dark at room temperature. Various concentrations of test substances (1000, 500, 250, 100, 50, 25 and 10 μg/mL) were incubated with the ABTS⁺ solution for 30 min. The absorbance was measured at 734 nm, the inhibition was calculated using Eq. (1) and the IC_{50} was calculated. Ascorbic acid was used as the positive control.

Molecular docking protocol

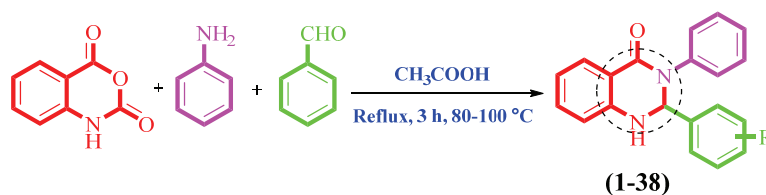
Acetylcholinesterase and butyrylcholinesterase. Molecular docking was performed using molecular operating environment (MOE)³¹ to explore the binding mode of the synthetic compounds against acetylcholinesterase (AChE) and butyrylcholinesterase (BChE) enzymes. First, the 3D structures for all the compounds were generated using the MOE-builder module. Next, the compounds were protonated, and energy was minimized using the default parameters of the MOE. The structural coordinates for AChE and BChE was retrieved from protein data-bank (PDB code; 1acl & 1p0p). All the structures were subjected to MOE for preparation. Further, the protonation was done using default parameters of the structure preparation module of MOE. Next, the energy was minimized for both the coordinates to get minimal energy conformation. Finally, the refined structures were used for the docking study using the default parameters of MOE. Before running the docking protocol, we have selected a total of often conformations for each compound. The top-ranked conformations based on docking score (S) were selected for the protein–ligand interaction (PL) analysis.

RESULTS AND DISCUSSION

Chemistry

Dihydroquinazolin-4(1H)-ones **1–38** were synthesized by treating isatoic anhydride, substituted aldehyde, and aniline under reflux for 3 h. The reaction was carried out in acetic acid as a solvent at 80–90 °C, Scheme 1. After the reaction completion, it was cooled to room temperature. The solution was added to ice water to form a precipitate. The mixture was filtered and the crude product was washed continuously with an excess of water. The obtained crude product was washed with different solvents to remove impurities, on crystallization from etha-

nol gave the corresponding pure products having 60–85 % yields.²³ The molecular structures of all compounds **1–38** were identified by EI-MS, HREI-MS, ¹H- and ¹³C-NMR.



Scheme 1. Synthesis of dihydroquinazolin-4(1*H*)-ones **1–38**.

In vitro AChE, BChE inhibitions and antioxidant activities

All synthetic dihydroquinazolin-4(1*H*)-ones **1–38** were screened for *in vitro* acetylcholinesterase and butyrylcholinesterase inhibitions, and antioxidant activities. All compounds exhibited good to moderate inhibitory activities in the range of IC_{50} values 23.08–89.7 and 26.01–89.7 μ M against AChE and BChE inhibitions, and 16.33–96.65 and 18.01–94.97 μ M against DPPH and ABTS activities when compared to the donepezil ($IC_{50} = 15.08 \pm 0.07 \mu$ M) and ascorbic acid as the standards ($IC_{50} = 15.08 \pm 0.07$ and $16.09 \pm 0.17 \mu$ M), respectively (Table I). The structure–activity relationship (SAR) proposed that all structural features such as benzene ring, carbonyl group, quinazoline moiety, phenyl ring and aryl ring “R” were taking part in the activity, and due to the presence of different groups “R” at the aryl part some significant fluctuation in the activity was observed (Fig. S-3 of the Supplementary material to this paper).

TABLE I. *In vitro* acetylcholinesterase, butyrylcholinesterase activity, and antioxidant activity ($IC_{50} \pm SEM^a$ in μ M, SEM – standard error of the mean) after using dihydroquinazolin-4(1*H*)-one derivatives **1–38**; NA – not active

Compd. No.	R	AChE activity	BChE activity	DPPH radical activity	ABTS radical activity
1	4-Cl (C ₆ H ₄)	35.04±0.20	37.13±0.18	41.7±0.06	42.97±0.19
2	2-Cl (C ₆ H ₄)	23.08±0.03	26.08±0.43	17.65±0.23	19.47±0.03
3	2,6-Cl (C ₆ H ₃)	24.94±0.12	27.13±0.08	30.7±0.06	32.97±0.19
4	2,4-Cl (C ₆ H ₃)	24.57±0.07	27.57±0.07	16.33±0.02	18.01±0.12
5	2-OH, 3,5-Cl (C ₆ H ₂)	61.89±0.12	67.91±0.18	57.33±0.02	58.01±0.12
6	2-Cl, 6-NO ₂ (C ₆ H ₃)	NA	NA	70.7± 0.06	71.97± 0.19
7	5-Cl, 2-OH (C ₆ H ₃)	81.94±0.12	82.13±0.08	83.57±0.17	83.68±0.36
8	3,5-OCH ₃ (C ₆ H ₃)	NA	NA	96.65±0.03	94.47±0.13
9	2,5-OCH ₃ (C ₆ H ₃)	88.15±0.12	87.15±0.12	84.04±0.02	85.99±0.09
10	2,6-OCH ₃ (C ₆ H ₃)	26.94±0.12	27.99±0.09	24.33±0.02	25.01±0.12
11	3,4-OCH ₃ (C ₆ H ₃)	87.27±0.18	86.08±0.43	87.57±0.08	89.27±0.18
12	2-Br, 4,5-OCH ₃ (C ₆ H ₃)	67.91±0.18	69.02±0.11	51.65±0.03	52.47±0.13
13	2,4-OCH ₃ (C ₆ H ₃)	89.7±0.16	85.97±0.19	82.17±0.14	82.01±0.09

TABLE I. Continued

Compd. No.	R	AChE activity	BChE activity	DPPH radical activity	ABTS radical activity
14	3,4,5-OCH ₃ (C ₆ H ₂)	NA	NA	86.65±0.23	87.47±0.03
15	2,3,4-OCH ₃ (C ₆ H ₂)	NA ^b	NA ^b	83.33±0.02	85.01±0.12
16	3-OC ₂ H ₅ , 4-OCH ₃ (C ₆ H ₃)	27.57±0.07	29.13±0.18	30.04±0.02	31.99 ±0.09
17	3-OCH ₃ , 4-OC ₂ H ₅	NA ^b	NA ^b	92.7± 0.06	94.97± 0.19
18	3,5-OCH ₃ , 4-OH (C ₆ H ₂)	87.27± 0.18	89.7± 0.16	83.46± 0.03	84.61± 0.11
19	4-Br, 3,5-OCH ₃ (C ₆ H ₂)	83.08±0.03	84.94±0.12	76.33±0.02	79.01±0.12
20	4-F, 3-OCH ₃ (C ₆ H ₃)	51.94±0.12	53.33±0.02	48.65±0.23	49.47±0.03
21	3-Br, 2-OCH ₃ (C ₆ H ₃)	89.17±0.16	88.33±0.12	81.7±0.06	85.97±0.19
22	2-F, 4-OCH ₃ (C ₆ H ₃)	27.91±0.18	29.02±0.11	31.33±0.12	32.01±0.12
23	2-Cl, 3-OCH ₃ (C ₆ H ₃)	88.15±0.12	87.13±0.12	83.04±0.02	84.99±0.09
24	3-OC ₂ H ₅ , 2-OH (C ₆ H ₃)	61.01±0.17	64.57±0.07	49.84±0.03	52.71±0.11
25	2-OCH ₂ (C ₆ H ₅)	NA	NA	72.7±0.06	74.97±0.19
26	3-OCH ₂ (C ₆ H ₅), 4-OCH ₃ (C ₆ H ₃)	NA	NA	88.89±0.10	89.09±0.09
27	4-OCH ₂ (C ₆ H ₅)	NA	NA	84.89±0.20	89.09±0.19
28	4-Br (C ₆ H ₄)	25.33±0.02	26.27±0.18	27.33±0.02	28.01±0.12
29	4-CF ₃ (C ₆ H ₄)	NA	NA	92.13±0.08	92.79±0.17
30	2-Thiophene	43.08±0.03	46.08±0.43	47.65±0.23	49.47±0.03
31	3-Bromo, 4-OH (C ₆ H ₃)	85.33±0.02	87.47±0.13	83.01±0.07	83.11±0.15
32	4-OCH ₃ , 3-OH (C ₆ H ₃)	77.27±0.18	75.04±0.52	71.7±0.06	72.97±0.19
33	3-OH (C ₆ H ₄)	47.17±0.15	48.15±0.12	42.33±0.12	43.01±0.12
34	2-OH (C ₆ H ₄)	27.57±0.07	29.02±0.11	28.46±0.03	30.71±0.11
35	4-OH (C ₆ H ₄)	37.7±0.16	38.94±0.12	39.7±0.16	40.97±0.14
36	3,4-OH (C ₆ H ₃)	45.04±0.52	47.7±0.16	48.46±0.03	52.71±0.11
37	2,5-OH (C ₆ H ₃)	77.33±0.02	79.7±0.16	76.65±0.03	77.47±0.13
38	2,3-OH (C ₆ H ₃)	81.94±0.12	83.33±0.02	82.7±0.06	84.97±0.19
	Standard= asc. acid ^a	–	–	15.08±0.03	16.09±0.17
	Standard = donepezil ^b	15.08 ± 0.03	15.08±0.03	–	–

^cStandard for DPPH and ABTS activities; ^dstandard for AChE and BChE inhibitions

SAR for AChE and BChE inhibitions and antioxidant activities

SAR was discussed for all synthetic compounds which were screened for *in vitro* acetylcholinesterase, butyrylcholinesterase inhibitions and antioxidant (DPPH and ABTS) activities.

SAR for AChE and BChE inhibitory activities. Compounds **1–7**, **28** and **29** were halogen-substituted including F, Cl and Br. These compounds displayed inconsistent inhibitory activities against acetylcholinesterase (AChE) and butyrylcholinesterase (BChE) enzymes. Of these, compound **2** with the *ortho*-chloro substitution was found to be the most potent AChE and BChE inhibitor with *IC*₅₀ values of 23.08±0.03 and 26.08±0.43 μM, respectively. A comparison of the inhibitory activities of compounds **1** and **2** showed a positional effect on the inhibitory potential. Namely, in compound **1** the presence of chloro group at

para-position reduces the inhibitory activity, as shown by the IC_{50} values $35.04 \pm 0.20 \mu\text{M}$ for AChE and $37.13 \pm 0.18 \mu\text{M}$ for BChE enzymes. Correspondingly, in compounds **3** ($IC_{50} = 24.94 \pm 0.12, 27.13 \pm 0.08 \mu\text{M}$) and **4** ($IC_{50} 24.57 \pm 0.07$ and $27.57 \pm 0.07 \mu\text{M}$), a slight decrease in the inhibitory potential was seen by the addition of chloro groups at the *ortho*-, *para*- and di-*ortho*-positions against AChE and BChE enzymes, respectively. However, the presence of chloro groups in compounds **5–7**, along with other groups such as NO_2 and OH, demonstrated lower potential against AChE and BChE enzymes. *para*-Bromo substituted compound **28** ($IC_{50} 25.33 \pm 0.02$ and $26.27 \pm 0.18 \mu\text{M}$), exhibited pronounced activity against both AChE and BChE enzymes, respectively. However, compound **29** with trifluoromethyl substitution was found to be inactive against both enzymes which indicates that the trifluoromethyl group is not actively involved in the binding interaction to the active site of the enzyme (Fig. S-4 of the Supplementary material).

Quinazolinone derivatives as cholinesterase inhibitors show superior inhibitory activity compared to the standard drug tacrine. Among them, halogenated compounds showed potential activity against AChE and BChE enzymes. In our work, halogenated compounds showed potential activities when compared to the standard donepezil.

It has been found that the incorporation of methoxy substitutions in compounds **8–17** at different positions of aryl moiety (R) has a varying degree of inhibition. Among them, *ortho*-dimethoxy substituted compound **10** was found significantly active with IC_{50} of 26.94 ± 0.12 and $27.99 \pm 0.09 \mu\text{M}$ for AChE and BChE enzymes, when compared to its *ortho*, *meta*-dimethoxy derivative compound **9**. Surprisingly, it was found that its *meta*-dimethoxy substituted positional isomer **8** was completely inactive. There might be a possibility that compound **8** attained such a conformation that does not fit well into the active site of the enzyme. However, when methoxy groups are present at the adjacent positions in compound **11** ($IC_{50} 87.27 \pm 0.02$ and $86.08 \pm 0.43 \mu\text{M}$) a noticeable decline in the activity was observed when compared to compound **12** ($IC_{50} 67.91 \pm 0.18, 69.02 \pm 0.11 \mu\text{M}$), where an additional bromo group is present at *ortho*-position. The positional isomer of **11** *i.e.*, compound **13** demonstrated weak inhibitory potential against both enzymes. In the case of trimethoxy substituted derivatives (compounds **14** and **15**), a complete loss of activity was observed. This might be due to the steric hindrance and bulkiness of the groups. Compounds **16** with *para*-methoxy and *meta*-ethoxy substitutions displayed considerable inhibitory potential with IC_{50} of 27.57 ± 0.07 and $29.13 \pm 0.18 \mu\text{M}$ against acetylcholinesterase and butyrylcholinesterase enzymes, respectively. In contrast, compound **17** was found to be inactive against both enzymes (Fig. S-5, Supplementary material). Compounds **18–24** and **32** with the combinations of ethoxy/methoxy and other substitutions such as OH, Cl, F and Br, exhibited moderate inhibition

activities against both enzymes. *ortho*-Fluoro and *para*-methoxy substituted compound **22** was found to have relatively good activity in comparison to its other positional analogs. Compound **18** displayed IC_{50} values 27.91 ± 0.18 and 27.91 ± 0.18 μM against AChE and BChE enzymes, respectively. In contrast its positional isomer (compound **20**), compound **18** exhibited low inhibitory potential with IC_{50} of 51.41 ± 0.12 and 53.33 ± 0.02 μM against acetylcholinesterase and butyrylcholinesterase enzymes. The activity of the combination of Cl, Br and OH with methoxy substituted compounds **18**, **19**, **21**, **23**, **24** and **32**, displayed moderate to weak inhibitory activities which indicate that these groups are creating steric hindrance and less binding interaction in the enzyme's active site or their positive mesomeric effect is negatively contributing in the activity (Fig. S-6, Supplementary material).

Surprisingly, *ortho*, *meta* and *para* benzyloxy-substituted derivatives **25–27** were found to be inactive against acetylcholinesterase and butyrylcholinesterase enzymes. It might be due to bulky groups that do not favourably fit in the active site of the enzyme, which displayed that the presence of hydrophobic groups on the aryl part more specifically the presence of benzyloxy group, resulted in the loss of activity profile of compounds **25–27**, respectively. Exceptionally, thiophene substituted analogue **30** showed moderate activity against AChE and BChE enzymes with IC_{50} values 43.08 ± 0.03 and 46.08 ± 0.43 μM , respectively (Fig. S-7, Supplementary material). Mono-hydroxyl substituted compounds **31–35** showed good to moderate results against acetylcholinesterase and butyrylcholinesterase enzymes. The activity of five hydroxy-substituted derivatives, such as **31–35**, was different from each other against both enzymes. However, the structures of all five derivatives is very similar to each other but differ only in the position of hydroxyl at aryl part "R". Amongst them, compound **34** (IC_{50} 27.57 ± 0.07 and 29.02 ± 0.11 μM) has *ortho*-hydroxyl group exhibited better activity against AChE and BChE enzymes when compared with compounds **33** and **35**, respectively, which indicate that groups and position displayed significant role in the enzyme inhibition. However, compounds **31** and **32** with the combination of bromo and methoxy with a hydroxyl group, respectively, exhibited weak inhibitory activities against AChE and BChE enzymes. This activity pattern demonstrated the involvement of di-substituted hydroxy compounds **36–38**, which also displayed moderate to weak inhibitory activities. Compound **36** (IC_{50} 45.04 ± 0.52 and 47.7 ± 0.16 μM) with *meta*, *para* di-hydroxy substitution showed better activity when compared to compounds **37** and **38** against acetylcholinesterase and butyrylcholinesterase enzymes (Fig. S-8, Supplementary material).

SAR for DPPH and ABTS radical scavenging activities. Based on SAR, the variations observed in DPPH and ATBS activities of quinazolinones **1–38** were discussed and compared against standard ascorbic acid with IC_{50} of 15.08 ± 0.03 and 16.09 ± 0.17 μM , respectively. Dichloro-substituted compound **4** showed

DPPH ($IC_{50} = 16.33 \pm 0.02 \mu\text{M}$) and ABTS ($IC_{50} = 18.01 \pm 0.12 \mu\text{M}$) radical scavenging activities, respectively, and was found to be most active in the series. Its positional isomer (compound **3**) displayed a decline in activity against both radicals. However, mono-substituted compound **2** having chloro group at *meta* position (IC_{50} 17.65 ± 0.23 and $19.47 \pm 0.03 \mu\text{M}$), showed better DPPH and ABTS radical scavenging activities when compared to its positional isomer **1**. Antiradical activity depends on proton and electron transfer between the radical and the scavenging agent. Here 1,4 disubstituted chloro compounds seem to involve electron transfer and free radical scavenging, compared to monosubstituted and 1,3 disubstituted chloro compounds. The addition of hydroxyl and nitro substitution at aryl ring in compounds **5–7**, respectively, showed moderate to weak potential against DPPH and ABTS radical scavenging activities. The activity of di-methoxy substituted compounds **8, 9** and **11–13** showed a further decrease in the activity when compared to *ortho*-dimethoxy substituted compound **10** which showed enhanced DPPH and ABTS radical scavenging activities. The addition of the methoxy group in compounds **14** and **15** further reduced the activity (Fig. S-9, Supplementary material). In the case of compound **16** (IC_{50} 30.04 ± 0.02 and $31.99 \pm 0.99 \mu\text{M}$) with *para*-methoxy and *meta*-ethoxy groups showed better activities when compared to compound **17** (Fig. S-9). Another combination of methoxy with OH, Br, F and Cl substitutions in compounds **18–23** showed weak potential against DPPH and ATBS activities. Compounds **25–27** bearing benzyloxy substitution displayed decreased radical scavenging activities against DPPH and ATBS. The incorporation of bromo group as “R” in compound **28** with IC_{50} value 27.33 ± 0.02 and $28.01 \pm 0.12 \mu\text{M}$, showed better potential than compound **31**. Mono-hydroxy and di-hydroxy substituted compounds **32, 33, 35** and **38** demonstrated good potential against DPPH and ABTS radical scavenging activities as compared to compound **34**. Compounds **23, 29** and **30** showed a further decline in the activities as compared to the standard ascorbic acid (Fig. S-9).

Kinetic studies on acetylcholinesterase inhibitors

Kinetic studies on the most active AChE enzyme inhibitors (compounds **2–4, 10, 16, 28** and **34**) were analysed to interpret the enzyme inhibition mechanisms by using graph fitting analysis in the Sigma-Plot enzyme kinetic software (Fig. S-10A and B, Supplementary material).

In 2,3-dihydroquinazolin-4(1*H*)-ones all the seven compounds (**2–4, 10, 16, 28** and **34**) acetylcholinesterase inhibition rate V_{max} and K_{m} were in the range of 60.5 to $79.8 \mu\text{M min}^{-1} \text{mg}^{-1}$ and 3.0 to 3.6 mM , respectively (Table II and Fig. S-10A). The K_{i} values were confirmed from the Dixon plot by plotting the reciprocal of the rate of reaction against different concentrations of compounds, where K_{i} values of all the eight compounds were in the range of 5.0 to $5.9 \mu\text{M}$ (Fig. S-10B). The inhibitor constant, K_{i} , is an indication of how potent an inhi-

bitor is; it is the concentration required to produce half maximum inhibition. In the uncompetitive type of inhibition, only V_{\max} values are affected and no changes in K_m value. The low V_{\max} and no effect in K_m value of these compounds indicated an uncompetitive type of inhibition.

TABLE II. Kinetic studies of active compounds for acetylcholinesterase inhibition; type of inhibition: uncompetitive

Cmpd. No.	$V_{\max} / \mu\text{M min}^{-1}\text{mg}^{-1}$	K_m / mM	$K_i / \mu\text{M}$
2	79.8±1.2	3.2±0.01	5.2±0.1
3	70.4±1.0	3.6±0.02	5.4±0.2
4	60.5±2.2	3.0±0.01	5.5±0.5
10	66.8±1.8	3.3±0.02	5.8±0.1
16	71.0±1.2	3.1±0.01	5.0±0.2
28	65.4±1.0	3.2±0.02	5.3±0.1
34	53.2±2.2	3.4±0.01	5.9±0.2
Donepezil	62.0±1.0	3.0±0.01	5.1±0.1

Kinetic studies on butyrylcholinesterase inhibition

Kinetic studies on the most active AChE enzyme inhibitors compounds **2–4**, **10**, **16**, **28** and **34** were analysed to interpret their inhibition mechanisms (Fig. S-11, Supplementary material). In 2,3-dihydroquinazolin-4(1H)-ones the V_{\max} and K_m of all the seven compounds were in the range of 80.3 to 85.4 $\mu\text{M min}^{-1} \text{mg}^{-1}$ and 3.1 to 31.8 mM, respectively (Table III and Fig. S-11A). The K_i values were confirmed from the Dixon plot by plotting the reciprocal of the rate of reaction against different concentrations of compounds, where K_i values of all the five compounds were in the range of 10.3 to 10.9 μM (Fig. S-11B). The inhibitor constant, K_i , is an indication of how potent an inhibitor is; it is the concentration required to produce half maximum inhibition. In the competitive type of inhibition, only K_m values are affected and there are no changes in the V_{\max} value. The high K_m and no effect in V_{\max} of these compounds indicated a competitive type of inhibition.

TABLE III. Kinetic studies of active compounds for butyrylcholinesterase inhibition; type of inhibition: competitive

Cmpd. No.	$V_{\max} / \mu\text{M min}^{-1}\text{mg}^{-1}$	K_m / mM	$K_i / \mu\text{M}$
2	82.0±2.2	3.1±0.2	10.6±0.5
3	80.3±2.7	9.2±0.1	10.4±0.3
4	82.2±5.3	20.2±0.2	10.7±0.2
10	85.4±1.2	2.1±0.1	10.6±0.4
16	82.0±1.4	3.7±0.2	10.4±0.1
28	84.1±2.4	31.8±0.1	10.3±0.1
34	82.5±2.9	4.7±0.1	10.9±0.2
Donepezil	80.1±1.6	13.5±0.1	10.2±0.1

Molecular docking (MD) studies

AChE and BChE MD study. MD was performed to explore the binding mode of the synthesized compounds against the targeted enzyme (AChE and BChE). MD results are in good agreement with the experimental results. We have noticed that compounds bearing the electron-withdrawing groups (EWGs) showed the best inhibitory activity against both targets. Interestingly, when compared with the other activity (α -amylase and α -glucosidase),²³ we have noted that the compounds bearing 1,3-dichlorobenzene showed high inhibitory potency when compared to 1-chlorobenzene. Similarly, the following compounds showed invert phenomena in the activity against both the targets. Those compounds bearing 1-chlorobenzene/1-bromobenzene substitution were found to be active. The protein–ligand interaction (PLI) profile was enlisted for all docked compounds in Tables S-IV and S-V of the Supplementary material.

Acetylcholinesterase (AChE) molecular docking study. The docking results for most active compound **2** against AChE revealed that the 3-methyl-tetrahydro pyrimidine-4(1*H*)-one moiety of the compound adopted several favourable interactions with catalytic residues (Fig. 1A, surface representation), including acidic residue Glu72, hydrophobic side chain Tyr334, Trp279 and Phe331, respectively (Fig. 1B). The reason for high potency might include the high number of adopted favourable interactions with catalytic residues. In the case of the 2nd ranked active compound **4**, where the substitution groups are the 2,3-dichloro, a similar interaction was observed. But the only difference so far found is; the active compound adopted π -stacking interaction with the 1-chloro moiety, whereas it lacks in the 2nd active compound (Fig. 1C). This might be one of the reasons for reduced activity in compound **4**. The PLI profile was enlisted for all docked compounds (Table S-IV).

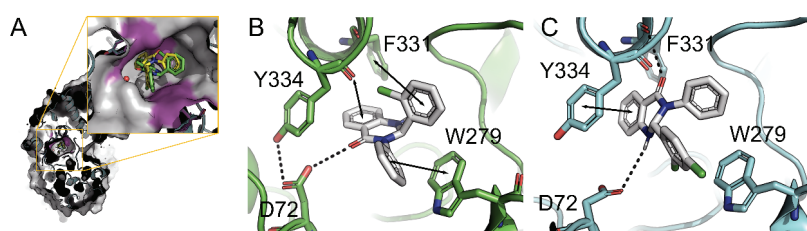


Fig. 12. The PLI profile for synthesized compounds against the acetylcholinesterase (AChE) enzymes. A) The surface representation of the enzyme, B) the binding mode of the most potent compound **2** in the series and C) for compound **4**. A double-sided arrow represents the π -stacking.

Butyrylcholinesterase (BChE) molecular docking study. In the case of the docking results for most active compounds against BChE (Fig. S-2A) activity revealed that the compound bearing electron-withdrawing groups (EWG), *i.e.*,

1-chlorobenzene (Fig. 2B) and 1-bromobenzene (Fig. 2C), *etc.*, showed best inhibitory activity against the BChE enzyme. The PLI profile for the most active compound **2** and 2nd-ranked active compound **28** revealed an interesting observation that both the compound shared similar interaction with the hydrophobic residue Phe329. More interestingly, the most active compound **2** adopted interaction with the acidic residue Glu70 while compound **28** with Glu197, which suggested that might be these two residues play a vital role in enhancing the enzymatic activity. The hydrophobic residue Trp82, which is an active residue in the active site and play a vital role in the enzymatic activity, adopted two π -stacking interactions with the substituted benzene ring while the compound **28** is not capable of adapting interaction even though this residue is found in proximity with the 6-ring of the compound.

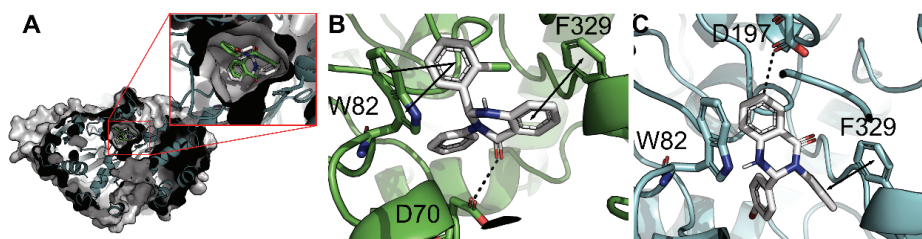


Fig. 2. The PLI profile for synthesized compounds against the butyrylcholinesterase (BChE) enzymes. A) The surface representation of the enzyme, B) the binding mode of the most potent compound **2** in the series and C) for compound **28**. The π -stacking is represented by a double-sided arrow.

Overall these results describe that the compounds bearing the EWG either at *ortho*- or *meta*-position displayed good inhibitory potential against the enzyme while others bearing both *ortho*- and *meta*- or *ortho*- and *para*-positions showed less activity. The PLI profiles were enlisted for all docked compounds in (Table S-V).

CONCLUSION

In the present study, compounds showed moderate to good inhibition against AChE, BChE, and antioxidant activities as compared with the standards donepezil and ascorbic acid, respectively. A structure-activity relationship was also established. *In silico* modeling studies revealed the binding mode of the quinazolinone derivatives. The kinetic studies on the seven most active compounds **2–4**, **10**, **16**, **28** and **34** were carried out. The compounds **2–4**, **10**, **16**, **28** and **34** were found to have an uncompetitive mode for acetylcholinesterase enzyme and the compounds **2–4**, **10**, **16**, **28** and **34** were found to be in the competitive mode for butyrylcholinesterase enzymes.

SUPPLEMENTARY MATERIAL

Additional data and information are available electronically at the pages of journal website: <https://www.shd-pub.org.rs/index.php/JSCS/article/view/11370>, or from the corresponding author on request.

Acknowledgement. The authors acknowledge the financial support of Sindh Higher Education Commission (SHEC), Pakistan *vide* letter No. NO.DD/SHEC/1-14/2014, Project Code SHEC/SRSP/Med-3/15/2021-21.

ИЗВОД

ИЗУЧАВАЊЕ ДЕРИВАТА 2,3-ДИХИДРОХИНАЗОЛИН-4(1H)-ОНА КАО ИНХИБИТОРА
ХОЛИНЕСТЕРАЗА И ЊИХОВЕ АНТИОКСИДАТИВНЕ АКТИВНОСТИ: *IN VITRO*,
IN SILICO И КИНЕТИЧКА ИСПИТИВАЊА

OLUWATOYIN BABATUNDE¹, SHEHRYAR HAMEED¹, KINGSLEY ADIBE MBACHU^{1,2}, FAIZA SALEEM¹, SRIDEVI CHIGURUPATI³, ABDUL WADOOD⁴, ASHFAQ UR REHMAN⁴, VIJAYAN VENUGOPAL⁵, KHALID MOHAMMED KHAN^{1,7}, MUHAMMAD TAHAN⁷, OLUSEGUN EKUNDAYO² и MARIA AQEEL KHAN⁶

¹H. E. J. Research Institute of Chemistry, International Center for Chemical and Biological Sciences, University of Karachi, Karachi-75270, Pakistan, ²Department of Chemistry, University of Ibadan, Nigeria, ³Department of Medicinal Chemistry and Pharmacognosy, College of Pharmacy, Qassim University, Buraydah-52571, Saudi Arabia, ⁴Department of Biochemistry, Computational Medicinal Chemistry Laboratory, UCSS, Abdul Wali Khan University, Mardan, Pakistan, ⁵Faculty of Pharmacy, AIMST University, Kedah-08100, Malaysia, ⁶Third World Center for Science and Technology, H. E. J. Research Institute of Chemistry, International Center for Chemical and Biological Sciences, University of Karachi, Karachi-75270, Pakistan и ⁷Department of Clinical Pharmacy, Institute for Research and Medical Consultations (IRMC), Imam Abdulrahman Bin Faisal University, P.O. Box 1982, Dammam, 31441, Saudi Arabia

Током истраживања нових активних инхибитора холинестераза и антиоксидативних агенаса, испитивани су синтетички деривати дихидрохиназолин-4(1H)-она **1–38** као потенцијални агенси за третман Алцхајмерове болести инхибицијом ацетилхолин-естеразе (AChE), бутирлихолин-естеразе (BChE) и као хватачи слободних радикала (DPPH и ABTS). Доминантан утицај на инхибицију ензима и способност хватања слободних радикала имају супституенти на ароматичном језгру. На основу резултата испитивања кинетике закључено је да једињења делују некомпетентним механизмом инхибиције. Молекулским моделовањем су испитане могуће интеракције током везивања киназолинских деривата у активним местима оба ензима.

(Примљено 6. новембра 2021, ревидирано 17. маја 2022, прихваћено 2. фебруара 2023)

REFERENCES

1. S. Kumar, D. S. Brijeshlata, S. Dixit, *Int. J. Pharm. Bio. Sci.* **3** (2012) 59 (<https://www.mendeley.com/catalogue/e895c115-5ca8-3d1b-956e-0477555aecc6/Int-J-Pharma-Bio-Sci>)
2. B. Desgranges, J. C. Baron, V. de la Sayette, M. C. Petit-Taboue, K. Benali, B. Landeau, F. Eustache, *J. Neurol.* **121** (1998) 611 (<https://doi.org/10.1093/brain/121.4.611>)
3. R. M. Lane, S. G. Potkin, A. Enz, *Int. J. Neuropsychopharmacol.* **9** (2006) 101 (<https://doi.org/10.1017/S1461145705005833>)
4. T. Zhao, K. M. Ding, L. Zhang, X. M. Cheng, C. H. Wang, Z. T. Wang, *J. Chem.* (2013) 717232 (<https://doi.org/10.1155/2013/717232>)

5. H. Guo, S. Albrecht, M. Bourdeau, T. Petzke, C. Bergeron, A. C. LeBlanc, *Am. J. Clin. Pathol.* **165** (2004) 523 ([https://doi.org/10.1016/S0002-9440\(10\)63317-2](https://doi.org/10.1016/S0002-9440(10)63317-2))
6. S. Kumar, *Ind. J. Pharmacol.* **47** (2015) 444 (<https://doi.org/10.4103/0253-7613.161274>)
7. N. H. Greig, D. K. Lahiri, K. Sambamurti, *Int. Psychogeriatr.* **14** (2002) 77 (<https://doi.org/10.1017/S1041610203008676>)
8. M. Asif, *Int. J. Med. Chem.* (2014) 395637 (<https://doi.org/10.1155/2014/395637>)
9. E. Jafari, M. R. Khajouei, F. Hassanzadeh, G. H. Hakimelahi, G. A. Khodarahmi, *Res. Pharm. Sci.* **11** (2016) 1 (<https://www.mendeley.com/catalogue/fde6c1f7-4ecf-310e-b761-c9a2f037543e/Res-Pharm-Sci>)
10. S. K. Wahan, B. Sharma, P. A. Chawla, *J. Heterocycl. Chem.* **59** (2022) 239 (<https://doi.org/10.1002/jhet.4382>)
11. D. Wang, F. Gao, *Chem. Cent. J.* **7** (2013) 1 (<https://doi.org/10.1186/1752-153X-7-95>)
12. P. S. Auti, G. George, A. T. Paul, *RSC Adv.* **10** (2020) 41353 (<https://doi.org/10.1039/D0RA06642G>)
13. S. S. AlNeyadi, N. Amer, T. G. Thomas, R. Al Ajeil, P. Breitener, N. Munawar, *Heterocycl. Comm.* **26** (2020) 112 (<https://doi.org/10.1515/hc-2020-0112>)
14. K. N. Mohana, C. B. P. Kumar, *Int. Scholarly Res. Notices* (2013) 620718 (<https://doi.org/10.1155/2013/620718>)
15. F. Z. Fang, S. Yang, G. Wu, *Nutr.* **18** (2002) 872 ([https://doi.org/10.1016/S0899-9007\(02\)00916-4](https://doi.org/10.1016/S0899-9007(02)00916-4))
16. S. Cuzzocrea, D. P. Riley, A. P. Caputi, D. Salvemini, *Pharmacol. Rev.* **53** (2001) 135 (<https://www.mendeley.com/catalogue/a54c6abb-aa6e-343f-91cf-06f546524153/Pharmacol-Rev>)
17. A. Choudhary, R. Sharma, M. Nagar, M. Mohsin, H. S. Meena, *J. Chil. Chem. Soc.* **56** (2011) 911 (<http://dx.doi.org/10.4067/S0717-97072011000400019>)
18. F. Rahim, M. T. Javed, H. Ullah, A. Wadood, M. Taha, M. Ashraf, K. M. Khan, *Bioorg. Chem.* **62** (2015) 106 (<https://doi.org/10.1016/j.bioorg.2015.08.002>)
19. M. A. Abbasi, M. Ilyas, A. Sonia, D. Shahwar, M. A. Raza, K. M. Khan, N. Ambreen, *Sci. Iran* **19** (2012) 1580 (<https://doi.org/10.1016/j.scient.2012.10.014>)
20. K. Mohammed Khan, U. Rasool Mughal, N. Ambreen, N. Hasan Rama, F. Naz, S. Perveen, M. Iqbal Choudhary, *Lett. Drug Des. Discov.* **7** (2010) 716 (<https://www.mendeley.com/catalogue/e16f7904-d62c-3e15-9d04-773c212f8746/Lett-Drug-Des-Discov>)
21. K. Mohammed Khan, M. Rani, N. Ambreen, A. Ejaz, S. Perveen, S. Moazzam Haider, W. Voelter, *Lett. Drug Des. Discov.* **9** (2012) 135 (<https://www.mendeley.com/catalogue/42ad6641-237f-3505-b9af-9360184eee91/Lett-Drug-Des-Discov>)
22. K. Javaid, S. M. Saad, S. Rasheed, S. T. Moin, N. Syed, I. Fatima, M. Choudhary, M. *Bioorg. Med. Chem.* **23** (2015) 7417 (<https://doi.org/10.1016/j.bmc.2015.10.038>)
23. O. Babatunde, S. Hameed, U. Salar, S. Chigurupati, A. Wadood, A. U. Rehman, S. Perveen, *Mol. Divers.* (2021) 1 (<https://doi.org/10.1007/s11030-021-10196-5>)
24. K. M. Khan, S. M. Saad, N. N. Shaikh, S. Hussain, M. I. Fakhri, S. Perveen, S. M. I. Choudhary, *Bioorg. Med. Chem.* **22** (2014) 3449 (<https://doi.org/10.1016/j.bmc.2014.04.039>)
25. S. Perveen, S. M. Saad, S. Perveen, A. Hameed, M. T. Alam, K. M. Khan, M. I. Choudhary, *J. Chem. Soc. Pak.* **38** (2016) (<https://www.mendeley.com/catalogue/ecd7844f-d565-3fcd-8bb0-28a836aefd53/J-Chem-Soc-Pak>)

26. G. L. Ellman, K. D. Courtney, Jr. V. Andres, R. M. Featherstone, *Biochem. Pharmacol.* **7** (1961) 88 ([https://doi.org/10.1016/0006-2952\(61\)90145-9](https://doi.org/10.1016/0006-2952(61)90145-9))
27. P. Molyneux, Songklanakarin, *J. Sci. Technol.* **26** (2004), 211
28. M. S. Blois, *Nature* **181** (1958) 1199 (<https://doi.org/10.1038/1811199a0>)
29. U. Kulsoom, U. Salar, K. M. Khan, S. Chigurupati, S. Syed, A. Wadood, A. Ur Rehman, B. Fatima, F. Saleem, M. Taha, S. G. Felemban, S. R. Dachani, S. Perveen, *Monatsh. Chem.* **153** (2022) 949 (<https://doi.org/10.1007/s00706-022-02972-2>)
30. R. Re, N. Pellegrini, A. Proteggente, A. Pannala, M. Yang, C. Rice-Evans, *Free Radic. Biol. Med.* **26** (1999) 1231 ([https://doi.org/10.1016/S0891-5849\(98\)00315-3](https://doi.org/10.1016/S0891-5849(98)00315-3))
31. Molecular Operating Environment (MOE), 2016.08; Chemical Computing Group Inc., Montreal, QC, 2016 (<https://www.mendeley.com/catalogue/89d1dadd-e734-39ed-beda-f3d9995d868b/Montreal-QC-Canada>)
32. S. Di Giovanni, A. Borloz, A. Urbain, A. Marston, K. Hostettmann, P. A. Carrupt, M. Reist, *Eur. J. Pharm. Sci.* **33** (2008) 109 (<https://doi.org/10.1016/j.ejps.2007.10.004>).

SUPPLEMENTARY MATERIAL TO
**Evaluation of derivatives of 2,3-dihydroquinazolin-4(1H)-one as
inhibitors of cholinesterases and their antioxidant activity: *In
vitro*, *in silico* and kinetics studies**

OLUWATOYIN BABATUNDE¹, SHEHRYAR HAMEED¹, KINGSLEY ADIBE
MBACHU^{1,2}, FAIZA SALEEM¹, SRIDEVI CHIGURUPATI³, ABDUL WADOOD⁴,
ASHFAQ UR REHMAN⁴, VIJAYAN VENUGOPAL⁵, KHALID MOHAMMED KHAN^{1,7*},
MUHAMMAD TAHA⁷, OLUSEGUN EKUNDAYO² and MARIA AQEEL KHAN⁶

¹H. E. J. Research Institute of Chemistry, International Center for Chemical and Biological
Sciences, University of Karachi, Karachi-75270, Pakistan, ²Department of Chemistry,
University of Ibadan, Nigeria, ³Department of Medicinal Chemistry and Pharmacognosy,
College of Pharmacy, Qassim University, Buraydah-52571, Saudi Arabia, ⁴Department of
Biochemistry, Computational Medicinal Chemistry Laboratory, UCSS, Abdul Wali Khan
University, Mardan, Pakistan, ⁵Faculty of Pharmacy, AIMST University, Kedah-08100,
Malaysia, ⁶Third World Center for Science and Technology, H. E. J. Research Institute of
Chemistry, International Center for Chemical and Biological Sciences, University of Karachi,
Karachi-75270, Pakistan and ⁷Department of Clinical Pharmacy, Institute for Research and
Medical Consultations (IRMC), Imam Abdulrahman Bin Faisal University, P.O. Box 1982,
Dammam, 31441, Saudi Arabia

J. Serb. Chem. Soc. 88 (9) (2023) 825–840

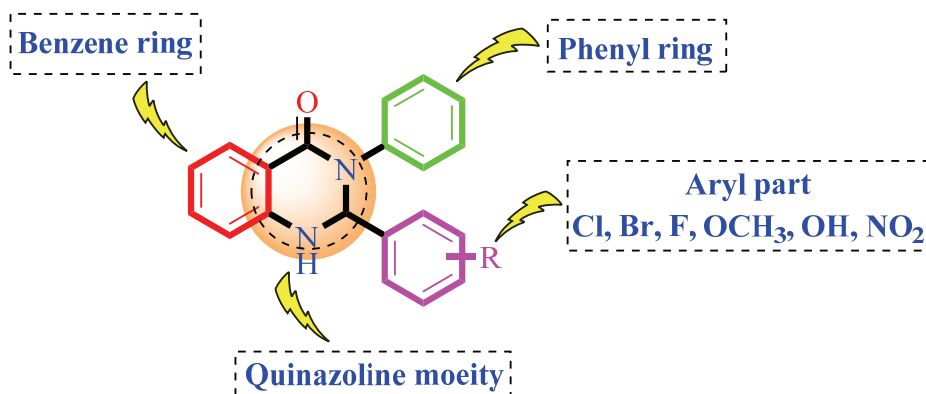


Fig. S-1. General structure of synthetic dihydroquinazolin-4(1H)-one derivative.

* Corresponding author. E-mail: khalid.khan@iccs.edu; drkhalidhej@gmail.com

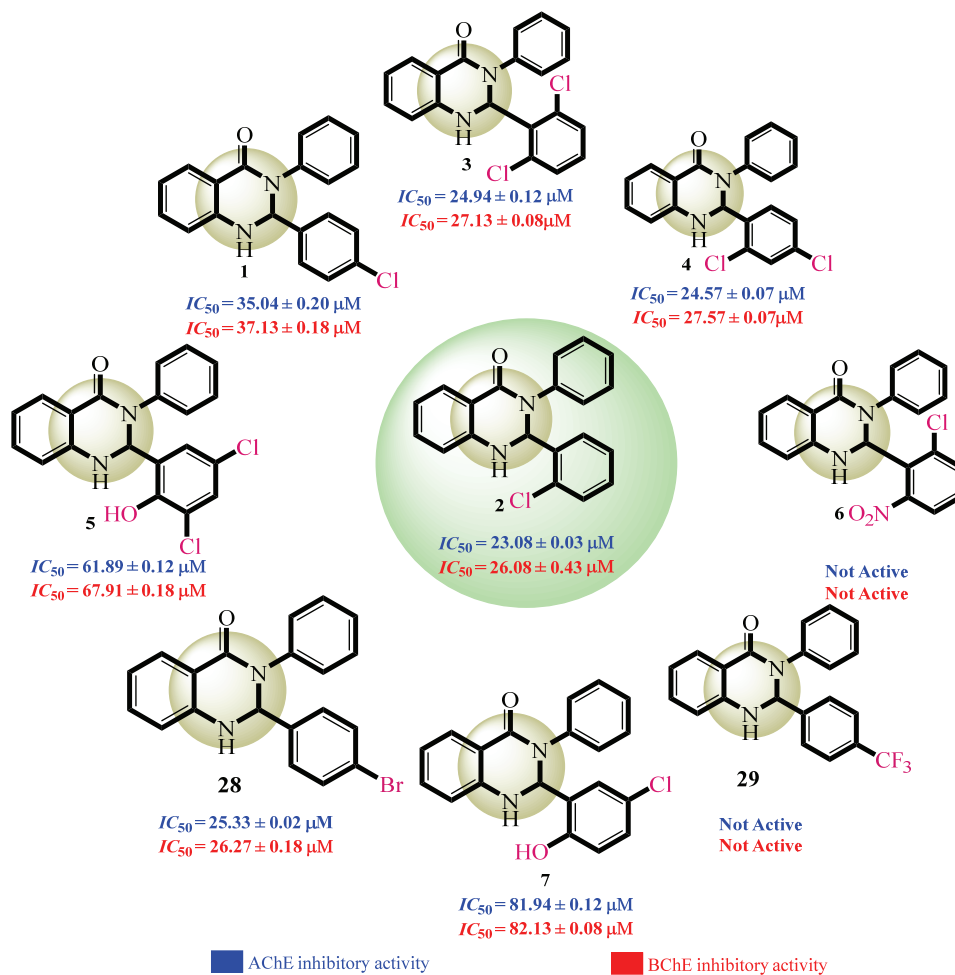


Fig. S-2. SAR of compounds 1–7, 28 and 29.

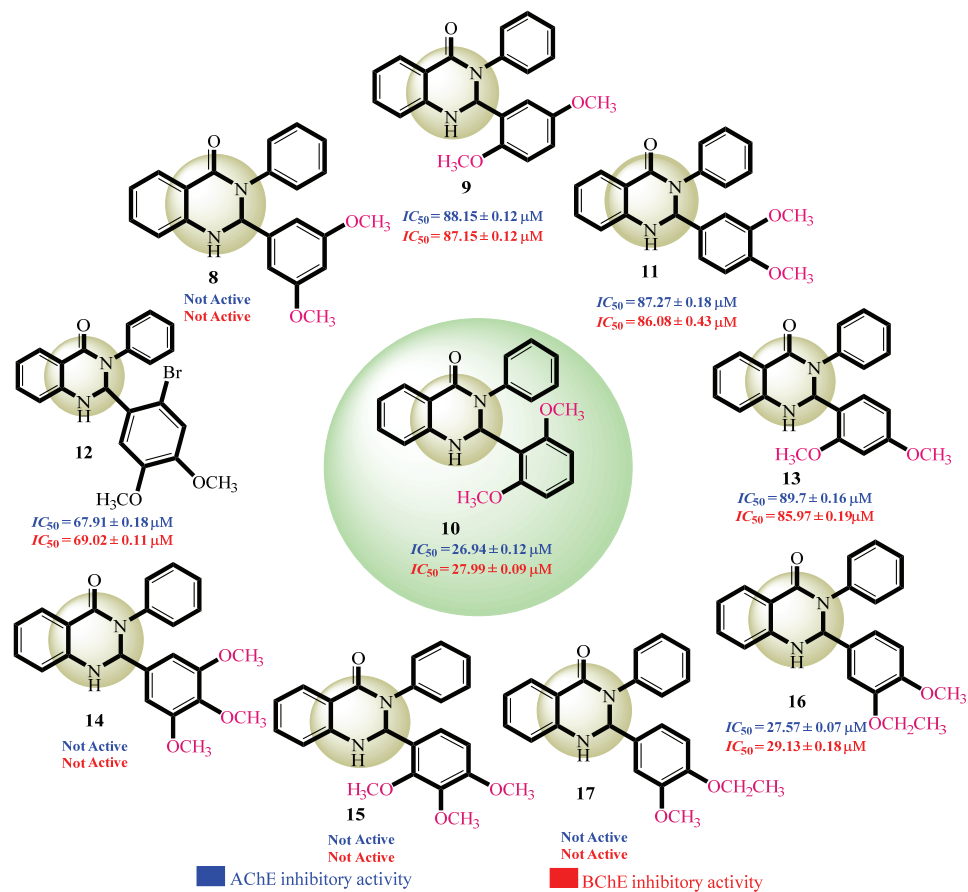


Fig. S-3. SAR of compounds 8–17.

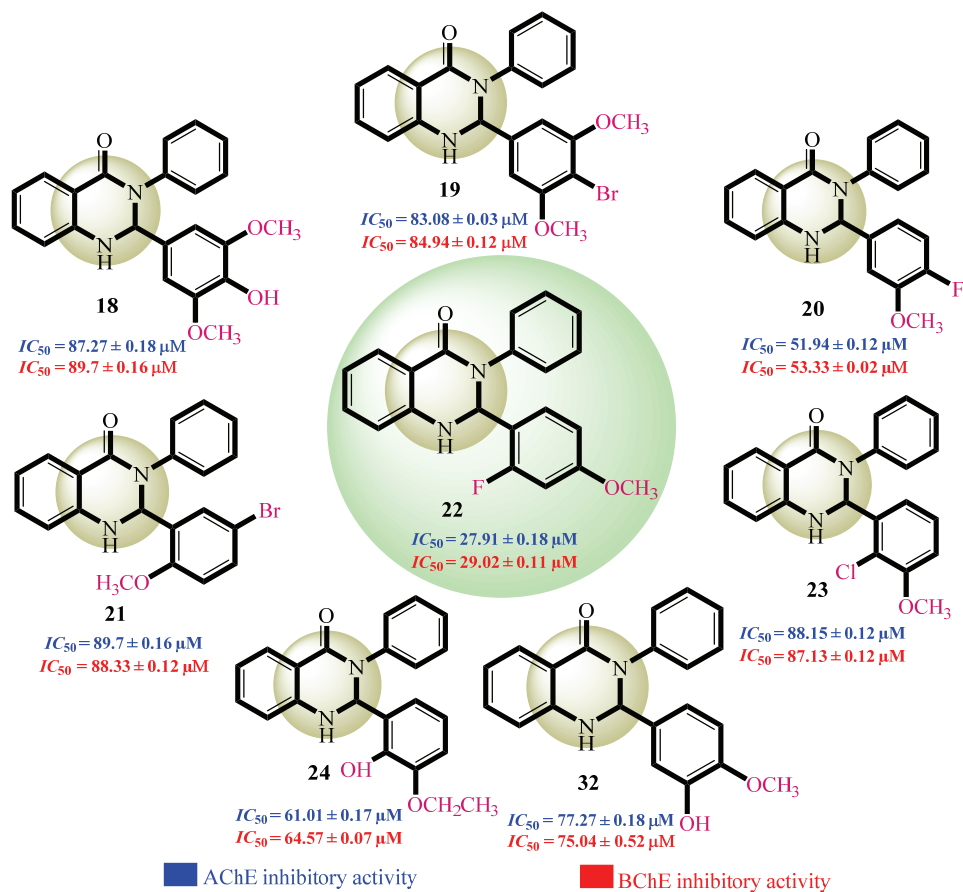


Fig. S-4. SAR of compounds 18–24 and 32.

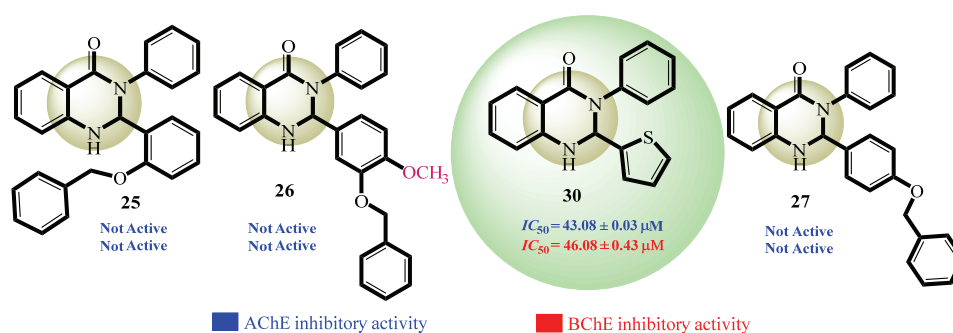


Fig. S-5. SAR of compounds 25–27 and 30.

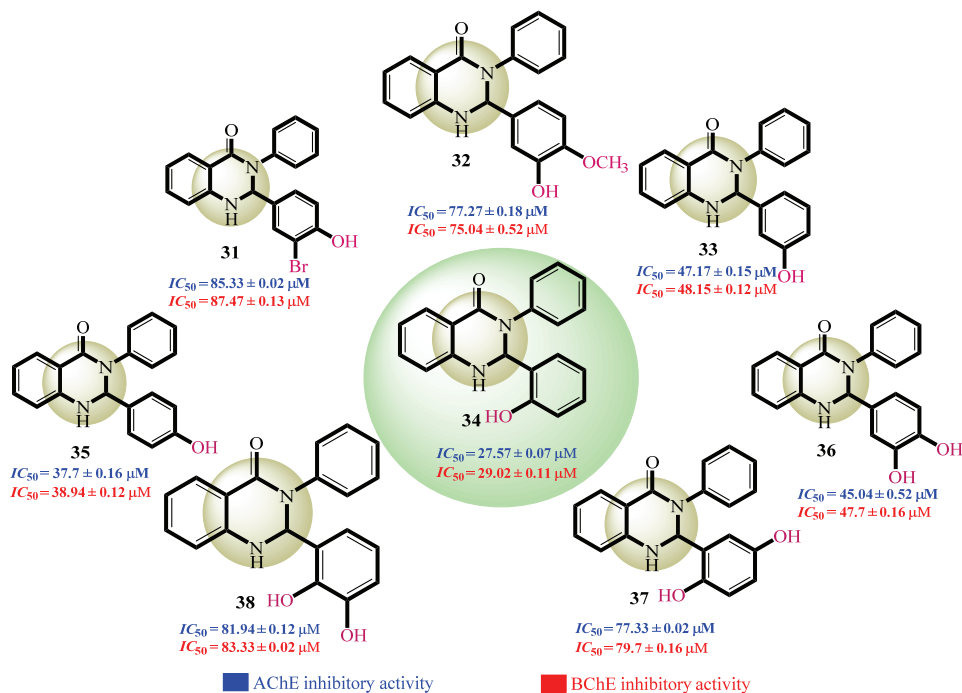


Fig. S-6. SAR of compound 31–38.

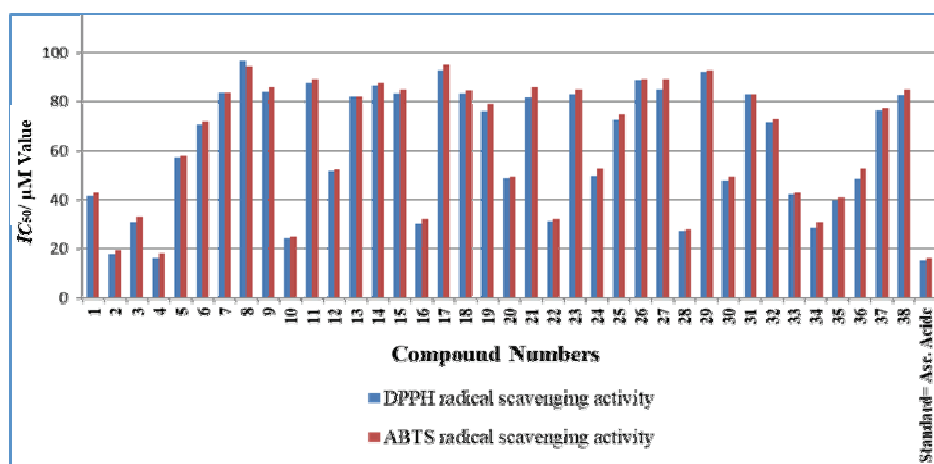


Fig. S-7. Comparison of radical scavenging activities (DPPH and ABTS) of compounds 1–38.

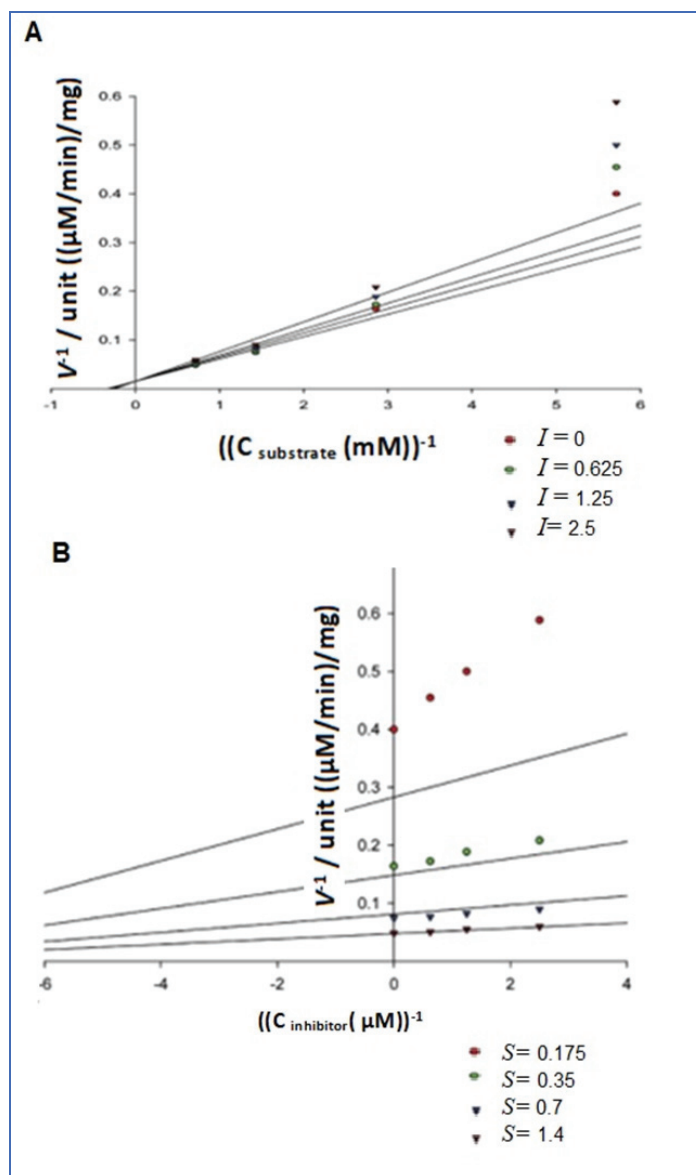


Fig. S-8. Graph of compound 2: A-Lineweaver-Burk plot of reciprocal of rate of reaction (velocities) vs. reciprocal of different concentrations of inhibitor (0, 0.625, 1.25 and 2.5 μM) in the substrate (acetyl thiocholine iodide (ATCI)), whereas V_{max} and K_{m} values were calculated from Lineweaver- Burk plot; B - the plot of reciprocal of rate of reaction (velocities) vs. different concentrations of inhibitor, whereas the K_{i} value was calculated from the Dixon plot.

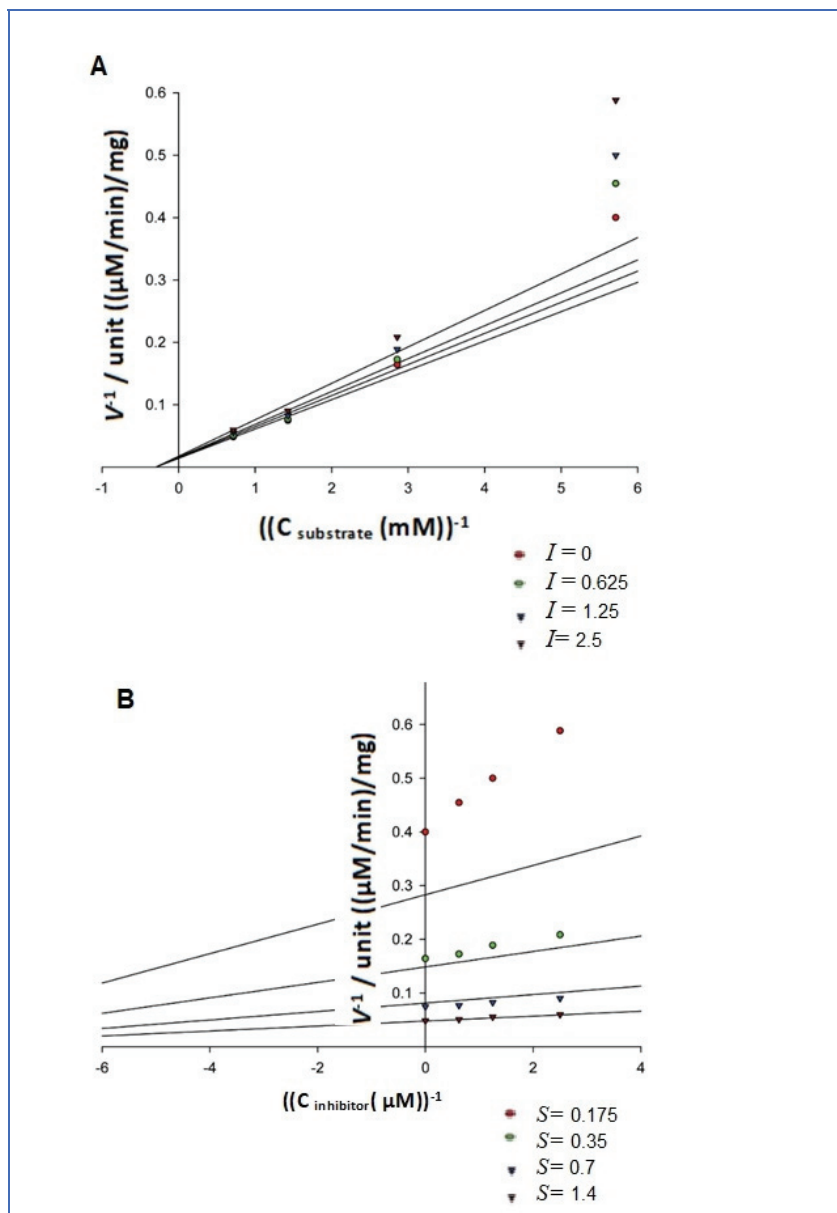


Fig. S-9. Graph of compound 2: A - Lineweaver- Burk plot of reciprocal of rate of reaction (velocities) vs. reciprocal of the substrate (butyryl thiocholine iodide (BTCI)) in the different concentrations of inhibitor (0, 0.625, 1.25 and 2.5 μM). Whereas V_{max} and K_m values were calculated from Lineweaver- Burk plot; B - Dixon plot of the reciprocal of rate of reaction (velocities) vs. different concentrations of inhibitor, whereas the K_i value was calculated from the Dixon plot.

Table S-I. Interaction details for all derivatives (1-38) with the acetylcholinesterase (AChE) enzyme

S. No	Interaction details (AChE)						Docking score
	Ligands	Receptor	Interaction	Distance Å	$E / \text{cal mol}^{-1}$	Residue	
1	C 23	6-ring	H- π	4.52	-0.5	TRP 279	-5.66273642
	C 3	6-ring	π - π	4.42	-0.0	PHE 331	
2	6-ring	O1	H-donor	3.27	-0.9	TYR 334	-6.7638814
	O 1	OD1	H-donor	3.85	-0.0	ASP 72	
	C 6	6-ring	π - π	3.87	-0.0	TRP 279	
3	O 11	CA	H-acceptor	3.54	-0.8	PHE 331	-5.60079002
	6-ring	6-ring	π - π	3.75	-0.0	TYR 334	
4	O 11	O 1	H-acceptor	3.27	-1.2	PHE 331	-6.31296978
	C 6	6-ring	H-donor	3.27	-0.9	TYR 334	
5	NH 1	OD1	H-donor	3.85	-2.0	ASP 72	-5.77625036
	O 24	OD1	H-donor	3.02	-0.7	ASP 72	
6	NA						NA
7	O 25	O	H-donor	2.91	-1.0	TYR 334	-6.00905561
	C 8	6-ring	H- π	4.09	-0.5	TRP 279	
8	NA						NA
9	O 26	CA	H-acceptor	3.36	-0.7	GLY 335	-5.63523006
10	O 11	CA	H-acceptor	3.53	-0.6	GLY 335	-5.57175112
11	O 11	CA	H-acceptor	3.73	-0.5	PHE 331	-5.98022985
	6-ring	6-ring	π - π	3.96	-0.0	TYR 334	
12	C 8	6-ring	H- π	4.12	-0.5	TRP 279	-5.69548988
13	C 8	6-ring	H- π	4.07	-0.5	TRP 279	-5.54778252
14	NA						NA
15	NA						NA
16	O 11	CA	H-acceptor	3.30	-1.2	PHE 331	-6.12902689
	C 22	5-ring	H- π	4.01	-0.8	TRP 279	
17	NA						NA
18	O 24	OG	H-donor	2.89	-1.2	SER 200	-5.65914297
19	C 8	6-ring	H- π	4.08	-0.6	TRP 279	-5.58714533
20	C 8	O	H-donor	3.42	-0.5	TYR 334	-5.81397343
21	C 8	6-ring	H- π	4.08	-0.5	TRP 279	-5.70436907
22	6-ring	6-ring	π - π	3.55	-0.0	TRP 279	-5.86824417
23	C 14	5-ring	H- π	4.13	-0.7	TRP 84	-6.00569773
24	C 27	6-ring	H- π	4.31	-0.8	PHE 331	-5.71659184
25	NA						NA

26	NA						NA
27	NA						NA
28	C 23	6-ring	H- π	4.44	-0.5	TRP 279	-5.36408567
29	NA						NA
30	S 22	OG	H-donor	2.90	-0.9	SER 200	-5.40765858
31	6-ring	5-ring	π - π	3.57	-0.0	TRP 279	-5.71627712
	6-ring	6-ring	π - π	3.65	-0.0	TRP 279	
32	C 8	6-ring	H- π	4.15	-0.5	TRP 279	-5.90167618
33	O 24	O	H-donor	2.95	-2.6	SER 286	-5.36855221
34	O 24	O	H-donor	2.91	-1.0	TYR 334	-6.03559828
	C 8	6-ring	H- π	4.09	-0.5	TRP 279	
35	O 24	O	H-donor	2.94	-0.6	SER 286	-5.34506702
36	O 24	O	H-donor	2.87	-1.3	SER 286	-5.79665184
	O 25	O	H-donor	2.89	-2.9	TYR 334	
37	C 8	O	H-donor	3.51	-0.5	TYR 334	-5.36489582
38	O 11	O 11	H-acceptor	3.30	-1.2	PHE 331	-5.43194532

Table S-II. Interaction detail for all derivatives with the butyrylcholinesterase (BChE) enzyme

S. No.	Interaction details (BChE)					Residue	Docking score
	Ligands	Receptor	Interaction	Distance Å	$E / \text{cal mol}^{-1}$		
1	O 11	CD2	H-acceptor	3.29	-0.5	HIS 438	-4.25291157
	6-ring	6-ring	π - π	3.63	-0.0	PHE 329	
2	6-ring	6-ring	π - π	4.00	-0.0	TRP 82	-6.74273882
	6-ring	5-ring	π - π	3.82	-0.0	TRP 82	
3	6-ring	6-ring	π - π	3.95	-0.0	TYR 332	-5.12142467
4	6-ring	6-ring	π - π	3.97	-0.0	TRP 82	-5.40873098
5	O 24	O	H-donor	3.53	-0.5	PRO 285	-4.97462296
6	NA						NA
7	6-ring	6-ring	π - π	3.69	-0.0	PHE 329	-5.44320917
8	NA						NA
9	O 11	CD2	H-acceptor	3.36	-0.6	HIS 438	-5.18472815
10	6-ring	6-ring	π - π	4.00	-0.0	TRP 82	-4.85872316
11	6-ring	6-ring	π - π	3.90	-0.0	PHE 329	-5.36547041
12	6-ring	6-ring	π - π	4.00	-0.0	PHE 329	-5.75709534
13	6-ring	6-ring	π - π	3.94	-0.0	TRP 82	-5.33182621
14	NA						NA
15	NA						NA
16	6-ring	6-ring	π - π	3.88	-0.0	PHE 329	-4.68446302

17	NA						NA
18	O 11	CD2	H-acceptor	3.33	-0.5	HIS 438	-5.10889292
19	O 11	CD2	H-acceptor	3.39	-0.5	HIS 438	-5.250278
20	6-ring	6-ring	π - π	3.99	-0.0	PHE 329	-5.82584286
21	6-ring	6-ring	π - π	3.95	-0.0	TRP 82	-5.19997549
22	6-ring	6-ring	π - π	3.79	-0.0	PHE 329	-5.3220067
23	6-ring	6-ring	π - π	3.90	-0.0	PHE 329	-4.97137928
24	6-ring	OG1	π -H	3.95	-1.1	THR 120	-5.39356089
25	NA						NA
26	NA						NA
27	NA						NA
28	6-ring	6-ring	π - π	3.92	-0.0	PHE 329	-6.4467145
	C 26	OE2	H-donor	3.36	-0.5	GLU 197	
29	NA						NA
30	S 22	OG1	H-donor	4.14	-0.6	THR 120	-4.30858469
31	6-ring	6-ring	π - π	3.95	-0.0	PHE 329	-5.26759958
32	O 24	OG1	H-donor	3.26	-0.7	THR 120	-4.33135366
33	O 24	OG1	H-donor	3.35	-0.6	THR 120	-5.12208843
34	6-ring	6-ring	π - π	3.97	-0.0	PHE 329	-5.07936764
35	6-ring	6-ring	π - π	3.89	-0.0	PHE 329	-4.48091221
36	O 25	OG1	H-donor	3.31	-0.7	THR 120	-4.88316011
37	6-ring	6-ring	π - π	3.90	-0.0	PHE 329	-4.97137928
38	6-ring	6-ring	π - π	3.94	-0.0	TYR 332	-5.09215164



J. Serb. Chem. Soc. 88 (9) 841–857 (2023)
JSCS–5666

Impaired local hydrophobicity, structural stability and conformational flexibility due to point mutations in SULT1 family of enzymes

SILVANA CEAURANU, VASILE OSTAFE and ADRIANA ISVORAN*

Department of Biology-Chemistry and Advanced Environmental Research Laboratories, West University of Timisoara, 4 V. Pirvan, 300223 Timisoara, Romania

(Received 10 February, revised 15 March, accepted 9 April 2023)

Abstract: Sulfotransferases (SULTs) are enzymes involved in phase II of the metabolism of xenobiotics. Single nucleotide polymorphisms were identified for genes encoding the SULTs leading to allozymes with modified sulfating activity. This study aims to analyse the effects of the most frequently identified amino acid mutations in the sequences of enzymes belonging to the SULT1 family on their local properties and structural stability. The outcomes reveal that single point mutations alter the local hydrophobicity and flexibility, mainly due to destabilization of the protein structures, may consequently lead to changes in the dynamic of the active site activity reducing the affinity for the substrate. Elucidation of how the single point mutations influence the activity of enzymes contributes to understanding the molecular basis of the specificity of enzymatic activity and mitigating anomalies in the metabolism of xenobiotics.

Keywords: protein plasticity; protein stability; hydrophobicity profile; mutations; metabolism, bioinformatics.

INTRODUCTION

Sulfotransferases (SULTs) are enzymes involved in phase II of the metabolism of a wide range of both xenobiotics and endogenous compounds (hormones, bile acids, neurotransmitters, carbohydrates, proteins). They act by transferring a sulfate group from the cofactor 3'-phosphoadenosine 5'-phosphosulfate (PAPS) to the hydroxyl group of an acceptor substrate.¹ Sulfoconjugation increases the water solubility of chemical compounds and the formation of more excretable products contributing to detoxification, but it also may lead to potentially carcinogenic metabolites.²

* Corresponding author. E-mail: adriana.isvoran@e-uvt.ro
<https://doi.org/10.2298/JSC230210022C>



There were identified 13 human cytosolic sulfotransferase genes in humans conducting to proteins divided into four families differing in the tissue distribution and substrate specificity:³ SULT1, SULT2, SULT4 and SULT6. The present study focuses on the SULT1 family, respectively on the subfamilies SULT1A1, SULT1A2, SULT1A3, SULT1B1, SULT1C2 (former SULT1C1), and SULT1E1 as they reveal frequently identified allozymes with modified biological functions. These enzymes are involved in sulfation of phenols, thyroid hormones, and numerous drugs.⁴ SULT1A1 and SULT1A2 are usually active against the phenolic compounds, with SULT1A1 revealing a higher activity. Furthermore, SULT1A1 and SULT1B1 have an extensive overlap in their substrate profiles, but the sulfation efficiency of SULT1A1 is higher.⁵ SULT1A3 displays selectivity for catecholamines and structurally related compounds (serotonin, dopamine).⁶ SULT1C2 enzyme sulfonates thyroid hormones, and SULT1E1 is involved in the sulfation of hormones, mainly estrogens and iodothyronines.^{7,8}

Single nucleotide polymorphisms (SNPs) were identified for genes encoding the SULTs conducting to SULTs allozymes with modified stability and/or sulfating activity impairing the therapeutic response of numerous drugs.^{2,9-11} In the case of SULT1A1, the frequent identified polymorphic variants are: SULT1A1*1 (the wild type, WT), SULT1A1*2 (amino acid substitution R213H), SULT1A1*3 (M223V) and SULT1A1*4 (R37Q), with SULT1A*2, SULT1A*3 and SULT1A*4 usually revealing lower catalytic activity than the WT enzyme.^{2,10,12,13} In the case of SULT1A2, the frequent allozymes are SULT1A2*1 (WT), SULT1A2*2 (I7T, N235T) and SULT1A2*3 (P19L). SULT1A2*2 displays lower thermostability and decreased catalytic activity, and SULT1A2*3 exposes higher thermostability and increased activity compared to WT.¹⁴ The frequent variants of the SULT1A3 are SULT1A3*1 (WT), SULT1A3*2 (K234N), SULT1A3*3 (P101L), SULT1A3*4 (P101H), and SULT1A3*5 (R144C). SULT1A3*2 and SULT1A3*3 usually reveal decreased activity, and SULT1A3*4 and SULT1A3*5 reveal increased activities against numerous drugs when compared to WT.^{6,15,16} Only two allozymes are known for SULT1B1, SULT1B1 (WT) and SULT1B1-L145V, the last one showing significantly decreased sulfation of *p*-nitrophenol than the WT.¹⁷ There are registered five variants for SULT1C2: SULT1C2*1 (WT), SULT1C2*2 (S255A), SULT1C2*3 (D60A), SULT1C2*4 (R73Q) and SULT1C2*5 (S111F). SULT1C2*3 and SULT1C2*4 reveal reduced activity toward *p*-nitrophenol when compared to the WT and SULT1C2*2, whereas SULT1C2*5 did not show detectable activity toward this substrate.¹⁸ The frequent variants of SULT1E enzyme are SULT1E1*1 (WT), SULT1E1*2 (D22Y), SULT1E1*3 (A32V) and SULT1E1*4 (P253H). The allelic variants exhibit lower sulfation activity for estradiol compared to WT.^{19,20} An up-to-date synthesis regarding the catalytic activities

of all these variants toward various substrates and drugs has been recently published.²¹

Elucidation of the structures of the SULT1 enzymes in complex with different ligands highlights the dominant role of their structural flexibility/plasticity in controlling both the activity and specificity.^{22–28} Furthermore, it is also widely presumed that structural features and biological functions of proteins are closely linked to their sequence compositions.²⁹ A single amino acid change in the protein sequence can disturb the network of intramolecular interactions and affect how the protein folds, its structural stability, dynamics, and, consequently, its biological function.³⁰ Consequently, in order to understand the molecular effects of a single point mutation, it is also necessary to consider changes in protein structural stability and dynamics.

This study aims to predict, compare and analyze the changes in the local hydrophobicity, structural stability and flexibility due to single point mutations in the sequences of the SULT1 enzymes using a computational approach.

EXPERIMENTAL

This study focuses on the human SULT1 enzymes having frequently identified polymorphic variants (Table I). The sequences of the wild type enzymes were extracted from the UniProt database³¹ and used for further analysis.

For assessing the changes produced by the mutations present in the frequently identified allozymes of the SULT1 family in the profiles of hydrophobicity and average flexibility, the ProtScale computational tool³² has been considered. Several parameters can be chosen when using the ProtScale computational tool: window size, the window edge relative weight value, weight variation model, and scale normalization. The window size is defined as the number of amino acids considered for determining one point of the computed property. It means that computing the value of the investigated property for a given residue *i*, the amino acids in the interval of the chosen length, positioned around residue *i*, are considered. Regarding the window edge relative weight value, the computational tools always consider that amino acid from the center of the window has a weight of 100 %, and the user may choose weight values between 0 and 100 % for the amino acids at the remaining positions in that window. If weight values are chosen lower than 100 %, the user may select a linear or exponential decrease of the weight between the center and the edges. Furthermore, the user may choose whether to use the unmodified selected scale values or to normalize these values so that they fit into the range from 0 to 1.³² The following settings were considered in this study: windows of 3, 5 and, respectively, 9 amino acids, the relative weight of the window edges compared to the window center was set to 100 %, and the unmodified selected scales values were used. We also specify that for obtaining the hydrophobicity profiles, the Kyte&Doolittle scale³² has been used.

In order to explore the local flexibility in the structures of the SULT1 enzymes, the PDBFlex database³³ has been considered. This database offers information on the intrinsic global and local flexibilities of protein structures based on the analysis of variations appearing between the different structural files of the same protein deposited in the Protein Data Bank (PDB). PDBFlex collects information on all depositions having at least 95 % sequence identity with the sequence of the query structural file, performs the analysis of the structural differences, and clusters them according to the structural similarities.³³ Consequently, the available

elucidated structural files for the investigated enzymes and their complexes with various ligands (cofactor, substrates, drugs) have been considered. These structural files are available in PDB,³⁴ and the information regarding their active and binding sites has been also retrieved (Table II).

TABLE I. The frequently identified polymorphic variants of the enzymes belonging to SULT1 family considered in this study: WT – the wild type enzyme

SULT1 subfamily	Polymorphic variant	Amino acid substitution
SULT1A1	SULT1A1*1	WT
	SULT1A1*2	R213H
	SULT1A1*3	M223V
	SULT1A1*4	R37Q
SULT1A2	SULT1A2*1	WT
	SULT1A2*2	I7T, N235T
	SULT1A2*3	P19L
SULT1A3	SULT1A3*1	WT
	SULT1A3*2	K234N
	SULT1A3*3	P101L
	SULT1A3*4	P101H
	SULT1A3*5	R144C
SULT1B1	SULT1B1	WT
	SULT1B1-L145V	L145V
SULT1C2	SULT1C2*1	WT
	SULT1C2*2	S255A
	SULT1C2*3	D60A
	SULT1C2*4	R73Q
	SULT1C2*5	S111F
SULT1E	SULT1E1*1	WT
	SULT1E1*2	D22Y
	SULT1E1*3	A32V
	SULT1E1*4	P253H

Structures of the WT variants of the SULT 1 enzymes highlighting the positions of the amino acids that suffer mutations are revealed in Fig. 1. UCSF Chimera tool³⁵ has been used to visualize these structures.

Data presented in Table II and Fig. 1 reveal that some amino acids that support mutations corresponding to allozymes situated in the regions or their close vicinity are involved in the interactions with the cofactor and/or substrate: M223V for SULT1A1*3, N235T for SULT1A2*2, K234N for SULT1A3*2, P253H for SULT1E1*4. Some residues that support mutations are missing in the structural files: I7T for SULT1A2, R73 and S255 for SULT1C2.

UCSF Chimera tool has been also considered for illustrating the changes in the hydrophobicity and Coulombic electrostatic potential of the regions of SULT1A1 containing the point mutations R213H and M223V compared to the WT enzyme. This analysis has been made only for SULT1A1, as this enzyme has solved structures of mutants deposited in PDB.

DynaMut2 web server (<http://biosig.unimelb.edu.au/dynamut2/>) has been considered for predicting the changes in stability caused by single point mutations in the sequences of investigated enzymes.³⁰ The changes in the enzymes stability are assessed by predicting the variations in folding free energy ($\Delta\Delta G$, expressed in kJ mol^{-1}) for single point mutations: $\Delta\Delta G <$

< 0.0 corresponds to mutations destabilizing the structure and $\Delta\Delta G > 0.0$ to mutations contributing to the stabilization of the structure. The predictions are based on an experimental data set collected for 4633 mutations (2640 destabilizing and 1993 stabilizing) that were divided into 4022 entries for the training set and 611 entries for the test set. DynaMut2 has a good accuracy of predictions achieving Pearson's correlation of up to 0.72 for single point mutations across 10-fold cross-validation and independent blind tests.³⁰

TABLE II. Uniprot and Protein Data Bank (PDB) identifiers (ID) for the analyzed sequences and structures of the enzymes belonging to SULT1 family: aa – amino acid, PAPS – 3'-phosphoadenosyl-5'-phosphosulfate, the cofactor for these enzymes

SULT1 enzyme	Uniprot ID	PDB ID	Binding site	Mutations corresponding to allozymes
SULT1A1	P50225	4GRA ^{a,36} , 1LS6 ^b , 1Z28 ^c , 2D06 ^b , 3U3J ^b , 3U3K ^b , 3U3M ^b , 3U3O ^b , 3U3R ^b , 3QVU ^b , 3QVV ^b	PAPS: 48-53, 106-108, 130, 138, 193, 227- 232, 255-259; Substrate: 106-108	R37Q, R213H, M223V
SULT1A2	P50226	1Z29	PAPS: 48-53, 106-108, 130, 138, 193, 227- 232, 255-259; Substrate: 106-108	I7T, P19L, N235T
SULT1A3	PODMM9	2A3R ^a , 1CJM	PAPS: 48-53, 130, 138, 146, 193, 227-232, 255-259; Substrate: 86	P101L, P101H, R144C, K234N
SULT1B1	O43704	2Z5F, 3CKL ^a	PAPS: 48-53, 131, 139, 194, 228- 233, 256-260; Substrate: 107-109	L145V
SULT1C2	O00338	3BFX ^a	PAPS: 49-54, 131, 139, 194, 228- 233, 256-260; Substrate: 107-109	D60A, R73Q, S111F, S255A
SULT1E1	P49888	1G3M ^a , 1HY3, 4JVL, 4JVM, 4JVN	PAPS: 47-52, 129, 137, 192, 226- 231, 256-258 Substrate: 105- 107	D22Y, A32V P253H

^aWhen multiple structural files have been detected for an enzyme, these structural files have been chosen as they have a better resolution or a lower number of missing residues and/or missing atoms; ^bthese structural files correspond to the allelic variant SULT1A1*2 (R213H),^{23,26,37,38} ^cstructural file 1Z28 corresponds to the allelic variant SULT1A1*3 (M223V)²⁵

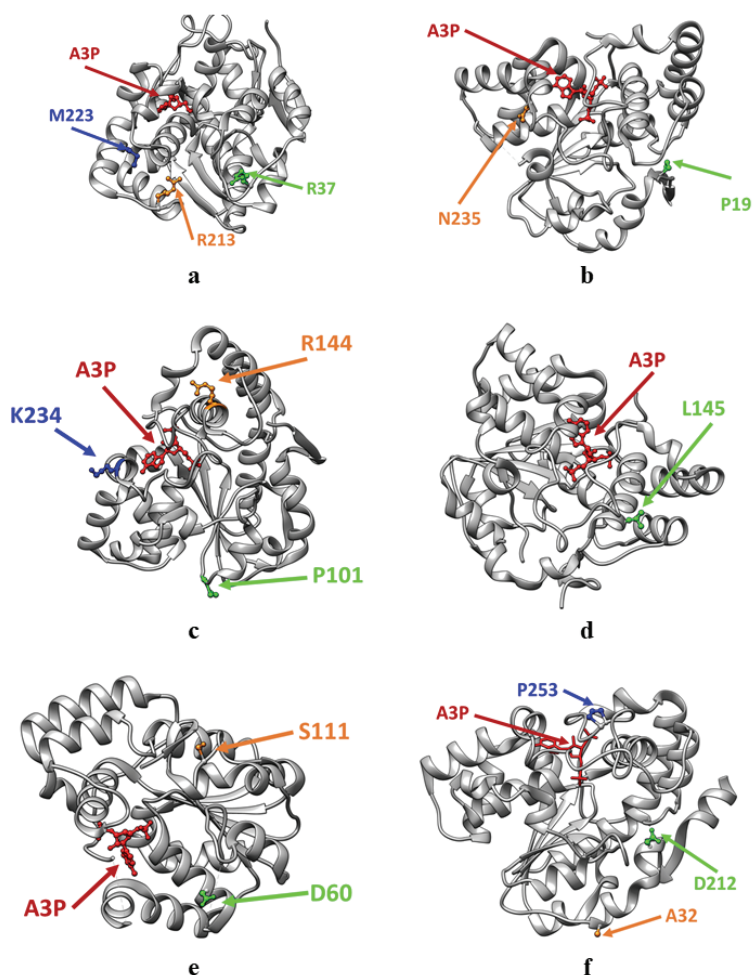


Fig. 1. Illustration of the positions of the residues that support mutations in the SULT1 enzymes: SULT1A1 (a), SULT1A2 (b), SULT1A3 (c), SULT1B1 (d), SULT1C2 (e) and SULT1E1 (f). Some residues that support mutations are missing in the structural files: I7T for SULT1A2, R73 and S255 in SULT1C2. A3P – adenosine-3'-5'-diphosphate.

RESULTS AND DISCUSSION

Analysis of the influence of mutations present in the frequently identified allozymes belonging to SULT1 family on their average flexibility and hydrophobicity profiles

The effect of the mutations corresponding to the main allelic variants of the SULT1 family of enzymes on their local hydrophobicity are shown in Fig. 2 for a window of 3 amino acids and in Tables S-I–S-VI of the Supplementary material to this paper for windows of 5 and 9 amino acids, respectively. Fig. 2 and the

data presented in Tables S-I-S-VI reveal that the punctual amino acid mutations corresponding to the frequently identified allozymes of the SULT1 enzymes conduct to altered local hydrophobicity profiles. Some mutations cause decreased local hydrophobicity, but others produce increased local hydrophobicity. Even if only one amino acid is changed, this point mutation affects the local hydrophobic profile over a range of at least 9 residues. A molecular dynamics study revealed that in the case of SULT1A1*3, the M223V mutation led to the loss of a hydrophobic contact between M223 and M60 and may be responsible for the altered sulfonation activity of the SULT1A1*3.²¹

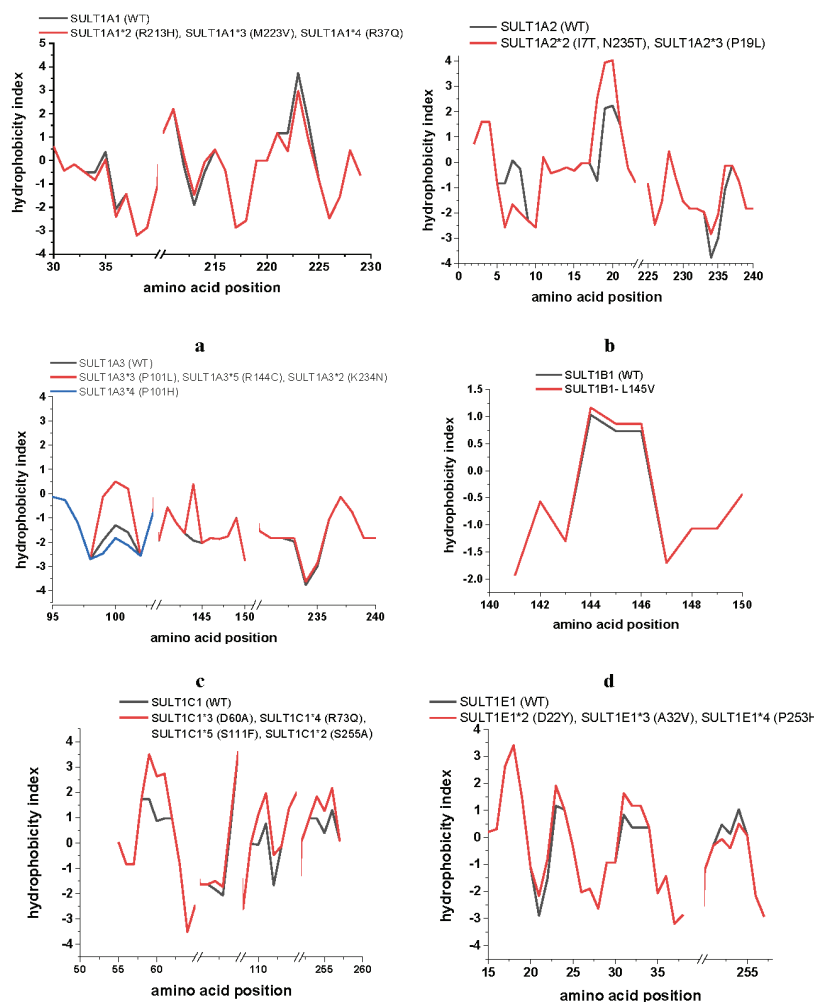


Fig. 2. Hydrophobicity profiles obtained using ProtScale tool for a window of 3 amino acids for the enzymes belonging to the SULT1 family and for their frequently identified allozymes: WT – wild type protein.

The flexibility profiles of the enzymes belonging to the SUL1 family and of their frequently identified allozymes are shown in Fig. 3 for a window of 3 amino acids and in Tables S-VII–S-XII of the Supplementary material for windows of 5 and 9 amino acids, respectively. Fig. 3 and Tables S-VII–S-XII reveal that the amino acid mutations corresponding to the frequently identified allozymes of the SUL1 enzymes also alter the local flexibility profiles.

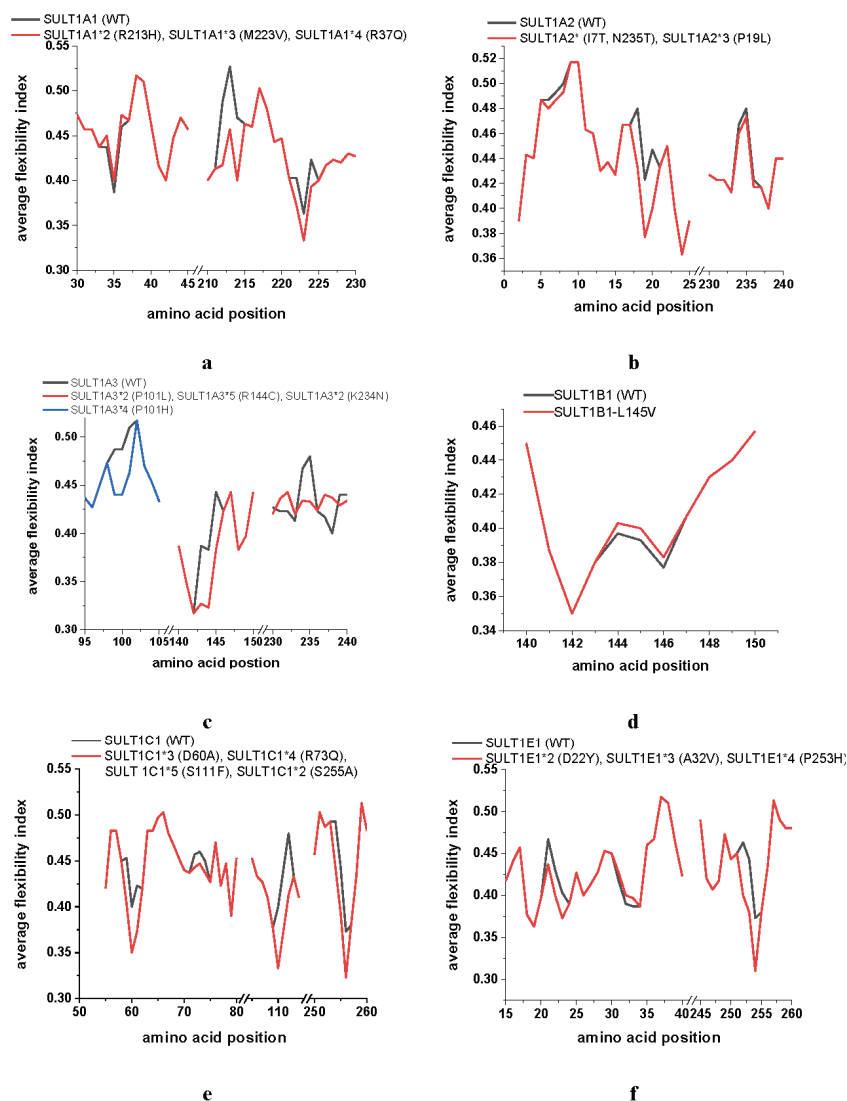


Fig. 3. Average flexibility profiles obtained using ProtScale tool for a window of 3 amino acids for the enzymes belonging to the SUL1 family and for their frequently identified allozymes: WT – wild type protein.

Being well known that the flexibility of SULTs is responsible for recognizing the diverse types of substrates,³⁹ this outcome becomes important. A molecular dynamics simulation study involving the major allozymes of SULT1A1 (WT, R213H and M223V) revealed increased flexibility in the region of the binding site for the mutants compared to the WT enzyme and alteration of the protein dynamics.²¹ It should be noted that neither R213 nor M223 are in the substrate-binding loops,³⁹ but their mutations induce conformational changes affecting the flexibility of at least one of these loops.⁴⁰ These changes may be responsible for the observed alternation of sulfation activities of mutants compared with WT toward numerous endogenous compounds and drugs.^{2,10,12,13}

These outcomes revealing the altered local hydrophobicity and flexibility for the allozymes are not unexpected, being known that polar or charged residues are more flexible and less hydrophobic, whereas nonpolar residues are more hydrophobic and quite inflexible.⁴¹ Furthermore, the alteration of the local hydrophobicity and/or flexibility may cause the proteins dysfunctionalities, such as long-range correlations concerning hydrophobicity and flexibility along the proteins chains which have been observed for sequences of numerous proteins.^{42–45} As the protein hydrophobicity and flexibility are closely related to the primary structure, it is expected that the amino acid mutations affect not only the spatial structure of the protein but also the structural flexibility of the protein and its biological function.⁴⁶ Consequently, a better understanding of the relationship between the local hydrophobicity and flexibility of SULT1 enzymes and their functional properties is essential for understanding the metabolism of numerous drugs.

Analysis of the flexibility of enzymes belonging to the SULT1 family taking into account structural data

For the investigated SULT1 enzymes, their local structural flexibility has been analysed using PDBFlex. The identified clusters for the structural files corresponding to these enzymes are revealed in Table S-XIII of the Supplementary material. SULT1A1 and SULT1A2 enzymes are considered as members of the same cluster due to their high sequence similarity, about 95 %.⁴⁷ The regions with local flexibility identified in the structures of SULT1 enzymes are presented in Table III.

The N- and C-terminal regions are not mentioned in this table as it is known that they can be disordered and flexible in many proteins.⁴⁸ As expected, the regions with higher structural flexibility involve amino acids that interact with the cofactor and/or the substrate. Several mutations corresponding to allozymes of the investigated SULTs correspond to the identified flexible regions revealing their possible effects on the local structural stability and flexibility of the proteins.

TABLE III. Regions with local structural flexibility in SULT1 enzymes identified using PDBFlex computational utility

SULT1 member	Maximum <i>RMSD</i> in the cluster, Å	Average <i>RMSD</i> in the cluster, Å	Region (amino acid interval)	Average <i>RMSD</i> , Å	Ligand interacting with amino acids belonging to this region	Amino acid mutation corresponding to allelic variant that is present in the flexible region
SULT1A1, SULT1A2	0.596 for 3U3K and 1Z28	0.363	110–122 210–225	0.053 0.034	<i>p</i> -Nitrophenol, 3-hydroxy-7,7-dimethyl-2-phenyl-4-(thiophen-2-yl)-2,6,7,8-tetrahydro-5H-pyrazolo[3,4- <i>b</i>]-quinolin-5-one, 7-hydroxy-2-oxo-2 <i>H</i> -chromene-3-carbonitrile, estradiol	R213H, M223V
SULT1A3	1.167 for 2A3R and 1CJM ^a	0.793	24–63 94–104 141–156	0.072 0.182 0.036	Adenosine-3'-5'-diphosphate, L-dopamine L-Dopamine Adenosine-3'-5'-diphosphate, L-dopamine	P101L in SULT1A3*3, P101H in SULT1A3*4 R144C in SULT1A3*5
SULT1B1	0.562 for 2Z5F and 3CKL	0.395	83–89	0.282	L-Dopamine	–
SULT1E1	0.625 for 1HY3 and 4JVL	0.384	79–94 141–157 210–229 240–252	0.362 0.036 0.027 0.041	Adenosine-3'-5'-diphosphate L-dopamine Resveratrol –	– – – P243H in SULT1E1*4

^aMany regions are missing in the structure of SULT1A3 with the PDB ID 1CJM, and these regions were not considered for the local flexibility analysis

Analysis of the influence of mutations that are present in the frequently identified allozymes belonging to SULT1 family on their local hydrophobicity and electrostatic potential

For SULT1A1, the output of the PDBFlex tool reveals local structural flexibility for the region 210–225, taking into account the different structural files of this protein deposited in the PDB. This region incorporates two mutations corresponding to SULT1A1*2 (R213H) and SULT1A1*3 (M223V), respectively. The output of the ProtScale tool reveals that mutations corresponding to SULT1A1*2 and SULT1A1*3 reduce the local hydrophobicity and flexibility and may facilitate the electrostatic interactions with the solvent. This output strongly correlates with data presented in Fig. 4 obtained using Chimera software for the regions 210–225 of the SULT1A1 WT and of the enzyme containing the mutations

R213H and M223V. Fig. 4 reveals changes in both the local hydrophobicity and Coulombic electrostatic potential of this region for the allozymes compared with the WT enzyme.

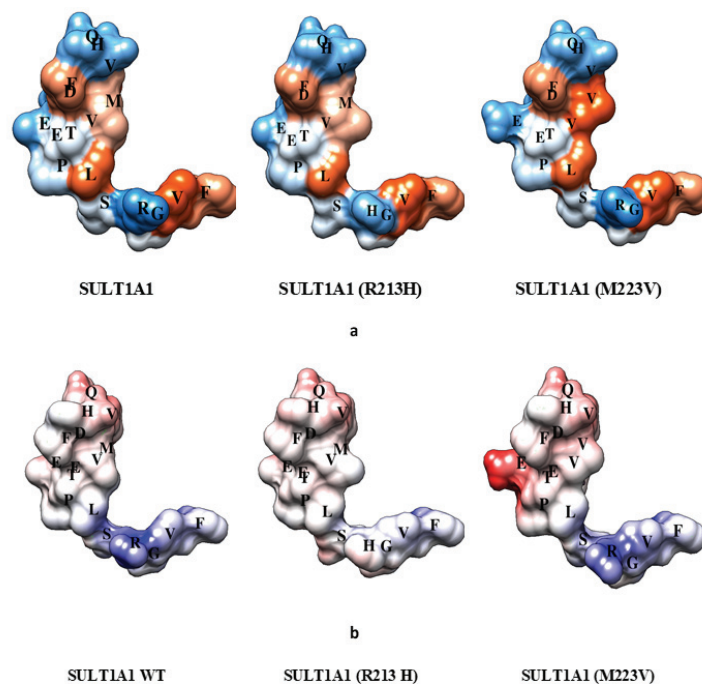


Fig. 4. Changes in the local hydrophobicity (a) and Coulombic electrostatic potential (b) of the 210–225 region of SULT1A1 due to the point mutations R213H and M223V compared to the wild type (WT) enzyme. The following structural files have been considered when mapping the hydrophobicity and electrostatic potential: 4GRA (WT), 1LS6 (R213H), and 1Z28 (M223V). Blue regions in a correspond to the hydrophilic surface, and orange regions correspond to the hydrophobic surface. As the color is more intense, the higher is hydrophilicity/hydrophobicity of the surface. In b, red regions illustrate the negative potential, and blue regions correspond to the positive potential.

These changes may influence the activity of these allozymes as their sulfation activity toward both endogenous and numerous xenobiotic compounds is decreased compared with the sulfation activity of the WT.²¹ Furthermore, the literature data reveal that other two mutations in the SULT1A1 sequence, D249G and Y240C (both amino acids located in the vicinity of the active site), lead to lower affinity for 3-cyano-7-hydroxycoumarin and *p*-nitrophenol. Analysis of the D249G mutant structure shows an increase in the local flexibility of this region and a significant change in the charge distribution around the active site.²⁶ The importance of the local electrostatic interactions for determining the structure,

stability, and conformational adaptabilities has been revealed for numerous proteins.^{49,50}

There are no structures determined for the allozymes of the others SULT1 enzymes considered in this study, and consequently, the changes in the local hydrophobicity and electrostatic potential could not be analyzed for these enzymes using structural data. Taking into account the very good correlation between the information obtained using ProtScale and PDBFlex computational tools for the SULT1A1 subfamily, we may extrapolate that the punctual amino acid mutations that appear in the allozymes of the SULT1 enzymes conduct to the alteration of local structural flexibility, local hydrophobicity, and consequently on the electrostatic potential.

Analysis of the influence of mutations that are present in the frequently identified allozymes belonging to SULT1 family on their structural stability

It is already known that even small reductions in protein stability can lead to dysfunctional proteins.⁵¹ The stabilization/destabilization effects of the single point mutations in the sequences of SULT1 enzymes leading to the most frequently identified allozymes have been analysed using DynaMut2 webserver, and the results are presented in Table IV.

Data presented in Table IV reveal that the typical point mutations corresponding to allozymes usually destabilize the structure. It is in good correlation with the known data revealing that the allozymes containing point mutations that destabilize the structure usually have lower sulfation activity compared to the WT enzymes. In the case of SULT1A1, it was shown that the position of residue 213 precedes a flexible region, whereby mutation of this residue affects both stability and flexibility of the enzyme.³⁸ Among the frequent point mutations appearing in the SULT1A1 enzyme, R213H produces the lower destabilizing effect, which is also in correlation with the published data revealing that R213H induces local conformational changes affecting the substrate-binding loop and has only a low impairing effect on the overall stability of the protein structure.⁴⁰

It should be noted that several amino acids that correspond to the mutations of SULT1 enzymes have ionizable sidechains. The frequently identified polymorphic variants of SULT1A are R37Q and R213H, with arginine and histidine being among the amino acids having ionizable sidechains. Histidine is neutral, and arginine is protonated under physiological conditions. Consequently, the standard protonation states have been considered for the arginine and histidine residues. Both histidine and arginine play essential structural and functional roles in proteins, which correlate with the ionization state of their side chains. It emphasizes that a more accurate approach should include electrostatic calculations by solving the Poisson–Boltzmann equation with subsequent Monte Carlo titration⁵² or employing DFT/solvation electrostatic calculations.⁵³

TABLE IV. Illustration of the $\Delta\Delta G$ values produced by the single point mutations corresponding to the frequently identified allozymes of the SULT1 enzymes. $\Delta\Delta G < 0.0$ values correspond to mutations destabilizing the structure, and $\Delta\Delta G > 0.0$ values to mutations contributing to the stabilization of the structure

SULT1 enzyme	Single point mutation	$\Delta\Delta G / \text{kJ mol}^{-1}$	Effect	Observations
SULT1A1	R37Q	-2.18	Destabilizing	
	R213H	-0.54	Destabilizing	
	M223V	-1.92	Destabilizing	
SULT1A2	I7T	-	-	T7 Residue is missing in the crystallographic structure
SULT1A3	P19L	-1.84	Destabilizing	
	N235T	0.09	Stabilizing	
	P101L	-2.05	Destabilizing	
	P101H	-1.04	Destabilizing	
	R144C	-3.93	Destabilizing	
SULT1B1	K234N	0.29	Stabilizing	
	L145V	-9.07	Destabilizing	
SULT1C2	D60A	1.04	Stabilizing	
	R73Q	-	-	Q73 Residue is missing in the crystallographic structure
	S111F	-1.71	Destabilizing	
	S255A			A225 residue is missing in the crystallographic structure
SULT1E1	D22Y	5.68	Stabilizing	
	A32V	-2.38	Destabilizing	
	P253H	-5.85	Destabilizing	

The mutation L145V corresponding to SULT1B1 conducts to a substantial destabilization of the structure ($\Delta\Delta G = -9.07 \text{ kJ mol}^{-1}$), and the literature data show that this mutation results in a significantly decreased sulfation of *p*-nitrophenol compared to the WT.¹⁷

Single amino acid mutations in the sequences of the enzymes belonging to the C2 family of the human cytochromes (CYP2C) have also been suggested to be structurally destabilizing in close connection with the observed interindividual differences in CYP2C-mediated drug metabolism.⁵⁴

CONCLUSIONS

The data obtained in the current study reveal that the point mutations present in the most frequently observed polymorphic variants of the enzymes belonging

to the SULT1 family result in altering the local hydrophobicity and flexibility and usually conduct to destabilize the protein structure. Such changes may be responsible for the reduced affinity for the substrate due to possible effects on the dynamics and flexibility of the binding region of the protein. The outcomes of this study contribute to elucidating how SULT SNPs may influence the metabolism of drugs and endogenous compounds and may allow for the improvement of strategies for mitigating anomalies in the metabolism of xenobiotics. Furthermore, these results may contribute to understanding the molecular basis for the altered specificity of other enzymes having polymorphic variants.

SUPPLEMENTARY MATERIAL

Additional data and information are available electronically at the pages of journal website: <https://www.shd-pub.org.rs/index.php/JSCS/article/view/12271>, or from the corresponding author on request.

ИЗВОД

СМАЊЕНА ЛОКАЛНА ХИДРОФОБНОСТ, СТРУКТУРНА СТАБИЛНОСТ И ФЛЕКСИБИЛНОСТ КОНФОРМАЦИЈЕ УСЛЕД ТАЧКАСТИХ МУТАЦИЈА SULT1 ФАМИЛИЈЕ ЕНЗИМА

SILVANA CEAURANU, VASILE OSTAFE и ADRIANA ISVORAN

Department of Biology-Chemistry and Advanced Environmental Research Laboratories, West University of Timisoara, 4 V. Pirvan, 300223 Timisoara, Romania

Сулфотрансферазе (SULT) су ензими укључени и фазу II метаболизма ксенобиотика. Идентификовани су полиморфизми појединачних нуклеотида за гене који кодирају SULT ензиме, доводећи до синтезе алоензима са измењеном сулфатационом активношћу. У овој студији су испитани ефекти најчешћих мутација аминокиселина у секвенци ензима SULT1 фамилије на њихове локалне особине и структурну стабилност. Показано је да тачкасте мутације мењају локалну хидрофобност и флексибилност, претежно због дестабилизације структуре протеина, што може довести до промене у активности активног места и смањења афинитета за супстрат. Сазнања о начину на који тачкасте мутације утичу на активност ензима доприносе разумевању молекулских основа специфичности ензимске активности и ублажавање аномалија у метаболизму ксенобиотика.

(Примљено 10. фебруара, ревидирано 15. марта, прихваћено 9. априла 2023)

REFERENCES

1. M. W. Duffel, *Comprehensive Toxicology*, Elsevier, Amsterdam, 2010, p. 367 (<https://doi.org/10.1016/B978-0-08-046884-6.00418-8>)
2. H. Glatt, W. Meinel, Naunyn-Schmiedeb, *Arch. Pharmacol.* **55** (2004) 369 (<http://doi.org/10.1007/s00210-003-0826-0>)
3. M.W.H. Coughtrie, *Chem. Biol. Interact.* **259** (2016) 2 (<http://doi.org/10.1016/j.cbi.2016.05.005>)
4. Z. Riches, E. L. Stanley, J. C. Bloomer & M. W. H. Coughtrie, *Drug Metab. Dispos.* **37** (2009) 2255 (<http://doi.org/10.1124/dmd.109.028399>)

5. Z. Riches, J.C. Bloomer, M.W.H. Coughtrie, *Biochem. Pharmacol.* **74** (2007) 352 (<http://doi.org/10.1016/j.bcp.2007.04.006>)
6. A. F. Bairam, M. I. Rasool, F. A. Alherz, M. S. Abunnaja, A. A. El Daibani, S. A. Gohal, M.-C. Liu, *Biochem. Pharmacol.* **151** (2018) 104 (<http://doi.org/10.1016/j.bcp.2018.03.005>)
7. A.C.S. Barbosa, Y. Feng, C. Yu, M. Huang, W. Xie, *Expert. Opin. Drug. Metab. Toxicol.* **15** (2019) 329 (<http://doi.org/10.1080/17425255.2019.1588884>)
8. K. Kurogi, M. I. Rasool, F. A. Alherz, A. A. El Daibani, A. F. Bairam, M. S. Abunnaja, M.-C. Liu, *Expert. Opin. Drug. Metab. Toxicol.* **17** (2021) 767 (<http://doi.org/10.1080/17425255.2021.1940952>)
9. K.-A. Kim, S.-Y. Lee, P.-W. Park, J.-M. Ha, J.-Y. Park, *Eur. J. Clin. Pharmacol.* **61** (2005) 743 (<http://doi.org/10.1007/s00228-005-0989-3>)
10. N. Hempel, N. Gamage, J. L. Martin & M. E. McManus, *Int. J. Biochem. Cell Biol.* **39** (2007) 685 (<http://doi.org/10.1016/j.biocel.2006.10.002>)
11. S.-J. Lee, W.-Y. Kim, Y. B. Jarrar, Y.-W. Kim, S. S. Lee, J.-G. Shin, *Drug Metab. Pharmacokinet.* **28** (2013) 372 (<http://doi.org/10.2133/dmpk.dmpk-12-sc-110>)
12. S. Nagar, S. Walther, R. L. Blanchard, *Mol. Pharmacol.* **69** (2006) 2084 (<http://doi.org/10.1124/mol.105.019240>)
13. M.I. Rasool, A.F. Bairam, S.A. Gohal, A.A. El Daibani, F.A. Alherz, M.S. Abunnaja, E.S. Alatwi, K. Kurogi, M.C. Liu, *Pharmacol. Rep.* **71** (2019) 257 (<http://doi.org/10.1016/j.pharep.2018.12.001>)
14. W. Meinel, J. H. Meerman, H. Glatt, *Pharmacogenetics* **12** (2002) 677 (<http://doi.org/10.1097/00008571-200212000-00002>)
15. Y. Hui, M.-C. Liu, *Eur. J. Pharmacol.* **761** (2015) 125 (<http://doi.org/10.1016/j.ejphar.2015.04.039>)
16. A. F. Bairam, M. I. Rasool, F. A. Alherz, M. S. Abunnaja, A. A. El Daibani, K. Kurogi & M.-C. Liu, *Arch. Biochem. Biophys.* **648** (2018b) 44 (<http://doi.org/10.1016/j.abb.2018.04.019>)
17. Z. E. Tibbs, A. L. Guidry, J. L. Falany, S. A. Kadlubar, C. N. Falany, *Xenobiotica* **48** (2017) 79 (<http://doi.org/10.1080/00498254.2017.1282646>)
18. R. R. Freimuth, B. Eckloff, E. D. Wieben, R. M. Weinshilboum, *Pharmacogenetics* **11** (2001) 747 (<http://doi.org/10.1097/00008571-200112000-00002>)
19. A. A. Adjei, B. A. Thomae, J. L. Prondzinski, B. W. Eckloff, E. D. Wieben, R. M. Weinshilboum, *Br. J. Pharmacol.* **139** (2003) 1373 (<http://doi.org/10.1038/sj.bjp.0705369>)
20. A. A. El Daibani, F. A. Alherz, M. S. Abunnaja, A. F. Bairam, M. I. Rasool, K. Kurogi, M.-C. Liu, *Eur. J. Drug Metab. Pharmacokinet.* **46** (2020) 105 (<http://doi.org/10.1007/s13318-020-00653-1>)
21. A. Isvoran, & Y. Peng, S. Ceauranu, L. Schmidt, A. Nicot, M. Miteva, *Drug Discov. Today.* **27** (2022) 103349 (<http://doi.org/10.1016/j.drudis.2022.103349>)
22. L. M. Bidwell, M. E. McManus, A. Gaedigk, Y. Kakuta, M. Negishi, L. Pedersen, J. L. Martin, *J. Mol. Biol.* **293** (1999) 521 (<http://doi.org/10.1006/jmbi.1999.3153>)
23. N. U. Gamage, S. Tsvetanov, R. G. Duggleby, M. E. McManus and J. L. Martin, *J. Biol. Chem.* **280** (2005) 41482 (<http://doi.org/10.1074/jbc.m508289200>)
24. J.-H. Lu, H.-T. Li, M.-C. Liu, J.-P. Zhang, M. Li, X.-M. An & W.-R. Chang, *Biochem. Biophys. Res. Commun.* **335** (2005) 417 (<http://doi.org/10.1016/j.bbrc.2005.07.091>)
25. J. Lu, H. Li, J. Zhang, M. Li, M.-Y. Liu, X. An, W. Chang, *Biochem. Biophys. Res. Commun.* **396** (2010) 429 (<http://doi.org/10.1016/j.bbrc.2010.04.109>)

26. I. Berger, C. Guttman, D. Amar, R. Zarivach, A. Aharoni, *PLoS ONE* **6** (2011) e26794 (<http://doi.org/10.1371/journal.pone.0026794>)
27. R. A. Gosavi, G. A. Knudsen, L. S. Birnbaum, L. C. Pedersen, *Environ. Health Perspect.* (2013) (<http://doi.org/10.1289/ehp.1306902>)
28. Z. E. Tibbs, C. N. Falany, *Pharmacol. Res. Perspect.* **3** (2015) e00147 (<http://doi.org/10.1002/prp2.147>)
29. K. Evgeny, *Bioinformatics* **23** (2007) 717 (<http://doi.org/10.1093/bioinformatics/btm006>)
30. C. H. M. Rodrigues, D. E. V. Pires, D. B. Ascher, *Protein Sci.* (2020) (<http://doi.org/10.1002/pro.3942>)
31. A. Bateman, M.-J. Martin, S. Orchard, M. Magrane, R. Agivetova, S. Ahmad, E. Alpi, E. H. Bowler-Barnett, R. Britto, B. Bursteinas, H. Bye-A-Jee, R. Coetzee, A. Cukura, A. Da Silva, P. Denny, T. Dogan, T. Ebenezer, J. Fan, D. Teodoro, *Nucleic Acids Res.* **49** (2020) 480 (<http://doi.org/10.1093/nar/gkaa1100>)
32. M. R. Wilkins, E. Gasteiger, A. Bairoch, J. C. Sanchez, K. L. Williams, R. D. Appel, D. F. Hochstrasser, *Methods Mol Biol.* **112** (1999) 531 (<http://doi.org/10.1385/1-59259-584-7:531>)
33. T. Hrabe, Z. Li, M. Sedova, P. Rotkiewicz, L. Jaroszewski, A. Godzik, *Nucleic Acids Res.* **44** (2015) 423 (<http://doi.org/10.1093/nar/gkv1316>)
34. H. M. Berman, J. Westbrook, Z. Feng, G. Gilliland, T. N. Bhat, H. Weissig, I. N. Shindyalov, *Nucleic Acids Res.* **28** (2000) 235 (<http://doi.org/10.1093/nar/28.1.235>)
35. E. F. Pettersen, T. D. Goddard, C. C. Huang, G. S. Couch, D. M. Greenblatt, E. C. Meng, T. E. Ferrin, *J. Comput. Chem.* **25** (2004) 1605 (<http://doi.org/10.1002/jcc.20084>)
36. I. Cook, T. Wang, S. C. Almo, J. Kim, C. N. Falany, T. S. S. Leyh, *Biochemistry* **52** (2013) 415 (<https://doi.org/10.1021/bi301492j>)
37. N. U. Gamage, R. G. Duggleby, A. C. Barnett, M. Tresillian, C. F. Latham, N. E. Liyou, M. E. McManus, J. L. Martin, *J. Biol. Chem.* **278** (2003) 7655. (<https://doi.org/10.1074/jbc.M207246200>)
38. U. Alcolombri, M. Elias, D. S. Tawfik, *J. Mol. Biol.* **411** (2011) 837 (<https://doi.org/10.1016/j.jmb.2011.06.037>)
39. I. Cook, T. Wang, T. S. Leyh, *Biochemistry* **54** (2015) 6114 (<https://doi.org/10.1021/acs.biochem.5b00406>)
40. R. Dash, M. C. Ali, N. Dash, M. A. K. Azad, S. M. Z. Hosen, M. A. Hannan, I. S. Moon, *Int. J. Mol. Sci.* **20** (2019) 6256 (<http://doi.org/10.3390/ijms20246256>)
41. S. Zhao, D. S. Goodsell, A. J. Olson, *Proteins: Struct. Funct. Gen.* **43** (2001) 271 (<http://doi.org/10.1002/prot.1038>)
42. D. Craciun, A. Isvoran N. M. Avram, *Rom. J. Phys.* **56** (2011) 185 (https://rjp.nipne.ro/2011_56_1-2/0185_0195.pdf)
43. D. Craciun, A. Isvoran N. M. Avram, *AIP Conf. Proc.* **1262** (2010) 173 (<http://doi.org/10.1063/1.3482227>)
44. D. Craciun, A. Isvoran N. M. Avram, *Phys., A* **388** (2009) 4609 (<http://doi.org/10.1016/j.physa.2009.07.042>)
45. A. Ciorsac, D. Craciun, V. Ostafe, A. Isvoran, *Chaos Solit. Fractals* **44** (2011) 191 (<http://doi.org/10.1016/j.chaos.2011.01.008>)
46. Y. Zhu, S. Fu, C. Wu, B. Qi, F. Teng, Z. Wang, L. Jiang, *Food Hydrocoll.* (2020) 105709 (<http://doi.org/10.1016/j.foodhyd.2020.105709>)
47. N. Hempel, M. Negishi, M. E. McManus, *Methods Enzymol.* **400** (2005) 147 ([http://doi.org/10.1016/s0076-6879\(05\)00009-1](http://doi.org/10.1016/s0076-6879(05)00009-1))

48. M. Y. Lobanov, E. I. Furletova, N. S. Bogatyreva, M. A. Roytberg, O. V. Galzitskaya, *PLoS Comput. Biol.* **6** (2010) e1000958 (<http://doi.org/10.1371/journal.pcbi.1000958>)
49. N. Sinha, S. Smith-Gill, *Curr. Protein Pept. Sci.* **3** (2002) 601 (<http://doi.org/10.2174/1389203023380431>)
50. A. Isvoran, C. T. Craescu, E. Alexov, *Eur. Biophys. J.* **36** (2007) 225 (<http://doi.org/10.1007/s00249-006-0123-1>)
51. R. L. Redler, J. Das, J. R. Diaz, N. V. Dokholyan, *J. Mol. Evol.* **82** (2015) 11 (<http://doi.org/10.1007/s00239-015-9717-5>)
52. D. M. Popović, I. S. Đorđević, *J. Serb. Chem. Soc.* **85** (2020) 1429 (<https://doi.org/10.2298/JSC200720047P>)
53. D. V. Makhov, D. M. Popović, A. A. Stuchebrukhov, *J. Phys. Chem., B* **110** (2006) 12162 (<https://doi.org/10.1021/jp0608630>)
54. A. Isvoran, M. Louet, D. L. Vladoiu, D. Craciun, M.-A. Lorient, B. O. Villoutreix, M. A. Miteva, *Drug Discov. Today* **22** (2017) 366 (<http://doi.org/10.1016/j.drudis.2016.09.015>).



SUPPLEMENTARY MATERIAL TO
**Impaired local hydrophobicity, structural stability and
conformational flexibility due to point mutations in
SULT1 family of enzymes**

SILVANA CEAURANU, VASILE OSTAFE and ADRIANA ISVORAN*

*Department of Biology-Chemistry and Advanced Environmental Research Laboratories, West
University of Timisoara, 4 V. Pirvan, 300223 Timisoara, Romania*

J. Serb. Chem. Soc. 88 (9) (2023) 841–857

ProtScale tool¹ has been considered in order to obtain the hydrophobicity profiles of SULT1 enzymes. For this purpose, the Kyte&Doolittle hydrophobicity scale has been chosen as it is widely used for detecting hydrophobic regions in proteins.² This hydrophobicity scale contains values that define the hydrophobicity index, i.e., the relative hydrophobicity/hydrophilicity for every amino acid. The more positive the value, the more hydrophobic is the amino acid. In order to generate the hydrophobicity profile, the sequence of the analysed protein is scanned with a sliding window of a given size (the number of amino acids examined at a time to determine a point of hydrophobic character). For every position, the arithmetic mean value of the indexes of amino acids within the window is computed, and that value is attributed to the amino acid in the midpoint of the window. Window sizes of 5-9 amino acids are considered suitable for predicting surface-exposed or buried regions.¹

TABLE S-I. Hydrophobicity profiles of the SULT1A1 enzyme (WT) and its frequently identified allozymes obtained using the ProtScale tool for a window of 5 and 9 amino acids, respectively. Only the regions covered by the windows of 5 and respectively 9 amino acids are highlighted in grey.

Window of 5 amino acids			Window of 9 amino acids		
	SULT1A1 WT	SULT1A1*4 (R37Q), SULT1A1*2 (R213H), SULT1A1*3 (M223V)		SULT1A1 WT	SULT1A1*4 (R37Q), SULT1A1*2 (R213H), SULT1A1*3 (M223V)
33	-0.440	-0.440	33	-0.767	-0.656
34	-0.840	-0.840	34	-0.900	-0.789
35	-1.040	-0.840	35	-1.111	-1.000
36	-1.200	-1.000	36	-1.922	-1.811

* Corresponding author. E-mail: adriana.isvoran@e-uvt.ro



37	-2.460	-2.260	37	-1.111	-1.000
38	-2.260	-2.060	38	-0.600	-0.489
39	-1.860	-1.660	39	-0.411	-0.300
40	-0.200	-0.200	40	0.000	0.111
41	1.020	1.020	41	-0.278	-0.167
209	2.360	2.360	209	-0.056	0.089
210	1.380	1.380	210	0.244	0.389
211	-0.280	-0.020	211	1.100	1.244
212	0.260	0.520	212	0.422	0.567
213	0.460	0.720	213	-0.389	-0.244
214	-0.700	-0.440	214	-0.389	-0.244
215	-1.320	-1.060	215	-0.778	-0.633
216	-1.120	-1.120	216	-0.778	-0.633
217	-1.100	-1.100	217	-1.122	-0.978
219	-1.400	-1.400	219	-0.011	0.244
220	-0.140	-0.140	220	0.033	0.289
221	0.940	1.400	221	-0.178	0.078
222	1.920	2.380	222	-0.144	0.111
223	0.380	0.840	223	0.167	0.422
224	0.440	0.900	224	0.156	0.411
225	-0.260	0.200	225	0.000	0.256
226	-0.800	-0.800	226	-0.044	0.211
227	-1.080	-1.080	227	-0.744	-0.489

TABLE S-II. Hydrophobicity profiles of the SULT1A2 enzyme (WT) and its frequently identified allozymes obtained using the ProtScale tool for a window of 5 and 9 amino acids, respectively. Only the regions covered by the windows of 5 and respectively 9 amino acids are highlighted in grey.

	Window of 5 amino acids		Window of 9 amino acids		
	SULT1A2 WT	SULT1A2*2 (I7T, N235T), SULT1A2*3 (P19L)	SULT1A2 WT	SULT1A2*2 (I7T, N235T), SULT1A2*3 (P19L)	
5	1.160	0.120	5	-0.122	-0.700
6	0.240	-0.800	6	-0.511	-1.089
7	-1.560	-2.600	7	-0.300	-0.878
8	-1.180	-2.220	8	-0.300	-0.878
9	-0.800	-1.840	9	-1.189	-1.767
10	-0.940	-0.940	10	-0.944	-1.522
11	-1.480	-1.480	11	-0.089	-0.667
12	-0.840	-0.840	12	-1.022	-1.022
13	0.320	0.320	13	-0.978	-0.978
15	-0.980	-0.980	15	-0.011	0.589
16	0.560	0.560	16	0.589	1.189
17	0.500	1.580	17	0.667	1.267

18	0.420	1.500	18	0.622	1.222
19	2.100	3.180	19	0.622	1.222
20	1.400	2.480	20	0.467	1.067
21	0.300	1.380	21	1.100	1.700
22	1.180	1.180	22	0.756	1.356
23	0.780	0.780	23	0.489	1.089
231	-1.320	-1.320	231	-1.722	-1.411
232	-2.660	-2.660	232	-1.822	-1.511
233	-2.580	-2.020	233	-1.522	-1.211
234	-2.200	-1.640	234	-1.911	-1.600
235	-2.200	-1.640	235	-1.867	-1.556
236	-1.560	-1.000	236	-1.622	-1.311
237	-1.480	-0.920	237	-1.911	-1.600
238	-1.040	-1.040	238	-1.556	-1.244
239	-0.860	-0.860	239	-0.656	-0.344

TABLE S-III. Hydrophobicity profiles of the SULT1A3 enzyme (WT) and its frequently identified allozymes obtained using the ProtScale tool for a window of 5 and 9 amino acids, respectively. Only the regions covered by the windows of 5 and respectively 9 amino acids are highlighted in grey.

Window of 5 amino acids				Window of 9 amino acids			
SULT1A3 WT	SULT1A3*2 (K234N), SULT1A3*3 (P101L), SULT1A3*5 (R144C)	SULT1A3*4 (P101H)	SULT1A3 WT	SULT1A3*2 (K234N), SULT1A3*3 (P101L), SULT1A3*5 (R144C)	SULT1A3*4 (P101H)		
97	-1.000	-1.000	-1.000	97	-0.878	-0.278	-1.056
98	-1.180	-1.180	-1.180	98	-1.478	-0.878	-1.656
99	-2.260	-1.180	-2.580	99	-1.589	-0.989	-1.767
100	-1.800	-0.720	-2.120	100	-1.089	-0.489	-1.267
101	-2.000	-0.920	-2.320	101	-1.011	-0.411	-1.189
102	-1.100	-0.020	-1.420	102	-1.011	-0.411	-1.189
103	0.120	1.200	-0.200	103	-0.711	-0.111	-0.889
104	-0.340	-0.340	-0.340	104	-0.989	-0.389	-1.167
105	-0.180	-0.180	-0.180	105	-0.389	0.211	-0.567
140	-0.760	-0.760		140	-0.611	0.167	
141	-1.240	-1.240		141	-0.600	0.178	
142	-1.880	-0.480		142	-1.456	-0.678	
143	-1.240	0.160		143	-1.800	-1.022	
144	-1.300	0.100		144	-1.456	-0.678	
145	-2.640	-1.240		145	-1.667	-0.889	
146	-1.640	-0.240		146	-1.489	-0.711	
147	-1.380	-1.380		147	-2.189	-1.411	
148	-2.080	-2.080		148	-2.011	-1.233	

230	-0.700	-0.700	230	-1.689	-1.644
231	-1.320	-1.320	231	-1.722	-1.678
232	-2.660	-2.580	232	-1.822	-1.778
233	-2.580	-2.500	233	-1.522	-1.478
234	-2.200	-2.120	234	-1.911	-1.867
235	-2.200	-2.120	235	-1.867	-1.822
236	-1.560	-1.480	236	-1.622	-1.578
237	-1.480	-1.480	237	-1.911	-1.867
238	-1.040	-1.040	238	-1.556	-1.511

TABLE S-IV. Hydrophobicity profiles of the SULT1B1 enzyme (WT) and its frequently identified allozymes obtained using the ProtScale tool for a window of 5 and 9 amino acids, respectively. Only the regions covered by the windows of 5 and respectively 9 amino acids are highlighted in grey.

Window of 5 amino acids			Window of 9 amino acids		
	SULT1B1 WT	SULT1B1 (L145V)		SULT1B1 WT	SULT1B1 (L145V)
141	-0.760	-0.760	141	-0.011	0.033
142	-1.300	-1.300	142	0.289	0.333
143	-0.280	-0.200	143	-0.567	-0.522
144	0.360	0.440	144	-0.867	-0.822
145	0.300	0.380	145	-0.300	-0.256
146	-0.960	-0.880	146	-0.544	-0.500
147	0.500	0.580	147	-0.367	-0.322
148	-0.960	-0.960	148	-0.367	-0.322
149	-1.660	-1.660	149	-0.156	-0.111

TABLE S-V. Hydrophobicity profiles of the SULT1C1 enzyme (WT) and its frequently identified allozymes obtained using the ProtScale tool for a window of 5 and 9 amino acids, respectively. Only the regions covered by the windows of 5 and respectively 9 amino acids are highlighted in grey.

Window of 5 amino acids			Window of 9 amino acids		
	SULT1C1 WT	SULT1C1*2 (S255A), SULT1C1*3 (D60A), SULT1C1*4 (R73Q), SULT1C1*5 (S111F)		SULT1C1 WT	SULT1C1*2 (S255A), SULT1C1*3 (D60A), SULT1C1*4 (R73Q), SULT1C1*5 (S111F)
56	0.220	0.220	56	0.044	0.633
57	1.240	1.240	57	0.333	0.922
58	-0.360	0.700	58	0.911	1.500
59	0.720	1.780	59	0.622	1.211
60	2.320	3.380	60	-0.267	0.322
61	0.720	1.780	61	-0.267	0.322
62	-0.820	0.240	62	0.078	0.667
63	-0.820	-0.820	63	-0.811	-0.222
64	-1.280	-1.280	64	-0.811	-0.222
69	-0.840	-0.840	69	-1.789	-1.678
70	-0.840	-0.840	70	-1.200	-1.089

71	-2.580	-2.380	71	-0.656	-0.544
72	-1.520	-1.320	72	0.233	0.344
73	0.160	0.360	73	-0.622	-0.511
74	0.560	0.760	74	-0.589	-0.478
75	0.560	0.760	75	-0.656	-0.544
76	0.820	0.820	76	-1.289	-1.178
77	-0.440	-0.440	77	-1.078	-0.967
107	0.100	0.100	107	-0.289	0.111
108	-0.040	-0.040	108	-0.189	0.211
109	-0.960	-0.240	109	-0.078	0.322
110	-0.320	0.400	110	-0.156	0.244
111	-0.880	-0.160	111	-0.156	0.244
112	0.520	1.240	112	0.100	0.500
113	0.520	1.240	113	0.000	0.400
114	0.360	0.360	114	0.267	0.667
115	0.180	0.180	115	0.156	0.556
251	0.100	0.100	251	0.289	0.578
252	-0.820	-0.820	252	0.689	0.978
253	-0.280	0.240	253	0.400	0.689
254	0.980	1.500	254	-0.522	-0.233
255	1.520	2.040	255	-0.567	-0.278
256	-0.280	0.240	256	-0.222	0.067
257	-0.900	-0.380	257	-0.211	0.078
258	-0.820	-0.820	258	-0.244	0.044
259	-1.520	-1.520	259	-0.200	0.089

TABLE S-VI. Hydrophobicity profiles of the SULT1E1 enzyme (WT) and its frequently identified allozymes obtained using the ProtScale tool for a window of 5 and 9 amino acids, respectively. Only the regions covered by the windows of 5 and respectively 9 amino acids are highlighted in grey.

	Window of 5 amino acids		Window of 9 amino acids		
	SULT1E1 WT	SULT1E1*2 (D22Y), SULT1E1*3 (A32V), SULT1E1*4 (P253H)	SULT1E1 WT	SULT1E1*2 (D22Y), SULT1E1*3 (A32V), SULT1E1*4 (P253H)	
18	1.700	1.700	18	0.233	0.478
19	1.000	1.000	19	0.078	0.322
20	-0.600	-0.160	20	0.900	1.144
21	-0.800	-0.360	21	0.511	0.756
22	-0.340	0.100	22	-0.133	0.111
23	-0.860	-0.420	23	-0.656	-0.411
24	-0.340	0.100	24	-1.256	-1.011
25	0.180	0.180	25	-1.500	-1.256
26	-1.080	-1.080	26	-0.600	-0.356
28	-1.000	-1.000	28	-0.711	-0.444
29	-1.440	-1.440	29	-0.867	-0.600

30	-0.900	-0.420	30	-0.822	-0.556
31	0.360	0.840	31	-0.478	-0.211
32	0.360	0.840	32	-0.878	-0.611
33	-0.120	0.360	33	-0.667	-0.400
34	-0.320	0.160	34	-0.667	-0.400
35	-1.000	-1.000	35	-1.522	-1.256
36	-2.260	-2.260	36	-0.711	-0.444
249	-1.040	-1.040	249	-0.733	-0.911
250	-1.580	-1.580	250	-0.033	-0.211
251	-1.200	-1.520	251	-0.322	-0.500
252	0.060	-0.260	252	-1.033	-1.211
253	1.220	0.900	253	-1.078	-1.256
254	-0.440	-0.760	254	-0.733	-0.911
255	-1.060	-1.380	255	0.200	0.022
256	-0.820	-0.820	256	-0.300	-0.478
257	-0.480	-0.480	257	-0.256	-0.433

ProtScale tool¹ has also been considered in order to obtain the flexibility profiles of SULT1 enzymes. In this case, the average flexibility scale has been chosen³. This scale contains values that define the flexibility index for every type of amino acid, i.e., the fluctuational displacement of each residue in a protein. The lowest value (0.300) corresponds to methionine, and the highest value (0.540) to glycine. To generate the flexibility profile, the sequence of the analyzed protein is also scanned with a sliding window of a given size. For every position, the mean value of the flexibility indexes of amino acids within the window is computed, which is attributed to the amino acid in the midpoint of the window. Window sizes of 5-9 amino acids are considered similar to those used to obtain the hydrophobicity profiles.

TABLE S-VII. Average flexibility profiles of the SULT1A1 enzyme (WT) and its frequently identified allozymes obtained using the ProtScale tool for a window of 5 and 9 amino acids, respectively. Only the regions covered by the windows of 5 and respectively 9 amino acids are highlighted in grey.

	Window of 5 amino acids		Window of 9 amino acids		
	SULT1A1 WT	SULT1A1*4 (R37Q), SULT1A1*2 (R213H), SULT1A1*3 (M223V)	SULT1A1 WT	SULT1A1*4 (R37Q), SULT1A1*2 (R213H), SULT1A1*3 (M223V)	
33	0.442	0.442	33	0.461	0.457
34	0.440	0.440	34	0.458	0.453
35	0.448	0.440	35	0.458	0.453
36	0.448	0.440	36	0.473	0.469
37	0.488	0.480	37	0.460	0.456
38	0.484	0.476	38	0.444	0.440
39	0.486	0.478	39	0.461	0.457
40	0.454	0.454	40	0.459	0.454

41	0.444	0.444	41	0.468	0.463
209	0.406	0.406	209	0.451	0.428
210	0.422	0.422	210	0.453	0.430
211	0.454	0.412	211	0.442	0.419
212	0.456	0.414	212	0.448	0.424
213	0.468	0.426	213	0.462	0.439
214	0.492	0.450	214	0.462	0.439
215	0.484	0.442	215	0.477	0.453
216	0.478	0.478	216	0.477	0.453
217	0.464	0.464	217	0.473	0.450
219	0.468	0.468	219	0.426	0.436
220	0.430	0.430	220	0.428	0.438
221	0.390	0.408	221	0.426	0.436
222	0.380	0.398	222	0.406	0.416
223	0.400	0.418	223	0.399	0.409
224	0.362	0.380	224	0.407	0.417
225	0.388	0.406	225	0.398	0.408
226	0.430	0.430	226	0.393	0.403
227	0.414	0.414	227	0.414	0.424

TABLE S-VIII. Average flexibility profiles of the SULT1A2 enzyme (WT) and its frequently identified allozymes obtained using the ProtScale tool for a window of 5 and 9 amino acids, respectively. Only the regions covered by the windows of 5 and respectively 9 amino acids are highlighted in grey.

Window of 5 amino acids			Window of 9 amino acids		
	SULT1A2 WT	SULT1A2*2 (I7T, N235T), SULT1A2*3 (P19L)		SULT1A2 WT	SULT1A2*2 (I7T, N235T), SULT1A2*3 (P19L)
5	0.458	0.454	5	0.459	0.457
6	0.486	0.482	6	0.482	0.480
7	0.500	0.496	7	0.483	0.481
8	0.504	0.500	8	0.483	0.481
9	0.504	0.500	9	0.488	0.486
10	0.486	0.486	10	0.480	0.478
11	0.484	0.484	11	0.467	0.464
12	0.462	0.462	12	0.468	0.468
13	0.438	0.438	13	0.471	0.471
15	0.464	0.464	15	0.456	0.440
16	0.442	0.442	16	0.440	0.424
17	0.460	0.432	17	0.450	0.434
18	0.456	0.428	18	0.447	0.431
19	0.454	0.426	19	0.447	0.431
20	0.440	0.412	20	0.438	0.422
21	0.446	0.418	21	0.426	0.410
22	0.406	0.406	22	0.421	0.406

23	0.404	0.404	23	0.418	0.402
231	0.410	0.410	231	0.437	0.434
232	0.442	0.442	232	0.444	0.442
233	0.440	0.436	233	0.421	0.419
234	0.442	0.438	234	0.436	0.433
235	0.442	0.438	235	0.434	0.432
236	0.436	0.432	236	0.426	0.423
237	0.434	0.430	237	0.441	0.439
238	0.426	0.426	238	0.438	0.436
239	0.412	0.412	239	0.429	0.427

TABLE S-XI. Average flexibility profiles of the SULT1A3 enzyme (WT) and its frequently identified allozymes obtained using the ProtScale tool for a window of 5 and 9 amino acids, respectively. Only the regions covered by the windows of 5 and respectively 9 amino acids are highlighted in grey.

Window of 5 amino acids				Window of 9 amino acids			
	SULT1A3* 2 (K234N), SULT1A3* 3 (P101L), SULT1A3* 5 (R144C)	SULT1 A3*4 (P101H)		SUIT 1A3 WT	SULT1A3* 2 (K234N), SULT1A3* 3 (P101L), SULT1A3* 5 (R144C)	SULT1A3* 4 (P101H)	
97	0.446	0.446	0.446	97	0.458	0.442	0.437
98	0.460	0.460	0.460	98	0.473	0.458	0.452
99	0.488	0.460	0.450	99	0.477	0.461	0.456
100	0.496	0.468	0.458	100	0.469	0.453	0.448
101	0.500	0.472	0.462	101	0.479	0.463	0.458
102	0.486	0.458	0.448	102	0.479	0.463	0.458
103	0.476	0.448	0.438	103	0.479	0.463	0.458
104	0.468	0.468	0.468	104	0.466	0.450	0.444
105	0.468	0.468	0.468	105	0.450	0.434	0.429
140	0.396	0.396		140	0.398	0.378	
141	0.358	0.358		141	0.391	0.371	
142	0.380	0.344		142	0.403	0.383	
143	0.356	0.320		143	0.399	0.379	
144	0.392	0.356		144	0.392	0.372	
145	0.424	0.388		145	0.381	0.361	
146	0.432	0.396		146	0.402	0.382	
147	0.390	0.390		147	0.423	0.403	
148	0.432	0.432		148	0.444	0.424	
230	0.418	0.418		230	0.420	0.421	
231	0.410	0.410		231	0.436	0.437	
232	0.440	0.442		232	0.443	0.444	
233	0.438	0.440		233	0.420	0.421	
234	0.440	0.442		234	0.434	0.436	

235	0.440	0.442	235	0.433	0.434
236	0.434	0.436	236	0.424	0.426
237	0.434	0.434	237	0.440	0.441
238	0.426	0.426	238	0.437	0.438

TABLE S-X. Average flexibility profiles of the SULT1B1 enzyme (WT) and its frequently identified allozymes obtained using the ProtScale tool for a window of 5 and 9 amino acids, respectively. Only the regions covered by the windows of 5 and respectively 9 amino acids are highlighted in grey.

Window of 5 amino acids			Window of 9 amino acids		
	SULT1B1 WT	SULT1B1 (L145V)		SULT1B1 WT	SULT1B1 (L145V)
141	0.396	0.396	141	0.418	0.420
142	0.396	0.396	142	0.394	0.397
143	0.386	0.390	143	0.402	0.404
144	0.362	0.366	144	0.397	0.399
145	0.390	0.394	145	0.391	0.393
146	0.420	0.424	146	0.399	0.401
147	0.392	0.396	147	0.420	0.422
148	0.416	0.416	148	0.420	0.422
149	0.458	0.458	149	0.420	0.422

TABLE S-XI. Average flexibility profiles of the SULT1C1 enzyme (WT) and its frequently identified allozymes obtained using the ProtScale tool for a window of 5 and 9 amino acids, respectively. Only the regions covered by the windows of 5 and respectively 9 amino acids are highlighted in grey.

Window of 5 amino acids			Window of 9 amino acids		
	SULT1C1 WT	SULT1C1*2 (S255A), SULT1C1*3 (D60A), SULT1C1*4 (R73Q), SULT1C1*5 (S111F)		SULT1C1 WT	SULT1C1*2 (S255A), SULT1C1*3 (D60A), SULT1C1*4 (R73Q), SULT1C1*5 (S111F)
56	0.444	0.444	56	0.444	0.428
57	0.460	0.460	57	0.429	0.412
58	0.470	0.440	58	0.431	0.414
59	0.432	0.402	59	0.452	0.436
60	0.424	0.394	60	0.456	0.439
61	0.432	0.402	61	0.452	0.436
62	0.452	0.422	62	0.457	0.440
63	0.442	0.442	63	0.462	0.446
64	0.490	0.490	64	0.462	0.446
69	0.444	0.444	69	0.471	0.467
70	0.440	0.440	70	0.460	0.456
71	0.468	0.460	71	0.451	0.447

72	0.440	0.432	72	0.446	0.441
73	0.438	0.430	73	0.457	0.452
74	0.460	0.452	74	0.437	0.432
75	0.460	0.452	75	0.443	0.439
76	0.418	0.418	76	0.440	0.436
77	0.452	0.452	77	0.442	0.438
107	0.412	0.412	107	0.442	0.420
108	0.394	0.394	108	0.434	0.412
109	0.422	0.382	109	0.430	0.408
110	0.416	0.376	110	0.420	0.398
111	0.426	0.386	111	0.420	0.398
112	0.436	0.396	112	0.424	0.402
113	0.436	0.396	113	0.432	0.410
114	0.436	0.436	114	0.453	0.431
115	0.450	0.450	115	0.447	0.424
251	0.468	0.468	251	0.481	0.464
252	0.496	0.496	252	0.459	0.442
253	0.496	0.466	253	0.441	0.424
254	0.460	0.430	254	0.459	0.442
255	0.418	0.388	255	0.454	0.438
256	0.432	0.402	256	0.460	0.443
257	0.424	0.394	257	0.452	0.436
258	0.430	0.430	258	0.444	0.428
259	0.456	0.456	259	0.448	0.431

TABLE S-XII. Average flexibility profiles of the SULT1E1 enzyme (WT) and its frequently identified allozymes obtained using the ProtScale tool for a window of 5 and 9 amino acids, respectively. Only the regions covered by the windows of 5 and respectively 9 amino acids are highlighted in grey.

Window of 5 amino acids			Window of 9 amino acids		
	SULT1E1 WT	SULT1E1*2 (D22Y), SULT1E1*3 (A32V), SULT1E1*4 (P253H)		SULT1E1 WT	SULT1E1*2 (D22Y), SULT1E1*3 (A32V), SULT1E1*4 (P253H)
18	0.418	0.418	18	0.420	0.410
19	0.404	0.404	19	0.411	0.401
20	0.414	0.396	20	0.419	0.409
21	0.402	0.384	21	0.411	0.401
22	0.420	0.402	22	0.407	0.397
23	0.430	0.412	23	0.400	0.390
24	0.420	0.402	24	0.423	0.413
25	0.380	0.380	25	0.428	0.418
26	0.420	0.420	26	0.419	0.409

28	0.418	0.418	28	0.423	0.427
29	0.434	0.434	29	0.414	0.418
30	0.444	0.450	30	0.417	0.420
31	0.404	0.410	31	0.410	0.413
32	0.410	0.416	32	0.434	0.438
33	0.404	0.410	33	0.434	0.438
34	0.410	0.416	34	0.440	0.443
35	0.440	0.440	35	0.453	0.457
36	0.480	0.480	36	0.439	0.442
249	0.418	0.418	249	0.452	0.431
250	0.460	0.460	250	0.431	0.410
251	0.470	0.432	251	0.413	0.392
252	0.434	0.396	252	0.439	0.418
253	0.400	0.362	253	0.440	0.419
254	0.432	0.394	254	0.446	0.424
255	0.424	0.386	255	0.444	0.423
256	0.430	0.430	256	0.452	0.431
257	0.460	0.460	257	0.456	0.434

TABLE S-XIII. The clusters identified by the PDBFlex computational tool for assessing the structural flexibility of the SULT1 enzymes that revealing frequently identified allozymes.

Subfamily of SULT1	PDBFlex cluster	Members of the cluster
		1LS6
		2D06 chains A and B
		3U3J chains A and B
		3U3K chains A and B
		3U3O
SULT1A1 / SULT1A2	3U3M_A	3U3R
		1Z28
		3QVU chains A and B
		3QVV chains A and B
		1Z29 ^a
		1Z28 ^b
		4GRA ^c chains A and B
SULT1A3	2A3R_A	1CJM
		2A3R
SULT1B1	3CKL_B	2Z5F chains A and B
		3CKL
	4JVM_A	1G3M chains A and B

Subfamily of SULT1	PDBFlex cluster	Members of the cluster
SULT1E1		1HY3 chains A and B 4JVL chains A and B 4JVN chains A and B

^aSULT1A2, ^bSULT1A1*3, ^cSULT1A1*2

REFERENCES

1. M. R. Wilkins, E. Gasteiger, A. Bairoch, J.C. Sanchez, K.L. Williams, R.D. Appel, D.F. Hochstrasser, *Methods Mol Biol.* **112** (1999) 531 (<http://doi.org/10.1385/1-59259-584-7:531>)
2. J. Kyte, R. F. Doolittle, *J Mol Biol.* **157** (1982) 105 ([https://doi.org/10.1016/0022-2836\(82\)90515-0](https://doi.org/10.1016/0022-2836(82)90515-0))
3. R. Bhaskaran, P. K. Ponnuswamy, *Int J Pept Protein Res.* **32** (1998) 241 (<https://doi.org/10.1111/j.1399-3011.1988.tb01258.x>).



J. Serb. Chem. Soc. 88 (9) 859–876 (2023)
JSCS–5667

Natural flavonoids in *Delonix regia* leaf as an antimycobacterial agent: An *in silico* study

PUTRA JIWAMURWA PAMA TJITDA^{1*}, FEBRI ODEL NITBANI², DOMINUS MBUNGA¹ and TUTIK DWI WAHYUNINGSIH³

¹Department of Pharmacy, Health Polytechnic of Kupang, Indonesia, ²Department of Chemistry, Faculty of Science and Engineering, Nusa Cendana University, Indonesia and

³Department of Chemistry, Faculty of Mathematics and Natural Sciences, Universitas Gadjah Mada, Indonesia

(Received 13 September, revised 23 December 2022, accepted 21 July 2023)

Abstract: Multi-drug resistant (MDR) and extensively-drug resistant (XDR) as results of continuous use of antibiotics encourage the development of new antimycobacterial drugs. In this study, 13 flavonoid compounds from the flamboyant leaf plant were studied for their inhibitory properties of *MtKasA*, *MtDprE* and *MtPank* which are significant enzymes in *Mycobacterium tuberculosis*, as well as for their molecular docking, molecular dynamics and prediction of ADMET-drug likeness. The results of molecular docking studies revealed that compound F13 (apigenin) was the most potent compound because it was able to bind the most amino acids as indicated by the native ligand of each enzyme. Molecular dynamics studies showed that compound F13 forms a stable complex with *MtKasA*. The results of the ADMET-drug likeness analysis concluded that compound F13 was the most promising compound. Overall, compound F13 has the potential to be used as a treatment therapy against *M. tuberculosis*.

Keywords: tuberculosis; molecular docking; *MtKasA*; *MtDprE*; *MtPank*.

INTRODUCTION

Tuberculosis (TB) is a deadly disease caused by *Mycobacterium tuberculosis*. Many parties have and are paying special attention to the handling of tuberculosis. WHO, in the Global Tuberculosis Report 2021, reported that the pandemic of COVID-19 has a negative impact on efforts to treat tuberculosis. Limited access to diagnosis and treatment of tuberculosis has increased the number of tuberculosis deaths by 1.2 million since 2019.¹ WHO also noted four countries contributed the most prominent TB cases, namely India (41 %), Indonesia (14 %), the Philippines (12 %) and China (8 %). Another report noted that cases of drug-

* Corresponding author. E-mail: putrachemist_jc@yahoo.com
<https://doi.org/10.2298/JSC220913045T>



-resistant TB against first-line drug usage for TB therapy have increased by 15%.¹ This is primarily due to the prolonged treatment of TB, as well as the use of antibiotic combinations with side effects that result in the development of multi-drug resistant (MDR) and extensively drug-resistant (XDR).² As a result of all these reports, tuberculosis treatment needs urgent attention as well as appropriate and quick solutions.

There are still many drug discovery studies underway to overcome the problem of drug resistance, including tuberculosis.³ Molecular docking is a computational method for new drug discovery based on structure-based design. Application of molecular docking methods includes virtual screening, prediction of adverse drug reactions, drug repositioning, and drug mechanism of action against the targeted protein.⁴ Therefore, molecular docking is an excellent and powerful method for predicting drug activity against specific proteins. Several targeted proteins to predict drug activity against the growth of *M. tuberculosis* are *MtKasA*, *MtDprE1* and *MtPank*.⁵ *MtKasA* and *MtDprE1* are necessary enzymes used for cell wall biosynthesis. *MtKasA* is responsible for elongating the fatty acid carbon chain in the FAS-II pathway and provides a precursor for mycolic acid biosynthesis.⁶ *MtDprE1* performs the epimerization reaction of decaprenyl phosphoryl- β -D-ribose (DPR) to decaprenyl phosphoryl- β -D-arabinofuranose (DPA) in the periplasmic space of the cell membrane. DPA is used for the biogenesis of arabinogalactan and lipoarabinomannan.^{7,8} *MtPank* is also an essential drug target to overcome drug-resistant TB. *MtPank* enzyme plays a role in the growth of *M. tuberculosis* through the biosynthesis of coenzyme-A (CoA).⁹

Various studies have been conducted to study the plant's active compounds and their biological activity against *M. tuberculosis*.¹⁰⁻¹³ The content of secondary metabolites in plants significantly contributes to certain biological activities and is always accompanied by low side effects.¹⁴ Among the secondary metabolites, flavonoids have been reported to have inhibitory activity against the growth of *M. tuberculosis*.¹⁵⁻¹⁷ Chemically, flavonoids have two benzene rings, A and B, which are connected by a pyran heterocyclic ring (C ring). Flavonoid groups include flavonols, flavanones, flavones, isoflavones, flavanols and anthocyanins.¹⁸

Flamboyant (*Delonix regia*) is a plant that comes from the *Caesalpinaceae* family and is widely found in various regions of Indonesia. Previous studies reported that the isolation of flamboyant leaves with ethanol as a solvent produced 13 flavonoid compounds.¹⁹ The presence of flavonoids led to the investigation of their ability to inhibit 3 key enzymes in the growth of *M. tuberculosis*. Therefore, this study aimed to identify the potential of flavonoid compounds contained in flamboyant leaves as antimycobacterial agents using an *in silico* study approach. As a result, the potential compounds obtained could be used as reference compounds for laboratory testing.

EXPERIMENTAL

Materials

As test ligands, natural flavonoids were obtained from previous studies investigating the HPLC profiles of *Delonix regia* leaves extract.¹⁹ The proteins analyzed in this study include *MtKasA*, *MtDprE1* and *MtPank* taken from the RSCB database with PDB ID were 2WGE, 4FF6 and 4BFT, respectively. The software used for molecular docking was AutoDock Vina; the structures of ligand compounds were drawn with ChemOffice Professional 16 and Chem3D Professional 16, and structure optimization was performed using Gaussian 09. Molecular docking results were visualized in Discovery Studio client 2021.

Validation of docking protocol

Each receptor protein was prepared by separating the native ligand from the protein using AutoDock Tool (ADT) 1.5.6. Missing atoms of the receptor protein were checked and corrected through ADT. Furthermore, the water molecule on the receptor protein was cleaned and the protein was added with Kollman charge and then stored in the pdbqt extension format. The separated native ligands were prepared by adding hydrogen atoms and Gasteiger charge.

Prepared proteins and native ligands were then docked by following several parameters. The molecular docking for *MtKasA* protein used a grid box dimension of 25×25×25 Å³ with cartesian coordinates *x*, *y* and *z* of 37.883, 0.813 and -5.898, respectively. *MtDprE1* protein used a grid box size of 12×12×12 Å³ with cartesian coordinates *x*, *y* and *z* of 14.697, -21.165 and 36.955, respectively, and for *MtPank* protein, it was 14×14×14 Å³ with cartesian coordinates *x*, *y* and *z* of -19.242, -10.217 and 12.648, respectively. An exhaustiveness of 16 was applied to the protocol docking validation process. In order to dock all proteins, the spacing value of 1 Å was used. *RMSD* value was determined using Pymol. The docking protocol was used to dock the tested compound if it had an *RMSD* value below 2 Å.²⁰

Preparation of natural flavonoid as tested ligand

The structure of natural flavonoids from *D. regia* leaf extract was taken from the PubChem database. Compounds that were not found in the database were drawn with ChemDraw Professional 16, as shown in Table I. Furthermore, all compounds were converted to 3-dimensional structure and geometric optimization using Gaussian 09 with the DFT method with a base set B3LYP 6-31G.²¹ Furthermore, the test compound was prepared using ADT, which involved the addition of hydrogen atoms, merging non-polar hydrogen atoms and adding Gasteiger charge. All compounds that had been prepared were then stored in a pdbqt format file.

Antimycobacterial profile prediction

The antimycobacterial properties of 13 flavonoids contained in flamboyant leaf extract were predicted. Each SMILES code of the flavonoid compound was inputted into PASS online (<http://www.way2drug.com/passonline/predict.php>). Activity predicted values (*Pa*) and inactive predictions were recorded, tabulated and presented in graphical form.

Molecular docking

Natural flavonoids that had been optimized were docked to the three receptor proteins. Docking was conducted using AutoDock Vina following a validated docking protocol. The docking results generated binding energy as a value that indicated the binding energy between the ligands and the receptor protein. The 2D and 3D interactions of the tested compound with key amino acid residues of the receptor protein were visualized using Discovery Studio client 2021.

ADMET-drug-likeness analysis

Pharmacokinetic properties of natural flavonoid compounds, including adsorption, distribution, metabolism, excretion, and toxicity, were predicted using the pkCSM tool.²² The drug-likeness properties were studied using the MolSoft tool (<https://www.molsoft.com/publications.html>).

Molecular dynamic simulation

The lead compounds obtained from molecular docking simulations were then studied for the stability of their interactions with amino acid receptors, in this case *MtKasA*, *MtDprE1* and *MtPank*. This was done through molecular dynamic simulations. Simulations used CABS Flex 2.0 server (<http://biocomp.chem.uw.edu.pl/CABSflex2/index>). The simulation setting used a number of cycles and 50 trajectory frames. Furthermore, the temperature of the simulation and the global weight were respectively 1.4 and 1.0.

RESULTS AND DISCUSSION

Validation of docking protocol

The molecular docking method is a powerful *in silico* method for predicting the interaction between ligands and receptors.²³ To study the antimycobacterial properties of natural flavonoids in the ethanolic extract of *Delonix regia* leaves, three significant proteins were used to inhibit *Mycobacterium tuberculosis* activities. These proteins were *MtKasA*, *MtDprE1* and *MtPank*. Docking protocol validation was performed before molecular docking of the test compounds was carried out on the three proteins. As shown in Fig. 1, the native ligands are superimposed and include *MtKasA* complexes with thiolactomycin (TLM), *MtDprE1* complexes with 3-(hydroxyamino)-*N*-[(1*R*)-1-phenylethyl]-5-(trifluoromethyl)-benzamide (0T4) and *MtPank* with 2-chloro-*N*-[1-(5-[[2-(4-fluorophenoxy)sulfanyl]-4-methyl-4*H*-1,2,4-triazo-3-yl)]benzamide (ZVT). Validation results in the form of RMSD values for *MtKasA*, *MtDprE1* and *MtPank* were 0.828, 1.512 and 0.689 Å, respectively.

Antimycobacterial profile prediction

Prediction of the antimycobacterial profile of flavonoid compounds was carried out using the PASS server and gave results as shown in Fig. 2. The results of

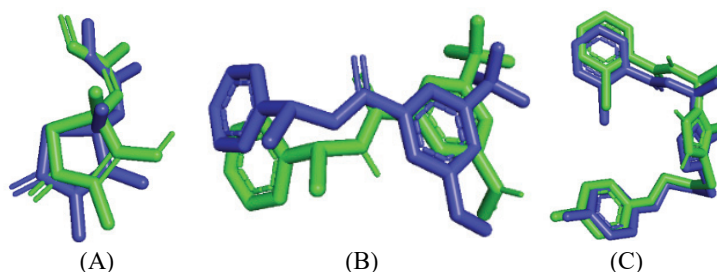


Fig. 1. Superimpose re-docking ligand (green) into native ligand (blue) of protein receptor: A) complex of *MtKasA* (id pdb: 2wge) – TLM; B) complex of *MtDprE1* (id pdb: 4ff6) – 0T4; C) complex of *MtPank* (id pdb: 4bft) – ZVT.

the analysis from the PASS server showed that all compounds had a *Pa* value >0.3 , however the value was still <0.7 except for compound F5 (0.276). This means that the compound was predicted to have moderate antimycobacterial potential in the laboratory.²⁴ Furthermore, this compound could be further confirmed through molecular docking.

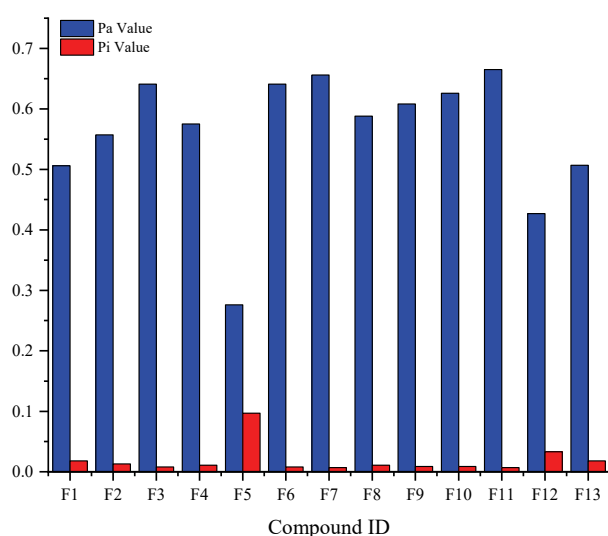


Fig. 2. Graph of antimycobacterial profile prediction by flavonoid compounds from flamboyant leaves.

Molecular docking

The chemical structure of flavonoid compounds contained in flamboyant leaf extract that were used as tested ligands, is shown in Table I. In this study, molecular docking of flavonoids in flamboyant plants was conducted to determine potential compounds for antituberculosis drugs. The binding energy and chemical interactions of each flavonoid with the targeted protein were studied and compared to natural inhibitors of each enzyme.

Molecular docking of the *MtKasA* enzyme was carried out on 13 flavonoids contained in flamboyant leaves and the results are shown in Table II. For *MtKasA* molecular docking, TLM which acted as a natural inhibitor, produced a binding energy value of -32.22 kJ/mol, while some other test compounds also demonstrated satisfactory inhibitory activity compared to natural inhibitors. Compound F6 had the highest binding energy (-38.91 kJ/mol), followed by the compound F5 with a binding energy value of -36.40 kJ/mol, while compounds F3, F12 and F13 showed the same binding energy value of -35.95 kJ/mol.

An investigation of the chemical interaction of TLM in the *MtKasA* enzyme binding pocket has been carried out (Table S-I of the Supplementary material to

TABLE I. Natural flavonoid compounds from Flamboyant leaves (*D. regia*)

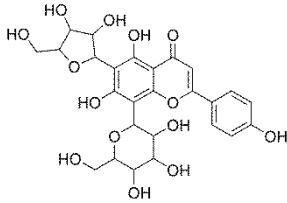
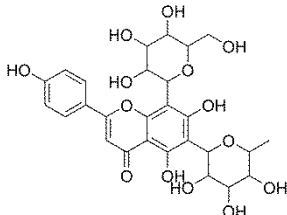
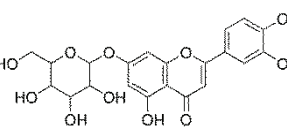
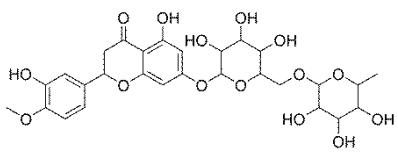
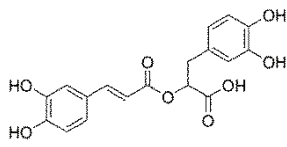
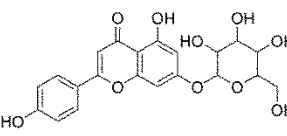
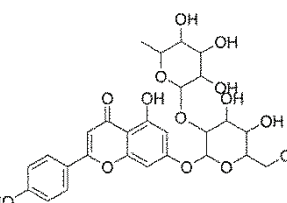
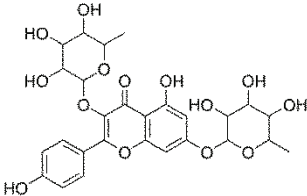
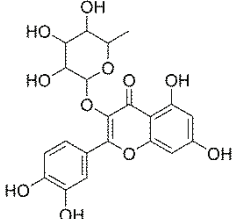
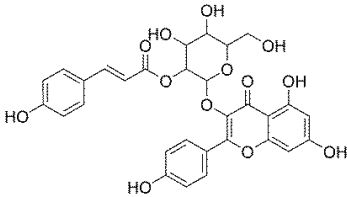
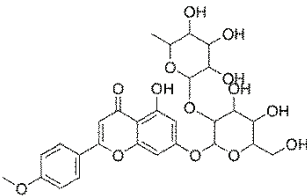
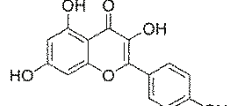
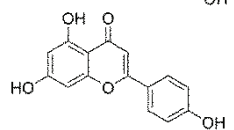
Comp. ID	Chemical structure	PubChem ID	IUPAC name (PubChem generated)
F1		137832345	6-[3,4-Dihydroxy-5-(hydroxymethyl)oxolan-2-yl]-5,7-dihydroxy-2-(4-hydroxyphenyl)-8-[3,4,5-trihydroxy-6-(hydroxymethyl)oxan-2-yl]chromen-4-one
F2		74977441	5,7-Dihydroxy-2-(4-hydroxyphenyl)-8-[3,4,5-trihydroxy-6-(hydroxymethyl)oxan-2-yl]-6-(3,4,5-trihydroxy-6-methyloxan-2-yl)chromen-4-one
F3		5291488	2-(3,4-Dihydroxyphenyl)-5-hydroxy-7-[3,4,5-trihydroxy-6-(hydroxymethyl)oxan-2-yl]oxychromen-4-one
F4		3594	5-Hydroxy-2-(3-hydroxy-4-methoxyphenyl)-7-[3,4,5-trihydroxy-6-(3,4,5-trihydroxy-6-methyloxan-2-yl)oxymethyl]oxan-2-yl]oxy-2,3-dihydrochromen-4-one
F5		5315615	3-(3,4-Dihydroxyphenyl)-2-[(E)-3-(3,4-dihydroxyphenyl)prop-2-enoyl]oxypropanoic acid
F6		5385553	5-Hydroxy-2-(4-hydroxyphenyl)-7-[3,4,5-trihydroxy-6-(hydroxymethyl)oxan-2-yl]oxychromen-4-one
F7		5459217	7-[4,5-Dihydroxy-6-(hydroxymethyl)-3-(3,4,5-trihydroxy-6-methyloxan-2-yl)oxyoxan-2-yl]oxy-5-hydroxy-2-(4-hydroxyphenyl)chromen-4-one

TABLE I. Continued

Comp. ID	Chemical structure	PubChem ID	IUPAC name (PubChem generated)
F8		12305415	5-Hydroxy-2-(4-hydroxyphenyl)-3,7-bis[(3,4,5-trihydroxy-6-methyloxan-2-yl)oxy]chromen-4-one
F9		5353915	2-(3,4-Dihydroxyphenyl)-5,7-dihydroxy-3-(3,4,5-trihydroxy-6-methyloxan-2-yl)oxychromen-4-one
F10		131752460	[2-[5,7-Dihydroxy-2-(4-hydroxyphenyl)-4-oxochromen-3-yl]oxy-4,5-dihydroxy-6-(hydroxymethyl)oxan-3-yl] (E)-3-(4-hydroxyphenyl)prop-2-enoate
F11		15559329	7-[4,5-Dihydroxy-6-(hydroxymethyl)-3-(3,4,5-trihydroxy-6-methyloxan-2-yl)oxyoxan-2-yl]oxy-5-hydroxy-2-(4-methoxyphenyl)chromen-4-one
F12		5280863	3,5,7-Trihydroxy-2-(4-hydroxyphenyl)chromen-4-one
F13		5280443	5,7-Dihydroxy-2-(4-hydroxyphenyl)chromen-4-one

this paper). The oxygen atom of the thiolactone ring is linked to Cys171 by hydrogen bonds. The binding of His311 was formed by the pi-sulfur bond on the S atom of the thiolactone ring. The bond stabilization in the enzyme *MtKasA* binding pocket was facilitated by hydrophobic interactions with amino acids Phe237, Phe404 and Pro280. This fact was in accordance with the results of a study conducted and reported by Luckner *et al.* that the catalytic triad Cys171-His311-

-His345 was the active site of the *MtKasA* binding pocket (Fig. 3).²⁵ Compounds F5 and F6 showed hydrogen bonds to the His311 amino acid. Hydrogen bonds also supported the stabilization of compound F6 in interacting with Pro280. Compound F5 has slightly lower binding energy, whereas binding of the compound to Pro280 involves hydrophobic interactions. The loss of hydrogen bonds in the catalytic triad was suspected as a reason for the lower binding energy of compounds F3, F12 and F13. Additionally, compounds F3, F12 and F13 involving hydrophobic interactions also bind to essential amino acids like Cys171, Pro280 and Phe404. This evidence was an indication that compounds F3, F12 and F13 also interact at the *MtKasA* enzyme active site.

TABLE II. Binding energy (kJ/mol) of natural flavonoid compound from *Delonix regia* leaf

ID compound	Name	Enzyme		
		<i>MtKasA</i>	<i>MtDprE1</i>	<i>MtPank</i>
TLM	Thiolactomycin	-32.22	-	-
OT4	3-(Hydroxyamino)- <i>N</i> -[(1 <i>R</i>)-1-phenylethyl]-5-(trifluoromethyl)benzamide	-	-37.66	-
ZVT	2-Chloro- <i>N</i> -[1-(5-{[2-(4-fluorophenoxy)ethyl]sulfanyl}-4-methyl-4 <i>H</i> -1,2,4-triazol-3-yl)ethyl]benzamide	-	-	-39.33
Flavonoid compounds				
F1	Apigenin-6-arabinose-8-galactose	-28.03	-33.47	-36.82
F2	Apigenin-6-rhamnose-8-glucosa	-28.87	-33.47	-34.31
F3	Luteolin-7-glucose	-35.98	-35.56	-36.82
F4	Hesperidin	-35.15	-34.31	-35.15
F5	Rosmarinate	-36.40	-33.47	-30.96
F6	Apigenin-7- <i>O</i> -glucose	-38.91	-37.66	-39.33
F7	Apigenin-7- <i>O</i> -neohespiroside	-31.38	-35.98	-32.64
F8	Lespedin	-30.96	-35.98	-31.38
F9	Quercetin-3- <i>O</i> -rhamnoside	-24.69	-33.47	-34.73
F10	2''- <i>O</i> -Trans- <i>P</i> -coumaroylastragalol	-30.54	-39.75	-39.33
F11	Fortunellin	-31.80	-34.31	-37.66
F12	Kaempferol	-35.98	-33.89	-34.31
F13	Apigenin	-35.98	-34.31	-33.05

Inhibition of the tested compounds against the *MtDprE1* enzyme was also studied. Molecular docking revealed that all analyzed compounds were potent inhibitors of the *MtDprE1* enzyme with binding energies ranging from -33.89 to -39.75 kJ/mol. Compound F10 was the tested compound with the largest binding energy of -39.75 kJ/mol, while the compound F6 produced the same binding energy as the native ligand (OT4) of -37.66 kJ/mol. In this study, we have also found that the core structure of flavonoid compounds in apigenin and kaempferol had excellent binding ability. Compounds F7 and F13 with an apigenin core structure had binding energies of -35.98 and -34.31 kJ/mol, respectively. Com-

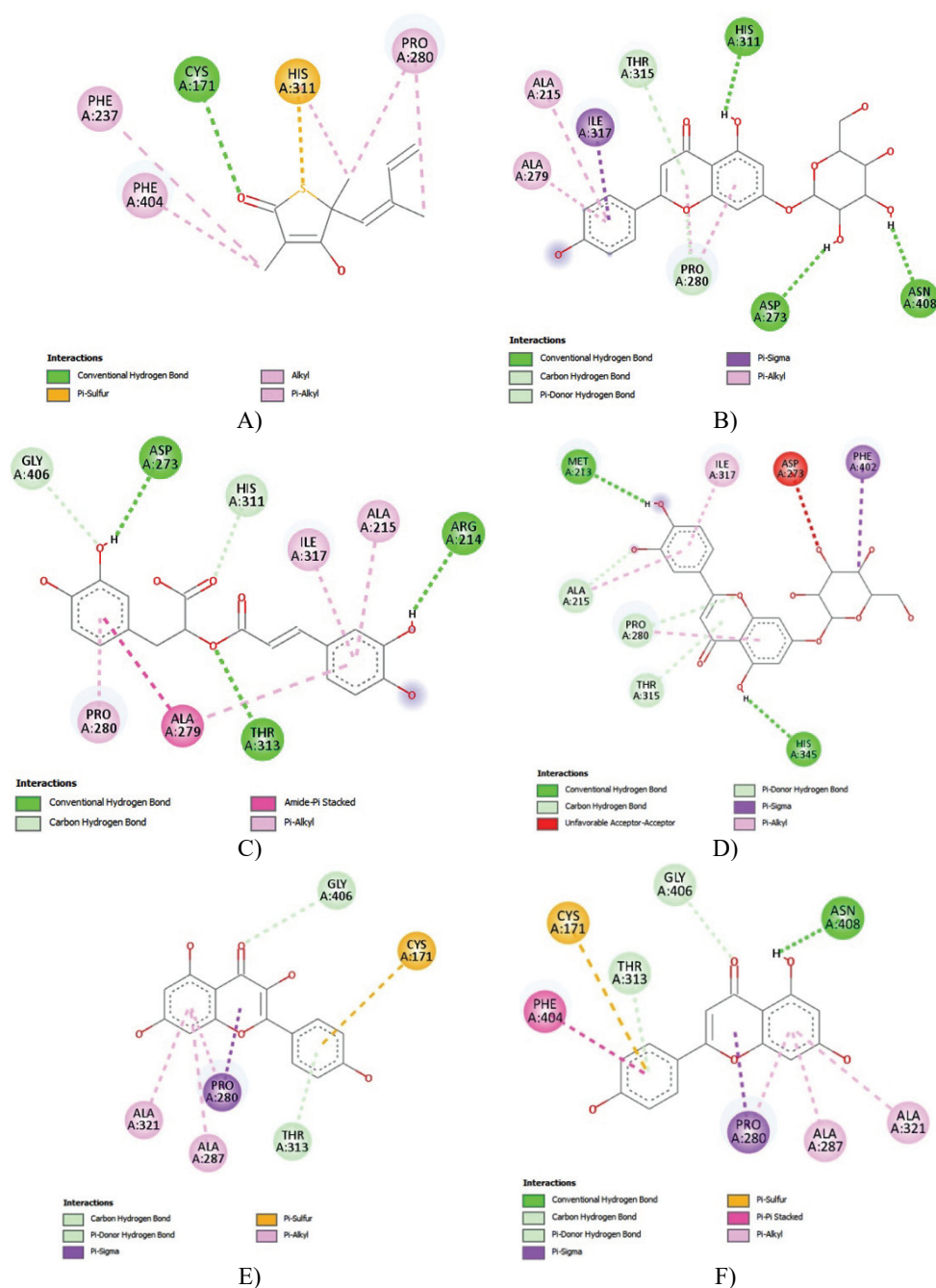


Fig. 3. Chemical interaction of *MtKasA* enzyme with: A) TLM; B) compound F6; C) compound F5; D) compound F3; E) compound F12; F) compound F13.

pounds F8 and F12, which had a kaempferol core structure, gave bond affinities of -35.98 and -33.89 kJ/mol, respectively.

The chemical interaction visualization of the tested compounds against the *MtDprE1* enzyme provided data to support data binding energy. OT4 compound as a native ligand bound several key amino acids (Table S-II of the Supplementary material). Cys387 amino acid is found in the substrate-binding domain of *MtDprE1* enzyme.²⁶ In addition, several amino acids, such as Lys134, Gly117 and Gly113, which are located in the FAD-interacting domain,⁷ were also seen in Fig. 4. Compound F10 was able to bind the amino acid Cys387 through hydrogen bonding. Lys134 and Gly117 amino acids were also bonded *via* hydrogen bonding with the compound F10. For the compound F7, adherence to Cys387 and Lys134 amino acids involved hydrophobic interactions, and the compound F13 only attached Lys134 *via* hydrogen bonding. In this case, the hydroxyl group of the rhamnoside substituent is used to bond the compound F8 to Cys387 essential amino acid. The weak binding affinity of the compound F12 was due to hydrophobic interactions attached to Cys387 amino acid, according to binding energy data.

Molecular docking studies of the tested compounds were also carried out on pantothenate kinase (*MtPank*). Binding energy data showed that all the tested compounds had excellent affinity potential for the *MtPank* enzyme, ranging from -30.96 to -39.33 kJ/mol. This study used the native ligand ZVT as a comparison ligand. The molecular docking results showed that flavonoid core structures in apigenin and kaempferol gave the most effective binding affinity, as could be seen for compounds F6 and F10 with a binding energy value of -39.33 kJ/mol. It was also revealed that compounds derived from the apigenin core structure, such as those in compounds F1 and F2 resulted in slightly lower binding energy in molecular docking results. With the *MtPank*, the compound F11 also produced a fairly significant binding affinity of -37.66 kJ/mol compared to *MtKasA* and *MtDprE1* enzymes. In accordance with the binding energy value, the compound F11 did not have the ability to bond to *MtKasA* or *MtDprE1*.

It was interesting to discuss the chemical interactions between all tested compounds and the *MtPank* enzyme. ZVT compounds as native ligands showed interactions in the *MtPank* binding pocket (Table S-III of the Supplementary material). The triazole ring of ZVT compound formed hydrogen bonds with Tyr235 and Asn277 with bond lengths of 1.94 and 2.46 Å, respectively (Fig. 5). These two amino acids were active sites for binding to pantothenate.^{9,27} Bond stabilization was also formed through binding the ZVT with Arg238 *via* hydrogen bonding. In addition, the hydrophobic interaction of ZVT with Met242 in the presence of a benzene ring also played a role in stabilizing the bonding of the ZVT–*MtPank* complex. In general, all the tested compounds showed the same inhibitory mechanism. All tested compounds were in the binding pocket and bound to

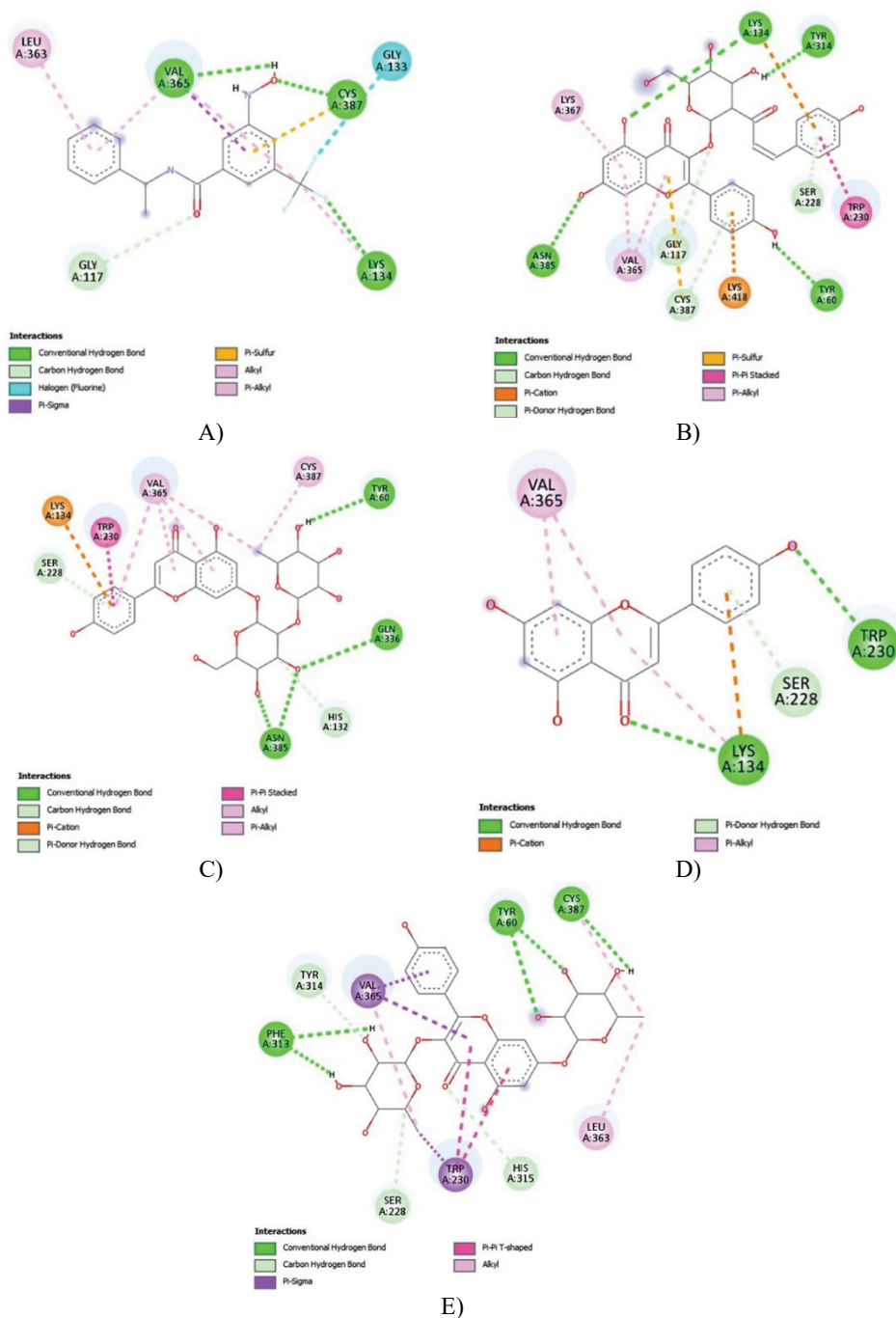


Fig 4. Chemical interaction of *MtDprE1* enzyme with: A) OT4 and compounds: B) F10, C) F7, D) F13 and E) F8.

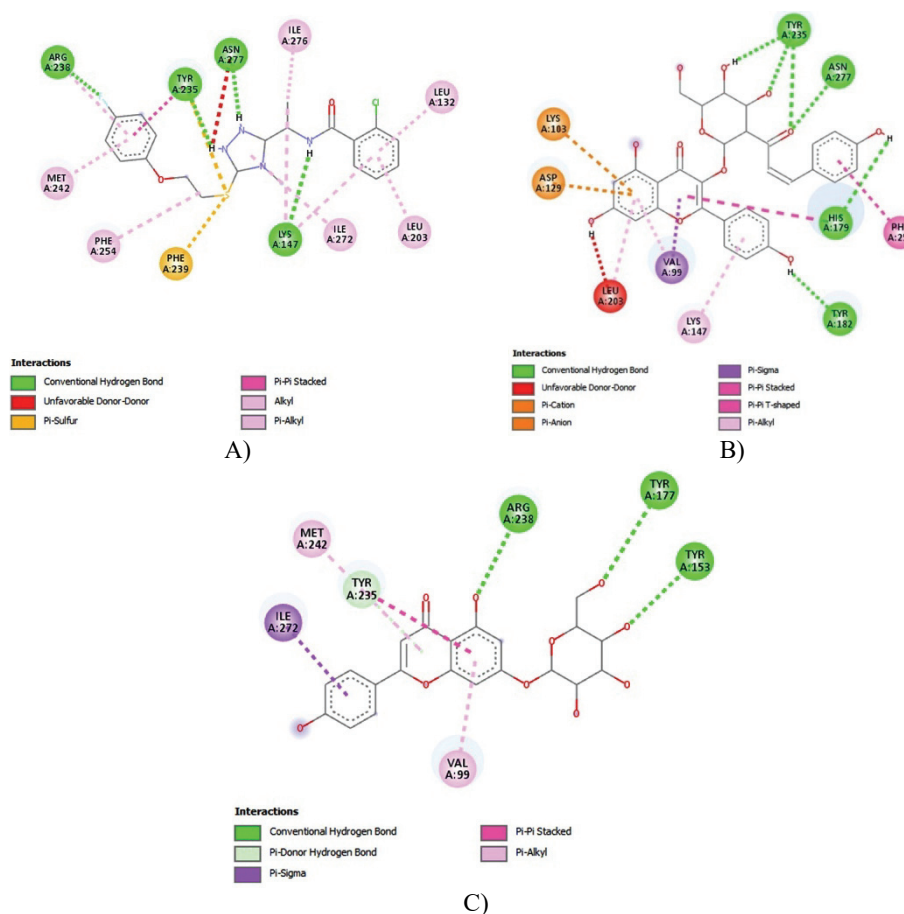


Fig 5. Chemical interaction of *MtPank* enzyme with: A) ZVT and compounds: B) F10 and C) F6.

the active site of the *MtPank* enzyme. For the compound F10, the hydroxyl group of the glucose substituent facilitated hydrogen bonding with Tyr235. In contrast, the Asn277 amino acid was bonded by the oxygen atom of the coumaroyl carbonyl group. Compound F6 only binds Tyr235 with a bond length greater than 3.87 Å, which matches the binding energy value and is slightly lower than the compound F10.

It was strongly suspected that the presence of apigenin and kaempferol as core structures contributed to the inhibition of the tested compound against the *MtPank* enzyme. This was shown by the interactions of compounds F12 and F13. Visualization of the bond between these two compounds exhibited the presence of binding to two key amino acid residues of the *MtPank* enzyme. Compounds F12 and F13 showed very effective binding to Tyr235 and Asn277. This means

that these two compounds were in the binding pocket of *MtPank* and had the same inhibitory mechanism. These molecular docking results confirm that compounds F12 and F13 were potentially active as *MtPank* enzyme inhibitors.

ADMET-Drug-likeness analysis

The pharmacokinetic properties of the tested compounds were further analyzed using pkCSM web tools to reveal their bioavailability. The results are presented in Table II. In terms of absorption, the highest absorption ability across the intestinal membrane was shown by compounds F12 and F13 with values of >80 %. Furthermore, distribution character was studied through the value of volume of distribution (*VD*), blood–brain barrier permeability (*BBB*) and central nervous system permeability (*CNS*). All of the tested compounds showed moderate (–0.15–0.45) to low (<–0.15) log *VD* values. Compounds F8, F9, F10, F11 and F13 with low log *VD* indicated that these compounds tended to be distributed in plasma. Furthermore, the *BBB* value revealed that all compounds were unable to penetrate the blood–brain barrier (<1.00).²² The same case was also shown by the *CNS* value of all tested compounds. The analysis showed that all compounds had poor absorption into the central nervous system.

TABLE II. ADMET properties of natural flavonoid compounds from *Delonix regia* leaf; metabolism not found for all compounds in cases of 2D6 and 3A4 substrates CYP and 2D6 inhibitor

ID Compd.	Intestinal absorption, %	Distribution			Metabolism for 3A4 inhibitor	Excretion, log (total clearance in mL min ⁻¹ kg ⁻¹)	AMES toxicity
		log (<i>VD</i> / L kg ⁻¹)	log <i>BBB</i>	log <i>CNS</i>			
F1	21.25	0.01	-2.87	-5.82	No	0.32	Yes
F2	30.96	0.04	-2.80	-5.79	No	0.34	Yes
F3	56.15	0.10	-1.82	-4.51	No	0.69	No
F4	38.87	0.36	-2.58	-5.18	No	0.59	Yes
F5	48.16	0.41	-1.59	-3.62	No	0.42	No
F6	41.10	0.11	-1.52	-4.03	No	0.60	No
F7	30.44	0.03	-2.33	-5.33	No	0.50	No
F8	26.98	-0.40	-1.81	-5.22	No	0.09	No
F9	60.01	-0.24	-2.11	-4.83	No	0.64	No
F10	61.35	-0.98	-1.80	-4.15	Yes	0.14	No
F11	34.94	-0.22	-2.32	-5.29	No	0.60	Yes
F12	84.79	0.01	-1.32	-2.44	Yes	0.62	Yes
F13	91.64	-0.18	-1.05	-2.25	Yes	0.67	No

Cytochrome P450 is an enzyme in charge of drug metabolism, and in this study, the isoforms used were 2D6 and 3A4. The analysis showed that only the compound F4 could act as a CYP3A4 substrate and compounds F10, F12 and F13 were inhibitors of CYP3A4. The next analysis was total clearance, a value describing the drug's ability to be metabolized in the liver and excreted through

the kidney.²⁸ The results revealed that almost all compounds had a fairly acceptable total clearance value ranging from 0.14–0.67, except for the compound F8, which had a low total clearance value (0.09). Furthermore, the toxicity properties of a drug were also a critical aspect of further drug development. The results of AMES toxicity analysis found that compounds F1, F2, F4, F11 and F12 had mutagenic and carcinogenic properties, but other compounds had the opposite properties. Thus, they had the potential to be further developed as drug candidates.

Drug-likeness evaluation of all tested compounds was then carried out and used as a screening stage based on the Lipinski rule.²⁹ Table III presents the data from the drug-likeness analysis of all tested compounds. Compounds F5, F12 and F13 did not violate the Lipinski rule. The molecular weight of the compound ($MW > 500$) indicated that the compound had poor absorption ability. Log P value described the lipophilic character and all tested compounds had a Log P value below the cut-off value (>5).

TABLE III. Drug-likeness of natural flavonoid compounds from *Delonix regia* leaf.

Compound	MW	Log P	Number of HBA	Number of HBD	$PSA \text{ \AA}^2$	Violation of Lipinski rule	Drug-likeness score
F1	564.49	-0.18	14	10	198.92	3	0.26
F2	578.16	-0.00	14	10	196.75	3	0.36
F3	448.10	0.47	11	7	151.29	2	0.60
F4	610.19	-0.81	15	8	186.70	3	0.94
F5	360.08	1.54	8	5	114.28	–	0.37
F6	432.11	0.91	10	6	135.81	1	0.59
F7	578.16	0.30	14	8	182.25	3	0.81
F8	578.16	-0.71	14	8	179.86	3	0.73
F9	448.10	0.32	11	7	150.41	2	0.82
F10	578.14	1.71	12	7	167.32	3	0.63
F11	592.18	0.82	14	7	172.17	3	0.70
F12	286.05	1.61	6	4	87.13	–	0.50
F13	270.05	3.22	5	3	73.57	–	0.39

Referring to the Lipinski rule, hydrogen bonding acceptor (HBA) must be below 10, and hydrogen bonding donor (HBD) must be below 5.³⁰ These two values were correlated with the polar surface area (PSA) value. When a compound has a violation of HBA and HBD , it tends to have low bioavailability with a PSA value greater than 140.00 \AA^2 . All the tested compounds had $HBA > 10$ and $HBD > 5$ except compounds F5, F12 and F13. For the drug-likeness score, all compounds gave a fairly acceptable value with a range of 0.26–0.94. Compound F4 had the largest drug-likeness score, namely 0.94. Unfortunately, this compound also had toxic properties based on the results of the AMES toxicity analysis. Compared with the results of ADMET analysis and drug-likeness analysis, the compound F12 had toxic properties while the compound F5 had poor ads-

orption characteristics. As a result, compound F13 as the lead compound is further investigated for its stability against all 3 enzymes.

Molecular dynamic simulation

Molecular dynamics using the CABS Flex 2.0 server was performed and provided a root mean square fluctuation (*RMSF*) graph to evaluate the stability of compound F13 key important enzymes of *M. tuberculosis* (Fig. 6). As reported by Jamroz *et al.*, *RMSF* analysis using the CABS Flex 2.0 server demonstrated significant correlation with NMR spectroscopy analysis.³¹ As shown in Fig. 6, compound F13 formed the most stable complex against the *MtKasA* enzyme. It was found that the fluctuating value of all amino acid residues was 1–3 Å.³² The F13–*MtDprE1* complex showed high fluctuations at residue numbers 17, 60, 166, 258 and 284. Meanwhile, high fluctuation levels for residue numbers 85, 248, 249, 250, 251 and 252 were found in the F13–*MtPank* complex. The high

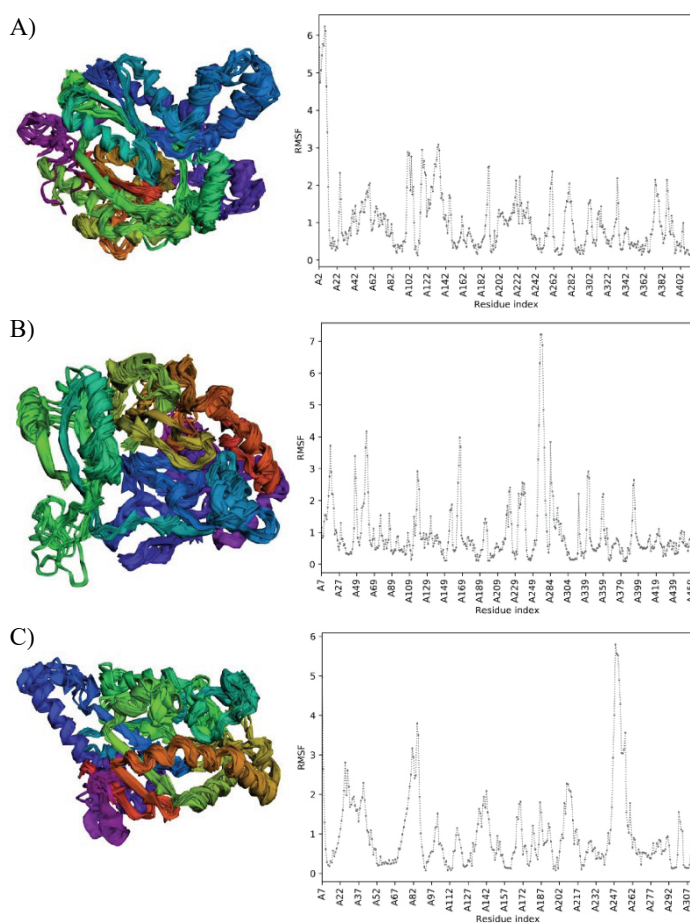


Fig 6. Multimodel and RMSF of compound F13 against: A) *MtKasA*, B) *MtDprE1* and C) *MtPank* enzymes.

fluctuating value means that the flexibility of amino acid residues is very considerable. This reduces the stability of the complex.

The results of *in silico* studies indicated that compound F13 was the most effective compound in inhibiting *M. tuberculosis* by forming a stable complex with the *MtKasA* enzyme. However, there is still a need to confirm compound F13 activity *in vitro* and *in vivo* through laboratory experiments.

CONCLUSION

In silico study of natural flavonoid compounds from *Delonix regia* leaves extract showed that all tested compounds had antimycobacterial properties, based on *in silico* analysis. ADMET and drug-likeness screening showed that among all the existing test compounds, only compound F13 had the potential to be studied further as an antimycobacterial candidate with binding energy values for *MtKasA*, *MtDprE1* and *MtPank* of -35.98 , -34.31 and -33.05 kJ/mol, respectively. The molecular dynamics simulation results suggested that compound F13 formed the most stable complex against the *MtKasA* enzyme compared to *MtDprE1* and *MtPank*.

SUPPLEMENTARY MATERIAL

Additional data and information are available electronically at the pages of journal website: <https://www.shd-pub.org.rs/index.php/JSCS/article/view/12064>, or from the corresponding author on request.

ИЗВОД

ПРИРОДНИ ФЛАВОНОИДИ У ЛИСТОВИМА *Delonix regia* КАО АНТИМИКОБАКТЕРИЈСКИ АГЕНСИ: *IN SILICO* СТУДИЈА

PUTRA JIWAMURWA RAMA TJITDA¹, FEBRI ODEL NITBANI², DOMINUS MBUNGA¹
и TUTIK DWI WAHYUNINGSIH³

¹Department of Pharmacy, Health Polytechnic of Kupang, Indonesia, ²Department of Chemistry, Faculty of Science and Engineering, Nusa Cendana University, Indonesia и ³Department of Chemistry, Faculty of Mathematics and Natural Sciences, Universitas Gadjah Mada, Indonesia

Отпорност на многоструке лекове (MDR) и екстензивна отпорност на лекове (XDR) као резултат сталне употребе антибиотика охрабрује развијање нових антимикобактеријских лекова. У овом раду је проучавано 13 флавоноидних једињења из листова биљке *Delonix regia* због њихових инхибиторних особина за *MtKasA*, *MtDprE* и *MtPank*, који су значајни ензими код *Mycobacterium tuberculosis*, као и њиховог молекулског докинга, молекулске динамике, те предвиђања ADMET сличности са лековима. Резултати студије молекулског докинга откривају да је једињење F13 (arigenin) било најпотентније једињење пошто је било у стању да веже већину аминокиселина на које указује нативни лиганд сваког ензима. Студије молекулске динамике су показале да једињење F13 формира стабилан комплекс са *MtKasA*. Из резултата ADMET-анализе сличности са лековима закључује се да је једињење F13 оно које највише обећава. Све у свему, једињење F13 има потенцијал да се користи као терапија лечења *M. tuberculosis*.

(Примљено 13. септембра, ревидирано 23. децембра 2022, прихваћено 21. јула 2023)

REFERENCES

1. World Health Organization, *Global Tuberculosis Report 2021*, https://reliefweb.int/report/world/global-tuberculosis-report-2021?gclid=CjwKCAiA_vKeBhAdEiwAFb_nrRsQtL3Ty7CYBr8PzmQTr0a4NFLirHj97ujmUL8brrzoMgEruwWxoCVmYQAvD_BwE (accessed 22th September 2022)
2. I. Rossi, R. Bettini, F. Buttini, *Curr. Pharm. Des.* **27** (2021) 1436 (<https://doi.org/10.2174/1381612827666210122143214>)
3. G. F. S. Fernandes, A. M. Thompson, D. Castagnolo, W. A. Denny, J. L. Dos Santos, *J. Med. Chem.* **65** (2022) 7489–7531 (<https://doi.org/https://pubs.acs.org/doi/10.1021/acs.jmedchem.2c00227>)
4. L. Pinzi, G. Rastelli, *Int. J. Mol. Sci.* **20** (2019) 4331 (<https://doi.org/10.3390/IJMS20184331>)
5. S. A. Mir, *J. Pharm. Res. Int.* **33** (2021) 278 (<https://doi.org/10.9734/jpri/2021/v33i45b32805>)
6. M. K. S. Siam, M. U. S. Shohan, Z. Zafroon, *bioRxiv* **4** (2020) (<https://doi.org/10.1101/2020.04.28.067090>)
7. S. M. Batt, T. Jabeen, V. Bhowruth, L. Quill, P. A. Lund, L. Eggeling, L. J. Alderwick, K. Fütterer, G. S. Besra, *Proc. Natl. Acad. Sci. U.S.A.* **109** (2012) 11354 (<https://doi.org/10.1073/pnas.1205735109>)
8. M. Brecik, I. Centárová, R. Mukherjee, G. S. Kolly, S. Huszár, A. Bobovská, E. Kilacsková, V. Mokošová, Z. Svetlíková, M. Šarkan, J. Neres, J. Korduláková, S. T. Cole, K. Mikušová, *ACS Chem. Biol.* **10** (2015) 1631 (<https://doi.org/10.1021/acscchembio.5b00237>)
9. C. Bjorkelid, T. Bergfors, A. K. V. Raichurkar, K. Mukherjee, K. Malolanarasimhan, B. Bandodkar, T. A. Jones, *J. Biol. Chem.* **288** (2013) 18260 (<https://doi.org/10.1074/jbc.M113.476473>)
10. M. C. Martini, T. Zhang, J. T. Williams, R. B. Abramovitch, P. J. Weathers, S. S. Shell, *J. Ethnopharmacol.* **262** (2020) 113191 (<https://doi.org/10.1016/J.JEP.2020.113191>)
11. D. Das, S. Das, M. Pandey, D. Bhattacharyay, *Eur. J. Med. Plants* **31** (2020) 19 (<https://doi.org/10.9734/ejmp/2020/v31i430226>)
12. A. R. Elnaas, D. Grice, J. Han, Y. Feng, A. Di Capua, T. Mak, J. A. Laureanti, G. W. Buchko, P. J. Myler, G. Cook, R. J. Quinn, M. Liu, *Molecules* **25** (2020) 2384 (<https://doi.org/10.3390/MOLECULES25102384>)
13. E. Hernández-García, A. García, E. Garza-González, F. G. Avalos-Alanís, V. M. Rivas-Galindo, J. Rodríguez-Rodríguez, V. M. Alcantar-Rosales, C. Delgadillo-Puga, M. del Rayo Camacho-Corona, *J. Ethnopharmacol.* **230** (2019) 74 (<https://doi.org/10.1016/J.JEP.2018.10.031>)
14. M. Kumar, S. Prakash, Radha, N. Kumari, A. Pundir, S. Punia, V. Saurabh, P. Choudhary, S. Changan, S. Dhumal, P. C. Pradhan, O. Alajil, S. Singh, N. Sharma, T. Ilakiya, S. Singh, & M. Mekhemar, *Antioxidants* **10** (2021) 1061 (<https://doi.org/10.3390/ANTIOX10071061>)
15. A. A. Rabaan, S. Alhumaid, H. Albayat, M. Alsaeed, F. S. Alofi, M. H. Al-Howaidi, S. A. Turkistani, S. M. Alhajri, H. E. Alahmed, A. B. Alzahrani, M. M. Mashraqi, S. Alwarthan, M. Alhajri, F. S. Alshahrani, S. A. Almuthree, R. A. Alsubki, A. A. Abuzaid, M. Alfaresi, M. A. Al Fares, A. Al Mutair, *Molecules* **27** (2022) 1 (<https://doi.org/10.3390/MOLECULES27165335>)
16. P. K. Boniface, E. I. Ferreira, *Stud. Nat. Prod. Chem.* **65** (2020) 85 (<https://doi.org/10.1016/B978-0-12-817905-5.00003-2>)

17. A. Pawar, P. Jha, M. Chopra, U. Chaudhry, D. Saluja, *Sci. Rep.* **10** (2020) 1 (<https://doi.org/10.1038/s41598-020-57658-8>)
18. Y. Liu, A. R. Fernie, T. Tohge, *Plants* **11** (2022) 564 (<https://doi.org/10.3390/PLANTS11040564>)
19. H. El-gizawy, A. Alazzouni, A. El-haddad, *Pharmacogn. Commun.* **8** (2018) 125 (<https://doi.org/https://doi.org/10.5530/pc.2018.3.26>)
20. A. Abdou, A. M. M. Abdel-Mawgoud, *Appl. Organomet. Chem.* **36** (2022) e6600 (<https://doi.org/10.1002/AOC.6600>)
21. N. Nagasundaram, K. Padmasree, S. Santhosh, N. Vinoth, N. Sedhu, A. Lalitha, *J. Mol. Struct.* **1263** (2022) 133091 (<https://doi.org/10.1016/j.molstruc.2022.133091>)
22. D. E. V. Pires, T. L. Blundell, D. B. Ascher, *J. Med. Chem.* **58** (2015) 4066 (<https://doi.org/https://pubs.acs.org/doi/10.1021/acs.jmedchem.5b00104>)
23. A. Tripathi, V. Bankaitis, *J. Mol. Med. Clin. Appl.* **2** (2018) 1 (<https://doi.org/10.16966/2575-0305.106>)
24. Y. Yuniwati, M. F. R. Syaban, S. G. Anoraga, F. L. Sabila, *Acta Inform. Medica* **30** (2022) 91 (<https://doi.org/10.5455/aim.2022.30.91-95>)
25. S. Luckner, C. Machutta, P. Tonge, C. Kisker, *Mol. Cell. Biochem.* **17** (2009) 1004 (<https://doi.org/10.1016/j.str.2009.04.012>)
26. M. T. Ali, N. Blicharska, J. A. Shilpi, V. Seidel, *Sci. Rep.* **8** (2018) 1 (<https://doi.org/10.1038/s41598-018-30209-y>)
27. B. K. K. Reddy, S. Landge, S. Ravishankar, V. Patil, V. Shinde, S. Tantry, M. Kale, A. Raichurkar, S. Menasinakai, N. V. Mudugal, A. Ambady, A. Ghosh, R. Tunduguru, P. Kaur, R. Singh, N. Kumar, S. Bharath, A. Sundaram, J. Bhat, V. K. Sambandamurthy, C. Björkelid, T. A. Jones, K. Das, B. Bhandodkar, K. Malolanarasimhan, K. Mukherjee, V. Ramachandran, *Antimicrob. Agents Chemother.* **58** (2014) 3312 (<https://doi.org/10.1128/AAC.00140-14>)
28. J. Chen, H. Yang, L. Zhu, Z. Wu, W. Li, Y. Tang, G. Liu, *Chem. Res. Toxicol.* **33** (2020) 640 (<https://doi.org/10.1021/acs.chemrestox.9b00447>)
29. D. Machado, M. Girardini, M. Viveiros, M. Pieroni, *Front. Microbiol.* **9** (2018) 1 (<https://doi.org/10.3389/fmicb.2018.01367>)
30. A. Abdou, H. M. Mostafa, A. M. M. Abdel-Mawgoud, *Inorg. Chim. Acta* **539** (2022) 121043 (<https://doi.org/10.1016/J.ICA.2022.121043>)
31. M. Jamroz, A. Kolinski, S. Kmiecik, *Bioinformatics* **30** (2014) 2150 (<https://doi.org/10.1093/bioinformatics/btu184>)
32. R. R. Renantha, A. R. Liga, C. B. Tanugroho, L. X. Denovian, S. L. Az, Z. Budiyanto, A. A. Parikesit, *J. Pharm. Pharmacogn. Res.* **10** (2022) 660 (https://doi.org/https://doi.org/10.56499/jppres22.1375_10.4.660).

SUPPLEMENTARY MATERIAL TO
Natural flavonoids in *Delonix regia* leaf as an antimycobacterial agent: An *in silico* study

PUTRA JIWAMURWA PAMA TJITDA^{1*}, FEBRI ODEL NITBANI², DOMINUS MBUNGA¹ and TUTIK DWI WAHYUNINGSIH³

¹Department of Pharmacy, Health Polytechnic of Kupang, Indonesia, ²Department of Chemistry, Faculty of Sains and Engineering, Nusa Cendana University, Indonesia and

³Department of Chemistry, Faculty of Mathematics and Natural Sciences, Universitas Gadjah Mada, Indonesia

J. Serb. Chem. Soc. 88 (9) (2023) 859–876

TABLE S-I. Chemical Interaction of natural flavonoid against *MtKasA*

Id compound	Interaction	
	Amino acid and type bond	Distance of hydrogen bond (Å)
TLM	Cys171 (HB), His311, Pro280, Phe237, Phe404 Flavonoid compounds	3.54
F1	Pro316 (HB), Val278 (HB), Thr313 (HB), Thr315 (HB), Pro280 (HB), His276 (HB)	3.37, 3.26, 2.62, 2.39, 3.54, 2.89
F2	Arg214 (HB); Met213 (HB); Met212 (HB)	3.02, 2.78, 2.31
F3	Thr315 (HB), Pro280 (HB), Ala215 (HB), Met213 (HB), His345 (HB)	4.12, 3.75, 3.50, 2.89, 2.72
F4	Phe402 (HB), Ala215 (HB), Met213 (HB), Pro280 (HB), Ile317 (HB), Cys171, His311, Phe404,	3.43, 3.23, 2.28, 2.17, 2.92
F5	Gly406 (HB), Asp273 (HB), His311 (HB), Arg214 (HB), Thr313 (HB), Pro280	3.45, 2.50, 3.27, 2.56, 3.10
F6	Thr315 (HB), His311 (HB), Asn408 (HB), Asp273 (HB), Pro280 (HB)	4.13, 2.30, 2.33, 2.67, 3.51
F7	Thr315 (HB), Ala215 (HB), His276 (HB), Pro280	4.14, 3.53, 3.43
F8	Thr315 (HB), Thr313 (HB), Gly318 (HB), Pro280, Phe404	2.26, 2.92, 3.70
F9	Met213 (HB)	2.56
F10	Arg214 (HB), Thr315 (HB), Pro280, Phe404	2.36, 3.99
F11	Ala215 (HB), Met213 (HB), Pro280, His311	3.70, 2.56
F12	Gly406 (HB), Thr313 (HB), Cys171, Pro280	3.31, 4.05
F13	Thr313 (HB), Gly406 (HB), Asn408 (HB), Cys171, Pro280, Phe404	4.06, 3.27, 1.55

*Corresponding author. E-mail: putrachemist_jc@yahoo.com

*HB = Hydrogen Bond

TABLE S-II. Chemical Interaction of natural flavonoid against *MtDprE1*

Id compound	Interaction	
	Amino acid and type bond	Distance of hydrogen bond (Å)
0T4	Val365 (HB), Cys387 (HB), Lys134 (HB), Gly117 (HB), Leu363, Gly133 Flavonoid compounds	2.49, 3.22, 2.98, 3.73
F1	Ser246 (HB), Ser228 (HB), Tyr314 (HB), Lys134, Val365	3.71, 3.29, 2.20
F2	Ser228 (HB), Tyr60 (HB), Asn385 (HB), Val365	2.31, 2.63, 2.86
F3	Ser228 (HB), His132 (HB), Gln336 (HB), Tyr60 (HB), Cys387 (HB), Lys134, Val365	3.66, 2.76, 2.76, 2.85, 3.68
F4	Trp230 (HB), Ser228 (HB), Lys134 (HB), Gly133 (HB), Pro116 (HB), His132 (HB), Tyr60 (HB), Cys387 (HB), Val365	3.02, 3.40, 3.20, 3.21, 3.35, 2.37, 3.10, 3.53
F5	Gly117 (HB), Tyr314 (HB), Ser228 (HB), His132 (HB), Gln336 (HB), Val365, Cys387, Lys134, Gly133	3.17, 2.05, 3.03, 2.27, 2.47
F6	Trp230 (HB), Lys134 (HB), Tyr60 (HB), Asp389 (HB), Ser228 (HB), Val365	3.04, 3.26, 2.79, 3.71, 3.32
F7	Ser228 (HB), Tyr60 (HB), Gln336 (HB), Asn385 (HB), Val365, Lys134, Cys387	3.35, 2.85, 3.28, 2.62
F8	Phe313 (HB), Thr314 (HB), Tyr60 (HB), Cys387 (HB), His315 (HB), Ser228 (HB), Val365, Leu363	2.42, 2.94, 2.83, 2.35, 3.76, 3.21
F9	Asn385 (HB), His315 (HB), Gly117 (HB), Ser228 (HB), His132 (HB), Val365, Lys134, Cys387, Leu363	2.89, 2.55, 2.73, 2.88, 2.56
F10	Asn385 (HB), Lys134 (HB), Tyr314 (HB), Ser228 (HB), Tyr60 (HB), Cys387 (HB), Gly117 (HB), Val365	2.80, 2.94, 2.39, 3.13, 2.89, 4.14, 3.10
F11	Gln336 (HB), Asn385 (HB), Cys387 (HB), His132 (HB), Tyr60 (HB), Val365, Leu363	2.80, 3.07, 3.37, 3.06, 2.43
F12	Lys418 (HB), His132 (HB), Ser228 (HB), Val365, Cys387, Lys134,	3.31, 2.70, 3.58
F13	Lys134 (HB), Ser228 (HB), Trp230 (HB), Val365	3.11, 3.48, 3.08

*HB = Hydrogen Bond

Table S-III. Chemical Interaction of natural flavonoid against *MtPank*

Id compound	Interaction	
	Amino acid and type bond	Distance of hydrogen bond (Å)
ZVT	Arg238 (HB), Tyr235 (HB), Asn277 (HB), Lys147 (HB), Met242, Phe254, Phe239, Ile272, Leu203, Leu132, Ile276	3.13, 1.94, 2.46, 2.74
F1	Flavonoid compounds Tyr182 (HB), Tyr235 (HB), Asn277 (HB), Lys147 (HB), Phe254, Ile272	4.11, 3.80, 2.46, 2.98
F2	Tyr257 (HB), Tyr182 (HB), Lys147 (HB), Tyr153 (HB), His179 (HB), Tyr235 (HB), Phe254, Ile272, Ile276	3.17, 3.98, 2.14, 2.29, 2.41, 3.14
F3	Tyr235 (HB), Tyr153 (HB), Ile272, Phe254, Met242	3.86, 2.42
F4	Glu201 (HB), Gly148 (HB), Asn277 (HB), Tyr182 (HB), Tyr235 (HB), His179 (HB), Leu203, Met242	3.46, 3.54, 2.74, 3.54, 3.73, 2.87
F5	Asn277 (HB), Tyr235 (HB)	2.55, 2.29
F6	Tyr235 (HB), Arg238 (HB), Tyr177 (HB), Tyr153 (HB), Ile272, Met242	3.87, 3.21, 3.06, 3.10
F7	Asp129 (HB), Gly148 (HB), Asn277 (HB), Lys103 (HB), Leu203, Leu132	2.63, 3.58, 2.34, 3.39
F8	Tyr235 (HB), Met242 (HB), Tyr153 (HB), Lys103 (HB), Lys147 (HB), Ile272, Ile276, Leu203 (HB), Asp129 (HB), Tyr182 (HB), Phe239, Lys147	3.13, 2.77, 2.11, 3.13, 2.34
F9	Tyr235 (HB), Asn277 (HB), His179 (HB), Tyr182 (HB), Lys147, Phe254	2.97, 2.81, 2.15, 2.49
F10	Tyr235 (HB), His179 (HB), Tyr182 (HB), Glu201 (HB), Phe254, Ile272, Met242, Leu203	3.90, 2.62, 3.04, 2.75
F11	Tyr153 (HB), Tyr235 (HB), Asn277 (HB), Lys147	2.38, 2.25, 3.16
F12	Tyr153 (HB), Asn277 (HB), Tyr235 (HB), Lys147	2.48, 3.08, 2.64
F13		

*HB = Hydrogen Bond



J. Serb. Chem. Soc. 88 (9) 877–888 (2023)
JSCS–5668

Binuclear azide-bridged hydrazone Cu(II) complex: Synthesis, characterization and evaluation of biological activity

TEODORA VITOMIROV¹, BOŽIDAR ČOBELJIĆ^{1#}, ANDREJ PEVEC², DUŠANKA RADANOVIĆ³, IRENA NOVAKOVIĆ^{3#}, MILICA SAVIĆ³, KATARINA ANĐELKOVIĆ^{1#} and MAJA ŠUMAR-RISTOVIĆ^{1#*}

¹University of Belgrade – Faculty of Chemistry, Studentski trg 12–16, 11000 Belgrade, Serbia, ²Faculty of Chemistry and Chemical Technology, University of Ljubljana, Večna pot 113, 1000 Ljubljana, Slovenia and ³University of Belgrade, Institute of Chemistry, Technology and Metallurgy, Department of Chemistry, Njegoševa 12, 11000 Belgrade, Serbia

(Received 23 June, revised 27 June, accepted 21 July 2023)

Abstract: The condensation product of 7-acetyl-6-azaindole and Girard's T reagent ((*E*)-2-(2-(1-(1*H*-pyrrolo[2,3-*c*]pyridin-7-yl)ethylidene)hydrazineyl)-*N,N,N*-trimethyl-2-oxoethan-1-aminium, **HL** ligand) was used as a ligand in the reaction with Cu(BF₄)₂·6H₂O and NaN₃. The reaction led to the formation of a binuclear Cu(II) complex containing two end-to-end (di-μ-_{1,3}-N₃) azide bridges, as well as two NNO-donor hydrazone ligands, forming an axially elongated square pyramidal geometry around each Cu(II) center. This end-to-end (di-μ-_{1,3}-N₃) azide bridge binding mode has not yet been reported, in Cu(II) complexes containing the NNO-donor hydrazone ligands, which makes the structure of the complex even more interesting for further studies. The complex was characterized by elemental analysis, IR spectroscopy and X-ray crystallography, and it was found that it crystallizes in the triclinic space group P-1 with the asymmetric unit comprising one Cu(II) centre, zwitterionic ligand **L**, one azide (N₃⁻) ligand and BF₄⁻ counter anion. Examination of antimicrobial activity of the complex shows higher antifungal and antibacterial activity towards tested Gram-positive bacteria in comparison to the hydrazone ligand, with the antifungal activity of the complex even being comparable to the activity of amphotericin B.

Keywords: Girard's T reagent; X-ray crystallography; antibacterial activity; antifungal activity.

INTRODUCTION

Azide-bridged binuclear copper(II) complexes have been the subject of considerable research in the field of coordination chemistry due to their interesting

* Corresponding author. E-mail: majas@chem.bg.ac.rs

Serbian Chemical Society member.

<https://doi.org/10.2298/JSC230623044V>



structural and magnetic properties.^{1–3} These complexes consist of two copper(II) ions bridged by an azide group *via* either end-on (EO) or end-to-end (EE) coordination mode, forming single or double ligand bridges: $\mu_{1,1}$ -N₃ (EO) and $\mu_{1,3}$ -N₃ (EE).⁴

The azide group provides a unique building block for the construction of complex architectures and is a versatile bridging ligand that can adopt different coordination modes, such as mono-, bi- or tri-dentate,¹ depending on the nature of the metal ion and the reaction conditions. Furthermore, it also acts as a strong magnetic coupler facilitating ferromagnetic and antiferromagnetic coupling between metal ions within a binuclear complex.² On the other hand, the binuclear copper(II) complexes are known to exhibit either antiferromagnetic or ferromagnetic behavior, depending on the nature of the bridging ligand, the Cu–X–Cu angle and the geometry of the complex.^{3,5–9}

In recent years, there has been growing interest in the biological activity of binuclear copper(II) complexes due to their potential applications as anticancer^{10,11} and antibacterial^{12–14} agents. The ability of these complexes to catalyze the formation of reactive oxygen species (ROS) and to interact with DNA and proteins makes them attractive candidates for the development of new therapeutic agents. When discussing the azide-bridged binuclear Cu(II) complexes, several studies have reported the potential antibacterial activity of these complexes, all containing a tridentate NNO-donor hydrazone ligand, against various strains of bacteria.^{10,15,16} The mechanism of action is believed to be the disruption of the bacterial cell membrane due to the reduced polarity of the metal ion and increased lipophilicity of the formed complex, compared to lone metal ions and ligands.¹⁷

In addition to their biological applications, azide-bridged binuclear copper(II) complexes have also shown promising catalytic properties under sustainable and user-friendly conditions. These complexes have been reported to exhibit catalytic activity towards various reactions, including the N-arylation of imidazole and benzimidazole¹⁸ as well as the synthesis of 1,2,3-triazoles.¹⁹ The catalytic activity of these complexes is attributed to the redox properties of copper(II) ions and the Cu–N₃–Cu bridge, which can facilitate electron transfer processes.

In this study, we have synthesized and fully characterized a new binuclear copper(II) complex containing double end-to-end ($\text{di-}\mu_{1,3}$ -N₃) azide bridge, along with NNO-donor hydrazone ligands, and investigated its antibacterial and antifungal activities. The results of our study provide a detailed characterization of a binuclear copper(II) complex, as well as an overview of the potential of this complex as a new therapeutic agent.

EXPERIMENTAL

Materials and methods

All chemicals and solvents (reagent grade) were obtained from commercial suppliers (NaN₃ from Riedel-de-Haën; all other chemicals from Sigma–Aldrich) and used without further purification. Elemental analyses (C, H and N) were performed by standard micro-methods using the Elementar Vario ELIII C.H.N.S.O analyzer. IR spectra were recorded on a Nicolet 6700 FT-IR spectrometer using the ATR technique from 4000–400 cm⁻¹ (strong – *s*, medium – *m*, weak – *w*). NMR spectra were recorded with a Varian 400/54 PS spectrometer in deuterated dimethyl sulfoxide (DMSO-*d*₆).

Ligand synthesis

The ligand synthesis was carried out in two steps – the first step was obtaining 7-acetyl-6-azaindole using 7-bromo-6-azaindole as a starting compound. The reaction was performed by adding 0.75 mmol (18.2 mg) of Mg to 0.75 mmol (147 mg) of 7-bromo-6-azaindole in anhydrous diethyl ether and making a Grignard's reagent, which then reacted with equimolar amount (0.75 mmol, 58.9 mg) of acetyl chloride and a small amount (2 mol %) of FeCl₃ as a catalyst. This reaction was carried out at –60 °C using dry ice as a cooling bath.

The next step was to synthesize the condensation product of 7-acetyl-6-azaindole and Girard's T reagent, ((*E*)-2-(2-(1-(1*H*-pyrrolo[2,3-*c*]pyridin-7-yl)ethylidene)hydrazineyl)-*N,N,N*-trimethyl-2-oxoethan-1-aminium). The reaction was carried out by dissolving 0.5 mmol (80 mg) of 7-acetyl-6-azaindole in methanol and adding 0.5 mmol (83.8 mg) of Girard's T reagent to the reaction mixture, which was then refluxed for 3 h. After cooling down to room temperature, the bright yellow precipitate was filtered and rinsed with ethanol. The reaction yield was 81 % (125.2 mg) and the ligand was then characterized by elemental analysis, IR and NMR spectroscopy. Labelling of C and H atoms described by NMR spectroscopy is presented in Fig. 1.

Complex synthesis

The synthesis of the complex was performed by dissolving 0.25 mmol (77.3 mg) of ligand in 20 mL of methanol and then adding 0.25 mmol (86.3 mg) of Cu(BF₄)₂·6H₂O, previously dissolved in 5 mL of H₂O, and 1 mmol (65 mg) of NaN₃ directly into the reaction mixture. The mixture was refluxed for 2 h, and after 10 days dark green monocrystals of complex were obtained and filtered from the solution. The reaction yield was 73 % (169.6 mg) and the complex was characterized by elemental analysis, IR spectroscopy and X-Ray crystallography.

Analytical and spectral data of the ligand and the complex are given in Supplementary material to this paper.

X-Ray structure determination

The crystal structure of compound [Cu₂L₂(μ_{1,3}-N₃)₂](BF₄)₂ was determined by single-crystal X-ray diffraction methods. Crystallographic data and refinement details are given in Table I. Diffraction data were collected with Agilent SuperNova dual source diffractometer using an Atlas detector and equipped with mirror-monochromated MoKα radiation (λ = 0.71073 Å). The data were processed by using CrysAlis PRO.²⁰ The structure was solved using SIR-92²¹ and refined against *F*² on all data by full-matrix least-squares with SHELXL-2016.²² All non-hydrogen atoms were refined anisotropically. The nitrogen N2 bonded hydrogen atom was located in the difference map and refined with the distance restraints (DFIX) with *d*(N–H) = 0.86 Å and with *U*_{iso}(H) = 1.2*U*_{eq}(N). All other hydrogen atoms were included

in the model at geometrically calculated positions and refined using a riding model. The F4 fluorine atom in BF_4^- is disordered over two orientations and was refined with the use of PART instruction. The occupancy of F4a and F4b refined to the ratio of 55 and 45 %, respectively. CCDC 2271001 contains the supplementary crystallographic data for this paper. These data can be obtained free of charge from The Cambridge Crystallographic Data Centre via www.ccdc.cam.ac.uk/data_request/cif.

TABLE I. Crystal data and structure refinement details for $[\text{Cu}_2\text{L}_2(\mu_{1,3}\text{-N}_3)_2](\text{BF}_4)_2$

Formula	$\text{C}_{28}\text{H}_{38}\text{B}_2\text{Cu}_2\text{F}_8\text{N}_{16}\text{O}_2$
$F_w / \text{g mol}^{-1}$	931.44
Crystal size, mm	0.50×0.40×0.10
Crystal color	green
Crystal system	triclinic
Space group	$P\bar{1}$
$a / \text{Å}$	7.8476(3)
$b / \text{Å}$	9.8765(6)
$c / \text{Å}$	13.2990(9)
$\alpha / ^\circ$	110.341(6)
$\beta / ^\circ$	103.742(5)
$\gamma / ^\circ$	92.524(4)
$V / \text{Å}^3$	929.70(10)
Z	1
Calcd. density, g cm^{-3}	1.664
$F(000)$	474
No. of collected reflns	8891
No. of independent reflns	4259
R_{int}	0.0430
No. of reflns observed	3639
No. parameters	279
$R[I > 2\sigma(I)]^a$	0.0595
wR_2 (all data) ^b	0.1815
Goof, S^c	1.051
$\Delta\rho_{\text{max}}/\Delta\rho_{\text{min}}$ (eÅ^3)	+0.88/−0.80

^a $R = \sum||F_o| - |F_c||/\sum|F_o|$; ^b $wR_2 = \{\sum[w(F_o^2 - F_c^2)^2]/\sum[w(F_o^2)^2]\}^{1/2}$; ^c $S = \{\sum[(F_o^2 - F_c^2)^2]/(n/p)\}^{1/2}$, where n is the number of reflections and p is the total number of parameters refined

Antimicrobial activity

In vitro antibacterial and antifungal activity was tested against four Gram-positive bacteria (*Bacillus subtilis* ATCC 6633, *Clostridium sporogenes* ATCC 19404, *Kocuria rhizophila* ATCC 9341, *Staphylococcus aureus* ATCC 6538), four Gram-negative bacteria (*Proteus hauseri* ATCC 13315, *Escherichia coli* ATCC 25922, *Pseudomonas aeruginosa* ATCC 9027, *Salmonella enterica* ATCC 13076), and three fungal strains (*Aspergillus brasiliensis* ATCC16404, *Candida albicans* ATCC 10231, *Saccharomyces cerevisiae* ATCC 9763), by the double dilution method in microtiter plates.²³ Antibacterial activity was determined using Mueller–Hinton broth, whereas antifungal activity was determined using Sabouraud dextrose broth. One hundred microliters of fresh Mueller–Hinton or Sabouraud dextrose broth were added to each well of the plate. Then, 100 μL of the compounds stock solution (10 mg/mL) prepared by dissolving compounds in DMSO was added. Each well was inoculated with 10

μL (10^6 cells per mL) of bacterial cultures and $10 \mu\text{L}$ (10^5 spores per mL) of fungal strains for antibacterial and antifungal determination, respectively. Bacterial strains were incubated at 37°C for 24 h. Erythromycin was used as a positive control, while water served as a negative control. Fungal strains were incubated at 28°C for 48 h. Amphotericin B was used as a positive control, while DMSO was used as a negative control. The bacterial growth was visualized by adding $20 \mu\text{L}$ of 0.5 % 2,3,5-triphenyltetrazolium chloride (TTC) aqueous solution.²⁴ The MIC was determined as the lowest concentration that resulted in inhibition of visible microbial growth.

The brine shrimp test

The brine shrimp test was performed against freshly hatched nauplii of *Artemia salina*.²⁵ The compounds were dissolved in DMSO and various amounts (0.01–1 mg) were added to artificial sea water containing 10–20 nauplii. After 24 h illumination at room temperature, the number of dead and surviving nauplii were counted and statistically analyzed. All samples were tested in triplicate. LC_{50} was defined as concentration of compounds that caused the death of 50 % of nauplii.

Assessment of radical-scavenging activity

Antioxidative activity of initial Cu(II) salt, appropriate ligand and the synthesized complex was determined using a 2,2-diphenyl-1-picrylhydrazyl (DPPH) free radical scavenging assay. All tested compounds were dissolved in DMSO (stock concentrations were 10 mg/mL). For each tested compound, two rows of the 96-well microplate were used: one for measuring the absorbance of the compounds themselves and the other for antioxidant activity. $50 \mu\text{L}$ of stock solutions of tested compounds were loaded into plate and double diluted by using multi-channel pipette. The rows used to measure the absorbance of the compounds were supplemented with $100 \mu\text{L}$ of pure methanol, while the other rows were supplemented with $100 \mu\text{L}$ of freshly prepared methanolic DPPH solution (6.58×10^{-5} M). In the control, $50 \mu\text{L}$ pure DMSO was loaded. Final concentrations of the compounds ranged from (0.5 mg per well) to (2.4×10^{-4} mg per well). After 30 min of incubation at 37°C in the dark, the absorption was measured at 517 nm. All measurements were done in triplicate. Free radical scavenging activity of compounds was measured using the equation:

$$\text{Activity} = \frac{100(A_{\text{control}} - (A_{\text{sample}} - A_0))}{A_{\text{control}}} \quad (1)$$

where A_{control} is the absorbance of DPPH in the control probe, A_{sample} is the absorbance of DPPH in the samples, and A_0 is the absorbance of solutions of complexes 1 and 2 in DMSO, due to their intensive green colors. IC_{50} is defined as the concentration of antioxidant agent necessary to reduce the starting amount of DPPH by 50 % and is calculated from the concentration-dependent free radical scavenging activity graph. Ascorbic acid was used as a control probe.

RESULTS AND DISCUSSION

The ligand synthesis was carried out in two steps, as presented in Fig. 1. After acetylation of 7-bromo-6-azaindole, the obtained 7-acetyl-6-azaindole reacted with Girard's T reagent in a mole ratio 1:1 and the ligand was formed. The complex was then obtained in the reaction of $\text{Cu}(\text{BF}_4)_2 \cdot 6\text{H}_2\text{O}$, ligand and NaN_3 in a mole ratio 1:1:4, as described in Fig. 2.

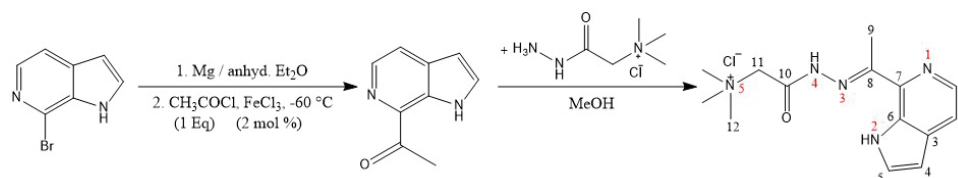


Fig. 1. Step by step ligand synthesis.

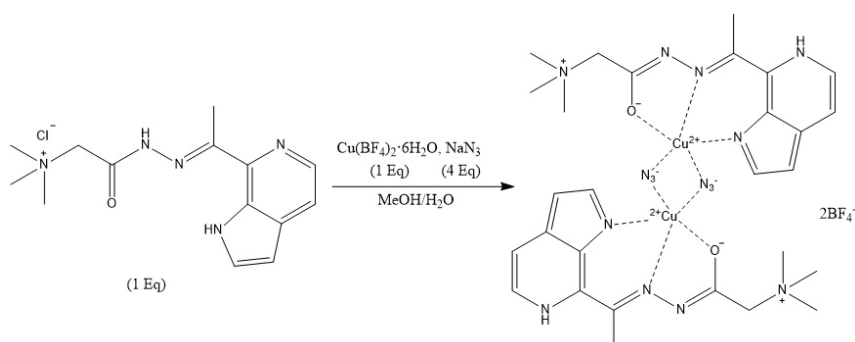


Fig. 2. Complex synthesis.

IR spectra

IR spectroscopy confirmed the coordination of the ligand *via* the pyrrole nitrogen of 7-acetyl-6-azaindole ring. The stretching vibrational mode of the N–H group appears in the IR spectrum of the ligand as a wide band at 3377.4 cm^{-1} and disappears in the spectrum of the complex. The ligand spectrum also shows a very intense band at 1703.4 cm^{-1} , corresponding to the C=O stretching vibration of the carbonyl group. This peak does not appear in the spectrum of the complex, instead, an intense peak appears at 1034.8 cm^{-1} , coming from the C–O stretching vibration. These all indicate the delocalization of the electron pair of the carbonyl group towards oxygen, which then favors the coordination of the ligand *via* the now negatively charged oxygen atom. The strong band appearing in the IR spectrum of the complex at 2063.4 cm^{-1} points out the presence of the N_3^- group in the complex structure.

X-ray crystal structure determination

Complex crystallizes in the triclinic space group $P\bar{1}$, with the asymmetric unit comprising one Cu(II) centre, zwitterionic ligand **L**, one azide (N_3^-) ligand and BF_4^- counter anion. The crystal structure displays a centrosymmetric binuclear complex with the crystallographically independent Cu1 centre being coordinated to three donor atoms (N1, N3 and O1) of **L** and two N atoms (N6 and N8^{*a*} where $a = -x, -y, -z+1$) from two azide ligands which bridge two Cu(II) centres by adopting a double end-to-end ($\text{di-}\mu\text{-}_{1,3}\text{-N}_3$) coordination mode. The

Cu1...Cu1^a separation is 4.8232(6) Å. The molecular structure of the dimeric cationic moiety in the [Cu₂L₂(μ_{1,3}-N₃)₂](BF₄)₂ complex and the atom-labelling scheme are shown in Fig. 3. Selected bond lengths and angles for the structure are given in Table S-I of the Supplementary material to this paper. The coordination polyhedron around Cu(II) is described as an axially elongated square pyramid with an index of trigonality (τ_5)²⁶ of 0.05 ($\tau_5 = (\beta - \alpha)/60$, where β and α are the two largest angles around the central atom). The τ_5 is 0 for regular square based pyramidal geometry and 1.00 for regular trigonal bipyramidal geometry. The four in-plane bond distances are: Cu1–N1 1.972(3), Cu1–N3 1.975(3), Cu1–O1 1.930(3) and Cu1–N6 1.957(3) Å, and the apical distance Cu1–N8^a (symmetry code $a = -x, -y, -z + 1$) is 2.426(4) Å. The azide anion bridges in an asymmetric (basal-apical) fashion so that the in-plane and axial Cu–N(N₃[−]) bond distances are significantly different. The tridentate NNO coordination of L to Cu(II) ion generates one six-membered chelate ring (Cu–N–C–C–C–N) and one five-membered chelate ring (Cu–N–N–C–O) fused along the Cu1–N3 bond. The chelate rings are non-coplanar, as indicated by the dihedral angle of 3.8 Å. In this complex the Cu–N_{Ar} and Cu–N_{imine} bonds are comparable in length (Cu1–N1 1.972(3) and Cu1–N3 1.975(3) Å, respectively). However, in Cu(II) complexes with two fused five-membered chelate rings generated by chelation of tridentate NNO donor hydrazone ligands the Cu–N_{Ar} bonds are longer than the Cu–N_{imine} bonds.^{27,28} Complex cations and BF₄[−] generate a three-dimensional structure by means of intermolecular N–H...F, C–H...F and C–H...N hydrogen bonds given in Table S-II of the Supplementary material. In addition, the complex cations are connected by means of intermolecular π ... π bonds extending in [110] direction (Table S-III and Fig. S-1 of the Supplementary material).

A search of the Cambridge Structural Database (CSD)²⁹ for the binuclear Cu(II)-azido complexes with hydrazone-based NNO-donor ligands revealed 12 crystal structures with double end-on (di-μ_{1,1}-N₃) coordination mode of bridging azide anions. No crystal structure of binuclear Cu(II)-azido complex with tridentate NNO-donor hydrazone ligand having double end-to-end (di-μ_{1,3}-N₃) coordination mode of bridging azides has been observed. The structure presented here is the first case. Details of CSD search are given in Table S-IV of the Supplementary material.

Crystallographic programs ORTEP-3 for Windows³⁰ and Mercury³¹ were used to prepare the drawings.

Antimicrobial activity

Antimicrobial activity of the complex and the starting compounds (Cu(BF₄)₂·6H₂O and the ligand) was studied in DMSO solution by examining their minimum inhibitory concentration (MIC) on Gram-positive and Gram-negative bacteria and fungal strains. Erythromycin and amphotericin B were used as the

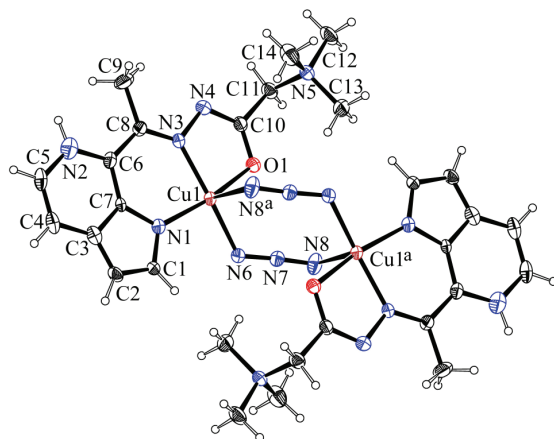


Fig. 3. ORTEP presentation of the complex cation $[\text{Cu}_2\text{L}_2(\mu_{1,3}\text{-N}_3)_2]^{2+}$ in $[\text{Cu}_2\text{L}_2(\mu_{1,3}\text{-N}_3)_2](\text{BF}_4)_2$. Thermal ellipsoids are drawn at the 30 % probability level. The unlabeled part of the dimeric molecule is generated by symmetry operation $-x, -y, -z+1$.

standard drugs to compare the minimum inhibitory concentration values and the results are presented in Table II. Comparing the activities of the complex and the ligand itself, the complex was shown to have higher antibacterial activity against all tested Gram-positive bacteria and half of the tested Gram-negative bacteria. The most significant difference between the antimicrobial activities of the complex and the ligand is the one against *S. aureus*, where the activity of the complex is 3 times higher than that of the ligand alone. The antifungal activities of the complex are significantly higher than those of the ligand, especially in the case of *S. cerevisiae*, where the antifungal activity of the complex is even comparable to the activity of amphotericin B.

TABLE II. Antimicrobial activity of the complex and the starting compounds (*MIC* values in mM)

Microorganism	Complex	Ligand	$\text{Cu}(\text{BF}_4)_2 \cdot 6\text{H}_2\text{O}$	Standard ^{a,b}
<i>E. coli</i>	0.671	1.011	1.821	0.038
<i>P. aeruginosa</i>	0.671	1.011	3.642	0.076
<i>P. hauseri</i>	1.342	1.011	3.642	0.038
<i>S. enterica</i>	0.671	0.505	3.642	0.038
<i>S. aureus</i>	0.671	2.022	3.642	0.076
<i>C. sporogenes</i>	0.671	1.011	3.642	0.076
<i>K. rhizophila</i>	1.342	2.022	3.642	0.076
<i>B. subtilis</i>	0.671	1.011	3.642	0.076
<i>S. cerevisiae</i>	0.084	2.022	3.673	0.011
<i>C. albicans</i>	0.168	4.044	7.346	0.022
<i>A. brasiliensis</i>	0.356	4.044	3.673	0.044

^aStandard used for bacterial strains was erythromycin; ^bstandard used for fungal strains was amphotericin B

The brine shrimp test

The brine shrimp lethality bioassay is an excellent predictive tool for the toxic potential of new bioactive compounds. The results of this test can be ext-

rapolated to cell-line toxicity and anti-tumor activity.^{25,32} The results presented in Table III showed high toxicity of the ligand, compared to moderate toxicities of the complex and the Cu(II) salt. This moderate toxicity of the synthesized complex may indicate its potential as a new active drug.

TABLE III. Results of the brine shrimp test for the complex and the starting compounds

Compound	LC_{50} / mM
Complex	0.613±0.051
Ligand	0.238±0.092
Cu(BF ₄) ₂ ·6H ₂ O	1.174±0.155
K ₂ Cr ₂ O ₇	0.077±0.016

Assessment of radical-scavenging activity

Assessment of radical-scavenging capacity was determined using a DPPH free radical scavenging assay and the results are presented in Table IV. According to the obtained results, the basic salt and ligand did not possess DPPH radical scavenging capacity, whereas the complex showed moderate antioxidant activity.

TABLE IV. DPPH radical scavenging of starting compounds and the complex

Compound	IC_{50} / mM
Complex	1.450±0.036
Ligand	7.834±0.126
Cu(BF ₄) ₂ ·6H ₂ O	>9.651
Ascorbic acid	0.079±0.003

CONCLUSION

In this paper we have thoroughly described the synthesis and characterization of a new binuclear azide-bridged Cu(II) complex containing NNO-donor hydrazone ligands obtained in a condensation reaction between 7-acetyl-6-azaindole and Girard's T reagent. The X-ray crystallographic analysis of the complex revealed a binuclear structure, in which two Cu(II) ions are bridged by two end-to-end (di- $\mu_{1,3}$ -N₃) azide ligands, while the hydrazone ligands coordinate to each Cu(II) center in a tridentate manner forming an axially elongated square pyramidal geometry around each metal ion. The complex crystallizes in the triclinic space group P-1. Detailed research of the Cambridge Structural Database revealed there are no crystal structures of binuclear Cu(II)-azido complexes with tridentate NNO-donor hydrazone ligands having double end-to-end (di- $\mu_{1,3}$ -N₃) coordination mode of bridging azides, making this complex structure unique and rather interesting. Antimicrobial activity of the complex was also examined, and it was shown that the complex exhibits higher antibacterial activity towards all tested Gram-positive bacteria than the ligand itself, while the antifungal activity of the complex towards all tested fungal strains was not only higher than that of

the ligand, but also comparable to the activity of the standard drug. Results obtained in the evaluation of antimicrobial activity of the complex may indicate its potential as an antifungal agent.

SUPPLEMENTARY MATERIAL

Additional data and information are available electronically at the pages of journal website: <https://www.shd-pub.org.rs/index.php/JSCS/article/view/12452>, or from the corresponding author on request.

Acknowledgment. This research has been financially supported by the Ministry of Science, Technological Development and Innovation of Republic of Serbia, contract numbers: 451-03-47/2023-01/200026, 451-03-47/2023-01/200168 and 451-03-47/2023-01/200288, as well as by the Science Fund of the Republic of Serbia, #7750288, Tailoring Molecular Magnets and Catalysts Based on Transition Metal Complexes – TMMagCat, and by the Slovenian Research Agency (ARRS), grant number P1-0175. We thank the EN-FIST Centre of Excellence, Ljubljana, Slovenia, for the use of the SuperNova diffractometer.

ИЗВОД

ДИНУКЛЕАРНИ ХИДРАЗОНСКИ КОМПЛЕКС Cu(II) СА АЗИДНИМ МОСТОМ: СИНТЕЗА, КАРАКТЕРИЗАЦИЈА И ЕВАЛУАЦИЈА БИОЛОШКЕ АКТИВНОСТИ

ТЕОДОРА ВИТОМИРОВ¹, БОЖИДАР ЧОБЕЉИЋ¹, ANDREJ PEVEC², ДУШАНКА РАДАНОВИЋ³, ИРЕНА НОВАКОВИЋ³, МИЛИЦА САВИЋ³, КАТАРИНА АНЂЕЛКОВИЋ¹ и МАЈА ШУМАР-РИСТОВИЋ¹

¹Универзитет у Београду – Хемијски факултет, Сивуђенички пут 12–16, 11000 Београд, ²Faculty of Chemistry and Chemical Technology, University of Ljubljana, Večna pot 113, 1000 Ljubljana, Slovenia и

³Универзитет у Београду, Институт за хемију, технологију и металургију, Центар за хемију, Њеишева 12, 11000 Београд

Кондензациони производ 7-ацетил-6-азаиндола и Жираровог Т реагенса (лиганд **HL**) коришћен је као лиганд у реакцији са $\text{Cu}(\text{BF}_4)_2 \cdot 6\text{H}_2\text{O}$ и NaN_3 . Реакција је довела до формирања бинуклеарног $\text{Cu}(\text{II})$ комплекса који садржи два азидна моста у „*end-to-end*“ ($\text{di-}\mu\text{-}_{1,3}\text{-N}_3$) моду, као и два NNO -донорска хидразонска лиганда који заједно формирају аксијално издужену квадратно–пирамидалну геометрију око сваког централног металног јона. Овај „*end-to-end*“ ($\text{di-}\mu\text{-}_{1,3}\text{-N}_3$) азидни мост се до сада није појављивао у структурама бакар(II)-комплекса који садрже NNO -донорске хидразонске лиганде, што чини структуру комплекса још интересантнијом за будућа испитивања. Овај комплекс је окарактерисан елементалном анализом, ИС спектроскопијом и рендгенском структурном анализом и пронађено је да кристалише у триклиничној просторној групи $P\text{-}1$ са асиметричном јединицом која се састоји из једног $\text{Cu}(\text{II})$ центра, цвтер-јонског лиганда (**L**), једног азидног лиганда (N_3^-) и BF_4^- контра-јона. Испитивање антимикробне активности комплекса показало је вишу антифунгалну активност, као и вишу антибактеријску активност према Грам-позитивним бактеријама, у односу на сам хидразонски лиганд, док је антифунгална активност комплекса чак упоредива са активношћу амфотерицина Б који је коришћен као стандард.

(Примљено 23. јуна, ревидирано 27. јуна, прихваћено 21. јула 2023)

REFERENCES

1. C. Adhikary, S. Koner, *Coord. Chem. Rev.* **254** (2010) 2933 (<https://doi.org/10.1016/j.ccr.2010.06.001>)

2. A. Escuer, G. Aromí, *Eur. J. Inorg. Chem.* **2006** (2006) 4721 (<https://doi.org/10.1002/ejic.200600552>)
3. K. Dankhoff, B. Weber, *CrystEngComm* **20** (2018) 818 (<https://doi.org/10.1039/C7CE02007D>)
4. M. R. Milenković, B. Čobeljić, K. Anđelković, I. Turel, *Eur. J. Inorg. Chem.* **2018** (2018) 838 (<https://doi.org/10.1002/ejic.201701387>)
5. P. Bhowmik, A. Bhattacharyya, K. Harms, S. Sproules, S. Chattopadhyay, *Polyhedron* **85** (2015) 221 (<https://doi.org/10.1016/j.poly.2014.08.021>)
6. M. Das, B. K. Shaw, B. N. Ghosh, K. Rissanen, S. K. Saha, S. Chattopadhyay, *J. Coord. Chem.* **68** (2015) 1361 (<https://doi.org/10.1080/00958972.2015.1014350>)
7. P. Mukherjee, O. Sengupta, M. G. B. Drew, A. Ghosh, *Inorganica Chim. Acta* **362** (2009) 3285 (<https://doi.org/10.1016/j.ica.2009.02.041>)
8. M. S. Ray, A. Ghosh, R. Bhattacharya, G. Mukhopadhyay, M. G. B. Drew, J. Ribas, *Dalton Trans.* (2004) 252 (<https://doi.org/10.1039/B311499F>)
9. S. Sen, S. Mitra, D. L. Hughes, G. Rosair, C. Desplanches, *Polyhedron* **26** (2007) 1740 (<https://doi.org/10.1016/j.poly.2006.12.015>)
10. M. M. Fousiamol, M. Sithambaresan, K. K. Damodaran, M. R. P. Kurup, *Inorg. Chim. Acta* **501** (2020) 119301 (<https://doi.org/10.1016/j.ica.2019.119301>)
11. T. Vitomirov, F. Dimiza, I. Z. Matić, T. Stanojković, A. Pirković, L. Živković, B. Spremo-Potparević, I. Novaković, K. Anđelković, M. Milčić, G. Psomas, M. Š. Ristović, *J. Inorg. Biochem.* **235** (2022) 111942 (<https://doi.org/10.1016/j.jinorgbio.2022.111942>)
12. T. Dimitrijević, I. Novaković, D. Radanović, S. B. Novaković, M. V. Rodić, K. Anđelković, M. Šumar-Ristović, *J. Coord. Chem.* **73** (2020) 702 (<https://doi.org/10.1080/00958972.2020.1740212>)
13. E. R. Sevda, H. Ünver, G. Dikmen, *Lett. Org. Chem.* **20** (2023) 376 (<https://doi.org/10.2174/1570178620666221202090558>)
14. D. Lj. Tomović, A. M. Bukonjić, V. V. Jevtić, Z. R. Ratković, J. V. Bogojeski, A. Đeković, I. D. Radojević, L. R. Čomić, S. B. Novaković, G. A. Bogdanović, S. R. Trifunović, G. P. Radić, S. Cupara, *Transit. Met. Chem.* **43** (2018) 137 (<https://doi.org/10.1007/s11243-018-0201-0>)
15. B. Shaabani, A. A. Khandar, F. Mahmoudi, M. A. Maestro, S. S. Balula, L. Cunha-Silva, *Polyhedron* **57** (2013) 118 (<https://doi.org/10.1016/j.poly.2013.04.016>)
16. B. Shaabani, A. A. Khandar, H. Mobaiyen, N. Ramazani, S.S. Balula, L. Cunha-Silva, *Polyhedron* **80** (2014) 166 (<https://doi.org/10.1016/j.poly.2014.03.033>)
17. P. Chakrabarti, *J. Mol. Biol.* **234** (1993) 463 (<https://doi.org/10.1006/jmbi.1993.1599>)
18. M. R. Milenković, A. T. Papastavrou, D. Radanović, A. Pevec, Z. Jagličić, M. Zlatar, M. Gruden, G. C. Vougioukalakis, I. Turel, K. Anđelković, B. Čobeljić, *Polyhedron* **165** (2019) 22 (<https://doi.org/10.1016/j.poly.2019.03.001>)
19. R. Bikas, M. S. Krawczyk, T. Lis, *ChemistrySelect* **5** (2020) 6759 (<https://doi.org/10.1002/slct.202001032>)
20. *CrysAlis PRO*, Oxford Diffraction Ltd., Yarnton, (n.d.)
21. A. Altomare, G. Cascarano, C. Giacovazzo, A. Guagliardi, *J. Appl. Crystallogr.* **26** (1993) 343 (<https://doi.org/10.1107/S0021889892010331>)
22. G.M. Sheldrick, *Acta Crystallogr., C* **71** (2015) 3 (<https://doi.org/10.1107/S2053229614024218>)
23. A. Rahman, M.I. Choudhary, W.J. Thomson, *Bioassay Techniques for Drug Development*, Harwood Academic Publishers, Reading, 2001

24. A. Sartoratto, A. L. M. Machado, C. Delarmelina, G. M. Figueira, M. C. T. Duarte, V. L. G. Rehder, *Braz. J. Microbiol.* **35** (2004) 275 (<https://doi.org/10.1590/S1517-83822004000300001>)
25. B. Meyer, N. Ferrigni, J. Putnam, L. Jacobsen, D. Nichols, J. McLaughlin, *Planta Med.* **45** (1982) 31 (<https://doi.org/10.1055/s-2007-971236>)
26. A. W. Addison, T. N. Rao, J. Reedijk, J. van Rijn, G. C. Verschoor, *J. Chem. Soc., Dalton Trans.* (1984) 1349 (<https://doi.org/10.1039/DT9840001349>)
27. T. Keškić, B. Čobeljić, M. Gruden, K. Andelković, A. Pevec, I. Turel, D. Radanović, M. Zlatar, *Cryst Growth Des.* **19** (2019) 4810 (<https://doi.org/10.1021/acs.cgd.9b00760>)
28. M. R. Milenković, A. T. Papastavrou, D. Radanović, A. Pevec, Z. Jagličić, M. Zlatar, M. Gruden, G. C. Vougioukalakis, I. Turel, K. Andelković, B. Čobeljić, *Polyhedron* **165** (2019) 22 (<https://doi.org/10.1016/j.poly.2019.03.001>)
29. C. R. Groom, I. J. Bruno, M. P. Lightfoot, S. C. Ward, *Acta Crystallogr., B* **72** (2016) 171 (<https://doi.org/10.1107/S2052520616003954>)
30. L. J. Farrugia, *J. Appl. Crystallogr.* **45** (2012) 849 (<https://doi.org/10.1107/S0021889812029111>)
31. C. F. Macrae, P. R. Edgington, P. McCabe, E. Pidcock, G. P. Shields, R. Taylor, M. Towler, J. van de Streek, *J. Appl. Crystallogr.* **39** (2006) 453 (<https://doi.org/10.1107/S002188980600731X>)
32. J. E. Anderson, C. M. Goetz, J. L. McLaughlin, M. Suffness, *Phytochem. Anal.* **2** (1991) 107 (<https://doi.org/10.1002/pca.2800020303>).



SUPPLEMENTARY MATERIAL TO

Binuclear azide-bridged hydrazone Cu(II) complex: Synthesis, characterization and evaluation of biological activity

TEODORA VITOMIROV¹, BOŽIDAR ČOBELJIĆ¹, ANDREJ PEVEC², DUŠANKA RADANOVIĆ³, IRENA NOVAKOVIĆ³, MILICA SAVIĆ³, KATARINA ANĐELKOVIĆ¹ and MAJA ŠUMAR-RISTOVIĆ^{1*}

¹University of Belgrade – Faculty of Chemistry, Studentski trg 12–16, 11000 Belgrade, Serbia, ²Faculty of Chemistry and Chemical Technology, University of Ljubljana, Večna pot 113, 1000 Ljubljana, Slovenia and ³University of Belgrade, Institute of Chemistry, Technology and Metallurgy, Department of Chemistry, Njegoševa 12, 11000 Belgrade, Serbia

J. Serb. Chem. Soc. 88 (9) (2023) 877–888

ANALYTICAL AND SPECTRAL DATA

Elemental analysis for C₁₄H₂₀ClN₅O (%). Calcd.: C 54.28, H 6.51, N 22.61. Found: C 54.68, H 7.09, N 22.13.

IR (ATR, cm⁻¹) selected peaks: 3377.4 (*m*), 3068.5 (*m*), 3019.4 (*m*), 2976.5 (*m*), 1703.4 (*s*), 1618.3 (*w*), 1571.8 (*m*), 1550.4 (*m*), 1491.2 (*m*), 1431.9 (*m*), 1398.4 (*s*), 1333.1 (*m*), 1280.2 (*m*), 1231.0 (*m*), 1164.0 (*m*), 1125.8 (*m*), 987.3 (*m*), 947.3 (*m*), 919.3 (*m*), 858.8 (*w*), 818.5 (*m*), 800.1 (*m*), 710.9 (*m*), 655.4 (*m*), 609.1 (*w*).

¹H-NMR (400 MHz, DMSO-*d*₆), δ (ppm): 11.66 (*s*, 1H, N2-H), 11.50 (*s*, 1H, N4-H), 8.15–7.72 (4H, C1-H, C2-H, C4-H, C5-H), 4.91 (*s*, 2H, C11-H), 3.34 (*t*, 9H, C12-H), 2.32 (*s*, 3H, C9-H).

¹³C-NMR (125 MHz, DMSO-*d*₆), δ (ppm): 167.24 (C10), 161.48 (C8), 156.29–120.21 (C1, C2, C3, C4, C5, C6, C7), 63.21 (C11), 53.74 (C12), 12.73 (C9).

Elemental analysis for C₂₈H₃₈B₂Cu₂F₈N₁₆O₂ (%). Calcd.: C 36.11, H 4.11, N 24.06. Found: C 35.74, H 4.25, N 24.58.

IR (ATR, cm⁻¹) selected peaks: 3350.3 (*w*), 3098.4 (*w*), 3044.3 (*w*), 2988.8 (*w*), 2063.4 (*s*), 1583.1 (*s*), 1557.8 (*s*), 1530.8 (*s*), 1501.3 (*m*), 1483.2 (*s*), 1441.4 (*m*), 1400.5 (*m*), 1347.7 (*m*), 1319.7 (*m*), 1296.1 (*m*), 1248.7 (*m*), 1185.3 (*m*), 1118.1 (*m*), 1034.8 (*s*), 997.2 (*m*), 972.1 (*m*), 926.3 (*m*), 910.6 (*m*), 815.7 (*m*), 733.2 (*m*), 655.2 (*w*).

* Corresponding author. E-mail: majas@chem.bg.ac.rs



TABLE S-I. Selected bond lengths (Å) and angles (°) for $[\text{Cu}_2\text{L}_2(\mu_{1,3}\text{-N}_3)_2](\text{BF}_4)_2$.

Cu1–O1	1.930(3)	O1–Cu1–N6	92.72(13)
Cu1–N1	1.972(3)	O1–Cu1–N1	170.34(13)
Cu1–N3	1.975(3)	N6–Cu1–N1	93.99(14)
Cu1–N6	1.957(3)	O1–Cu1–N3	82.34(13)
Cu1–N8 ^a	2.426(4)	N6–Cu1–N3	167.13(14)
N3–C8	1.297(5)	N1–Cu1–N3	89.64(14)
N3–N4	1.391(5)	O1–Cu1–N8 ^a	91.62(14)
N4–C10	1.301(5)	N6–Cu1–N8 ^a	95.51(14)
O1–C10	1.287(5)	N1–Cu1–N8 ^a	94.65(14)
N6–N7	1.188(5)	N3–Cu1–N8 ^a	96.49(14)
N7–N8	1.157(5)		

Symmetry code a = $-x, -y, -z+1$

TABLE S-II. Bridging modes of azido ligands in binuclear Cu(II)-complexes with hydrazone-based NNO-donor ligands.

CCDC numbers of binuclear Cu(II)-azido complexes with NNO donor hydrazone ligands	Bridging modes of azido ligands	Cu(II)-ligand chelate ring-system	References
$[\text{Cu}_2\text{L}_2(\mu_{1,3}\text{-N}_3)_2](\text{BF}_4)_2$	double EE ^a (di- $\mu_{1,3}\text{-N}_3$)	6-5	this work
978363	double EO ^b (di- $\mu_{1,1}\text{-N}_3$)	5-5	[1]
843830	double EO ^b (di- $\mu_{1,1}\text{-N}_3$)	5-5	[2]
615282	double EO ^b (di- $\mu_{1,1}\text{-N}_3$)	5-5	[3]
704271	double EO ^b (di- $\mu_{1,1}\text{-N}_3$)	5-5	[4]
649737	double EO ^b (di- $\mu_{1,1}\text{-N}_3$)	5-5	[5]
1920797	double EO ^b (di- $\mu_{1,1}\text{-N}_3$)	5-5	[6]
1886535	double EO ^b (di- $\mu_{1,1}\text{-N}_3$)	5-5	[7]
902698	double EO ^b (di- $\mu_{1,1}\text{-N}_3$)	5-5	[8]
1569840	double EO ^b (di- $\mu_{1,1}\text{-N}_3$)	5-5	[9]
797642	double EO ^b (di- $\mu_{1,1}\text{-N}_3$)	5-5	[10]
1945216	double EO ^b (di- $\mu_{1,1}\text{-N}_3$)	5-5	[11]
1983984	double EO ^b (di- $\mu_{1,1}\text{-N}_3$)	5-5	[12]

^aEE = end-to-end; ^bEO = end-onTABLE S-III. Hydrogen-bond parameters for $[\text{Cu}_2\text{L}_2(\mu_{1,3}\text{-N}_3)_2](\text{BF}_4)_2$

D–H...A	D–H (Å)	H...A (Å)	D...A (Å)	D–H...A (°)	Symm. Operation on A
N2–H2N...F3	0.92(4)	2.48(4)	3.390(8)	167(5)	2-x, 1-y, 1-z
C4–H4...F4A	0.93	2.39	3.249(12)	154	
C4–H4...F4B	0.93	2.50	3.418(16)	167	
C5–H5...N8	0.93	2.52	3.369(7)	151	1+x, 1+y, z
C11–H11A...F2	0.97	2.48	3.350(11)	149	1-x, -y, 1-z
C11–H11B...F2	0.97	2.38	3.316(10)	163	x, y, 1+z
C14–H14A...F1	0.96	2.55	3.460(9)	159	-1+x, y, 1+z

C14–H14B...F4A	0.96	2.48	3.181(10)	129	1-x, 1-y, 1-z
Intra C9–H9A...N4	0.96	2.26	2.675(8)	105	
Intra C13–H13B...O1	0.96	2.58	3.162(6)	119	

TABLE S-IV. Intermolecular $\pi\cdots\pi$ interaction parameters for complex **1**

$Cg(I)^a$	$Cg(J)^a$	$Cg(I)\cdots Cg(J)^b$ (Å)	α^c (°)	β^d (°)	γ^e (°)	Slippage ^f (Å)	Sym. code on (<i>J</i>)
Cg(1)	Cg(1)	3.460(3)	0.0(2)	4.0	4.0	0.240	1-x, 1-y, 1-z

^aLabels of aromatic rings: (1) = N(2),C(5),C(4),C(3),C(7),C(6).

^b $Cg(I)\cdots Cg(J)$ = Distance between ring centroids (Ang.).

^c α = Dihedral angle between planes (*I*) and (*J*) (Deg).

^d β = Angle between $Cg(I)-Cg(J)$ vector and normal to plane (*I*) (Deg).

^e γ = Angle between $Cg(I)-Cg(J)$ vector and normal to plane (*J*) (Deg).

Slippage = Distance between $Cg(I)$ and perpendicular projection of $Cg(J)$ on ring (*I*) (Ang).

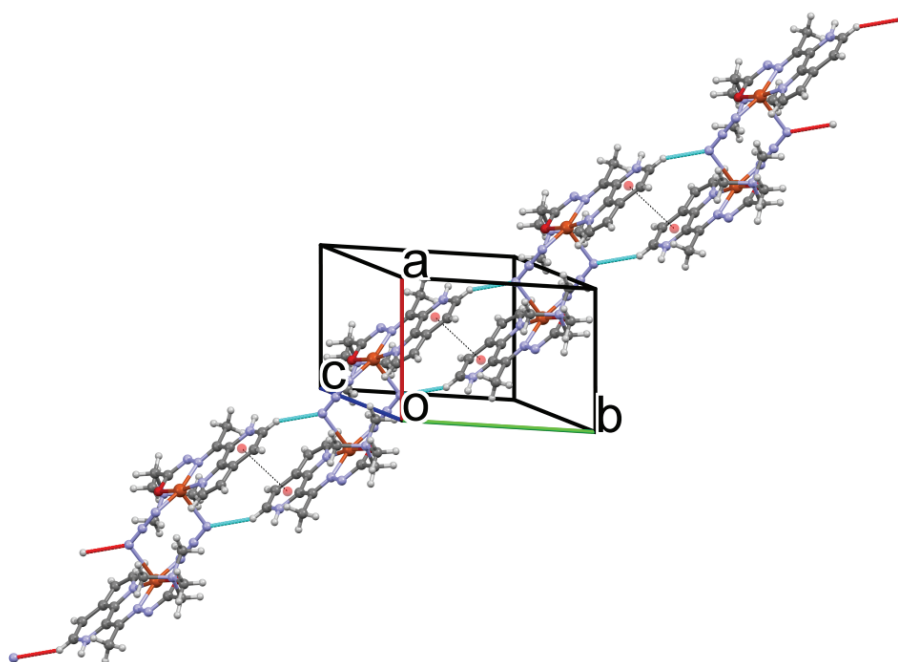


Fig. S-1. Crystal packing, showing intermolecular $\pi\cdots\pi$ and C–H...N contacts between dimeric complex cations extending in [110] direction.

REFERENCES

1. B. Shaabani, A. A. Khandar, H. Mobaiyen, N. Ramazani, S. S. Balula, L. Cunha-Silva, *Polyhedron* **80** (2014) 166 (<http://dx.doi.org/10.1016/j.poly.2014.03.033>)
2. B. Shaabani, A. A. Khandar, F. Mahmoudi, M. A. Maestro, S. S. Balula, L. Cunha-Silva, *Polyhedron* **57** (2013) 118 (<http://dx.doi.org/10.1016/j.poly.2013.04.016>)

3. S. Sen, S. Mitra, D. L. Hughes, G. Rosair, C. Desplanches, *Polyhedron* **26** (2007) 1740 (<http://dx.doi.org/10.1016/j.poly.2006.12.015>)
4. R. N. Patel, *J. Coord. Chem.* **63** (2010) 1207 (<http://doi.org/10.1080/00958971003735432>)
5. A. Ray, S. Banerjee, R. J. Butcher, C. Desplanches, S. Mitra, *Polyhedron* **27** (2008) 2409 (<http://dx.doi.org/10.1016/j.poly.2008.04.018>)
6. L.-Y. Xie, Y. Zhang, H. Xu, C.-D. Gong, X.-L. Du, Y. Li, M. Wang, J. Qin, *Acta Cryst., C* **75** (2019) 927 (<http://dx.doi.org/10.1107/S2053229619008040>)
7. M. R. Milenković, A. T. Papastavrou, D. Radanović, A. Pevec, Z. Jagličić, M. Zlatar, M. Gruden, G. C. Vougioukalakis, I. Turel, K. Anđelković, B. Čobeljić, *Polyhedron* **165** (2019) 22 (<http://dx.doi.org/10.1016/j.poly.2019.03.001>)
8. H. Hosseini-Monfared, R. Bikas, R. Szymczak, P. Aleshkevych, A. M. Owczarzak, M. Kubicki, *Polyhedron* **63** (2013) 74 (<http://doi.org/10.1016/j.poly.2013.06.055>)
9. M. M. Fousiamol, M. Sithambaresan, V. A. Smolenski, J. P. Jasinski, M. R. P. Kurup, *Polyhedron* **141** (2018) 60 (<http://dx.doi.org/10.1016/j.poly.2017.11.024>)
10. A. Datta, K. Das, Y.-M. Jhou, J.-H. Huang, H.M. Lee, *Acta Cryst., E* **66** (2010) m1271 (<https://dx.doi.org/10.1107/S16005368100348609>)
11. M. M. Fousiamol, M. Sithambaresan, K. K. Damodaran, M. R. P. Kurup, *Inorg. Chim. Acta* **501** (2020) 119301 (<http://dx.doi.org/10.1016/j.ica.2019.119301>)
12. R. Bikas, M. S. Krawczyk, T. Lis, *ChemistrySelect* **5** (2020) 6759 (<http://dx.doi.org/10.1002/slct.202001032>).



J. Serb. Chem. Soc. 88 (9) 889–904 (2023)
JSCS–5669

Bactericidal effects of copper–polypyrrole composites modified with silver nanoparticles against Gram-positive and Gram-negative bacteria

PATRICIA L. MARUCCI¹, MARIA G. SICA^{1,2}, LORENA I. BRUGNONI^{1,3}
and MARÍA B. GONZÁLEZ^{4*}

¹Department of Biology, Biochemistry and Pharmacy, National University of the South, Bahía Blanca, Argentina, ²Department of Health Sciences, National University of the South, Bahía Blanca, Argentina, ³Institute of Biological and Biomedical Sciences, National University of the South, CONICET, Bahía Blanca, Argentina and ⁴Chemical Engineering Department, Institute of Electrochemistry and Corrosion Engineering, National University of the South, CONICET, Bahía Blanca, Argentina

(Received 13 February, revised 26 March, accepted 2 August 2023)

Abstract: The aim of this research is to study the bactericidal effects of copper–polypyrrole (PPy) composites deposited onto 316L stainless steel (SS) modified with silver nanoparticles (Np). The antimicrobial properties were evaluated against twenty-four strains of Gram-positive and Gram-negative bacteria. Among the twenty-four strains studied, isolates included reference strains (*Escherichia coli* ATCC 25922, *Escherichia coli* 0157:H7 EDL 933, *Staphylococcus aureus* ATCC 25923 and *Listeria monocytogenes* ATCC 7644), as well as strains isolated from food and clinical samples. The antimicrobial activity of the composites demonstrated that all PPy-modified films had antibacterial properties. Notably, Cu-PPyAgNp₅₀₀ exhibited the strongest inhibitory activity against both Gram-negative and Gram-positive bacteria. Surface modification of 316L SS with these films is a promising and viable alternative for the development of novel antibacterial composites that can inhibit the growth of a significant number of bacteria.

Keywords: conducting polymer; antibacterial applications; metallic nanoparticles; stainless steel.

INTRODUCTION

Antibiotic resistance is considered by the World Health Organization as a critical problem of global concern, which causes higher medical costs, prolonged hospital stays, and increased mortality.¹ This threat is caused by the overuse and abuse of antibiotics, coupled with the natural evolutionary processes of bacteria.

* Corresponding author. E-mail: belen.gonzalez@uns.edu.ar
<https://doi.org/10.2298/JSC230213047M>



There is a significant interest from all nations in developing a global action plan to prevent and control the growth of antibiotic resistance.² In the biomedical field, bacterial infections at the site of implanted medical devices such as catheters and artificial prostheses are a serious and persistent problem. Although medical implants greatly improve the patients' quality of life, implant-related infections are recognized as a tragic problem, often requiring revision surgery for individuals with severe infections.³ To overcome this problem, surface modifications are used to improve the antibacterial properties of materials.^{4,5} Some antibacterial strategies for metal implants may include inhibiting the adhesion, the colonization, the biofilm formation and the proliferation of bacteria.^{6,7} Recently, many organic compounds, including conducting polymers or biopolymers, have demonstrated their potential as antibacterial and antiviral agents to combat infections caused by harmful bacteria and viruses.^{8,9}

In recent years, the research on conducting polymers and their composites as antibacterial agents has gained momentum.^{8,10} In particular, polypyrrole (PPy) has been successfully explored for new antibacterial systems due to its easy preparation, low cost, low toxicity and biocompatibility.¹¹ In a recent study, the antibacterial properties and the synergistic behavior of a composite consisting of silver nanoparticles, single-walled carbon nanotubes and PPy were reported. The prepared ternary composite exhibits the following order of performance within 24 h at a concentration of 0.048 mg/mL: *Bacillus cereus* > *Escherichia coli* > *Pseudomonas aeruginosa* > methicillin-resistant *Staphylococcus aureus*.¹² Another noteworthy composite consisting of PPy and zinc-doped copper oxide microparticles showed remarkable antimicrobial effects against *E. coli* and *S. aureus*. The authors postulated that the mechanism of cell death was mainly induced by the release of reactive oxygen species (ROS), which damage bacterial membranes, DNA and proteins.¹³ Recent studies conducted in our laboratory have demonstrated that hybrid antimicrobial coating materials containing PPy combined with copper,^{14,15} silver¹⁶ or zinc¹⁷ species have also shown great bactericidal effects.

Silver has a long history of use in pharmacology and medicine as an antibacterial agent. In the field of orthopedics, silver nanoparticles (AgNps) have yielded excellent results in modifying implant surfaces to prevent implant-related infections.¹⁸ Furthermore, the antibiotic activity of AgNps has been studied in various bacteria, yielding positive results.¹⁹ However, the exact mechanisms by which Ag acts as antimicrobial agent have not been fully clarified. Three hypotheses have been proposed: 1) Ag⁺ are taken up by bacteria, triggering a cascade of intracellular reactions that disrupt ATP production and DNA replication; 2) silver ions promote the generation of reactive oxygen species (ROS) both inside and outside bacterial cells, causing oxidative stress and subsequent damage to bacterial membrane lipids and DNA; 3) in the case of AgNps, it is believed that

these particles can penetrate cell membranes and activate one or all of the aforementioned mechanisms.²⁰

The incorporation of copper as antibacterial agent in metallic implants has also been considered.²¹ The interaction between copper and bacteria cells involves several important events that can be listed as follows: The first event (A) is the accumulation of Cu ions on the bacteria membrane or within the cell. This accumulation not only causes membrane damage through depolarization, but also leads to the leakage of intracellular components; B) the generation of ROS by copper ions may lead to further cell damage; C) Cu ions inside bacterial cells may bind with DNA molecules, resulting in the disruption of the helical structure and biochemical processes.²²

On the other hand, 316L stainless steel (316L SS) is the most commonly used alloy in medical implants due to its good corrosion performance, notable biocompatibility, high mechanical properties and low cost accessibility.²³ According to this, in our laboratory a microstructured PPy film was electrosynthesized onto 316L SS from a solution containing copper species. The results indicated that PPy/Cu-modified electrodes are effective for water disinfection contaminated with *E. coli*.¹⁴ Furthermore, it has been demonstrated that a salicylate-doped PPy film is an effective matrix for immobilizing Ag species, and the resulting composites exhibit excellent performance in inhibiting the activity of *S. aureus* bacteria. These findings suggest that the composite holds promise for biomedical applications.¹⁶

Considering the advantages of silver and copper species, as well as the synergistic effect of these metals with PPy in antibacterial studies, the aim of this research is to study the bactericidal effect of copper–polypyrrole composites modified with silver nanoparticles deposited on 316L SS. According to the bibliography consulted, this study is the first to evaluate the antibacterial properties of a PPy composite against a total of twenty-four strains of both Gram-positive and Gram-negative bacteria. These isolates include reference strains (*E. coli* ATCC 25922, *E. coli* 0157:H7 EDL 933, *S. aureus* ATCC 25923 and *Listeria monocytogenes* ATCC 7644) and strains isolated from food and clinical samples. Given the extensive range of bacteria examined, the resulting composite shows promise as a surface modification material for 316L SS, with potential applications in various fields such as medical instruments, water treatment devices, and food processing.

EXPERIMENTAL

Chemicals

Pyrrrole (99.9 % purity), silver nitrate (99.9 % purity) and sodium salicylate (99.9 % purity) were obtained from Sigma. Copper sulphate pentahydrate (98 % purity) and potassium nitrate (98 % purity) were obtained from Cicarelli Laboratorios (Santa Fe, Argentina). Pyrrrole (Sigma–Aldrich) was freshly distilled under reduced pressure prior to use.

Bacterial strains

The antibacterial properties of composites were tested against four reference strains (*Escherichia coli* ATCC 25922, *E. coli* 0157:H7 EDL 933, *Staphylococcus aureus* ATCC 25923 and *Listeria monocytogenes* ATCC 7644), four *E. coli* strains (named 6, 17, 19 and 28) isolated from recreational waters,²⁴ thirteen *S. aureus* strains (named 1 and 13) obtained from the nose of asymptomatic volunteers, *Pseudomonas aeruginosa* isolated from drinking water and *Salmonella* spp. and *Listeria innocua* isolated from meat products.

Electrosynthesis and characterization of composite

The composites were electrosynthesized onto 316L SS sheets (wt. %: 17.47 Cr, 10.32 Ni, 1.88 Mn, 1.90 Mo, 0.39 Si, 0.025 C and Fe balance) with an exposed area of 0.25 cm². Prior to each experiment, the exposed 316L SS surface was abraded with a 1200-grit finish using SiC, then degreased with acetone, and finally washed with triply distilled water. For the electrochemical experiments, a conventional three-electrode system and a 20 cm³ Metrohm cell were used. A Pt sheet served as the counter electrode, while a commercially available Ag/AgCl/3M KCl electrode (Metrohm) was used as the reference electrode. All potentials are referred to Ag/AgCl scale.

As described in our earlier work, PPy films and copper-PPy (Cu-PPy) composites were obtained potentiostatically at 0.90 V from a solution containing 0.25 M pyrrole + 0.50 M Na salicylate. In the case of the Cu-PPy composite, a concentration of 0.10 M CuSO₄·5H₂O was also incorporated in the electrosynthesis solution.¹⁵ Silver nanoparticles were electrodeposited onto PPy and Cu-PPy using a solution containing AgNO₃ + KNO₃, following the potentiostatic double-pulse technique introduced by Scheludko and Todorova.²⁵ The process is based on the following parameters: nucleation potential $E_1 = -0.8$ V for nucleation time $t_1 = 0.5$ s and growth potentials of $E_2 = 0.1$ V for growth time $t_2 = 30$ s. The size of the nanoparticles was controlled by the solution concentration.

Electrochemical experiments were performed using a potentiostat-galvanostat Autolab PGSTAT128 N. Morphological studies of gold metallized films were conducted using a scanning electron microscopy (SEM), specifically the LEO 1450 VP system, which was equipped with an energy-dispersive scanning (EDS) probe. Additionally, the electrical conductivity of the films was measured using a homemade device through the two-probe method.

Disk diffusion assay

The antimicrobial effectiveness of the coatings was tested using the Kirby-Bauer disk diffusion method, following the model of antibiogram execution.²⁶

Briefly, cultures of the strains under study were cultivated on Muller-Hinton agar (MHA) plates from Britania Laboratories S.A., Argentina, for 24 h at 37 °C. The resulting colonies were suspended in Muller-Hinton broth from the same manufacturer. The turbidity (expressed as optical density; *OD*) of the bacterial suspensions was measured using an optical spectrophotometer ($\lambda = 600$ nm). The suspensions were adjusted to a turbidity of 0.5 based on the McFarland standard (10⁶ CFU mL⁻¹). A sterilized cotton swab was dipped into the resulting suspension, and used to apply a bacterial lawn on MHA plates. Petri plates were left to dry for 10 min, after which the composites were distributed, using the bare alloy and the PPy covered electrode as control samples. Incubation was carried out at 37 °C, and after 24 h, the plates were examined to identify the presence or absence of zones of inhibition. When zones of inhibition were observed, their diameter was measured with a ruler with a resolution of up to 1 mm. For each type of composite and microbial strain, the mean and standard deviation (*SD*) were calculated based on data obtained from two independent replicates.

RESULTS AND DISCUSSION

Electrosynthesis and characterization of composites

The formation and characterization of PPy and Cu-PPy coatings on 316L SS were discussed in our prior work.¹⁵ As mentioned before, both films have a morphology composed of hollow rectangular-sectioned microtubes. The proposed mechanism for the formation of these microtubes consists in the early crystallization of salicylic acid (HSA) on a granular PPy. These crystals are formed due to the rapid production of H^+ , which protonate the salicylate anions, constituting the building blocks for the formation of the rectangular microtubes.²⁷

Firstly, the electrodeposition of silver nanoparticles onto PPy was performed using the potentiostatic double-pulse technique. The initial pulse is applied to facilitate the formation of nuclei, while the subsequent pulse, with a more positive potential than the first one, regulates the growth of the nuclei deposited during the preceding pulse.²⁵

To control the nanoparticles size, two solutions with different concentrations were used: For smaller nanoparticles, a solution with a concentration of 5 mM $AgNO_3 + 50$ mM KNO_3 was utilized. SEM/EDS analysis was performed to characterize the composite. In Fig. 1a, it can be observed that the surface of the PPy film is effectively decorated with AgNps, approximately 100 nm in size. EDS spectra (Fig. 1b) were used to demonstrate the presence of metallic silver, with the signal typically appearing between 3–3.6 keV.²⁸ The weight percentage registered for this element was 6.8 %. The spectrum also displayed signals of C and O associated with organic compounds.²⁹ In order to increase the size of the deposits on the PPy films, the concentration of the electrosynthesis solution was raised to 10 mM $AgNO_3 + 100$ mM KNO_3 . As seen in Fig. 1c, nanoparticles of approximately 500 nm were obtained. In this case, the EDS analysis (Fig. 1d) shows a signal indicating the presence of metallic silver, with a content of 13.8 wt. %. The results demonstrated a direct correlation between the increase in Ag weight percentage and the increment in the particle size. To facilitate comprehension, the obtained composites were named PPy/AgNp₁₀₀ and PPy/AgNp₅₀₀, according to the nanoparticle size. Regardless of the AgNps size, a rosette-like structure characterizes most of the deposits. These preliminary findings indicate that, when applying the same electrochemical procedure, a rise in the concentration of the electrosynthesis solution, would not only lead to a growth in nanoparticle size but also to an increase in the amount of metallic silver in the composites.

To verify the amount of metallic silver deposited in the composites, a cyclic voltammetry experiment was performed. The procedure involved cycling the electrodes, which were covered with PPy/AgNp₁₀₀ and PPy/AgNp₅₀₀ in a 0.25 M Na salicylate solution between the potentials of -0.60 and 1.20 V at 0.01 V s^{-1} . The polymer without nanoparticles was also cycled. Fig. 2 illustrates that the electro-

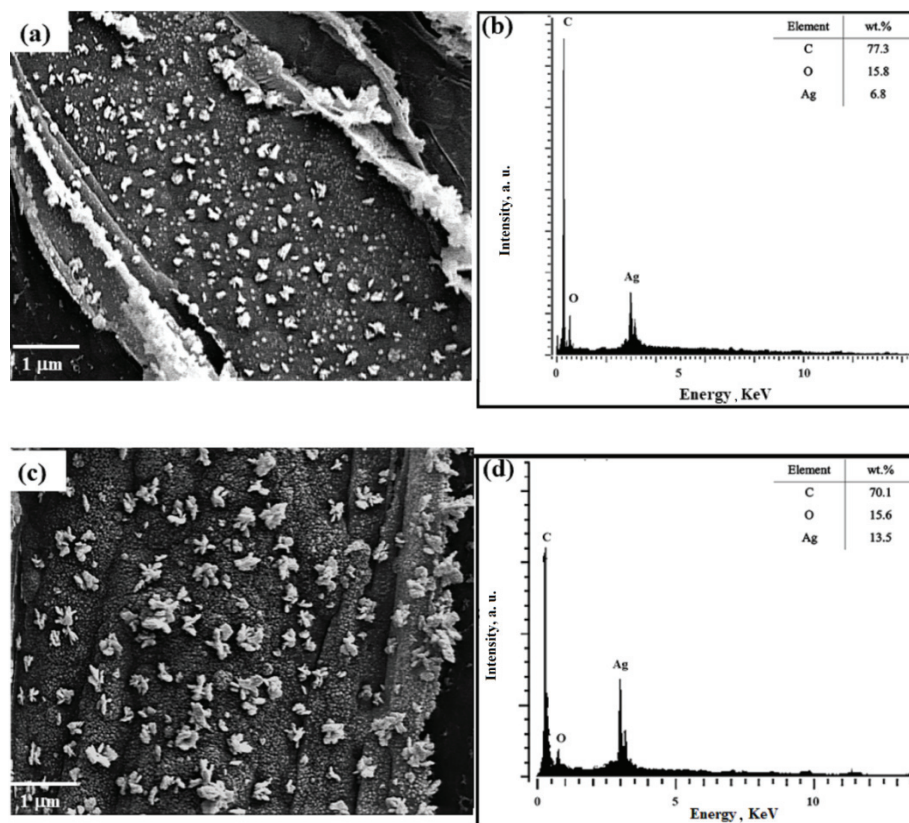


Fig. 1. SEM images and EDS spectra of PPy/AgNp100 (a, b) and PPy/AgNp500 (c, d).

chemical behavior of the composites differs significantly depending on the size of the silver nanoparticles. The strong and well-defined anodic peaks at 0.50 V are a result of the oxidation process of the deposited metal.¹⁶ For the PPy/AgNp₅₀₀ composite, the oxidation peak is associated with a current density of 6.5 mA/cm² (see curve b), while for the PPy/AgNp₁₀₀ composite, the oxidation peak is associated with a current density of 2.5 mA/cm² (see curve a). The peak area analysis of the oxidative peaks reveals that, as the nanoparticle size increases, the peak area also increases, indicating a higher concentration of metallic silver in the composite. Moreover, at approximately 1.0 V, a peak associated with the overoxidation of the polymer is observed in both composites.³⁰ In the reverse scan, cathodic peaks appear at 0.0 V, indicating the reduction of silver ions. Based on the comparison of the current density of reduction peaks, it can be concluded that a higher amount of silver ions redeposited back into the composites is associated with a larger size of AgNps. In contrast, regarding unmodified PPy, no peak is observed in this potential range (curve c).

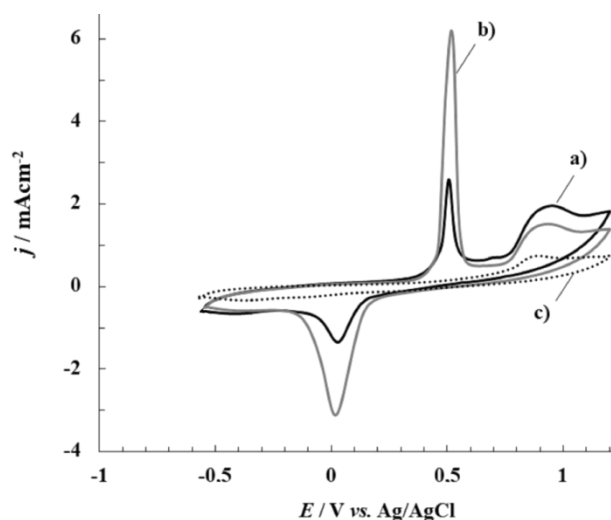


Fig. 2. Cyclic voltammograms registered in a 0.25 M Na salicylate solution at 0.01 V s^{-1} for 316L SS electrode coated with: a) PPy/AgNp₁₀₀ and b) PPy/AgNp₅₀₀. The data for unmodified PPy coated-316L SS is also provided (curve c).

With the aim of determining the amount of silver deposited in the composites, conductivity was measured. The values obtained were 28 S m^{-1} for PPy/AgNp₁₀₀ and 42 S m^{-1} for PPy/AgNp₅₀₀. These values fall within the range already reported for conductive polymers modified with nanoparticles.³¹ In the case of unmodified PPy, the conductivity value was 3.8 S m^{-1} . These values were estimated based on a film thickness of $7 \mu\text{m}$.³² Firstly, it can be observed that the incorporation of silver nanoparticles contributes to the improvement of the electrical conductivity of the PPy films.²⁸ The difference between the conductivity values of PPy/AgNp₁₀₀ and PPy/AgNp₅₀₀ could be attributed to the size of AgNps deposited in the composites. It is worth noting that an increase in the conductivity of the composites is associated with an augment of metallic silver deposited on the polymer. Indeed, Diantoro *et al.* proved conclusively that increased quantities of AgNps integrated into a conducting polymer enhance the conductivity of the composite.³³

Considering the excellent results obtained in water disinfection with Cu-PPy films,¹⁵ we decided to deposit AgNps onto Cu-PPy to study the antibacterial influence of both metals. In this process, silver nanoparticles were electrodeposited on Cu-PPy films, using the previously described double-pulse technique. The silver nanoparticles were obtained from a solution containing $10 \text{ mM AgNO}_3 + 100 \text{ mM KNO}_3$. SEM micrograph of the polymer surface confirms the presence of PPy microtubes decorated with approximately 500 nm -sized AgNps (Fig. 3a). The magnified image shows that most of the nanoparticles have rosette-like structures (Fig. 3b). In this case, the composite was named Cu-PPy/AgNp₅₀₀.

EDS spectra confirm the presence of Ag and Cu in the composite, with respective contents of 4.7 and 4.9 wt. %. The signals of C and O correspond to the polymer composition, as expected.

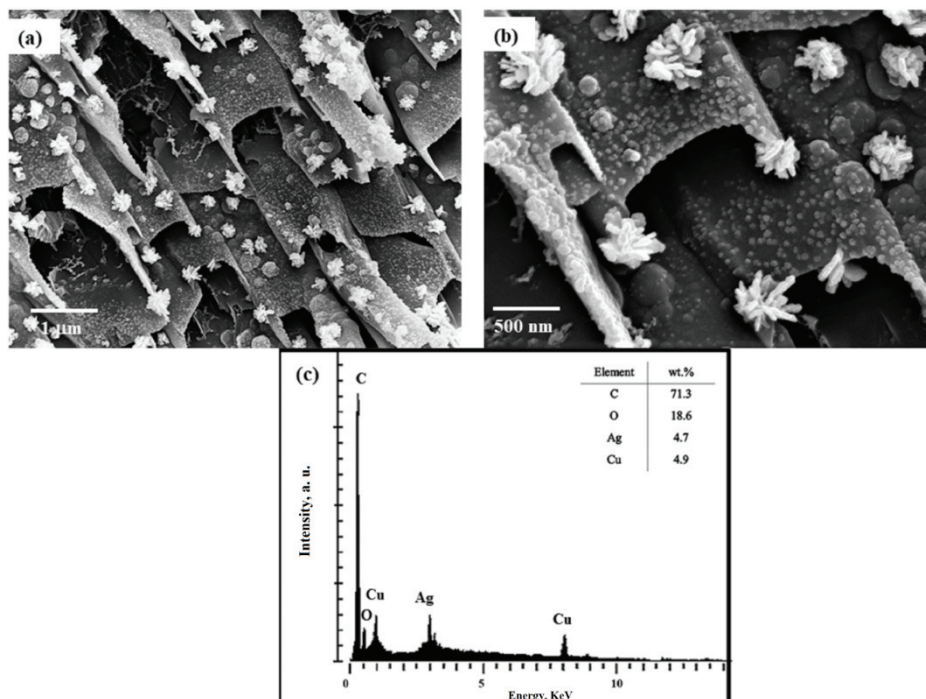


Fig. 3. SEM images (a, b) and EDS spectra (c) of Cu-PPy/AgNp₅₀₀.

To evaluate the chemical state of copper in the Cu-PPy and Cu-PPy/AgNp₅₀₀ composites, a cyclic voltammetry experiment was performed in a 0.25 M Na salicylate solution. In Fig. 4, the incorporation of Cu²⁺ is evidenced, in both films, by the presence of cathodic peaks at a potential of about -0.10 V, which are attributable to ion reduction.¹⁵ In the case of Cu-PPy/AgNp₅₀₀, an overlap of Ag⁺ and Cu²⁺ reduction peaks is registered. The inset in Fig. 4 shows the anodic peaks of copper metal dissolution in both composites. As it was expected, the presence of a strong and well-defined anodic peak at 0.50 V is showed for Cu-PPy/AgNp₅₀₀ as a result of the oxidation process of the AgNps (curve b). In this case, the current density associated with the oxidation peak of the silver nanoparticles is 6.0 mA/cm², a similar value to the one obtained previously. On the other hand, no peak is observed for the Cu-PPy composite (curve a) in this potential range.

XPS analysis was used to determine the specific electron binding energies of the elements on the surface of the composites. Fig. 5 displays the survey spectra of

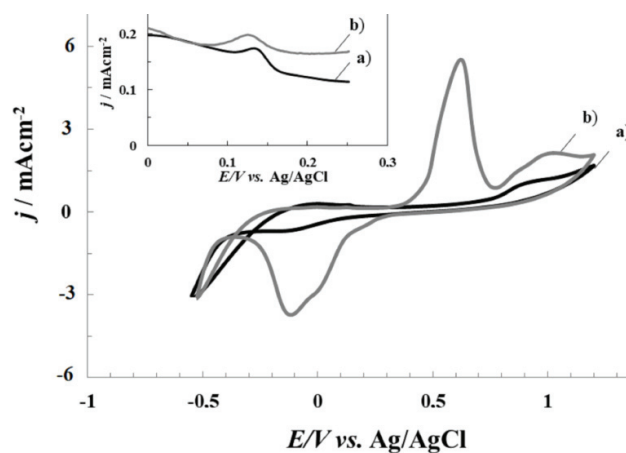


Fig. 4. Cyclic voltammograms registered in a 0.25 M Na salicylate solution at 0.01 V s^{-1} for 316L SS electrode coated with: a) Cu-PPy and b) Cu-PPy/AgNp₅₀₀. The inset shows the curves amplified.

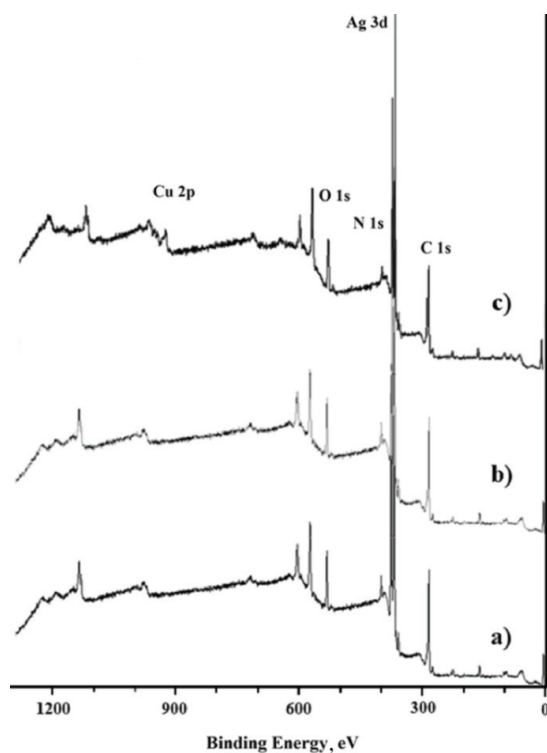


Fig. 5. XPS survey spectra of: a) PPy/AgNp₁₀₀, b) PPy/AgNp₅₀₀ and c) Cu-PPyAgNp₅₀₀.

the composites PPy/AgNp₁₀₀, PPy/AgNp₅₀₀ and Cu-PPyAgNp₅₀₀. The elements detected in all composites are C 1s, O 1s and N 1s, since they are the main

components of the polypyrrole matrix and the dopant (Sa/HsA).²² In Fig. 6a, the high-resolution spectrum of Ag 3d is presented. As can be seen, this element is also present in all samples. The two significant XPS signals, located at approximately 374.2 and 368.2 eV and separated by a distance of 6.0 eV, correspond to the Ag 3d_{5/2} and Ag 3d_{3/2} binding energies of Ag, respectively.³⁴ The results indicate the successful reduction of silver ions to zero-valent silver nanoparticles during the double pulse technique. On the other hand, the existence of Cu²⁺ is detected solely in the XPS survey of Cu-PPyAgNp₅₀₀ (Fig. 5, curve c), which is consistent with the Cu 2p signal. In Fig. 6b, the peaks at approximately 935.3 and 955.3 eV are assigned to Cu 2p_{3/2} and Cu 2p_{1/2}, respectively, while the peaks in the range of 940–945 eV and 964.1 eV correspond to the shake-up satellite peaks of Cu 2p, as supported by previous research.^{35,36} The XPS characterization supports the hypothesis that the polymer matrix contains Cu²⁺, as postulated in our previous study, where the presence of cathodic peaks during potentiodynamic polarization (Fig. 4) was attributed to ion reduction.¹⁵

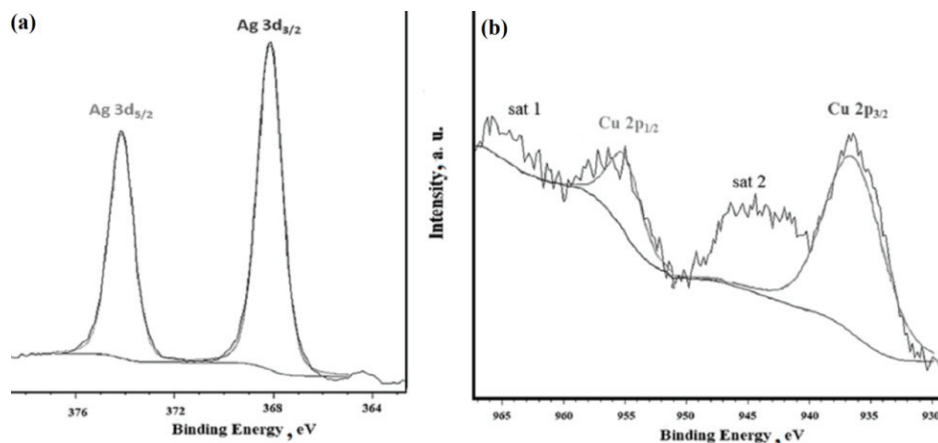


Fig. 6. XPS spectra of Cu-PPyAgNp₅₀₀: Ag 3d (a) and Cu 2p (b).

Agar diffusion assay

In order to assess the *in vitro* antibacterial efficacy of the resulting composites, the agar diffusion method was employed. The diameter of inhibition zones (DIZ) after 24 h is shown in Fig. 7.

Overall, Cu-PPy/AgNp₅₀₀ exhibited antibacterial activity against the majority of the species tested (23/24). This composite proved effective against all *S. aureus* strains and all Gram-negative bacteria under investigation. While several studies suggest that Gram-positive *S. aureus* is more resistant to silver nanoparticles compared to Gram-negative *E. coli*,^{37–39} this result does not consistently hold true.⁴⁰

PPy/AgNp₅₀₀ and Cu-PPy/AgNp₅₀₀ had a significant impact on the cellular viability of *S. aureus*, *E. coli*, *S. enterica*, *L. innocua* and *P. aeruginosa*. However, no activity was observed on the growth of *L. monocytogenes* ATCC 7644, which was only inhibited by PPy/AgNp₁₀₀.

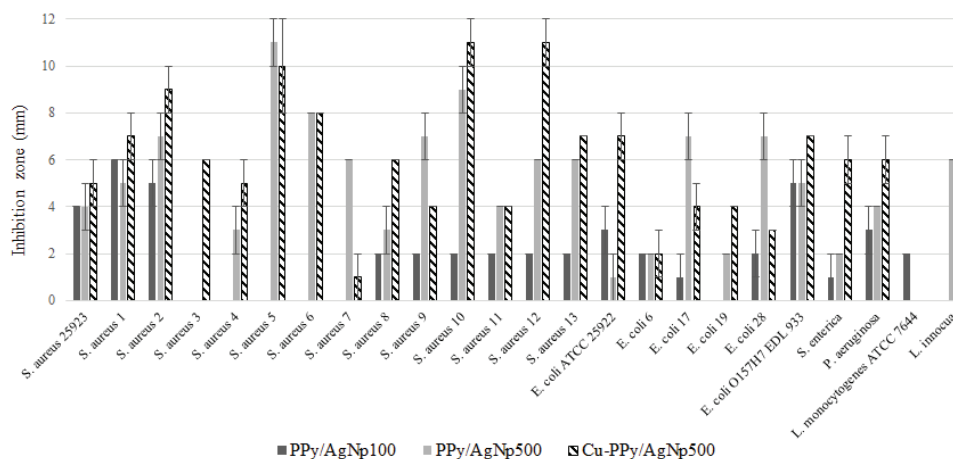


Fig. 7. Growth inhibition of different microbial species by copper and silver ions released from a coated specimen.

In particular, compared to PPy/AgNp₁₀₀, PPy/AgNp₅₀₀ and Cu-PPy/AgNp₅₀₀ exhibited higher antimicrobial activity against *S. aureus* strains 3, 8 and 12; *E. coli* ATCC 25922; *E. coli* strain 19; *S. enterica*; *P. aeruginosa*; *L. innocua*.

Given the nature of the agar diffusion method, which involves measuring the diameter of inhibition zones (*DIZ*) on agar plates using a ruler with a resolution of 1 mm, it is important to acknowledge the possibility of measurement errors. However, this method demonstrates the potential antibacterial effect of composites against various microbial strains. In the agar diffusion method, the *DIZ* surrounding a composite serves as an indicator of the microorganisms' sensitivity to the composite. While studies reporting *DIZ* values offer a quantitative measure of antibacterial activity, there is still significant non-uniformity in the experimental methods employed. The *DIZ* can exhibit variability, even within the context of the same microbial strain exposed to silver/copper composites. These variations may be attributed to several factors, including variations in the growth medium, differences in the initial concentration of microorganisms, and the size, shape and composition of nanoparticles. Thus, comparing the sensitivity of different strains to copper or silver nanocomposites is often not feasible, despite the wealth of available literature on the topic.⁴¹

Most research on bactericidal effects of silver and copper has been limited to a small number of microbial strains or, in some cases, only a single strain. However, this study sought to compare the antibacterial effects of silver and copper compounds across a wider spectrum of twenty-four bacterial strains. These strains included four reference strains, five strains isolated from water sources, thirteen strains obtained from human clinical samples and two strains isolated from food sources. The findings of this study revealed strain-specific characteristics, which can eventually contribute to the improved and effective utilization of these compounds for specific applications.

In recent years, numerous interconnected investigations have been conducted to enhance the utilization of AgNps for bacteria inhibition. However, an ongoing debate persists regarding the antibacterial action mechanism of AgNps. Previous studies have indicated that the bactericidal properties of AgNps are primarily attributed to a two-step mechanism. Firstly, Ag⁺ ions are released from the surfaces of nanoparticles. Subsequently, the released Ag⁺ interacts with cellular targets, resulting in their bactericidal effect.⁴²

The cellular uptake of AgNps is another mechanism associated with physical interaction, and occurs when Nps are small enough to cross the cell membrane.⁴³ Mukha *et al.* showed that the antibacterial activity of AgNps smaller than 10 nm is attributed to both membrane damage and their ability to penetrate into the cell.⁴⁴ Similarly, Dong *et al.* evaluated Nps of varying sizes and reached the conclusion that AgNps of smaller dimensions are more effective due to their ability to pierce the cell membrane.⁴⁵ In a separate study, Oves *et al.* synthesized AgNps with bacterial exopolysaccharides, spherical shape, and a size of about 35 nm.⁴⁶ They demonstrated that the antimicrobial activity of these Nps against *B. subtilis* and methicillin-resistant *S. aureus* (MRSA) is attributed to ROS production within bacterial cells. It has been suggested that AgNps smaller than the pore size can easily penetrate the pore networks and efficiently depolarize the inner membrane, causing a bactericidal effect.⁴⁷ In general, bacterial cells have a size in the micrometer range, whereas their outer cell membranes feature pores measuring in the nanometer range (<50 nm). Since AgNps used in this study are larger than the pores of the outer cell membrane, they are unable to penetrate the cell membrane. Conversely, the higher antibacterial efficacy of PPy/AgNp₅₀₀, in contrast with PPy/AgNp₁₀₀, can be attributed to the larger amount of ionic silver released as a result of the larger nanoparticle size.

The antibacterial activity of Cu-PPy/AgNp₅₀₀ composites encompasses a series of steps. One of these steps involves the dissolution of AgNps to release silver ions, along with the diffusion of copper ions from the PPy matrix. The release of silver ions leads to the disruption of the cytoplasm and the cell wall, while also triggering the production of ROS. This ROS production by respiratory enzymes inhibits the release of adenosine triphosphate.⁴⁸ It is possible that the

mechanism underlying the antibacterial action of copper ions may be attributed to the generation of ROS, which induces oxidative stress and/or damage in the bacteria.⁴⁹ In addition to ROS production, the cationic interaction of Ag⁺ and Cu²⁺ with negatively charged components of the bacteria cell membrane results in improved bactericidal efficacy at higher concentrations, achieved through the processes of cell lysis and bacteria collapse.⁵⁰ Hence, it is expected that both Cu and AgNps are able to interact with the entire surface of the bacterium. As a result, the copper and silver ions, which are toxic to bacteria, penetrate the cell wall, initiating a series of reactions that ultimately result in cell death.^{51,22} Drawing on these findings, it can be suggested that the antimicrobial activity primarily stems from the presence of silver in AgNp, while the addition of copper ions further enhances its antibacterial efficacy. Consistent with this, Mujeeb *et al.* found that silver–copper nanocomposites (Ag–CuNCs), synthesized using an *Olex scandens* leaf extract, exhibited a greater antimicrobial activity than mono-metallic AgNps. Importantly, this enhanced antimicrobial activity was associated with an increase in the production of ROS.⁵²

CONCLUSIONS

In the present study, PPy and Cu–PPy composites underwent electrochemical modification using two different sizes of AgNps. The results demonstrated that a higher concentration of metallic silver in the composite corresponded to a larger size of nanoparticles. Furthermore, it was found that the size of AgNps deposited on the PPy film influenced the antibacterial activity of the modified composites. It was proposed that the higher antibacterial efficacy of PPy/AgNp₅₀₀, compared to PPy/AgNp₁₀₀, can be attributed to a greater release of ionic silver resulting from the larger nanoparticle size. Although all PPy-modified films exhibited antibacterial properties, Cu–PPy/AgNp₅₀₀ emerged as the composite that exhibited the strongest antibacterial activity against most of the species tested. This heightened antibacterial activity can be largely ascribed to the synergistic potential of both metals for eradicating bacteria. The surface modification of 316L SS with these films holds promise as a viable alternative for the development of novel antibacterial composites capable of inhibiting the proliferation of large amounts of bacteria.

SUPPLEMENTARY MATERIAL

Additional data and information are available electronically at the pages of journal website: <https://www.shd-pub.org.rs/index.php/JSCS/article/view/12276>, or from the corresponding author on request.

Acknowledgements. The financial support provided by CONICET (2021-2023 GI-11220200102064CO), ANPCYT (PICT-2019-02758) and Universidad Nacional del Sur (PGI-UNS 24/M159), in Bahía Blanca, Argentina, are gratefully acknowledged.

ИЗВОД

БАКТЕРИЦИДНИ ЕФЕКАТ КОМПОЗИТА БАКАР–ПОЛИПИРОЛ МОДИФИКОВАНИХ НАНОЧЕСТИЦАМА СРЕБРА НА ГРАМ-ПОЗИТИВНЕ И ГРАМ-НЕГАТИВНЕ БАКТЕРИЈЕ

PATRICIA L. MARUCCI¹, MARIA G. SICA^{1,2}, LORENA I. BRUGNONI^{1,3} и MARÍA V. GONZÁLEZ⁴

¹Department of Biology, Biochemistry and Pharmacy, National University of the South, Bahía Blanca, Argentina, ²Department of Health Sciences, National University of the South, Bahía Blanca, Argentina, ³Institute of Biological and Biomedical Sciences, National University of the South, CONICET, Bahía Blanca, Argentina and ⁴Chemical Engineering Department, Institute of Electrochemistry and Corrosion Engineering, National University of the South, CONICET, Bahía Blanca, Argentina

У раду је испитиван бактерицидни ефекат композита бакар–полипирол (Cu–PPy) таложених на нерђајући челик 316L и модификованих сребром. Процењена су антимикробна својства према двадесет четири соја Грам-позитивних и Грам-негативних бактерија. Међу двадесет четири проучавана соја, изолати су укључивали референтне сојева (*Escherichia coli* ATCC 25922, *Escherichia coli* 0157:H7 EDL 933, *Staphylococcus aureus* ATCC 25923 и *Listeria monocytogenes* ATCC 7644), као и сојева изоловане из хране и клиничке узорке. Антимикробна активност композита показала је да сви филмови модификованог полипирила имају антибактеријска својства. Значајно је да је Cu–PPyAgNp₅₀₀ показао најјачу инхибиторну активност против Грам-негативних и Грам-позитивних бактерија. Модификација површине челика 316L овим филмовима је обећавајућа и одржива алтернатива за развој нових антибактеријских композита који могу инхибирати раст значајног броја бактерија.

(Примљено 13. фебуара, ревидирано 26. марта, прихваћено 2. августа 2023)

REFERENCES

1. World Health Organization (WHO), 2021, *Antimicrobial resistance*, Available from <https://www.who.int/news-room/fact-sheets/detail/antimicrobial-resistance> (accessed 26 October 2022)
2. World Health Organization (WHO), 2015, *Global Action plan antimicrobial resistance*, Document Production Services, Geneva, Switzerland. Available from <https://ahpsr.who.int/publications/i/item/global-action-plan-on-antimicrobial-resistance> (accessed 26 October 2022)
3. E. Seebach, K. F. Kubatzky, *Front. Immunol.* **10** (2019) 1724 (<https://doi.org/10.3389/fimmu.2019.01724>)
4. M. Z. Ibrahim, A. A. D. Sarhan, F. Y. M. Hamdi, *J. Alloys Compd.* **714** (2017) 636 (<https://doi.org/10.1016/j.jallcom.2017.04.231>)
5. N. F. Kamaruzzaman, L. P. Tan, R. H. Hamdan, S. S. Choong, W. K. Wong, A. J. Gibson, A. Chivu, M. de F. Pina, *Int. J. Mol. Sci.* **20** (2019) 2747 (<https://doi.org/10.3390/ijms20112747>)
6. K. Jlassi, M. H. Sliem, F. M. Benslimane, N. O. Eltai, A. M. Abdullah, *Prog. Org. Coat.* **149** (2020) 105918 (<https://doi.org/10.1016/j.porgcoat.2020.105918>)
7. M. Wang, and T. Tang, *J. Orthop. Transl.* **17** (2019) 42 (<https://doi.org/10.1016/j.jot.2018.09.001>)
8. M. Maruthapandi, A. Saravanan, A. Gupta, J. H. T. Luong, A. Gedanken, *Macromol.* **2** (2022) 78 (<https://doi.org/10.3390/macromol2010005>)
9. B. Balasubramaniam, Prateek, S. Ranjan, M. Saraf, P. Kar, S. P. Singh, V. K. Thakur, A. Singh, R. K. Gupta, *ACS Pharmacol. Transl. Sci.* **4** (2021) 8 (<https://doi.org/10.1021/acsptsci.0c00174>)

10. M. Talikowska, X. Fu, G. Lisak, *Biosens. Bioelectron.* **135** (2019) 50 (<https://doi.org/10.1016/j.bios.2019.04.001>)
11. E. N. Zare, T. Agarwal, A. Zarepour, F. Pinelli, A. Zarrabi, F. Rossi, M. Ashrafizadeh, A. Maleki, M. Shahbazi, T. K. Maiti, R. S. Varma, F. R. Tay, M. R. Hamblin, V. Mattoli, P. Makvandi, *Appl. Mater. Today* **24** (2021) 101117 (<https://doi.org/10.1016/j.apmt.2021.101117>)
12. A. Singh, A. Goswami, S. Nain, *Appl. Nanosci.* **10** (2020) 2255 (<https://doi.org/10.1007/s13204-020-01394-y>)
13. M. Balaji, P. Nithya, A. Mayakrishnan, S. Jegatheeswaran, S. Selvam, Y. Cai, J. Yao, M. Sundrarajan, *Appl. Surf. Sci.* **510** (2020) 145403 (<https://doi.org/10.1016/j.apsusc.2020.145403>)
14. M. B. González, D. O. Flamini, L. I. Brugnoli, L. M. Quinzani, S. B. Saidman, *J. Water Health* **16** (2018) 921 (<https://doi.org/10.2166/wh.2018.072>)
15. M. B. González, L. I. Brugnoli, D. O. Flamini, L. M. Quinzani, S. B. Saidman, *Environ. Monit. Assess.* **189** (2017) 53 (<https://doi.org/10.1007/s10661-016-5764-7>)
16. M. B. González, L. I. Brugnoli, M. E. Vela, S. B. Saidman, *Electrochim. Acta* **102** (2013) 66 (<https://doi.org/10.1016/j.electacta.2013.03.116>)
17. A. Martinez, L. Brugnoli, D. Flamini, S. Saidman, *Prog. Org. Coat.* **144** (2020) 105650 (<https://doi.org/10.1016/j.porgcoat.2020.105650>)
18. Y. Qing, L. Cheng, R. Li, G. Liu, Y. Zhang, X. Tang, J. Wang, H. Liu, L. Qin, *Int. J. Nanomed.* **13** (2018) 3311 (<http://dx.doi.org/10.2147/IJN.S165125>)
19. K. M. Rice, G. K. Ginjupalli, N. D. P. K. Manne, C. B. Jones, E. R. Blough, *Nanotechnology* **30** (2019) 372001 (<https://doi.org/10.1088/1361-6528/ab0d38>)
20. T. V. Basova, E. S. Vikulova, S. I. Dorovskikh, A. Hassan, N. B. Morozova, *Mater. Des.* **204** (2021) 109672 (<https://doi.org/10.1016/j.matdes.2021.109672>)
21. D. Mitra, E. T. Kang, K. G. Neoh, *Appl. Mater. Interfaces* **12** (2020) 21159 (<https://doi.org/10.1021/acsami.9b17815>)
22. I. Salah, I. P. Parkin, E. Allan, *RSC Adv.* **11** (2021) 18179 (<https://doi.org/10.1039/D1RA02149D>)
23. Y. Zhuang, S. Zhang, K. Yang, L. Ren, K. Dai, *J. Biomed Mater. Res., B* **108** (2020) 484 (<https://doi.org/10.1002/jbm.b.34405>)
24. P. L. Marucci, N. L. Olivera, L. I. Brugnoli, M. G. Sica, M. A. Cubitto, *Environ. Monit. Assess.* **175** (2011) 1 (<https://doi.org/10.1007/s10661-010-1488-2>)
25. A. Scheludko, M. Todorova, *Bull. Acad. Bulg. Sci. Phys.* **3** (1952) 61
26. A. W. Bauer, W. M. Kirby, J. C. Sherris, M. Turck, *Am. J. Clin. Pathol.* **45** (1966) 493
27. M. B. González, O. V. Quinzani, M. E. Vela, A. A. Rubert, G. Benítez, S. B. Saidman, *Synth. Met.* **162** (2012) 1133 (<http://doi.org/10.1016/j.synthmet.2012.05.013>)
28. A. Alqudami, S. Annapoorni, P. Sen, R. S. Rawat, *Synth. Met.* **157** (2007) 53 (<http://doi.org/10.1016/j.synthmet.2006.12.006>)
29. M. B. González, S. B. Saidman, *Corros. Sci.* **53** (2011) 276 (<https://doi.org/10.1016/j.corsci.2010.09.021>)
30. R. Holze *Polymers* **14** (2022) 1584 (<https://doi.org/10.3390/polym14081584>)
31. Q. Pei, R. Qian, *Electrochim. Acta* **37** (1992) 1075 ([https://doi.org/10.1016/0013-4686\(92\)85225-A](https://doi.org/10.1016/0013-4686(92)85225-A))
32. A. Singh, Z. Salmi, N. Joshi, P. Jha, A. Kumar, H. Lecoq, S. Lau, M. M. Chehimi, D. K. Aswal, S. K. Gupta, *RSC Adv.* **3** (2013) 5506 (<https://doi.org/10.1039/C3RA22981E>)

33. M. Diantoro, T. Suprayogi, U. Sa'adah, N. Mufti, A. Fuad, A. Hidayat, H. Nur, in *Silver Nanoparticles*, K. Maaz, Ed., InTech, Rijeka, 2018 (<https://doi.org/10.5772/intechopen.75682>)
34. K. F. Babu, P. Dhandapani, S. Maruthamuthu, M. A. Kulandainathan, *Carbohydr. Polym.* **90** (2012) 1557 (<https://doi.org/10.1016/j.carbpol.2012.07.030>)
35. N. Song, S. Chen, D. Tian, Y. Li, C. Wang, X. Lu, *Mat. Today Chem.* **18** (2020) 100374 (<https://doi.org/10.1016/j.mtchem.2020.100374>)
36. J. Shu, Z. Qiu, S. Lv, K. Zhang, D. Tang, *Anal. Chem.* **89** (2017) 11135 (<https://doi.org/10.1021/acs.analchem.7b03491>)
37. B. Chudasama, A. K. Vala, N. Andhariya, R. V. Mehta, R. V. Upadhyay, *J. Nanopart. Res.* **12** (2010) 1677 (<https://doi.org/10.1007/s11051-009-9845-1>)
38. J. S. Kim, E. Kuk, K. N. Yu, J. Kim, S. J. Park, H. J. Lee, S. H. Kim, Y. K. Park, Y. H. Park, C. Hwang, Y. Kim, Y. Lee, D. H. Jeong, M. Cho, *Nanomed.: Nanotechnol. Biol. Med.* **3** (2007) 95 (<https://doi.org/10.1016/j.nano.2006.12.001>)
39. J. Jain, S. Arora, J. M., P. Omray, S. Khandelwal, K. M. Paknikar, *Mol. Pharm.* **6** (2009) 1388 (<https://doi.org/10.1021/mp900056g>)
40. J. P. Ruparelia, S. P. Duttagupta, A. K. Chatterjee, S. Mukherji, *Acta Biomater.* **4** (2008) 707 (<https://doi.org/10.1016/j.actbio.2007.11.006>)
41. D. Longano, N. Ditaranto, L. Sabbatini, L. Torsi, N. Cioffi, in *Nano-Antimicrobials*, N. Cioffi, M. Rai, Eds., Springer, Berlin, 2011, pp. 85–117 (https://doi.org/10.1007/978-3-642-24428-5_3)
42. G. A. Sotiriou, A. Meye, J. T. Knijnenburg, S. Panke, S. E. Pratsinis, *Langmuir* **28** (2012) 15929 (<https://doi.org/10.1021/la303370d>)
43. J. S. McQuillan, A. M. Shaw, *Nanotoxicology* **8** (2014) 177 (<https://doi.org/10.3109/17435390.2013.870243>)
44. I. P. Mukha, A. M. Eremenko, N. P. Smirnova, A. I. Mikhienkova, G. I. Korchak, V. F. Gorchev, A. Y. Chunikhin, *Appl. Biochem. Microbiol.* **49** (2013) 199 (<http://doi.org/10.1134/S0003683813020117>)
45. Y. Dong, H. Zhu, Y. Shen, W. Zhang, L. Zhang, *PLoS ONE* **14** (2019) e0222322 (<https://doi.org/10.1371/journal.pone.0222322>)
46. M. Oves, M. A. Rauf, A. Hussain, H. A. Qari, A. A. P. Khan, P. Muhammad, M. T. Rehman, M. F. Alajmi, I. L. M. Ismail, *Front. Pharmacol.* **10** (2019) 801 (<https://doi.org/10.3389/fphar.2019.00801>)
47. J. R. Morones-Ramirez, J. A. Winkler, C. S. Spina, J. J. Collins, *Sci. Transl. Med.* **5** (2013) 190ra81 (<https://doi.org/10.1126/scitranslmed.3006276>)
48. S. Khorrami, A. Zarrabi, M. Khaleghi, M. Danaei, M. R. Mozafari, *Int. J. Nanomed.* **13** (2018) 8013 (<https://doi.org/10.2147/IJN.S189295>)
49. G. Applerot, J. Lellouche, A. Lipovsky, Y. Nitzan, R. Lubart, A. Gedanken, E. Banin, *Small* **8** (2012) 3326 (<https://doi.org/10.1002/sml.201200772>)
50. L-U. Rahman, A. Shah, S. K. Lunsford, C. Han, M. N. Nadagoud, E. Sahle-Demessie, R. Qureshi, M. S. Khan, H-B Kraatz, D. D. Dionysiou, *RSC Adv.* **5** (2015) 44427 (<https://doi.org/10.1039/C5RA03633J>)
51. T. V. Basova, E. S. Vikulova, S. I. Dorovskikh, A. Hassan, N. B. Morozova, *Mater. Des.* **204** (2021) 109672 (<https://doi.org/10.1016/j.matdes.2021.109672>)
52. A. Mujeeb, N. A. Khan, F. Jamal, K. F. Badre Alam, H. Saeed, S. Kazmi, A.W.F. Alshameri, M. Kashif, I. Ghazi M. Owais, *Front. Chem.* **8** (2020) 103 (<https://doi.org/10.3389/fchem.2020.00103>).



SUPPLEMENTARY MATERIAL TO
**Bactericidal effects of copper–polypyrrole composites modified
with silver nanoparticles against Gram-positive and
Gram-negative bacteria**

PATRICIA L. MARUCCI¹, MARIA G. SICA^{1,2}, LORENA I. BRUGNONI^{1,3}
and MARÍA B. GONZÁLEZ^{4*}

¹Department of Biology, Biochemistry and Pharmacy, National University of the South, Bahía Blanca, Argentina, ²Department of Health Sciences, National University of the South, Bahía Blanca, Argentina, ³Institute of Biological and Biomedical Sciences, National University of the South, CONICET, Bahía Blanca, Argentina and ⁴Chemical Engineering Department, Institute of Electrochemistry and Corrosion Engineering, National University of the South, CONICET, Bahía Blanca, Argentina

J. Serb. Chem. Soc. 88 (9) (2023) 889–904

TABLE S-I.

Strain	Coatings		
	PPy/AgNp ₁₀₀	PPy/AgNp ₅₀₀	Cu-PPy/AgNp ₅₀₀
<i>Staphylococcus aureus</i> ATCC 25923	4 ± 0	4 ± 1	5 ± 1
<i>Staphylococcus aureus</i> (1)	6 ± 0	5 ± 1	7 ± 1
<i>Staphylococcus aureus</i> (2)	5 ± 1	7 ± 1	9 ± 1
<i>Staphylococcus aureus</i> (3)	0	0	6 ± 0
<i>Staphylococcus aureus</i> (4)	0	3 ± 1	5 ± 1
<i>Staphylococcus aureus</i> (5)	0	11 ± 1	10 ± 2
<i>Staphylococcus aureus</i> (6)	0	8 ± 0	8 ± 0
<i>Staphylococcus aureus</i> (7)	0	6 ± 0	1 ± 1
<i>Staphylococcus aureus</i> (8)	2 ± 0	3 ± 1	6 ± 0
<i>Staphylococcus aureus</i> (9)	2 ± 0	7 ± 1	4 ± 0
<i>Staphylococcus aureus</i> (10)	2 ± 0	9 ± 1	11 ± 1
<i>Staphylococcus aureus</i> (11)	2 ± 0	4 ± 0	4 ± 0
<i>Staphylococcus aureus</i> (12)	2 ± 0	6 ± 0	11 ± 1
<i>Staphylococcus aureus</i> (13)	2 ± 0	6 ± 0	7 ± 1
<i>Escherichia coli</i> ATCC 25922	3 ± 1	1 ± 1	7 ± 1
<i>Escherichia coli</i> (6)	2 ± 0	2 ± 0	2 ± 0
<i>Escherichia coli</i> (17)	1 ± 1	7 ± 1	4 ± 0
<i>Escherichia coli</i> (19)	0	2 ± 0	4 ± 0
<i>Escherichia coli</i> (28)	2 ± 1	7 ± 1	3 ± 1
<i>Escherichia coli</i> O157H7 (933)	5 ± 1	5 ± 1	7 ± 1

* Corresponding author. E-mail: belen.gonzalez@uns.edu.ar



S272

MARUCCI *et al.*

<i>Salmonella enterica</i>	1 ± 1	2 ± 0	6 ± 0
<i>Pseudomonas aeruginosa</i>	3 ± 1	4 ± 0	6 ± 0
<i>Listeria monocytogenes</i> ATCC 7644	2 ± 0	0	0
<i>Listeria innocua</i>	0	6 ± 0	9 ± 1



J. Serb. Chem. Soc. 88 (9) 905–919 (2023)
JSCS–5670

Mass transfer in inverse fluidized beds

DARKO JAĆIMOVSKI¹, KATARINA ŠUĆUROVIĆ^{1#}, MIHAL ĐURIŠ^{1#*}, ZORANA ARSENIJEVIĆ^{1#}, SANJA KRSTIĆ² and NEVENKA BOŠKOVIĆ-VRAGOLOVIĆ^{3#}

¹*Institute of Chemistry, Technology and Metallurgy-National Institute of the Republic of Serbia, University of Belgrade, Belgrade, Serbia,* ²*Vinča institute of Nuclear Sciences-National Institute of the Republic of Serbia, University of Belgrade, Belgrade, Serbia and* ³*Faculty of Technology and Metallurgy, University of Belgrade, Belgrade, Serbia*

(Received 16 January, revised 27 February, accepted 22 March 2023)

Abstract: In this work, the coefficient of fluid-wall mass transfer in an inverse fluidized bed was determined using the adsorption method. The experiments were carried out in a column with a diameter of 45 mm with spherical and non-spherical particles of polypropylene and polyethylene with a diameter of 3.3–4.9 mm and a density of about 930 kg m⁻³. A diluted solution of methylene blue was used as a fluidization medium, which was adsorbed on part of the surface of the column on silica gel. The obtained results showed that the presence of particles during inverse fluidization does not contribute significantly to mass transfer compared to the influence of particles on transfer in conventional fluidized beds. Therefore, the pseudo-fluid concept was introduced into the analysis and an empirical correlation was performed to determine the mass transfer coefficient. The obtained results were compared with literature correlations for inverse and conventional fluidized beds.

Keywords: inverse fluidization; fluid-wall mass transfer; pseudo-fluid.

INTRODUCTION

Fluidized bed contactors, because of their efficiency and transfer intensity, are often used in systems where contact between liquids and solid particles is required. When the solid phase has a lower density than the liquid phase, fluidization can be achieved by the liquid flowing into the column from the top and forming the bed in the opposite way compared to a conventional bed. Such beds are inverse fluidized beds.

Inverse fluidization is most commonly used in wastewater treatment in bio-reactors or in some adsorption processes. The beds formed this way have been

* Corresponding author. E-mail: mihal.djuris@ihtm.bg.ac.rs

Serbian Chemical Society member.

<https://doi.org/10.2298/JSC230116016J>

shown to be effective for formation and maintenance of biofilm. For the practical application of inverse fluidized beds in various contactors, it is necessary to know the fluid dynamics of these systems and the mass transfer achieved.

Wang *et al.*¹ studied the removal of oil from an emulsion in water by inverse fluidization with a hydrophobic air gel. The authors used nanogel sizes: 0.5–0.85 mm; 0.7–1.2 mm; 1.7–2.35 mm, the density was 64 kg m^{-3} . The experiments were performed in columns with a diameter of 7.6 cm and lengths of 1.47 m and 0.77 m. The oil concentration is monitored using the *COD* (chemical oxygen demand). The authors have proposed a model that is consistent with the experimental data. It has been shown that the most important parameters affecting oil removal and thus mass transfer are granule size, bed height and fluid velocity.

Inverse fluidization is applied in bioreactors where the necessary oxygen is supplied to the microorganisms in a three-phase fluidized bed. The application of inverse fluidization in fluidized bed biofilm reactors (FBBR) is shown in the work of Begum and Radha² in which the aerobic biodegradation of phenol was studied using the microorganism *Pseudomonas fluorescens*. The authors performed the experimental tests in a column with a height of 105 cm and a diameter of 10 cm. Polystyrene particles with a diameter of 3.5 mm and a density of 863 kg m^{-3} were used as biofilm carriers. Mass transfer is monitored by the parameter *COD*. It was shown that the value of *COD* removal increases with the gas velocity and the ratio of the volume of settled bed to the working volume (V_b/V_R). In the best case, *COD* reduction is 98.5 %. Similarly, the biological treatment of wastewater in an inverse fluidized bed system was performed by Sokol *et al.*³ These authors performed the removal of phenol, cresol, isopropylphenol, dimethylphenol, benzene and toluene from wastewater in a column with an internal diameter of 20 cm and a height of 6 m with polypropylene particles of density 910 kg m^{-3} as biofilm carriers in an inverse fluidized bed. Mass transfer was monitored using the *COD* parameter. It is shown that the operating conditions that give the best results are $V_b/V_R = 0.55$ and a gas velocity of 0.024 m s^{-1} .

The inverse fluidized bed was used for the treatment of wastewater containing starch.⁴ The experiments were performed in a column with a diameter of 9.2 mm and a height of 1.6 m. Irregularly shaped polypropylene particles with a density of 870 kg m^{-3} were used as carrier particles. Mass transfer was monitored using the *COD* parameter. The reduction of the *COD* parameter increased with the air flow rate and with the duration of the experiment. Wastewater treatment in an inverse fluidized system was investigated by Karmanev and Nikolov.⁵ Spherical polystyrene particles with an average diameter of 2.5 mm and density of 200 kg m^{-3} were used as carriers. It can be seen that biochemical oxygen demand (*BOD*) decreases with time. It has been confirmed that inverse fluidization systems are an effective system for treating wastewater with low pollutant concentrations.

The knowledge of mass transfer is necessary for the application of inverse fluidized beds. One of the few papers dealing with the study of mass transfer in an inverse fluidized bed is the work of Nikov and Karamanev⁶ who showed that better mass transfer is achieved by increasing the density difference between fluid and particles. The experimental data were compared with the literature correlations for mass transfer and the following correlation was proposed:

$$\text{Sh} = 0.28(\text{GaMvSc})^{0.33} \quad (1)$$

The experiments were carried out with polystyrene and polyethylene particles with a diameter of 2.2–7.1 mm and a density of 80–930 kg m⁻³. The fluidization medium was water and an aqueous solution of polyethylene glycol with a concentration of 1.9 % by mass. In their work, Kumar *et al.*⁷ monitored mass transfer in an inverse fluidized system using electrochemical methods. Mass transfer of lead ions was monitored by an electrochemical method in an inverse fluidized bed, where the fluidization medium was an aqueous solution of ferrous salts and ferricyanide in the presence of sodium hydroxide. Cylindrical particles with a diameter of 2.151 mm and a height of 5 mm and a density of 877.6 kg m⁻³ were used. The inverse fluidization was performed in a column with a diameter of 25.4 mm. As a result of these investigations, a correlation was established for the determination of the mass transfer factor:

$$j_D \varepsilon = 0.18 \left(\frac{\text{Re}_p}{1 - \varepsilon} \right)^{-0.30} \quad (2)$$

The aim of this work is to investigate wall-fluid mass transfer in the presence of inverse fluidized particles using the adsorption method. The experimental results are presented as a function of particle and bed parameters and compared with mass transfers in conventional fluidized beds.

EXPERIMENTAL

The scheme of the experimental apparatus is shown in Fig. 1. A cylindrical column with an inner diameter of 45 mm was used. At the top of the column there is a ring, on the inside of which there is a thin aluminium foil coated with silica gel. The column's inner diameter was not affected by the presence of the foil. The fluidization medium was a dilute aqueous solution of methylene blue with a concentration of 2×10^{-3} g L⁻¹. The experiments were performed at a temperature of 20 °C. Spherical and non-spherical polypropylene and polyethylene particles were used for the experiments, and their properties are given in Table I.

During the fluid flow from the top of the column, an inverse fluidized bed was formed in which methylene blue adsorbed on silica gel during the experiment, *i.e.*, fluid-wall mass transfer occurred in the presence of inert particles. One of the conditions for the application of the method is a short adsorption time to avoid saturation of the adsorption surface, therefore the experiments lasted about 5 min.⁸⁻¹⁰

At the end of each experiment, the coloration of the surface of the silica gel foil, which is equivalent to the adsorbed amount of methylene blue, was analysed using SigmaScan Pro

software.¹⁰⁻¹² Based on the surface concentration, the mass transfer coefficient was determined according to the following equation:

$$k = \frac{c_p}{c_0 t} \quad (3)$$

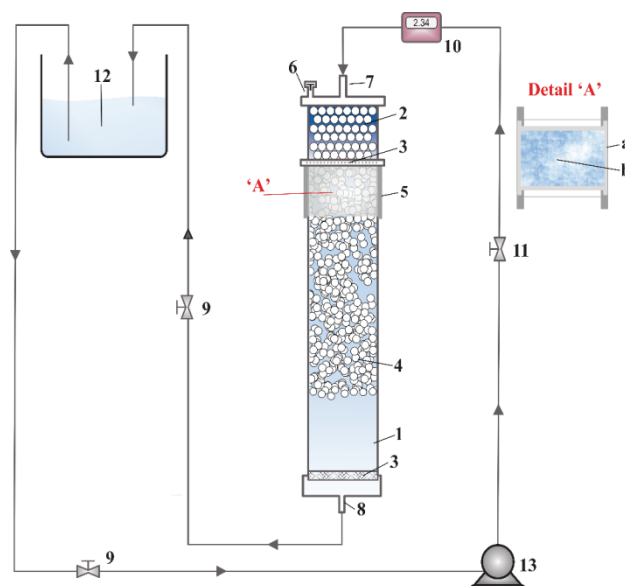


Fig. 1. Scheme of the experimental apparatus (1 – cylindrical column for inverse fluidization; 2 – distributor; 3 – grid; 4 – fluidized bed particles; 5 – inlet of the solution into the column; 6 – vent; 7 – piezometers; 8 – exit of the solution from the column; 9, 11 – valves; 10 – flow meter; 12 – reservoir; 13 – pump, 'A' – ring, a – silica gel foil, b – particles and methylene blue solution).

TABLE I. Properties of particles

Material	Diameter, mm	Sphericity	Density, kg m ⁻³
Polypropylene	3.3	1	935
Polypropylene	3.7	0.86	935
Polypropylene	4.4	0.85	937
Polyethylene	3.9	0.87	926

RESULTS AND DISCUSSION

Fig. 2 shows the dependence of the mass transfer coefficient (Eq. (3)) on the fluid velocity in the packed and in the inverse fluidized bed. The dependence shows a significant increase in the mass transfer coefficient at lower velocities, *i.e.*, in a packed bed of particles.

After reaching the fluidized state, the mass transfer coefficient increases slightly or is approximately constant. There are no significant differences in mass transfer in the bed with different particles because the differences in diameters

and sphericity are relatively small. For comparison, the mass transfer coefficient is also shown in the same diagram for a single-phase flow, *i.e.*, when only liquid (without particles) flows through the column. It can be seen that the presence of inert fluidized particles has no significant effect on mass transfer, probably due to the fact that the particle density is close to the liquid density.

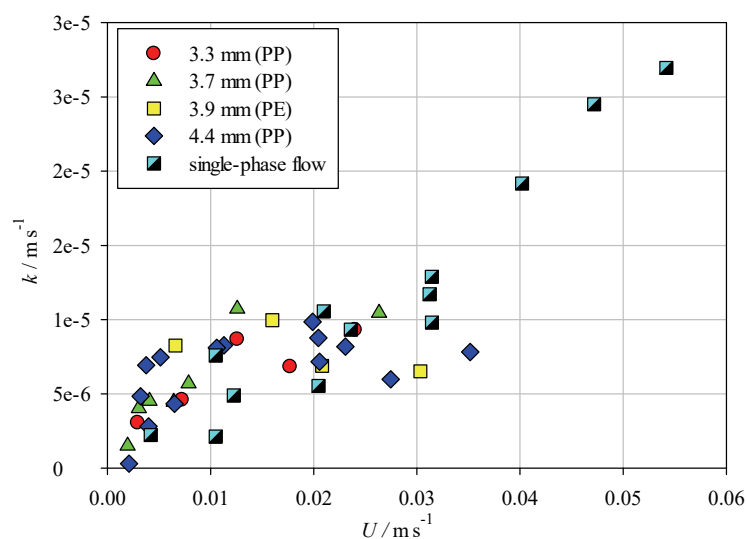


Fig. 2. Mass transfer coefficient in inverse fluidized bed and single-phase flow depending on fluid velocity.

A somewhat clearer dependence of the mass transfer coefficient on the bed parameters can be observed from the dependence of the Sherwood number (Sh) on the Reynolds number (Re), Fig. 3. From Fig. 3, it can be seen that the Sh in the fixed bed increases sharply with Re (*i.e.*, with the increase of the velocity U). In the fluidized bed, Sh also increases with the increase in Re , but somewhat less than in the packed bed. It is also evident that there is no effect of particle size and shape on the mass transfer coefficient in the inverse fluidized bed, since all the particles studied show a very similar dependence.

Fig. 4 shows the dependence of the mass transfer coefficient on the bed porosity ε . Since the bed porosity is a function of U , the dependence of $k = f(\varepsilon)$ practically follows the dependence of $k = f(U)$, Fig. 2. In a packed bed, where the porosity is constant, the mass transfer coefficient increases. During the transition to the fluidized bed state up to a bed porosity of about 0.7, the mass transfer coefficient continues to increase, while for higher values of bed porosity it becomes almost constant. Fig. 4 shows the appearance of a slight maximum on the curve, which also occurs with conventional fluidization.¹⁰ It is also evident that there is

no visible difference in the intensity of mass transfer in the inverse fluidized bed with different particle types and sizes.

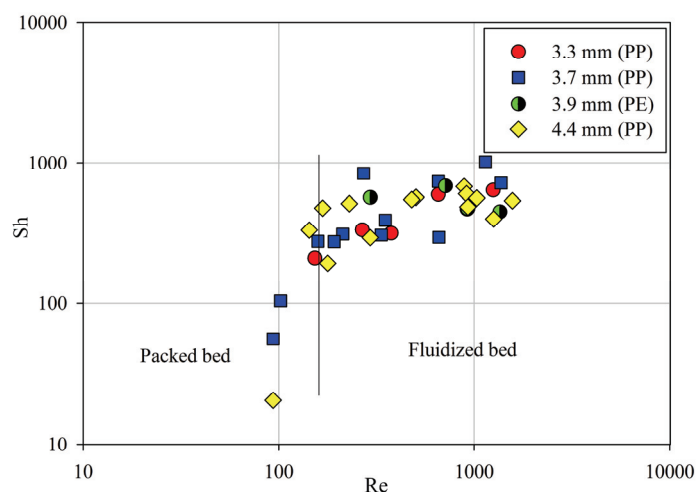


Fig. 3. Dependence of Sherwood on Reynolds number.

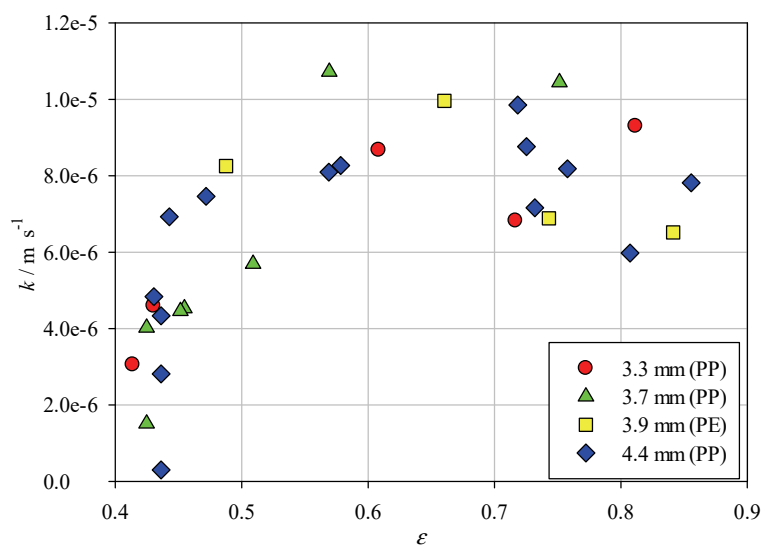


Fig. 4. Dependence of mass transfer coefficient on bed porosity for inverse fluidized bed (packed and fluidized bed).

The adsorption method used in this study to determine the mass transfer coefficient is also useful for flow visualization. Fig. 5 shows flow visualization images for different conditions (flows) of 4.4 mm diameter polypropylene particles in the bed. The chromatograms are shown for the same experimental con-

ditions (time duration, temperature, methylene blue concentration, *etc.*) but for different liquid flow rates. Fig. 5a–c are characteristic of the liquid flow where the particles are stable, *i.e.*, the packed bed. The flow patterns of the individual particles in the bed can be clearly seen. As the flow increases, it can be seen that the average colour intensity of the silica gel foil surfaces becomes higher. At the minimum fluidization velocity U_{mf} (Fig. 5d), the coloration of the silica gel foil surface is approximately uniform as the particles begin to oscillate slightly and mix the fluid. Fig. 5e and f are chromatograms taken in the fluidized bed and are characterized by the uniform coloration of the silica gel foil surface due to the intense mixing of the fluid by the particle fluidization. It can also be seen that the coloration of the surface is approximately the same at a higher flow rate in the fluidized bed.

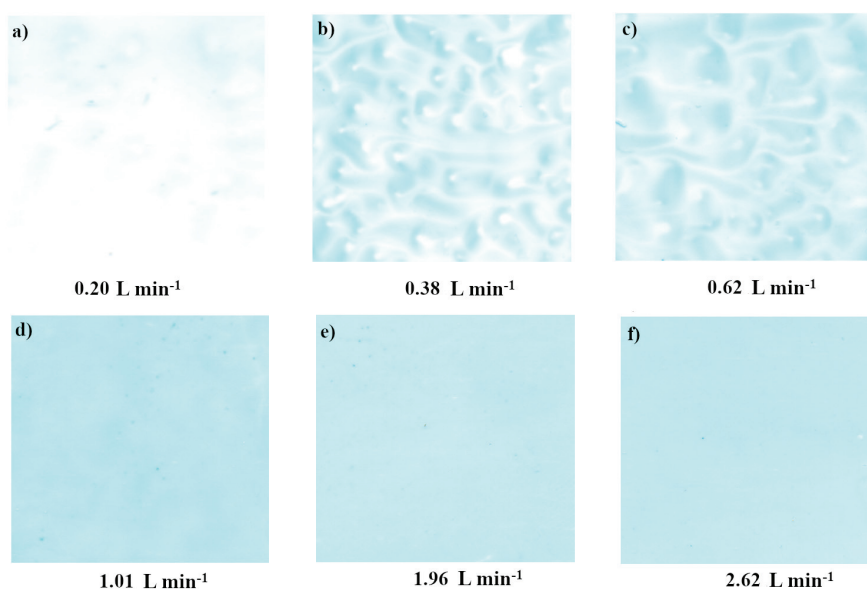


Fig. 5. Flow chromatogram in packed bed (a–c), at minimum fluidization (d) and in fluidized bed (e and f).

A comparison of the data obtained in inverse fluidized beds with those of a conventional fluidized bed as a function of bed porosity is shown in Fig. 6. The results presented for the conventional fluidized bed were carried out in a bed of spherical glass particles with a diameter of 3 mm and a density of $2,500 \text{ kg m}^{-3}$ with water as the fluidizing medium. These experiments were carried out under the same experimental conditions and in the same column. From the dependencies shown in Fig. 6, it can be seen that the influence of the particles on mass transfer in conventional fluidization is significantly greater than the influence of

the particles in inverse fluidization. This can be explained by the fact that significantly higher fluid velocities were used in conventional fluidization compared to inverse fluidization. Fig. 6 shows the occurrence of a maximum at a porosity of about 0.7, which is consistent with our previous studies.^{9,13}

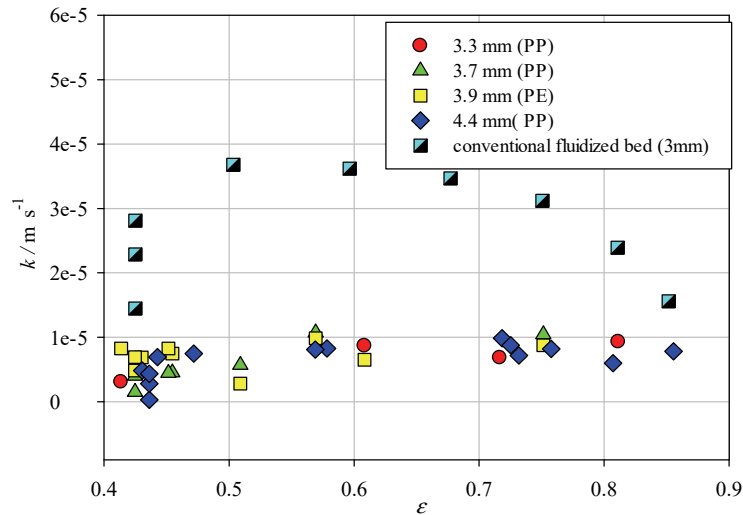


Fig. 6. Comparison of the mass transfer coefficient in inverse and conventional fluidized beds as a function of porosity.

Based on the experimentally determined results for the mass transfer coefficient, the mass transfer factor j_D was calculated. Fig. 7 shows the dependence of the mass transfer factor j_D on Re (Fig. 7a) and the porosity of the bed (Fig. 7b). Both dependences show a decrease in the mass transfer factor j_D with an increase in Re and the porosity of the bed which is consistent with our previous study.¹⁰

The diagram of the dependence of the mass transfer factor on Re also shows the data obtained for a single-phase fluid flow (Fig. 7a). It can be observed that the influence of the inverse fluidized particles on the mass transfer intensification is very small. This can be explained by the fact that in inverse fluidization the fluid velocity is low and therefore the collisions between the particles in the system are lower, so the influence on mass transfer is smaller.

The drag force in conventional fluidized beds is defined as:

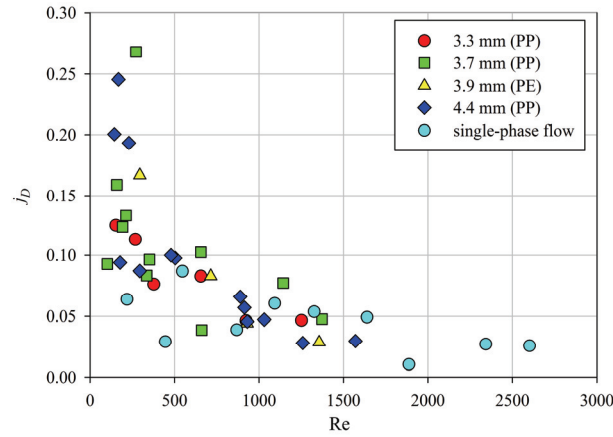
$$F_d = F_b - F_g = \frac{d_p^3 \pi}{6} (\rho_p - \rho_f) g \quad (4)$$

In inverse fluidized bed is defined as:

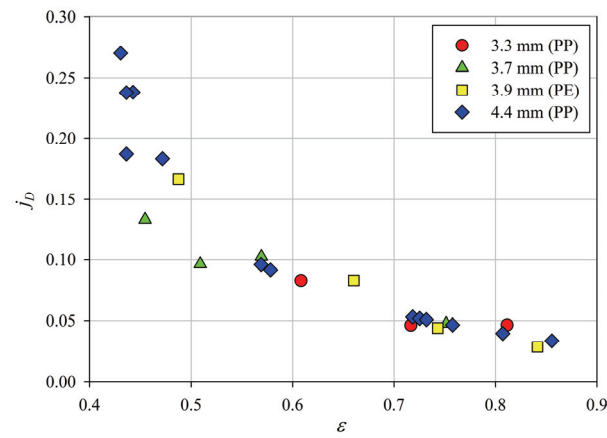
$$F_{d,inv} = F_g - F_b = \frac{d_p^3 \pi}{6} (\rho_f - \rho_p) g \quad (5)$$

The ratio of the drag force in these two systems is:

$$\frac{F_d}{F_{d,inv}} = \frac{d_p^3}{d_{p,inv}^3} \frac{\rho_p - \rho_f}{\rho_f - \rho_p} \quad (6)$$



(a)



(b)

Fig. 7. Dependence of the mass transfer factor on Reynolds number (a) and bed porosity (b).

Comparing conventional fluidization, in which particles with a diameter of 3 mm and a density of $2,500 \text{ kg m}^{-3}$ were used, with inverse fluidization, in which particles with a diameter of 3.7 mm and a density of 935 kg m^{-3} were used (the fluid density in both cases is 1000 kg m^{-3}), the following relationship is obtained:

$$\frac{F_d}{F_{d,inv}} = 3.63 \quad (7)$$

It is found that the friction in the inverse fluidized bed is 3.6 times lower than in the conventional fluidized bed. Due to the small effect of particle–fluid friction in the inverse fluidized bed, the entire bed can be treated as a pseudo-fluid. All this indicates that although the conventional and inverse fluidized beds are described by the same equations, the frictional force is lower in the case of the inverse fluidized bed, so it is mainly used in biofilm reactors where the frictional forces do not disturb the formed biofilm, which is important for mass transfer in such reactors. The system behaves like a pseudo-fluid, and the frictional forces do not damage the biofilm. On the other hand, the particles are still present and provide gentle mixing, which is ideal for biosystems where microorganisms are involved in the reaction:^{14,15}

$$\text{Re}_{\text{pf}} = \frac{d_p \rho_{\text{pf}} U_{\text{pf}}}{\mu_{\text{pf}}} \quad (8)$$

where pseudo-fluid density is defined as:

$$\rho_{\text{pf}} = \varepsilon \rho_f + (1 - \varepsilon) \rho_p \quad (9)$$

and pseudo-fluid dynamic viscosity as:

$$\mu_{\text{pf}} = \mu_f \exp\left(\frac{5(1 - \varepsilon)}{3\varepsilon}\right) \quad (10)$$

Superficial fluid velocity can be calculated:

$$U_{\text{pf}} = \frac{G_f}{\rho_f A} + \frac{G_p}{\rho_p A} \quad (11)$$

Since in a particulate fluidized bed the total particle motion in the column is zero ($G_p = 0$), the velocity of the pseudo-fluid is equal to the superficial fluid velocity:

$$U_{\text{pf}} = \frac{G_f}{\rho_f A} = U \quad (12)$$

Based on the experimental results, the equation for the mass transfer factor was established:

$$j_D = \text{Re}_{\text{pf}}^{-0.48}, \quad 13 < \text{Re}_{\text{pf}} < 980 \quad (13)$$

Fig. 8 shows the dependence of the mass transfer factor j_D on the Reynolds number of a pseudo-fluid, Re_{pf} . The obtained equation agrees well with the experimental data. The mean absolute deviation of the experimental data from the data calculated by the established equation is 14.1 %, while the relative deviation is –4 %.

Table II shows some selected correlations for the determination of mass transfer factors in conventional and inverse fluidized beds and compares them

with our experimentally obtained data. The comparison of the experimental data with the data calculated according to the above correlations is shown in Fig. 9.

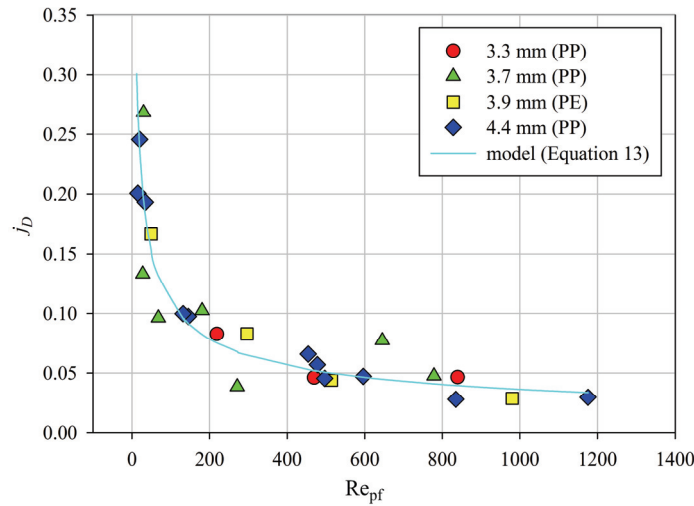


Fig. 8. Dependence of the mass transfer factor on the Reynolds number of a pseudo-fluid.

It is interesting to note that the correlation of Yutani *et al.*¹⁶ (Eq. (14)), was originally derived for conventional fluidized beds, and the correlation of Nikov and Karamanev⁶ (Eq. (17)) for inverse fluidized beds shows significant deviation from the experimental data. Very good agreement with the experimental data is shown by the correlations for conventional fluidization of Marooka *et al.*¹⁷ (Eq. (15)) and Kunii and Levenspiel¹⁸ (Eq. (16)), as can be seen in Table II.

TABLE II. Comparison of literature correlations with experimental data and the obtained model

Authors	Fluidization	Model	$\sigma_R, \%$	$\sigma_A, \%$
Yutani <i>et al.</i> ¹⁶ (Eq. (14))	Conventional	$j_D = \frac{0.4}{\varepsilon} Re_p^{0.4}$	71.5	73.5
Marooka <i>et al.</i> ¹⁷ (Eq. (15))	Conventional	$j_D = \frac{0.6}{\varepsilon} \left(\frac{Re_p}{1-\varepsilon} \right)^{-0.5}$	-6.93	14.9
Kunii and Levenspiel ¹⁸ (Eq. (16))	Conventional	$j_D = \frac{2}{Re_p} + \frac{0.51}{Re_p} [(1-\varepsilon)Re_p]^{-0.5}$	-0.89	14.6
Nikov and Karamanev ⁶ (Eq. (17))	Inverse	$j_D = \frac{0.28}{Re} (GaMv)^{0.33}$	-82.4	81.5
Our correlation (Eq. (13))	Inverse	$j_D = Re_{pf}^{-0.48}$	-4.0	14.1

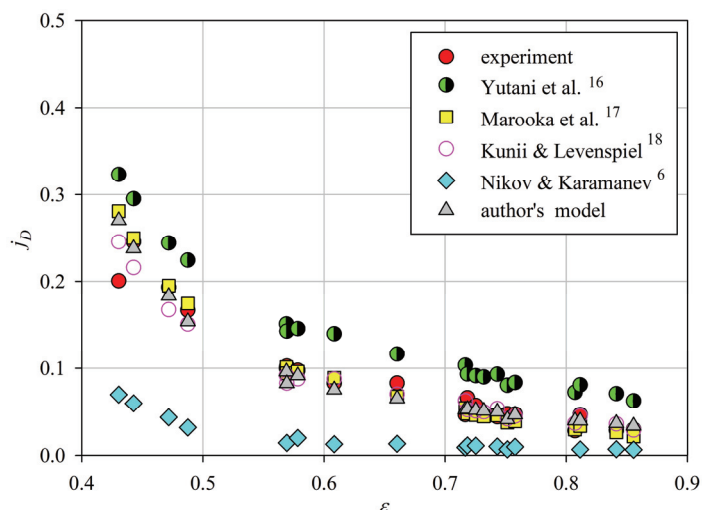


Fig. 9. Comparison of the experimental data with the obtained model and the correlations in the literature.

CONCLUSION

In the paper, the fluid–wall mass transfer coefficient was experimentally determined in an inverse fluidized bed. The results show a significant increase in the mass transfer coefficient with flow velocity in the packed bed, while a slight increase is observed in the fluidized bed. Compared to the mass transfers in a fluid flow without particles, it was found that the presence of particles does not contribute significantly to the intensification of the transfer, which is due to the low frictional force between particles and fluid. Based on the obtained results, the inverse fluidized bed was classified as a pseudofluid and a new correlation was presented, which represents the dependence of the mass transfer factor on the Reynolds number of a pseudo-fluid:

$$j_D = \text{Re}_{\text{pf}}^{-0.48}, \quad 13 < \text{Re}_{\text{pf}} < 980$$

The obtained experimental results deviate from the proposed correlation by less than 14.1 %, with the mean relative deviation being –4 %.

When comparing the experimentally obtained data with the correlations from the literature, it was found that the correlations of Marooka *et al.*¹⁷ (Eq. (15)) and Kunii and Levenspiel¹⁸ (Eq. (16)) for conventional fluidization show very good agreement with the experimental data.

NOMENCLATURE

<i>BOD</i>	biochemical oxygen demand
<i>COD</i>	chemical oxygen demand
<i>A</i>	cross section area, m ²
<i>c_p</i>	surface concentration of methylene blue on adsorbent layer, kg m ⁻²

c_0	bulk concentration of methylene blue, kg m^{-2}
$d_{p,\text{inv}}$	particle diameter in inverse fluidized bed, m
d_p	particle diameter, m
D_c	column diameter, m
F_D	drag force, N
F_b	buoyancy force, N
F_g	gravity force, N
g	gravitational acceleration, m s^{-2}
G_f	mass flow fluids, kg s^{-1}
G_p	mass flow particle, kg s^{-1}
j_D	mass transfer factor
k	coefficient mass transfer, m s^{-1}
t	time, s
U	superficial fluid velocity, m s^{-1}
U_{pf}	superficial pseudofluid velocity, m s^{-1}
V_b/V_R	ratio of the volume of the settled bed to the working volume
ε	bed porosity
μ_f	viscosity fluid, $\text{Pa}\cdot\text{s}$
μ_{pf}	viscosity pseudofluids, $\text{Pa}\cdot\text{s}$
ρ_f	fluid density, kg m^{-3}
ρ_p	particle density, kg m^{-3}
ρ_{pf}	pseudofluid density, kg m^{-3}
Ga	$(d_p^3 \rho_f^2 g / \mu_f^2)$, Galileo number
Mv	$((\rho_p - \rho_f) / \rho_f)$, relative density
Re	$(U_f D_c \rho_f / \mu_f)$, Reynolds number
Re_p	$(U_f d_p \rho_f / \mu_f)$, Reynolds number for particle
Re_{pf}	Reynolds number for pseudo-fluid
Sh	$(k D_c / D_{AB})$, Sherwood number
Sc	$(\mu_f / \rho_f D_{AB})$, Schmidt number
σ_A	$\left(\frac{1}{N} \sum_1^N \left \frac{X_{\text{exp}} - X_{\text{cal}}}{X_{\text{exp}}} \right \right)$, absolute deviations
σ_R	$\left(\frac{1}{N} \sum_1^N \frac{X_{\text{exp}} - X_{\text{cal}}}{X_{\text{exp}}} \right)$, relative deviations

Acknowledgement. This work was financially supported by the Ministry of Science, Technological Development and Innovation of the Republic of Serbia (Grant No. 451-03-47/2023-01/200026 and 451-03-47/2023- 01/200135).

ИЗВОД

ПРЕНОС МАСЕ У ИНВЕРЗНО-ФЛУИДИЗОВАНОМ СЛОЈУ

ДАРКО ЈАЃИМОВСКИ¹, КАТАРИНА ШУЋУРОВИЋ¹, МИХАЛ ЂУРИШ¹, ЗОРАНА АРСЕНИЈЕВИЋ¹, САЊА КРСТИЋ² и НЕВЕНКА БОШКОВИЋ-ВРАГОЛОВИЋ³

¹Институт за хемију, технологију и металургију-Институт од националног значаја за Републику Србију, Универзитет у Београду, Београд, ²Винча Институт за нуклеарне науке-Институт од националног значаја за Републику Србију, Универзитет у Београду, Београд и ³Технолошко-металуршки факултет, Универзитет у Београду, Београд

У овом раду је одређиван коефицијент преноса масе флуид-зид у инверзно-флуидизованом слоју применом адсорпционе методе. Експерименти су вршени у колони пречника 45 mm са сферичним и несферичним честицама полипропилена и полиетиленом пречника 3,3–4,9 mm и густине око 930 kg m⁻³. Као флуидизациони медијум коришћен је разблажени раствор метиленског плавог који је адсорбован на делу површине колоне на силикагелу. Добијени резултати показали су да присуство честица при инверзној флуидизацији не доприноси значајно преносу масе у поређењу са утицајем честица на пренос масе у конвенционално флуидизованим слојевима. Због тога је у анализи уведен концепт псеудофлуида и изведена је емпиријска корелација за одређивање коефицијента преноса масе. Извршено је поређење добијених резултата са литературним корелацијама за инверзну и конвенционалну флуидизације.

(Примљено 16. јануара, ревидирано 27. фебруара, прихваћено 22. марта 2023)

REFERENCES

1. D. Wang, T. Silbaugh, R. Pfeffer Y. S. Lin, *Powder Technol.* **203** (2010) 298 (<https://doi.org/10.1016/j.powtec.2010.05.021>)
2. S. S. Begum, K. V. Radha, *Korean J. Chem. Eng.* **31** (2014) 436 (<https://doi.org/10.1007/s11814-013-0260-z>)
3. W. Sokol, A. Ambaw, B. Woldeyes, *Chem. Eng. J.* **150** (2009) 63 (<https://doi.org/10.1016/j.cej.2008.12.021>)
4. M. Rajasimman, C. Karthikeyan, *Int. J. Environ. Res.* **3** (2009) 569 (<https://doi.org/10.22059/IJER.2010.72>)
5. D.G. Karamanev, L.N. Nikolov, *Environ. Prog.* **15** (1996) 3 (<https://doi.org/10.1002/ep.670150319>)
6. I. Nikov, D. Karamanev, *AIChE J.* **37** (1991) 781 (<https://doi.org/10.1002/aic.690370515>)
7. K.A. Kumar, G.V.S. Sarma, M. Vijay, K.V. Ramesh, *Test Eng. Manage.* **83** (2020) 14318 (<http://www.testmagazine.biz/index.php/testmagazine/article/view/9657/7397>)
8. S. Končar-Durđević, *Nature* **172**, 878 (1953) 858 (<https://doi.org/10.1134/S0036024409090246>)
9. D. Jaćimovski, *PhD Thesis*, Faculty of Technology and Metallurgy, Belgrade, 2017 (<http://phaidrabbg.bg.ac.rs/o:17299>)
10. N. Bošković-Vragolović, R. Garić-Grulović, Ž. Grbavčić, R. Pjanović, *Russ. J. Phys. Chem.* **83** (2009) 1550 (<https://doi.org/10.1134/S0036024409090246>)
11. *SigmaScan Software*, Jandel Scientific, Erkrath, 1999
12. M. Đuriš, T. Kaluđerović Radoičić, R. Garić-Grulović, Z. Arsenijević, Ž. Grbavčić, *Powder Technol.* **246** (2013) 98 (<https://doi.org/10.1016/j.powtec.2013.05.009>)
13. D. Jaćimovski, R. Garić-Grulović, N. Vučetić, R. Pjanović, N. Bošković-Vragolović, *Powder Technol.* **303** (2016) 68 (<https://doi.org/10.1016/J.powtec.2016.09.025>)

14. Ž.Grbavčić, Z. Arsenijević, R.Garić-Grulović, *Powder Technol.* **190** (2009) 283
(<https://doi.org/10.1016/j.powtec.2008.08.005>)
15. R. Garić-Grulović, Ž. Grbavčić, Z. Arsenijević, *J. Serb. Chem. Soc.* **70** (2005) 775
(<http://dx.doi.org/10.2298/JSC0505775G>)
16. N. Yutani, N. Ototake, L.T. Fan, *Ind. Eng. Chem. Res.* **26** (1987) 343
(<https://doi.org/10.1021/ie00062a028>)
17. S. Marooka, K. Kusakabe, Y. Kato, *Int. Chem. Eng.* **20** (1980) 433
18. D. Kunii, O. Levenspiel, *Fluidisation Engineering*, Wiley, New York, 1969, p. 195.



J. Serb. Chem. Soc. 88 (9) 921–935 (2023)
JSCS–5671

Copper ions biosorption onto bean shells: Kinetics, equilibrium and process optimization studies

MILJAN MARKOVIĆ*, MILAN GORGIEVSKI#, NADA ŠTRBAC#, KRISTINA BOŽINOVIĆ, VESNA GREKULOVIĆ, ALEKSANDRA MITOVSKI and MILICA ZDRAVKOVIĆ#

University of Belgrade Technical Faculty in Bor, Vojske Jugoslavije 12, Bor, Serbia

(Received 18 October 2022, revised 21 February, accepted 21 March 2023)

Abstract: The removal of copper ions from aqueous solutions using bean shells as an adsorbent is presented in this paper. The influence of the solution pH on the biosorption capacity was investigated. The biosorption capacity increased with the increase in the solution pH. The pseudo-second order kinetic model showed the best agreement with the analysed experimental data, indicating that chemisorption could be a possible way of binding the copper ions to the surface of the bean shells. The Langmuir isotherm model best fitted the analysed isotherm data. The SEM-EDS analysis was performed before and after the biosorption process. The change in the morphology of the sample after the biosorption process was evident, whereby K, Mg, Si and Ca were possibly exchanged with copper ions. Response surface methodology (RSM) based on the Box–Behnken design (BBD) was used to optimize the biosorption process, with the selected factors: the solution pH, initial copper ions concentration and contact time. The optimum biosorption conditions were determined to be: pH 3–4, initial copper ions concentration, 100 mg dm⁻³, and contact time, 10–30 min.

Keywords: biosorption; copper ions; bean shells; kinetics; Box–Behnken design.

INTRODUCTION

Concentrations of heavy metal ions in wastewaters originating from various industrial systems are often significant. These wastewaters can pose a serious threat to the surrounding ecosystems when discharged without previous treatment.¹

Wastewaters polluted with heavy metals are treated by well-known conventional technologies, such as: adsorption, coagulation and flocculation, ion exchange, membrane filtration, precipitation and others.^{2–4}

* Corresponding author. E-mail: mmarkovic@tfbor.bg.ac.rs

Serbian Chemical Society member.

<https://doi.org/10.2298/JSC221018014M>



Biosorption is a possible alternative method for heavy metal ions removal. This process is considered “user-friendly” with various advantages, including specific affinity, low cost and simple design. It is based on adsorption with agricultural or industrial by-products being used as adsorbents. These by-products are convenient for the described use due to their abundant availability, favourable physical, chemical and surface characteristics, and their low cost.⁴

Copper is a widely used metal due to its excellent electrical and thermal conductivity, excellent corrosion resistance, and good resistance to strength and fatigue. Pure copper is widely used in the production of cables and wires and many other parts in the electrical industry. Due to its excellent anti-corrosion properties, copper is used for pipes, valves, and fittings in systems that carry drinking water, process water or some other type of water. Copper extraction, as well as its production, is the main source of pollution with this heavy metal. The excessive copper concentrations in the environment are highly toxic for living organisms. It inhibits cell growth, impacts metabolism, and other processes. For this reason, it is very important to develop a sustainable, green remediation technique for copper removal, that is also economical, efficient and environment-friendly.⁵

The aim of this work is to determine whether bean shells can be used as an adsorbent for copper ions biosorption from aqueous solutions.

The successful use of bean shells as an adsorbent for lead ions biosorption produced the idea of investigating the potential use of this biomass as an adsorbent for other heavy metals.⁶

For this purpose, kinetics, isotherm and SEM-EDS analyses of the data were obtained and shown in this paper. The process was also modelled by response surface methodology using Box–Behnken design to analyse the influence of three variables on the biosorption process and to determine their optimal values.

EXPERIMENTAL

Bean shells collected on the fields in the village Rudna Glava (Eastern Serbia) were used as an adsorbent for copper ions biosorption experiments.

0.5 g of bean shells were used as samples for biosorption experiments. The bean shells samples were rinsed with 200 mL of distilled water, prior to the biosorption experiments, in order to remove the physical impurities.

Biosorption experiments were conducted using synthetic copper ions solutions prepared with $\text{CuSO}_4 \cdot 5\text{H}_2\text{O}$ (*p.a.* purity). The solutions were prepared by mixing different amounts of the copper sulfate with distilled water, in order to obtain the concentrations needed for the specific experiment. The stock solution concentrations varied based on the specifics of the experiment. The solution pHs was adjusted with 0.1 M HNO_3 and 0.1 M KOH solutions.

All experiments were performed in batch conditions. Cu(II) content was determined on a spectrophotometer (Spectroquant Pharo 300 – Merck, Rahway, NJ, USA), by forming a complex with NH_4OH (*p.a.* purity), at 610 nm wavelength. The SEM-EDS analysis was performed on a SEM scanning electron microscope (Vega 3 LMU, Tescan, Brno, Czech Rep-

ublic) with an integrated energy-dispersive X-ray detector (X act SDD 10 mm², Oxford Instruments, Abingdon, UK).

The full characterization and preparation of the biosorbent are reported in a previous publication.⁶

Process parameters, such as: process time, initial copper ions concentration, initial solution pH and temperature were adjusted depending on the performed experiment.

The biosorption capacity and the Removal in % were calculated using the following equations:

$$q_t = \frac{V(c_i - c_t)}{m} \quad (1)$$

$$\text{Removal} = 100 \left(1 - \frac{c_t}{c_i} \right) \quad (2)$$

where q_t is the adsorbent capacity defined as mass of the adsorbed metal per unit mass of the adsorbent (mg g⁻¹) at time t ; c_i is the initial metal ion concentration in the solution; c_t is the metal ion concentration in the solution at time t ; m is the adsorbent mass; V is the volume of the solution; Removal is the degree of the adsorbed copper ions.

RESULTS AND DISCUSSION

The influence of the solution pH on the adsorption capacity

To determine the influence of the solution pH on the biosorption capacity (Fig. 1), a number of experiments were performed, and the initial solution pHs was adjusted in the range from 2 to 5. 50 mL of copper ions solutions (initial concentration 200 mg dm⁻³) was brought into contact with 0.5 g of been shells for 60 min. The experiments were performed in batch conditions, at room temperature, on a magnetic stirrer (with the stirring rate set at 300 rpm).

As can be seen from Fig. 1, the solution pH had a significant effect on the biosorption capacity. An increase in the biosorption capacity with the increase of the solution pH could be noted. At pH 2, the biosorption capacity was 1.739 mg g⁻¹, while the maximum capacity of 12 mg g⁻¹ was achieved at pH 5.

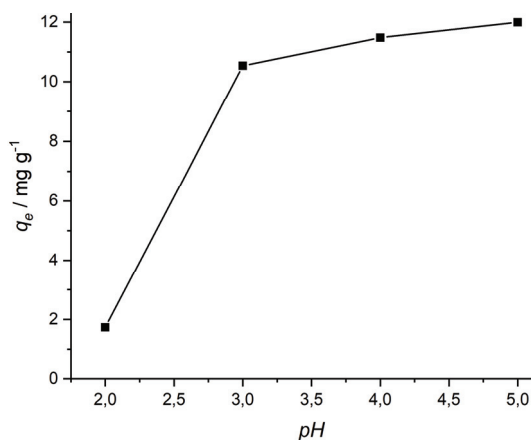


Fig. 1. The influence of solution pH on the adsorption capacity.

A lower biosorption capacity at lower solution pH could be a result of a higher concentration of H^+ , which occupied the active sites in the structure of bean shells and suppressed the already adsorbed Cu^{2+} . At higher pH, the concentration of H^+ in the solution were lower, resulting in a higher biosorption capacity.⁷

Adsorption kinetics

Kinetic models are often used for analysing the experimental data to determine the biosorption rate, the step that dictates the rate of the process and its mechanism.⁸

In this paper, pseudo-first order kinetic model, pseudo-second order kinetic model, intraparticle diffusion (Webber–Morris) kinetic model and Elovich kinetic model were used to analyse the obtained experimental data. Details are presented in Supplementary material to this paper.

In order to obtain the biosorption kinetic data, 50 mL of copper ion solutions (initial concentration 200 mg dm^{-3}) were brought into contact with 0.5 g of bean shells, for different process time (ranging from 1 to 90 min). The change in the biosorption capacity with time is shown in Fig. 2. It can be noted that the biosorption capacity increased rapidly at the beginning of the process (first 5 min), as a result of a large number of available active sites in the structure of the bean shells.⁹ After this initial period, a slower increase in the biosorption capacity was noted (10–90 min), reaching a constant value after 90 min of the process.

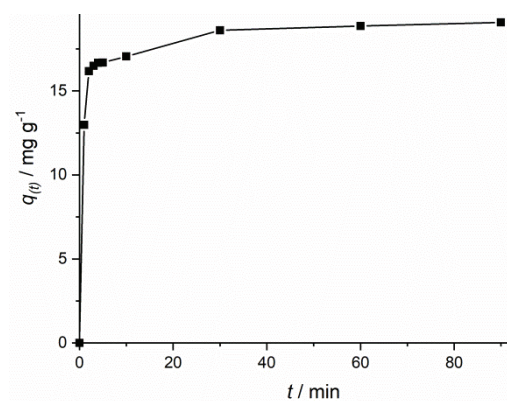


Fig. 2. Change in the adsorption capacity with time.

Pseudo-first order kinetic model

This model is based on the assumption that adsorption is a reversible process.¹⁰

The plot $\log (q_e - q(t))$ vs. t gives a linear dependence that serves as a base to determine the first-order kinetic model parameters. The obtained experimental data shown in Fig 2 were linearized and the obtained plot is shown in Fig. 3a. The obtained kinetic parameters corresponding to this model are given in Table I.

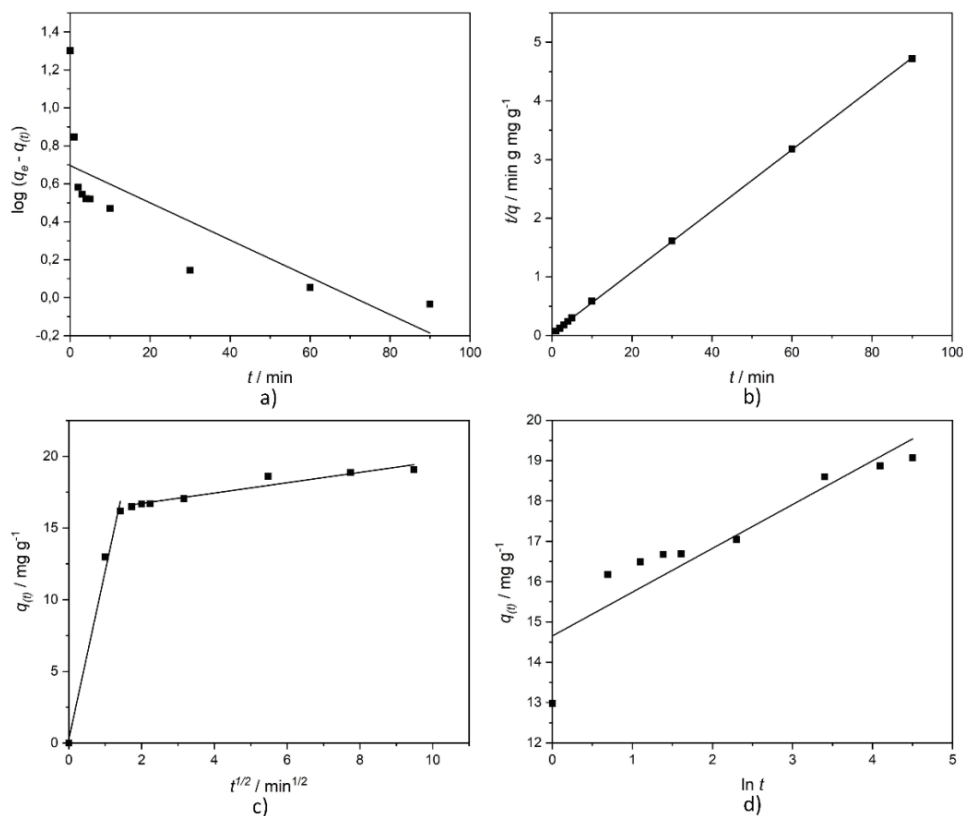


Fig. 3. a) Pseudo-first order kinetic model; b) pseudo-second order kinetic model; c) intraparticle diffusion kinetic model; d) Elovich kinetic model.

Pseudo-second order kinetic model

Pseudo-second order kinetic model is based on the assumption that adsorption and ion exchange take place on the surface of the adsorbent, and that the adsorbate is bound to the adsorbent surface by chemisorption.¹¹

Plot $t/q(t)$ vs. t , shown in Fig. 3b, was used to determine the kinetic parameters for this model, which are given in Table I.

Intraparticle diffusion kinetic model (Weber–Morris model)

This model assumes that the adsorption does not occur only on the surface of the adsorbent, but that the diffusion and adsorption inside the adsorbent structure are also present.¹²

The plot $t^{1/2}$ vs. $q(t)$, shown in Fig. 3c, is used to obtain the intraparticle diffusion kinetic model parameters shown in Table I.

Elovich kinetic model

This model was primarily used to analyse gas chemisorption onto solid adsorbents, but was later successfully applied on the adsorption of toxic materials from aqueous solutions.¹³

From the plot $q(t) = f(\ln t)$, shown in Fig. 3d, the Elovich kinetic model parameters were determined and given in Table I.

TABLE I. Kinetic model parameters for copper ions biosorption onto bean shells

Model	Parameter	Value
Pseudo-first order kinetic model	k_1 / min^{-1}	0.023
	$q_{e,\text{exp}} / \text{mg g}^{-1}$	19.07
	$q_{e,\text{cal}} / \text{mg g}^{-1}$	4.97
	R^2	0.596
Pseudo-second order kinetic model	$k_2 / \text{g mg}^{-1} \text{min}^{-1}$	0.077
	$q_{e,\text{exp}} / \text{mg g}^{-1}$	19.07
	$q_{e,\text{cal}} / \text{mg g}^{-1}$	19.16
	R^2	0.999
Intraparticle diffusion kinetic model	$k_{i1} / \text{g mg}^{-1} \text{min}^{-0.5}$	11.722
	$C_{i1} / \text{mg g}^{-1}$	0.285
	R_1^2	0.989
	$k_{i2} / \text{g mg}^{-1} \text{min}^{-0.5}$	0.360
	$C_{i2} / \text{mg g}^{-1}$	15.995
	R_2^2	0.929
Elovich kinetic model	$\alpha / \text{mg g}^{-1} \text{min}^{-1}$	14.652
	$\beta / \text{g mg}^{-1}$	1.086
	R^2	0.837

Based on the obtained correlation coefficients, it can be concluded that the adsorption kinetics could be fairly modelled with the pseudo-second order kinetic model, which led to the conclusion that chemisorption was a possible way of binding copper ions onto active sites in the adsorbent structure. This statement was also supported by the negligible difference in the values of calculated and experimentally obtained adsorption capacity ($q_{e,\text{cal}}$ and $q_{e,\text{exp}}$).

Adsorption isotherms

Adsorption isotherms are used to gain insight into the mechanism of the adsorption process, as well as to determine the maximum adsorption capacity.¹⁴

In this paper, the linear Langmuir, Freundlich and Temkin isotherm models were used to describe copper ions biosorption onto bean shells. Details are presented in Supplementary material.

Biosorption isotherm data was obtained by performing the following experiment: 0.5 g of bean shells samples were brought into contact with 50 mL of copper ions solutions, of different initial Cu^{2+} concentrations (in the range from 50

to 500 mg dm^{-3}). The suspension was stirred on a magnetic stirrer, at room temperature for 90 min.

The obtained experimental adsorption isotherm data for copper ions adsorption onto bean shells is shown in Fig. 4a.

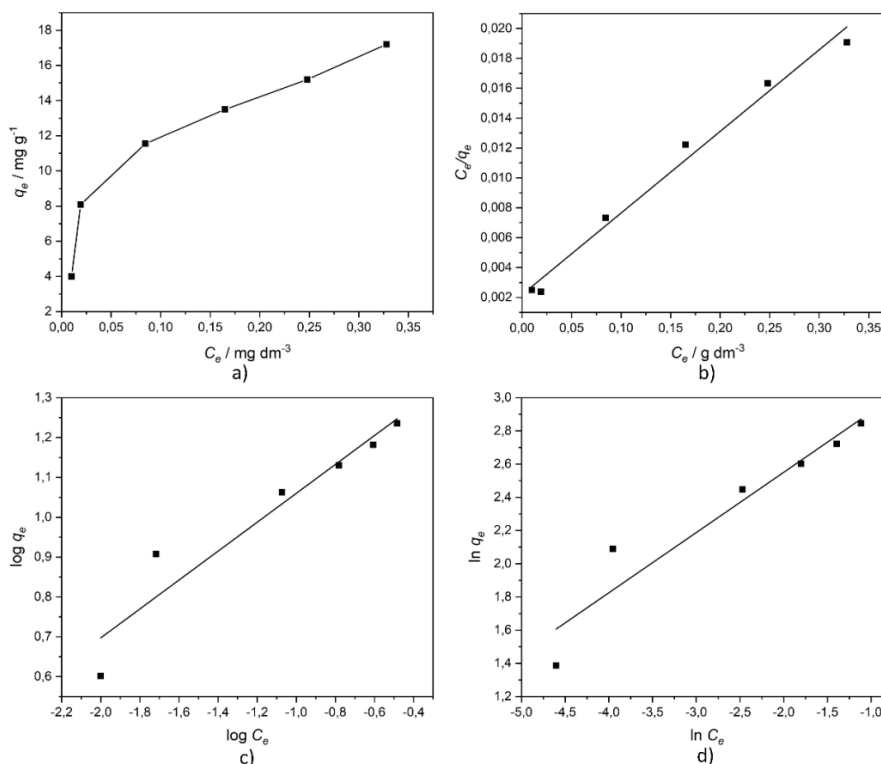


Fig. 4. a) Experimental adsorption isotherm data; b) Langmuir adsorption isotherm model; c) Freundlich adsorption isotherm model; d) Temkin adsorption isotherm model.

Langmuir isotherm model

This model is based on the assumption that the adsorption process occurs on specific homogenous sites inside the adsorbent structure.¹⁵

The Langmuir isotherm data were calculated from the plot C_e vs. C_e/q_e shown in Fig. 4b, and given in Table II.

Freundlich isotherm model

Freundlich model represents the earliest known relationship that describes the non-ideal and reversible adsorption. This model can also be used to study multilayer adsorption.¹⁶

The plot $\log q_e$ vs. $\log C_e$ (Fig. 4c) provided the required data for the Freundlich model isotherm data calculation, which are shown in Table II.

Temkin model

This model assumes that the heat of sorption of all molecules linearly increases with the coverage of the adsorbent surface and that there is a uniform distribution of binding energies up to maximum binding energy.¹⁶

Temkin constants B and K_T were determined from the plot $\ln C_e$ vs. q_e (Fig. 4d), and given in Table II.

Based on the analysed data and the obtained results (Table II), it can be concluded that the Langmuir isotherm model was the best fit for the experimental data ($R^2 = 0.986$), which indicated that the surface of the adsorbent was homogeneous, and the biosorption of copper ions onto bean shells occurred in a monolayer.¹⁷

TABLE II. Adsorption isotherm model parameters for copper ions biosorption onto bean shells

Langmuir		Freundlich			Temkin				
$K_L / \text{dm}^3 \text{ mg}^{-1}$	$q_{\text{exp}} / \text{mg g}^{-1}$	$q_m / \text{mg g}^{-1}$	R^2	K_F	$1/n$	R^2	$B / \text{J mol}^{-1}$	$K_T / \text{dm}^3 \text{ g}^{-1}$	R^2
24.9	17.2	18.3	0.99	1.42	0.36	0.92	0.36	3.28	0.92

The performance of the adsorbent is usually defined by the maximum biosorption capacity. Based on the results in copper removal with various biosorbents reported in other works (shown in Table III), it can be concluded that bean shells could play an important role as a cost-effective biosorbent for the copper ions removal.

TABLE III. Cu^{2+} biosorption on bean shells in comparison with other adsorbents

Biosorbent	Maximum biosorption capacity ($q_m / \text{mg g}^{-1}$)	Data
Bean shells	18.3	This work
Wheat straw	4.30	18
Sawdust of deciduous trees	9.90	19
<i>Myrica esculenta</i>	39.4	20
Activated sawdust powder	10.4	21
Rosa damascena leaves	25.1	22
Carbonized sunflower stem	20.0	23
<i>Combretum indicum</i>	12.1	24

SEM-EDS analysis

The SEM-EDS analysis was performed on samples before and after the biosorption of copper ions. The obtained results are shown in Fig. 5. Before the biosorption of copper ions (Fig. 5a) a porous structure was noticed, with visible cavities and macro-pores. The presence of these pores and cavities facilitated the penetration of the aqueous phase into the adsorbent structure.²⁵ The EDS spectrum of the sample before biosorption of copper ions (Fig. 5b) suggested the presence of O, Mg, Si, K and Ca.

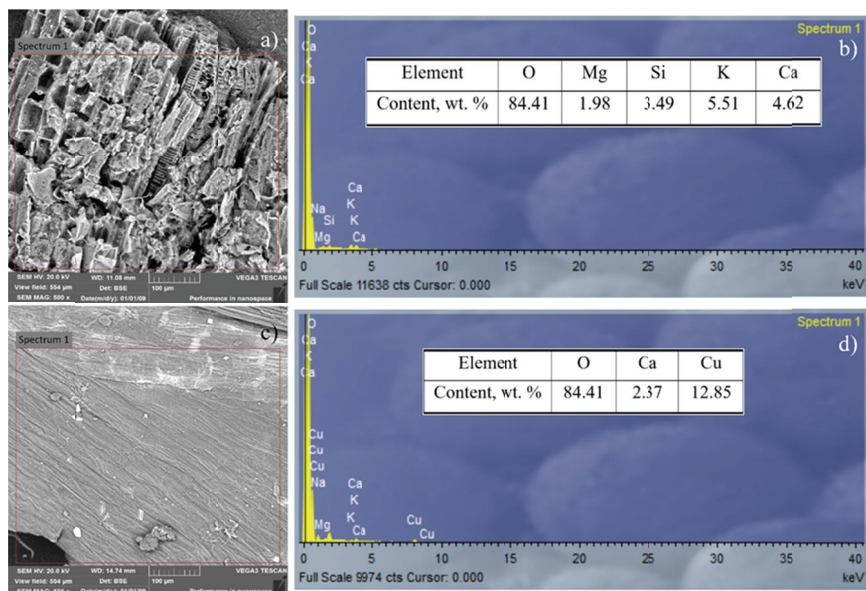


Fig. 5. SEM-EDS analysis before and after the biosorption of copper ions.

After the biosorption process, the SEM analysis (Fig. 5c) showed a more compact structure, with the absence of macro-pores and cavities, as a result of the incorporation of copper ions into the molecular structure of the bean shells. The obtained EDS spectrum after the biosorption of copper ions (Fig. 5d) demonstrated the presence of O, Ca and Cu. The absence of Mg, Si, K and detected lower levels of Ca, indicated that any of these ions could be exchanged with copper ions during the biosorption process.

Optimization of the biosorption conditions – Box–Behnken experimental design

Copper ions biosorption onto bean shells was optimized using an experimental design, in order to determine the effects of three selected independent variables on the percentage of Cu^{2+} removal (dependent variable).²⁶ The optimum biosorption conditions were determined by the means of Box–Behnken design (BBD) and response surface methodology (RSM). The RSM is a set of techniques useful for evaluating the relationships between a number of experimental factors and measured responses.²⁷ The BBD was applied, comparing three factors: solution pH (X_1), initial copper ions concentration (X_2), and contact time (X_3). The chosen experimental ranges and levels in the design are given in Table IV. The experimental design matrix, as well as the response Y (adsorption degree), are given in Table V. All the experiments are performed in batch conditions, at room temperature, on a magnetic stirrer (with the constant stirring rate, set at 300 rpm).

TABLE IV. Experimental ranges and levels in the experimental design

Factor	Range level		
	-1	0	1
X_1 – solution pH	2	3	4
X_2 – Initial metal ion concentration, mg/L	100	500	1000
X_3 – Contact time, min	10	30	60

TABLE V. Box–Behken Design matrix for three factors along with observed response for Cu^{2+} biosorption onto bean shells

Run	X_1 : solution pH	X_2 : Initial Cu^{2+} concentration, mg dm^{-3}	X_3 : Contact time, min	Y : Removal, %
1	2	100	30	32.95
2	4	100	30	86.52
3	2	1000	30	22.58
4	4	1000	30	11.89
5	2	500	10	30.55
6	4	500	10	23.84
7	2	500	60	20.86
8	4	500	60	39.75
9	3	100	10	87.79
10	3	1000	10	6.922
11	3	100	60	69.70
12	3	1000	60	7.102
13	3	500	30	25.07
14	3	500	30	31.36
15	3	500	30	38.86

The correlation between the independent variables are given in Supplementary material.

The statistical significance of the model was evaluated by the analysis of variance (ANOVA) and presented in Table VI. The significance of each coefficient was determined by the magnitude of the F -values and P -values, given in Table VI. The larger the F -value, and the smaller P -value, the corresponding coefficient was more significant. P -values less than 0.0500 indicated high significant regression at 95 % confidence level.²⁷

The suitability of the model was confirmed by the regression coefficients of the predicted and experimental responses ($R^2 = 0.924$ and $\text{adj-}R^2 = 0.787$). This suggested that 96 % of the responses were explained by the used model. The corresponding F -value (6.76) and P -value (0.024) indicated that the model was significant. P -values lower than 0.0500 in the cases of X_2 (initial Cu^{2+} concentration) and X_1X_2 (solution pH combined with the initial Cu^{2+} concentration) indicated that these were the significant model terms.

The relationship between the experimental responses and the responses predicted by the model is shown in Fig. 6.

TABLE VI. ANOVA analysis for response surface model in relation to Cu^{2+} biosorption onto bean shells

Source	DF	Adj-SS	Adj-MS	F-Value	P-Value
Model	9	8676.69	964.08	6.76	0.024
Linear	3	6920.46	2306.82	16.17	0.005
X_1	1	378.85	378.85	2.66	0.164
X_2	1	6524.53	6524.53	45.74	0.001
X_3	1	17.08	17.08	0.12	0.743
Square	3	476.86	158.95	1.11	0.426
X_1^2	1	50.70	50.70	0.36	0.577
X_2^2	1	401.23	401.23	2.81	0.154
X_3^2	1	1.76	1.76	0.01	0.916
2-Way interaction	3	1279.36	426.45	2.99	0.135
X_1X_2	1	1032.05	1032.05	7.23	0.043
X_1X_3	1	163.87	163.87	1.15	0.333
X_2X_3	1	83.45	83.45	0.58	0.479
Error	5	713.24	142.65	–	–
Lack-of-Fit	3	617.94	205.98	4.32	0.194
Pure error	2	95.30	47.65	–	–
Total	14	9389.93	–	–	–

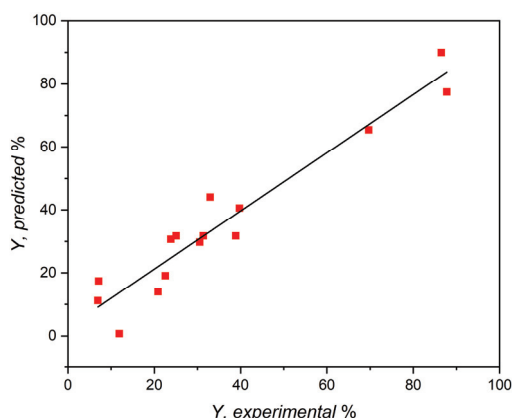


Fig. 6. Plot of experimental and predicted responses.

As can be seen from Fig. 6, there was a good relationship between the experimental and predicted responses, based on the correlation coefficient ($R^2 = 0.924$).

The contour plots showing the influence of the analysed process parameters on the adsorption degree are presented in Fig. 7. Fig. 7a indicates that the higher solution pH and lower initial Cu^{2+} concentration in the solution leads to higher metal ions removal. Further, the biosorption process was more favourable at lower initial Cu^{2+} concentration combined with shorter contact time (Fig. 7b). Lastly, Fig. 7c shows that a high solution pH combined with medium-to-longer contact time led to a higher Removal.

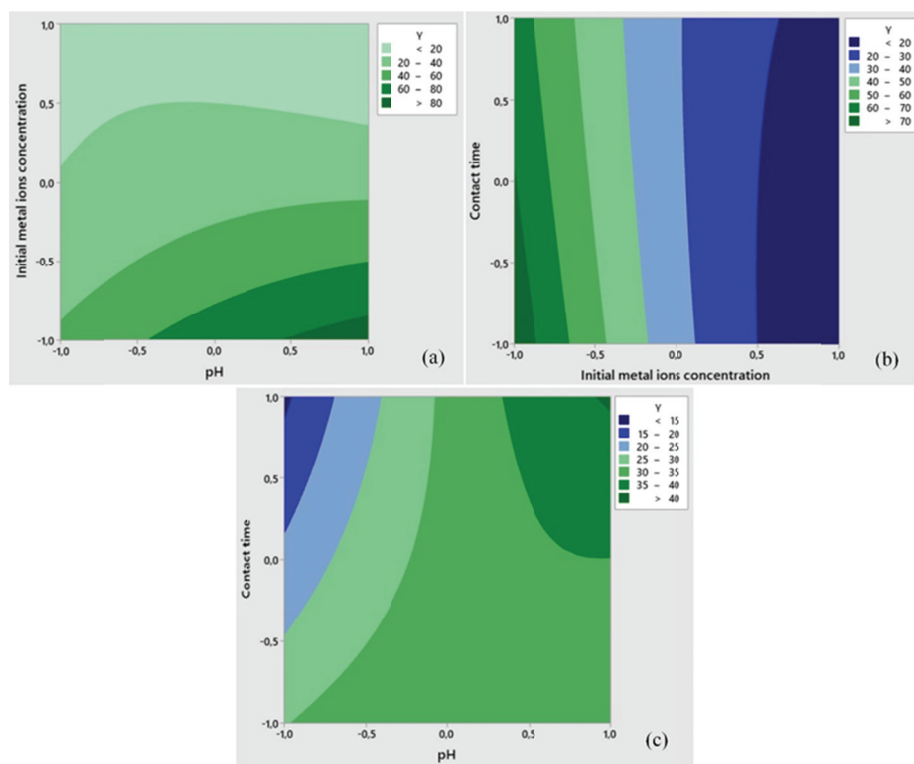


Fig. 7. Contour plots showing the interaction and the influence on the adsorption rate (Y): solution pH and the initial metal ions concentration (a); initial metal ions concentration and contact time (b) and solution pH and contact time (c).

RSM based on BBD was used to optimize the process of copper ions biosorption onto bean shells. The influence of three parameters (solution pH, initial metal ions concentration and contact time) was investigated. The obtained data indicated that the used model was statistically significant. The data showed that the initial metal ions concentration, as well as the combination of initial metal ions concentration and solution pH, had a significant influence on the biosorption efficiency. Using this model, the optimum biosorption conditions were determined to be: pH 3–4, initial metal ions concentration 100 mg/L and contact time 10–30 min.

CONCLUSIONS

The study of biosorption, as a potential method for copper ions removal from aqueous solutions, is presented in this paper. Bean shells were investigated as potential adsorbent. For that purpose, kinetics, equilibrium, SEM-EDS and process optimization studies were performed.

The solution pH was determined to have a significant influence on the biosorption capacity. An increase in the biosorption capacity with the increase in the solution pH from 2 (1.739 mg g^{-1}) to 5 (12 mg g^{-1}) was noted.

Experimentally obtained kinetics data were analysed using four adsorption kinetic models (the pseudo-first order kinetic model, pseudo-second order kinetic model, intraparticle diffusion kinetic model and Elovich kinetic model). The obtained kinetics parameters indicated that the pseudo-second order kinetic model best fitted the analyzed experimental data, which further suggested that chemisorption was a possible way of binding the copper ions to the surface of bean shells.

Experimental biosorption isotherm data were fitted using the Langmuir, Freundlich and Temkin adsorption isotherm models. Obtained results indicated that the Langmuir model served as the best fit for the analysed data, leading to the conclusion that the surface of the adsorbent was homogenous, and the biosorption of copper ions onto bean shells occurred in a monolayer.

The SEM-EDS analysis was performed on a bean shells sample before and after the biosorption of copper ions. The obtained SEM micrographs showed that the surface morphology of the sample changed after the biosorption process, from a porous to a more compact structure, possibly as a result of the incorporation of copper ions into the structure of the bean shells. The EDS spectrums of the samples before and after the biosorption process indicated that Mg, Si, K and Ca could potentially be involved in the biosorption process and exchanged with copper ions.

Process optimization studies were performed by the means of response surface methodology based on the Box–Behnken design. The influence of solution pH, initial metal ions concentration and contact time was investigated and modelled.

The used model was determined to be statistically significant. The data suggested that the initial metal ions concentration, as well as the combination of initial metal ions concentration and solution pH, had a significant influence on the biosorption efficiency. Using this model, the optimum biosorption conditions were determined to be: pH 3–4, initial metal ions concentration 100 mg dm^{-3} ; and contact time 10–30 min.

SUPPLEMENTARY MATERIAL

Additional data and information are available electronically at the pages of journal website: <https://www.shd-pub.org.rs/index.php/JSCS/article/view/12110>, or from the corresponding author on request.

Acknowledgements. The research presented in this paper was done with the financial support of the Ministry of Science, Technological Development and Innovation of the Republic of Serbia, within the funding of the scientific research work at the University of Belgrade, Technical Faculty in Bor, according to the contract with registration number 451-03-68/2022-

14/200131. The authors express their appreciation to Ms. Sandra Vasković, an English Lecturer at the Technical Faculty in Bor, University of Belgrade, for her help in editing the manuscript.

ИЗВОД

БИОСОРПЦИЈА ЈОНА БАКРА НА ЉУСКАМА ПАСУЉА: ИСПИТИВАЊА КИНЕТИКЕ, РАВНОТЕЖЕ И ОПТИМИЗАЦИЈА ПРОЦЕСА

МИЉАН МАРКОВИЋ, МИЛАН ГОРГИЈЕВСКИ, НАДА ШТРБАЦ, КРИСТИНА БОЖИНОВИЋ, ВЕСНА ГРЕКУЛОВИЋ, АЛЕКСАНДРА МИТОВСКИ И МИЛИЦА ЗДРАВКОВИЋ

Универзитет у Београду, Технички Факултет у Бору, Војске Југославије 12, Бор

У овом раду приказана је анализа уклањања јона бакра из водених раствора коришћењем љуски пасуља као адсорбенса. Испитан је утицај рН вредности раствора на капацитет биосорпције. Добијени резултати су показали да капацитет биосорпције расте са повећањем рН вредности раствора. Кинетичка испитивања су показала да модел псеудо-другог реда најбоље описује анализиране податке, што указује да је хемисорпција могућ начин везивања јона бакра за површину љуски пасуља. Испитивања равнотеже процеса су показала да Ленгмиров модел адсорпционе изотерме најбоље описује анализиране податке. SEM-EDS анализом су испитани узорци пре и након извођења процеса биосорпције. Ова анализа је показала евидентну промену у морфологији узорка након процеса биосорпције, при чему су EDS спектри указали на могућу измену К, Mg, Si и Ca јона са јонима бакра. Модел *response surface methodology* (RSM) базиран на Box–Behnken дизајну (BBD) је коришћен за оптимизацију процеса биосорпције, са изабраним факторима: рН вредности раствора, почетна концентрација јона бакра у раствору и време контакта. Помоћу модела су одређени оптимални услови за извођење процеса биосорпције, и то: рН вредности између 3 и 4, почетна концентрација јона бакра од 100 mg dm⁻³ и време контакта између фаза 10-30 min.

(Примљено 18. октобра 2022, ревидирано 21. фебруара, прихваћено 21. марта 2023)

REFERENCES

1. F. Shafique, Q. Ali, A. Malik, *Biol. Clin. Sci. Res. J.* **1** (2020) e027 (<https://doi.org/10.54112/bcsrj.v2020i1.27>)
2. N. Agasti, *CRGSC* **4** (2021), 100088 (<https://doi.org/10.1016/j.crgsc.2021.100088>)
3. D. Lakhterwal, *IJERD* **4** (2014) 41 (https://www.ripublication.com/ijerd_spl/ijerdv4n1spl_08.pdf)
4. S. K. Gunatilake, *JMESS* **1** (2015) 12 (<http://www.jmess.org/wp-content/uploads/2015/11/JMESSP13420004.pdf>)
5. C. Tu, Y. Liu, J. Wei, L. Li, K. G. Sheckel, Y. Luo, *Environ. Sci. Pollut. Res. Int.* **25** (2018) 24965 (<https://doi.org/10.1007/s11356-018-2563-4>)
6. M. Marković, M. Gorgievski, D. Božić, V. Stanković, M. Cakić, V. Grekulović, K. Božinović, *Rev. Chim.* **72** (2021), 118 (<https://doi.org/10.37358/RC.21.4.8462>)
7. S. Schiewer, B. Volesky, *Environ. Sci. Technol.* **31** (1997) 2478 (<https://doi.org/10.1021/es00012a024>)
8. U. Farooq, J. Kozinski, M. Khan, M. Athar, *Bioresour. Technol.* **101** (2010) 5043 (<https://doi.org/10.1016/j.biortech.2010.02.030>)
9. B. Nagy, C. Manzatu, A. Maicaneanu, C. Indolean, B. T. Lucian, C. Majdik, *Arab. J. Chem.* **10** (2017) 3569 (<https://doi.org/10.1016/j.arabjc.2014.03.004>)
10. S. Lagergren, *Sven. Vetenskapsakad. Handlingar* **241** (1898) 1

11. N. T. Coleman, A. C. McClung, D. P. Moore, *Science* **123** (1956) 330
12. S. M. Mousa, N. S. Ammar, H. A. Ibrahim, *J. Saudi Chem. Soc.* **20** (2016) 357 (<https://doi.org/10.1016/j.jscs.2014.12.006>)
13. R. S. Juang, M. L. Chen, *Ind. Eng. Chem. Res.* **36** (1997) 813 (<http://dx.doi.org/10.1021/ie960351f>)
14. S. A. Sadeek, N. A. Negm, H. H. Hefni, M. A. Abdel Wahab, *Int. J. Biol. Macromol.* **81** (2005) 400 (<https://doi.org/10.1016/j.ijbiomac.2015.08.031>)
15. R. Han, J. Zhang, W. Zou, J. Shi, H. Liu, *J. Hazard. Mater.* **125** (2005) 266 (<https://doi.org/10.1016/j.jhazmat.2005.05.031>)
16. X. Chen, *Information* **6** (2015) 14 (<https://doi.org/10.3390/info6010014>)
17. G. Murithi, C. O. Onindo, G. K. Muthakia, *Bull. Chem. Soc. Ethiop.* **26** (2012) 181 (<http://dx.doi.org/10.4314/bcse.v26i2.3>)
18. M. Gorgievski, D. Božić, V. Stanković, N. Štrbac, S. Šerbula, *Ecol. Eng.* **58** (2013) 113 (<https://doi.org/10.1016/j.ecoleng.2013.06.025>)
19. D. Božić, V. Stanković, M. Gorgievski, G. Bogdanović, R. Kovačević, *J. Hazard. Mater.* **171** (2009) 684 (<https://doi.org/10.1016/j.jhazmat.2009.06.055>)
20. R. Kumar, H. J. Kumar, M. C. Vishwakarma, H. Sharma, K. S. Joshi, N. S. Bhandari, *Environ. Nanotechnol. Monit. Manage.* **19** (2023) 100775 (<https://doi.org/10.1016/j.enmm.2022.100775>)
21. N. Ilavarasan, Y. S. Sirinivasa Rao, R. Gokulan, A. Aravindan, *Glob. Nest J.* **25** (2023) 47 (<https://doi.org/10.30955/gnj.004496>)
22. M. A. Fawzy, H. M. Al-Yasi, T. M. Galal, R. Z. Hamza, T. G. Abdelkader, E. F. Ali, S. H. A. Hassan, *Sci. Rep.* **12** (2022) 8583 (<https://doi.org/10.1038/s41598-022-12233-1>)
23. C. Sireesha, R. Subha, S. Sumithra, *RASAYAN J. Chem.* **15** (2022) 2267 (<http://doi.org/10.31788/RJC.2022.1548035>)
24. A. Tahir, M. Salman, *Desalination Water Treat.* **270** (2022) 127 (<https://doi.org/10.5004/dwt.2022.28775>)
25. G. F. Coelho, A. C. Goncalves, C. R. Teixeira Tarley, J. Casarin, N. Nacke, M. A. Fancziskowski, *Ecol. Eng.* **73** (2014) 514 (<https://doi.org/10.1016/j.ecoleng.2014.09.103>)
26. A. Choinska-Pulit, J. Sobolczyk-Bednarek, W. Laba, *Ecotoxicol. Environ. Saf.* **149** (2018) 275 (<https://doi.org/10.1016/j.ecoenv.2017.12.008>)
27. H. Turkyilmaz, T. Kartal, S. Yigitarlan Yildiz, *J. Environ. Health Sci. Eng.* **12** (2014) (<https://doi.org/10.1186/2052-336X-12-5>).

SUPPLEMENTARY MATERIAL TO
**Copper ions biosorption onto bean shells: Kinetics, equilibrium
and process optimization studies**

MILJAN MARKOVIĆ*, MILAN GORGIEVSKI, NADA ŠTRBAC, KRISTINA
BOŽINOVIĆ, VESNA GREKULOVIĆ, ALEKSANDRA MITOVSKI
and MILICA ZDRAVKOVIĆ

University of Belgrade Technical Faculty in Bor, Vojske Jugoslavije 12, Bor, Serbia

J. Serb. Chem. Soc. 88 (9) (2023) 921–935

MODELS

The pseudo-first order kinetic model is given by:¹

$$\frac{dq(t)}{dt} = k_1(q_e - q(t)) \quad (\text{S-1})$$

where: $q(t)$ – is the adsorbent capacity defined as the mass of the adsorbed metal per unit mass of the adsorbent (mg g^{-1}) at time t ; q_e – is the adsorption capacity defined as mass of the adsorbed metal per unit mass of the adsorbent (mg g^{-1}) at equilibrium; k_1 – is the adsorption rate constant for the pseudo-first order kinetic model (min^{-1}).

Integrating the Eq. (S-1), it follows:

$$\log(q_e - q(t)) = \log(q_e) - \frac{k_1}{2,303} \times t \quad (\text{S-2})$$

The pseudo-second order kinetic model can be expressed as:²

$$\frac{dq(t)}{dt} = k_2(q_e - q(t))^2 \quad (\text{S-3})$$

where: $q(t)$ - is the adsorbent capacity defined as the mass of the adsorbed metal per unit mass of the adsorbent (mg g^{-1}) at time t ; q_e - is the adsorption capacity defined as mass of the adsorbed metal per unit mass of the adsorbent (mg g^{-1}) at equilibrium; k_2 - is the adsorption rate constant for the pseudo-second order kinetic model ($\text{g mg}^{-1} \text{min}^{-1}$).³

The linear form of Eq. (S-3) is:

$$\frac{1}{(q_e - q(t))} = \frac{1}{q_e} + k_2 t \quad (\text{S-4})$$

The intraparticle diffusion kinetic model is given as:¹

$$q(t) = k_i t^{1/2} + C_i \quad (\text{S-5})$$

*Corresponding author. E-mail: mmarkovic@tfbor.bg.ac.rs

where: $q(t)$ - is the adsorption capacity defined as the mass of the adsorbed metal per unit mass of the adsorbent (mg g^{-1}) at time t ; k_i - is the internal particle diffusion rate constant ($\text{mg g}^{-1} \text{min}^{-0.5}$); and C_i - is a constant that provides insight into the thickness of the boundary layer. If the C_i value is higher, the boundary layer effect is greater, so the effect of surface adsorption in controlling the process speed is greater (mg g^{-1}).

Elovich kinetic model is given in the following form:¹

$$\frac{dq(t)}{dt} = \alpha e^{-\beta q(t)} \quad (\text{S-6})$$

where: α - is the starting adsorption rate ($\text{mg g}^{-1} \text{min}^{-1}$); β - is the parameter that expresses the degree of surface coverage and activation energy for chemisorption (g mg^{-1}); $q(t)$ - is the adsorption capacity defined as the mass of the adsorbed metal per unit mass of the adsorbent (mg g^{-1}) at time t .

The Langmuir model can be expressed as:¹

$$q_e = \frac{q_m K_L C_e}{1 + K_L C_e} \quad (\text{S-7})$$

where C_e - is the equilibrium concentration of metal ions (mg dm^{-3}); q_e - is the equilibrium adsorption capacity (mg g^{-1}); q_m - is the maximum adsorption capacity (mg g^{-1}); and K_L - is the Langmuir equilibrium constant ($\text{dm}^3 \text{g}^{-1}$).

Linearizing the Eq. (S-7) the following is obtained:

$$C_e/q_e = \frac{1}{K_L q_m} + \frac{1}{q_m} C_e \quad (\text{S-8})$$

This model can be expressed as:¹

$$q_e = K_f C_e^{1/n} \quad (\text{S-9})$$

where C_e - is the equilibrium concentration of copper ions in the solution (mg dm^{-3}); q_e - is the adsorbent capacity defined as mass of the adsorbed metal per unit mass of the adsorbent (mg g^{-1}) at equilibrium; K_f - is the Freundlich equilibrium constant ($(\text{mg g}^{-1}) (\text{dm}^3 \text{mg}^{-1})^{1/n}$); and $1/n$ - is the coefficient of heterogeneity in the Freundlich adsorption isotherm equation.

Linear form of Eq. (S-9) is:

$$\log q_w = \log K_f + \frac{1}{n} \log C_e \quad (\text{S-10})$$

The Temkin isotherm model is given as:

$$q_e = B \ln(K_T C_e) \quad (\text{S-11})$$

where: $B = RT/b$ - is the Temkin constant, which refers to the adsorption heat (J mol^{-1}); b - is the variation of adsorption energy (J mol^{-1}); R - is the universal gas constant ($\text{J mol}^{-1} \text{K}^{-1}$); T - is the temperature (K); K_T - is the Temkin equilibrium constant ($\text{dm}^3 \text{g}^{-1}$); q_e - is the adsorption capacity (mg g^{-1}) at equilibrium; and C_e - is the equilibrium concentration of metal ions in the solution (mg dm^{-3}).¹

Linear form of Eq. (S-11) is:

$$q_e = B \ln K_T + B \ln C_e \quad (\text{S-12})$$

The correlation between the following independent variables: linear ($\beta_1, \beta_2, \beta_3$), quadratic ($\beta_{11}, \beta_{22}, \beta_{33}$), interaction terms ($\beta_{12}, \beta_{13}, \beta_{23}$), and the response (Y), was described by fitting the following polynomial equation:⁴

$$Y = \beta_0 + \beta_1 X_1 + \beta_2 X_2 + \beta_3 X_3 + \beta_{11} X_1 X_1 + \beta_{22} X_2 X_2 + \beta_{33} X_3 X_3 + \beta_{12} X_1 X_2 + \beta_{13} X_1 X_3 + \beta_{23} X_2 X_3 \quad (\text{S-13})$$

The obtained results are displayed in Table VI. The biosorption of copper ions onto bean shells was expressed using the following equation:

$$Y = 31,76 + 6,88X_1 - 28,56X_2 - 1,46X_3 - 3,71X_1 \cdot X_1 + 10,42X_2 \cdot X_2 + 0,69X_3 \cdot X_3 - 16,06X_1 \cdot X_2 + 6,40X_1 \cdot X_3 + 4,57X_2 \cdot X_3 \quad (\text{S-14})$$

REFERENCES

1. M. Marković, M. Gorgievski, D. Božić, V. Stanković, M. Cakić, V. Grekulović, K. Božinović, *Rev. Chim.* **72** (2021), 118 (<https://doi.org/10.37358/RC.21.4.8462>)
2. M. Gorgievski, D. Božić, V. Stanković, N. Štrbac, S. Šerbula, *Ecol. Eng.* **58** (2013) 113 (<https://doi.org/10.1016/j.ecoleng.2013.06.025>)
3. S. M. Mousa, N. S. Ammar, H. A. Ibrahim, *J. Saudi Chem. Soc.* **20** (2016) 357 (<https://doi.org/10.1016/j.jscs.2014.12.006>)
4. A. Choinska-Pulit, J. Sobolczyk-Bednarek, W. Laba, *Ecotoxicol. Environ. Saf.* **149** (2018) 275 (<https://doi.org/10.1016/j.ecoenv.2017.12.008>).